
Διερεύνηση της πιθανότητας ανάπτυξης γεωμαγνητικώς
επαγομένων ρευμάτων στον Ελλαδικό χώρο

Investigating the possibility of the development of
Geomagnetically Induced Currents (GIC) in Greece

By

Adamantia Zoe Boutsis



HELLENIC REPUBLIC

**National and Kapodistrian
University of Athens**

— EST. 1837 —

Department of Physics

A dissertation submitted to the National and Kapodistrian
University of Athens in accordance with the requirements of
the degree of DOCTOR OF PHILOSOPHY in the Department of
Physics.

NOVEMBER 2023



HELLENIC REPUBLIC
**National and Kapodistrian
University of Athens**
— EST. 1837 —

Supervising Committee:

1. George Balasis, Research Director, National Observatory of Athens (Principal)
2. Ioannis A. Daglis, Professor, National & Kapodistrian University of Athens
3. Kanaris Tsinganos, Emeritus Professor, National & Kapodistrian University of Athens

«The implementation of the doctoral thesis was co-financed by Greece and the European Union (European Social Fund-ESF) through the Operational Programme «Human Resources Development, Education and Lifelong Learning» in the context of the Act “Enhancing Human Resources Research Potential by undertaking a Doctoral Research” Sub-action 2: IKY Scholarship Programme for PhD candidates in the Greek Universities».



This dissertation has been examined and approved in partial fulfillment of the requirements for the degree of Doctor of Philosophy in Space Physics by the:

Examination Committee:

1. George Balasis, Research Director, National Observatory of Athens
2. Ioannis A. Dagalos, Professor, National & Kapodistrian University of Athens
3. Kanaris Tsinganos, Emeritus Professor, National & Kapodistrian University of Athens
4. Despina Hatzidimitriou, Professor, National & Kapodistrian University of Athens
5. Nicholas Sarlis, Professor, National & Kapodistrian University of Athens
6. Anastasios Anastasiadis, Research Director, National Observatory of Athens
7. Anna Belehaki, Research Director, National Observatory of Athens

ΕΚΤΕΤΑΜΕΝΗ ΠΕΡΙΛΗΨΗ

Η εμφάνιση Γεωμαγνητικώς Επαγομένων Ρευμάτων (Geomagnetically Induced Currents – GICs) στην επιφάνεια της Γης σχετίζεται με έντονες διακυμάνσεις του γεωμαγνητικού πεδίου των οποίων η πηγή βρίσκεται σε ισχυρές διαταραχές στο εγγύς γεωδιάστημα [1, 2, 3]. Η ανάπτυξη GICs μπορεί να έχει ως πιθανό αποτέλεσμα την πρόκληση σοβαρών βλαβών στο δίκτυο μεταφοράς και παροχής ηλεκτρικής ενέργειας [4]. Κατά τη διάρκεια γεωδιαστημικών μαγνητικών καταιγίδων αναπτύσσονται ισχυρά ηλεκτρικά ρεύματα, που ρέουν στο εγγύς προς τη Γη διάστημα και “κλείνουν” μέσω της ανώτερης ατμόσφαιρας. Το μαγνητικό πεδίο που αναπτύσσεται σαν αποτέλεσμα αυτών των ρευμάτων με τη σειρά του επάγει ρεύματα στην επιφάνεια της Γης (GICs), η ένταση των οποίων εξαρτάται από την κατανομή των ηλεκτρικών ιδιοτήτων του στερεού φλοιού της Γης. Τα GICs είναι το τέλος της αλυσίδας του διαστημικού καιρού (space weather): Ήλιος – ηλιακός άνεμος – μαγνητόσφαιρα – ιονόσφαιρα – επιφάνεια της Γης. Ως εκ τούτου, σήμερα αποτελούν αναπόσπαστο μέρος της έρευνας του διαστημικού καιρού. Η παραδοσιακή άποψη ήταν ότι μόνο δίκτυα ηλεκτρικής ενέργειας σε υψηλά γεωγραφικά πλάτη (Βόρεια Αμερική, Σκανδιναβία) επηρεάζονται από GICs. Αυτό όμως δεν εξηγεί τα προβλήματα ηλεκτρικής ισχύος που έχουν πρόσφατα αναφερθεί σε χαμηλά πλάτη (π.χ. Ισπανία, Ν. Αφρική, Ιαπωνία, Κίνα), σε πλάτη δηλαδή παρόμοια με αυτά της Ελλάδας.

Η παρούσα διδακτορική διατριβή έχει επικεντρωθεί στους ακόλουθους βασικούς άξονες έρευνας:

- Ανάλυση χρονοσειρών μετρήσεων του γεωμαγνητικού πεδίου από επίγεια δίκτυα μαγνητομέτρων τα οποία βρίσκονται κυρίως στην Ευρώπη με έμφαση στην περιοχή της Μεσογείου, διαστημικών μαγνητομέτρων από τους δορυφόρους Swarm του Ευρωπαϊκού Οργανισμού Διαστήματος (European Space Agency - ESA) καθώς και δεικτών γεωμαγνητικής δραστηριότητας όσον αφορά μαγνητικές καταιγίδες και υποκαταιγίδες. Η ανάλυση έγινε με χρήση προηγμένων μεθόδων επεξεργασίας σήματος, που εδράζονται σε μετασχηματισμούς wavelet, υπολογισμό εκθέτη Hurst, και μέτρων εντροπίας, προκειμένου να αποτυπώσουμε την τυχόν ύπαρξη χαρακτηριστικών υπογραφών πριν από την έναρξη μαγνητικών καταιγίδων. Εφόσον τα GICs σχετίζονται με επεισόδια του διαστημικού καιρού, οι ενδείξεις για επικείμενες καταιγίδες συνεισφέρουν στην έγκαιρη προειδοποίηση για ανάπτυξη των GICs σε περιοχές που φιλοξενούν κρίσιμες τεχνολογικά υποδομές.
- Υπολογισμός ενός δείκτη δραστηριότητας GIC για την Ελλάδα και γενικότερα τη Νότια Ευρώπη, εστιάζοντας σε μαγνητικές καταιγίδες που συνέβησαν στη διάρκεια του προηγούμενου (24^{ου}) ηλιακού κύκλου.
- Υπολογισμός της έντασης του γεωηλεκτρικού πεδίου E , λαμβάνοντας υπόψη την ηλεκτρική αγωγιμότητα του υπεδάφους και, κατ' επέκταση αναλυτική εκτίμηση του βαθμού τρωτότητας των συστημάτων διανομής ηλεκτρικής ενέργειας της χώρας μας, καθώς και της νότιας Ευρώπης, κατά την εκδήλωση ακραίων φαινομένων του διαστημικού καιρού, όπως είναι οι μαγνητικές καταιγίδες.

Η κατανόηση του βαθμού που τα GICs μπορούν να επηρεάσουν τη λειτουργία των συστημάτων ηλεκτροδότησης βελτιώθηκε σημαντικά μετά από τα προβλήματα που δημιουργήθηκαν στη Β. Αμερική κατά τη διάρκεια της μαγνητικής καταιγίδας του Μαρτίου του 1989 [5]. Χαρακτηριστική συνέπεια ήταν το εκτεταμένο blackout διάρκειας 9 ωρών στο υδροηλεκτρικό εργοστάσιο της Hydro-Québec. Προφανώς, ο επακόλουθος κοινωνικός/οικονομικός αντίκτυπος σχετίζεται με την ένταση του φαινομένου, όπως υποδεικνύεται και από την έκθεση του National Research Council [6].

Οι δυσμενείς επιπτώσεις των GICs αρχικά αποτέλεσαν πεδίο μελέτης στα υψηλά γεωμαγνητικά πλάτη, όπου κυριαρχούν τα σελαϊκά ιονοσφαιρικά ρεύματα, οδηγώντας τις επίγειες διακυμάνσεις του μαγνητικού πεδίου σε υψηλές τιμές. Όμως, μεγάλες τιμές GICs έχουν πλέον παρατηρηθεί σε κάθε γεωγραφικό πλάτος. Στην Ευρώπη, μάλιστα, αυτό ενισχύεται και από το μοντέλο εμφάνισης των GICs σε όλη την έκταση της ηπείρου [7]. Σύμφωνα με τον Karpenman [8] η πηγή των διατηρούμενων GICs στα χαμηλά και μεσαία γεωγραφικά πλάτη σχετίζεται με υψηλές τιμές διακύμανσης, που οφείλονται στις αυθόρμητες εξάρσεις της δυναμικής πίεσης του ηλιακού ανέμου ή στην ισχυροποίηση του δακτυλιοειδούς ρεύματος. Στις περιοχές αυτές, οι μέγιστες τιμές της χρονικής μεταβολής της οριζόντιας συνιστώσας του μαγνητικού πεδίου (dB_H/dt) συνήθως συμπίπτουν με την απότομη έναρξη της καταιγίδας και όχι κατά τη διάρκεια της κύριας φάσης της, άρα η επικινδυνότητα είναι μεγαλύτερη τότε [9]. Η εκτίμηση των GICs στα χαμηλά και μεσαία γεωγραφικά πλάτη λαμβάνει ολοένα και περισσότερη προσοχή από την επιστημονική κοινότητα τα τελευταία χρόνια, με μελέτες να έχουν ήδη γίνει στην Ισπανία [10,11,12], την Ιταλία [13], την Αυστρία [14], την Ιαπωνία [15], την Κίνα [16] τη Ν. Ζηλανδία [17], την Αυστραλία [18], τη Ν. Αφρική [19] κ.ά.

Λαμβάνοντας υπόψη τα όσα αναφέρθηκαν παραπάνω, το ερώτημα που καλούμαστε να απαντήσουμε είναι το κατά πόσον το δίκτυο ηλεκτροδότησης της Ελλάδας, μιας περιοχής που βρίσκεται σε μεσαία γεωγραφικά πλάτη, κινδυνεύει και σε τι βαθμό από GICs που αναμένεται να αναπτυχθούν στην περίπτωση μιας ισχυρής μαγνητικής καταιγίδας. Ο υπολογισμός ενός δείκτη GIC μπορεί να συμβάλει καθοριστικά στη λήψη μέτρων προστασίας από τους παρόχους ηλεκτρικής ενέργειας καθώς και τους χειριστές των δικτύων διανομής ηλεκτρισμού στην Ελλάδα, αλλά και στην Ευρώπη γενικότερα, σε μελλοντική βάση, ενώ συνεισφέρει και στην έρευνα για την πρόγνωση του διαστημικού καιρού.

Είναι η πρώτη φορά που επιχειρείται η εκτίμηση των GICs στον Ελλαδικό χώρο, μελέτη που εναρμονίζεται απόλυτα με αντίστοιχες έρευνες ανά τον κόσμο. Επομένως, η διατριβή αυτή καλύπτει σε σημαντικό βαθμό το υπάρχον κενό στη βιβλιογραφία, πραγματοποιώντας κατ'αντιστοιχία μια εκτίμηση και δόμηση προτύπου κατανομής των GICs στην Ελλάδα.

Για την επεξεργασία των χρονοσειρών (δεδομένων γεωμαγνητικού πεδίου) εφαρμόστηκαν μέθοδοι φασματικής ανάλυσης, με όρους μετασχηματισμών wavelet σε προγραμματιστικό περιβάλλον MATLAB. Προκειμένου να γίνουν συγκρίσεις και να εξαχθούν χρήσιμα συμπεράσματα, συνεπικουρικά αναλύθηκαν δείκτες γεωμαγνητικής δραστηριότητας, συμπεριλαμβανομένων δεικτών που προέκυψαν από δορυφορικά δεδομένα της αποστολής Swarm [20] πέραν των κλασικών επίγειων δεικτών SYM-H (για καταιγίδες) και AE (για υποκαταιγίδες). Ακόμη, πραγματοποιήθηκε υπολογισμός του εκθέτη Hurst [2] και των μέτρων εντροπίας: Shannon entropy [21], Tsallis entropy [22, 23] και Fisher information [24]. Οι συγκεκριμένες στατιστικές μέθοδοι με βάση τη θεωρία της πληροφορίας

(Information Theory) χρησιμοποιούνται ευρέως μαζί με διάφορες άλλες μεθόδους, προκειμένου να εξαχθούν χρήσιμα συμπεράσματα από μελέτες πολύπλοκων συστημάτων, όπως για παράδειγμα το συζευγμένο σύστημα ηλιακός άνεμος-μαγνητόσφαιρα-ιονόσφαιρα. Συγκεκριμένα, ο εκθέτης Hurst είναι ένα στατιστικό μέτρο που χαρακτηρίζει τις επίμονες ή μη-επίμονες (persistent/non-persistent) ιδιότητες ενός σήματος. Η εντροπία Shannon είναι μία έννοια που χρησιμοποιείται για να διερευνηθεί το μέγεθος της πληροφορίας ενός μεταδιδόμενου μηνύματος, ενώ η εντροπία Tsallis αποτελεί μια γενίκευση της εντροπίας Boltzmann-Gibbs και χρησιμοποιείται ευρέως σε πολλά πεδία έρευνας. Τέλος, το στατιστικό μέτρο Fisher information αποτελεί μία ισχυρή μέθοδο μελέτης μη-στάσιμων και μη-γραμμικών χρονοσειρών.

Ο δείκτης GIC αποτελεί μία ένδειξη (proxy) του γεωηλεκτρικού πεδίου και υπολογίζεται αποκλειστικά από δεδομένα μαγνητικού πεδίου [18]. Έχει δύο εκδοχές (GIC_x-GIC_y) και υπολογίστηκε για τις ισχυρότερες γεωμαγνητικές καταιγίδες (δηλ., δείκτης Dst < -150 nT) που συνέβησαν κατά τη διάρκεια του 24^{ου} ηλιακού κύκλου (δηλ., Μάρτιος, Ιούνιος και Δεκέμβριος 2015, και Αύγουστος 2018), χρησιμοποιώντας δεδομένα από το δίκτυο μαγνητομέτρων ENIGMA (<http://enigma.space.noa.gr/>) [25]. Στη συνέχεια, η έρευνα επεκτάθηκε στην ευρύτερη περιοχή της Μεσογείου. Ο δείκτης GIC υπολογίστηκε χρησιμοποιώντας δεδομένα από τα γεωμαγνητικά παρατηρητήρια Castello Tesino (CTS) στην Ιταλία, Chambon la Forêt (CLF) στη Γαλλία, Ebro (EBR) και San Fernando (SFS) στην Ισπανία, Tamanrasset (TAM) στην Αλγερία και Iznik (IZN) στην Τουρκία. Στόχος ήταν να πραγματοποιηθεί μία πρώτη εκτίμηση του γεωηλεκτρικού πεδίου και κατ'επέκταση της έντασης των GICs στην περιοχή γύρω από τον εκάστοτε μαγνητικό σταθμό / παρατηρητήριο, καθώς και να μελετήσουμε τη συμπεριφορά του δείκτη κατά την αιφνίδια έναρξη της εκάστοτε καταιγίδας (sudden storm commencement – SSC).

Στην περίπτωση της καταιγίδας στις 17 Μαρτίου 2015 έγινε μία προσπάθεια εξαγωγής χαρτών μέγιστης ημερήσιας τιμής του δείκτη GIC, καθώς και της τιμής του δείκτη κατά τον SSC.

Στη συνέχεια, η έρευνα στράφηκε στην ενσωμάτωση μονοδιάστατων (1-D) μοντέλων αγωγιμότητας του εδάφους στους χάρτες της μέγιστης ημερήσιας τιμής του δείκτη GIC με στόχο την καλύτερη εκτίμηση του γεωηλεκτρικού πεδίου σε κάθε τοποθεσία. Συγκεκριμένα, προκειμένου να γίνει μια συσχέτιση με υπάρχοντα μοντέλα ηλεκτρικής αγωγιμότητας, ενσωματώσαμε έναν χάρτη αγωγιμότητας του εδάφους της Ευρώπης σε μορφή πλέγματος [26], κάθε κελί του οποίου αντιστοιχεί σε ένα 1-D μοντέλο, δηλ. η αγωγιμότητα μεταβάλλεται μόνο με το βάθος, χαρακτηριζόμενο από τις αντίστοιχες αγωγιμότητες σε βάθος 80 km. Χρησιμοποιήθηκαν οι τιμές από το ευρωπαϊκό πρόγραμμα EURISGIC (<https://cordis.europa.eu/project/id/260330>), μιας «συλλογής» μονοδιάστατων μοντέλων που καλύπτει σχεδόν ολόκληρη την Ευρώπη. Στην περίπτωσή μας, καλύπτονται κυρίως σταθμοί στις ηπειρωτικές περιοχές βόρεια της Μεσογείου θάλασσας, καθώς αντίστοιχη συλλογή για τις περιοχές νότια της Μεσογείου θάλασσας δεν υπάρχει, τουλάχιστον εν γνώσει μας. Η συνεκτίμηση των τιμών του δείκτη GIC και των τιμών του 1-D μοντέλου μας δίνουν μια καλύτερη εικόνα της επικινδυνότητας των GICs στις περιοχές γύρω από κάθε μαγνητικό σταθμό / παρατηρητήριο.

Επιπροσθέτως, η μελέτη επεκτάθηκε όσον αφορά τον υπολογισμό της έντασης του γεωηλεκτρικού πεδίου E , λαμβάνοντας υπόψιν την ηλεκτρική αγωγιμότητα του υπεδάφους, η οποία καθορίζει την τιμή της έντασης στη διάρκεια μιας καταιγίδας. Με βάση

το 1-D μοντέλο έγινε υπολογισμός του γεωηλεκτρικού πεδίου E , κι επομένως συσχετίσαμε τις τιμές του δείκτη GIC με τις τιμές του γεωηλεκτρικού πεδίου E , που αναπτύσσεται στη διάρκεια μιας καταιγίδας.

Τέλος, έγινε διερεύνηση και καταγραφή των μαγνητικών καταιγίδων που έλαβαν χώρα από τον Σεπτέμβριο του 2018 έως και τον Αύγουστο του 2022, προκειμένου να εμπλουτίσουμε τη μελέτη μας και με μαγνητικές καταιγίδες του 25^{ου} ηλιακού κύκλου. Με βάση τη συνθήκη “Dst < -150 nT” που υιοθετήσαμε για τον 24^ο ηλιακό κύκλο δεν έχει καταγραφεί καμία καταιγίδα. Μικρότερης έντασης καταιγίδα έχει καταγραφεί στις 4/11/2021 (Dst = -105 nT). Επιπλέον, στο χρονικό διάστημα αυτό έχουν σημειωθεί άλλες έξι καταιγίδες ακόμη μικρότερης έντασης (Dst < -80 nT).

Τα συμπεράσματα αυτής της διατριβής συνοψίζονται στα παρακάτω:

1. *Φασματική ανάλυση με όρους μετασχηματισμών wavelet, δείκτης Hurst και μέτρα εντροπίας σε χρονοσειρές μαγνητικού πεδίου της Γης (επίγεια και δορυφορικά δεδομένα) και σε δείκτες γεωμαγνητικής δραστηριότητας*

Η φασματική ανάλυση με όρους μετασχηματισμών **wavelet** έδειξε πως τόσο πριν όσο και μετά από κάθε καταιγίδα υπάρχει έντονο φασματικό περιεχόμενο, χαρακτηριστικό των επεισοδίων αυτών. Στην περίπτωση των δεικτών γεωμαγνητικής δραστηριότητας SYM-H και Swarm-derived SYM-H ο **εκθέτης Hurst** και τα μέτρα εντροπίας **Shannon entropy**, **nonextensive Tsallis entropy** και **Fisher information** έδειξαν την ύπαρξη δύο διαφορετικών μοτίβων: (i) ένα μοτίβο που σχετίζεται με τις ισχυρές μαγνητικές καταιγίδες, χαρακτηριστικό του οποίου είναι οι υψηλές τιμές του εκθέτη Hurst, κι επομένως υπάρχει μεγαλύτερη «οργάνωση» στη μαγνητόσφαιρα, και (ii) ένα μοτίβο που σχετίζεται με τις ήσυχες περιόδους της μαγνητόσφαιρας, χαρακτηριστικό του οποίου είναι οι χαμηλότερες τιμές του εκθέτη Hurst, κι επομένως υπάρχει μικρότερη «οργάνωση» στη μαγνητόσφαιρα. Στην περίπτωση των δεικτών γεωμαγνητικής δραστηριότητας AE και Swarm-derived AE, η φασματική ανάλυση με όρους μετασχηματισμών wavelet αποκάλυψε παρόμοια υποκείμενα χαρακτηριστικά στο φάσμα πριν και μετά από τις τρεις καταιγίδες, παρότι πρόκειται για δείκτες υποκαταιγίδων. Ωστόσο, ο εκθέτης Hurst και οι εντροπικές αναλύσεις δεν είχαν ως αποτέλεσμα την εικόνα δύο χαρακτηριστικών μοτίβων, καθώς πρόκειται για δείκτες που σχετίζονται με υποκαταιγίδες, οι οποίες είναι πιο βραχύβιες και λιγότερο δυναμικές, συμβαίνουν πιο συχνά από τις καταιγίδες κι έχουν διαφορετικές χαρακτηριστικές χρονικές κλίμακες καθώς και μηχανισμούς δημιουργίας απ’ ότι οι καταιγίδες. Τα αποτελέσματα αυτά παρουσιάζονται στην εργασία [27].

2. *Ανάλυση δείκτη GIC σε χρονοσειρές μαγνητικού πεδίου της Γης (επίγεια δεδομένα)*

Σχετικά με το **δείκτη GIC**, τα αποτελέσματά μας έδειξαν μία καλή συσχέτιση μεταξύ της αιφνίδιας έναρξης καταιγίδας (storm sudden commencement - SSC) και της αύξησης του δείκτη GIC. Μάλιστα, οι μέγιστες τιμές των δεικτών GICy και GICx εμφανίζονται μέσα στα πρώτα τέσσερα (4) λεπτά από την αιφνίδια έναρξη της εκάστοτε καταιγίδας σε όλους τους μαγνητικούς σταθμούς / παρατηρητήρια που συμπεριλαμβάνει η μελέτη μας. Σε μια πρώτη ανάγνωση και σύμφωνα με τις τιμές του δείκτη GIC που υπολογίσαμε για τα χρονικά διαστήματα των 4 μαγνητικών

καταιγίδων φαίνεται ότι παρά τις αυξημένες τιμές του δείκτη GIC, οι αναμενόμενες επιβλαβείς επιπτώσεις παραμένουν σε χαμηλά επίπεδα για τις περιοχές που καλύπτονται από τους συγκεκριμένους μαγνητικούς σταθμούς / παρατηρητήρια. Ωστόσο, ο εν λόγω δείκτης μας δίνει μία πρώτη εκτίμηση του βαθμού επικινδυνότητας από την ανάπτυξη τέτοιων ρευμάτων μίας κρίσιμης τεχνολογικά υποδομής χωρίς να λαμβάνεται υπόψη η γεωηλεκτρική δομή της ευρύτερης περιοχής, δηλ. η κατανομή της ηλεκτρικής αγωγιμότητας με το βάθος, η οποία μπορεί να συνεισφέρει στην αυξομείωση των τιμών των GICs στη διάρκεια μίας μαγνητικής καταιγίδας. Τα αποτελέσματα αυτά παρουσιάζονται στην εργασία [28].

3. *Συγκρίσεις μεταξύ των τιμών του δείκτη GIC και της ηλεκτρικής αγωγιμότητας του φλοιού της Γης*

Όσον αφορά τους **χάρτες της μέγιστης ημερήσιας τιμής του δείκτη GIC**, παρατηρούμε ότι οι γραμμές ίσης τιμής (contour) είναι σχετικά ακαθόριστες πριν (16 Μαρτίου 2015) και μετά (18 Μαρτίου 2015) από την καταιγίδα, όμως τείνουν να γίνονται πιο οριζόντιες και διαβαθμισμένης έντασης (αυξανόμενης από νότο προς βορρά) κατά τη διάρκεια της καταιγίδας (17 Μαρτίου 2015), επιβεβαιώνοντας την ύπαρξη μεγαλύτερης «οργάνωσης» στη γήινη μαγνητόσφαιρα. Η συνεκτίμηση των τιμών της αντίστασης (αγωγιμότητας) του εδάφους και του δείκτη GIC μας επιτρέπει, σε ένα βαθμό, να οπτικοποιήσουμε την επίδραση των GICs στη νότια Ευρώπη. Στους χάρτες μας παρατηρούμε πως οι γραμμές ίσης τιμής του δείκτη GIC φαίνονται μεν ομαλές, όμως διατέμνουν περιοχές με πολύ διαφορετικές αγωγιμότητες εδάφους κι άρα αυτό μπορεί να έχει διαφορετικές συνέπειες όσον αφορά την ανάπτυξη των GICs σε κρίσιμες υποδομές που βρίσκονται στις περιοχές αυτές. Συνεπώς, η συγκεκριμένη παράμετρος θα πρέπει να συνεκτιμηθεί για την επικινδυνότητα λόγω GICs. Τα αποτελέσματα αυτά παρουσιάζονται στην εργασία [28].

4. *Συγκρίσεις μεταξύ των τιμών του δείκτη GIC και του γεωηλεκτρικού πεδίου E*

Συγκρίνοντας τα εκτιμώμενα γεωηλεκτρικά πεδία E με τους αντίστοιχους δείκτες GIC, για τους σταθμούς Chambon la Forêt (CLF), Castello Tesino (CTS), Dionysos (DIO), Ebro (EBR), San Fernando (SFS), και Velies (VLI) κατά τη διάρκεια 3 ημερών γύρω από τη μαγνητική καταιγίδα της 17^{ης} Μαρτίου 2015 βρήκαμε ότι οι τιμές των συντελεστών συσχέτισης κυμαίνονται μεταξύ 0.54 και 0.65. Το αποτέλεσμα αυτό δείχνει την ύπαρξη μιας διακριτής θετικής γραμμικής συσχέτισης μεταξύ των δύο μεταβλητών, όμως υπάρχουν κι άλλοι παράγοντες που επηρεάζουν το γεωηλεκτρικό πεδίο.

Η έντονη διακύμανση των τιμών αγωγιμότητας του εδάφους στα μονοδιάστατα μοντέλα εδάφους για την Ευρώπη έχει ως αποτέλεσμα οι αγωγιμότητες τοπικά να διαφέρουν κατά ένα παράγοντα 100 ή και περισσότερο, ακόμη και σε χώρες με έκταση όπως η Ισπανία ή η Ελλάδα. Και τα ηλεκτρικά πεδία που υπολογίζονται με τη χρήση των μοντέλων αυτών διαφέρουν τοπικά το ίδιο ή και περισσότερο. Αυτό προστίθεται στις διακυμάνσεις μεταξύ των δεικτών GIC_x και GIC_y που

υπολογίζουμε γι' αυτές τις δύο χώρες κατά τη διάρκεια της κορύφωσης της καταιγίδας την ημέρα του St. Patrick's, που αντιστοιχούν σε έναν παράγοντα μεταξύ 1.5 και 2. Το παραπάνω δείχνει την ανεπάρκεια της χρήσης ενός μόνο παρατηρητηρίου μαγνητικού πεδίου για τον προσδιορισμό ενός δείκτη εθνικής εμβέλειας. Συνεπώς, προτείνεται η χρήση πολλών μαγνητόμετρων ανά μεγάλη ευρωπαϊκή χώρα, προκειμένου να αποτυπωθεί η πολυπλοκότητα των επαγόμενων ηλεκτρικών πεδίων E .

Η διδακτορική διατριβή είναι χωρισμένη σε επιμέρους κεφάλαια των οποίων η περίληψη ακολουθεί:

Στο *πρώτο κεφάλαιο* παρουσιάζεται το θεωρητικό πλαίσιο το οποίο είναι απαραίτητο για τη μελέτη των φαινομένων διαστημικού καιρού που μας ενδιαφέρουν – δίνεται έμφαση στις γεωμαγνητικές καταιγίδες καθώς και στα GICs. Παράλληλα, παρατίθεται και ένα πλήθος αποτελεσμάτων που υπάρχουν στη βιβλιογραφία τα οποία αποτελούν τη βάση και το έναυσμα για τη μελέτη που πραγματοποιήθηκε και παρουσιάζεται σε αυτήν τη διατριβή.

Στο *δεύτερο κεφάλαιο* παρουσιάζονται οι μέθοδοι ανάλυσης χρονοσειρών γεωμαγνητικού πεδίου (και των δεικτών γεωμαγνητικής δραστηριότητας) που χρησιμοποιήθηκαν στη διατριβή. Συγκεκριμένα, παρουσιάζονται η φασματική ανάλυση με όρους wavelet, ο εκθέτης Hurst και τα μέτρα εντροπίας Shannon entropy, nonextensive Tsallis entropy και Fisher information.

Στο *τρίτο κεφάλαιο* διερευνάται η δυναμική πολυπλοκότητα των δεικτών γεωμαγνητικής δραστηριότητας, με χρήση της θεωρίας πληροφορίας (Information Theory). Οι μέθοδοι που παρουσιάστηκαν στο *δεύτερο κεφάλαιο* εφαρμόστηκαν στους δείκτες γεωμαγνητικής δραστηριότητας SYM-H και AE, καθώς και στους δείκτες Swarm-derived SYM-H και Swarm-derived AE, δύο αντιστοιχούς δείκτες που προκύπτουν από δορυφορικά δεδομένα της συστοιχίας δορυφόρων Swarm της ESA [27].

Στο *τέταρτο κεφάλαιο* παρουσιάζονται τα δεδομένα που χρησιμοποιήθηκαν και η μεθοδολογία υπολογισμού του δείκτη GIC (GIC index). Ο δείκτης υπολογίζεται για τις ισχυρότερες μαγνητικές καταιγίδες (δηλ., ελάχιστη τιμή του δείκτη Dst < -150 nT) που συνέβησαν κατά τη διάρκεια του 24^{ου} ηλιακού κύκλου σε σταθμούς της Ελλάδας και της ευρύτερης περιοχής της Μεσογείου. Τα αποτελέσματα παρουσιάζονται σε γραφήματα με χρήση χρωματικής κλίμακας πέντε επιπέδων, που αντιστοιχούν στους βαθμούς επικινδυνότητας (πολύ χαμηλός έως ακραίος κίνδυνος). Γίνεται συσχέτιση με το SSC της κάθε καταιγίδας [28].

Στο *πέμπτο κεφάλαιο* παρουσιάζονται χάρτες μέγιστης τιμής του δείκτη GIC στην περιοχή της Μεσογείου για την περίπτωση της ισχυρότερης μαγνητικής καταιγίδας του 24^{ου} ηλιακού κύκλου, η οποία έλαβε χώρα στις 17 Μαρτίου 2015 (St. Patrick's Day storm). Οι χάρτες παρουσιάζουν είτε το δείκτη GIC σε συνδυασμό με την αγωγιμότητα του εδάφους (1-D model) είτε το υπολογισμένο γεωηλεκτρικό πεδίο E σε συνδυασμό με το δίκτυο ηλεκτροδότησης (<https://www.entsoe.eu/data/map/>) [28].

Στο έκτο κεφάλαιο παρουσιάζονται τα συμπεράσματα και προτείνονται μελλοντικά βήματα για τη συνέχεια της εν λόγω έρευνας.

Βιβλιογραφία

1. Daglis, I. A., J. U. Kozyra, Y. Kamide, D. Vassiliadis, A. S. Sharma, M. W. Liemohn, W. D. Gonzalez, B. T. Tsurutani, and G. Lu (2003), Intense space storms: Critical issues and open disputes, *J. Geophys. Res.*, 108, 1208, doi:10.1029/2002JA009722
2. Balasis, G., I. A. Daglis, P. Kapiris, M. Manda, D. Vassiliadis, and K. Eftaxias (2006), From pre-storm activity to magnetic storms: a transition described in terms of fractal dynamics, *Ann. Geophys.*, 24, 3557–3567
3. Boteler, D. H. (2003), Geomagnetic hazards to conducting networks, *Nat. Hazards*, 28, 537 – 561
4. Daglis, I. A., D. N. Baker, Y. Galperin, J. G. Kappenman, and L. J. Lanzerotti (2001), Technological impacts of space storms: Outstanding issues, *Eos Trans. AGU*, 82, 585, doi:10.1029/01EO00340
5. Kappenman, J. G., and V. D. Albertson (1990), Bracing for the geomagnetic storms, *IEEE Spectrum*, March 1990, 27–33
6. National Research Council (2008), Severe space weather events - Understanding societal and economic impacts: A workshop report, *Tech. rep.*, National Research Council (NRC), Washington, DC
7. Viljanen, A., R. Pirjola, E. Prácsér, J. Katkalov, and M. Wik (2014), Geomagnetically induced currents in Europe, *J. Space Weather Space Clim.*, 4, A09, doi:10.1051/swsc/2014006
8. Kappenman, J. G. (2005), An overview of the impulsive geomagnetic field disturbances and power grid impacts associated with the violent Sun-Earth connection events of 29–31 October 2003 and a comparative evaluation with other contemporary storms, *Space Weather*, 3, S08C01, doi:10.1029/2004SW000128
9. Kappenman, J. G. (2003), Storm sudden commencement events and the associated geomagnetically induced current risks to groundbased systems at low-latitude and midlatitude locations, *Space Weather*, 1(3), 1016, doi:10.1029/2003SW000009
10. Torta, J. M., L. Serrano, J. R. Regué, A. M. Sánchez, and E. Roldán (2012), Geomagnetically induced currents in a power grid of northeastern Spain, *Space Weather*, 10, doi:10.1029/2012SW000793
11. Torta, J. M., S. Marsal, and M. Quintana (2014), Assessing the hazard from geomagnetically induced currents to the Spanish entire high-voltage power network in Spain, *Earth, Planets Sp.*, 66(1), 1– 17, doi:10.1186/1880-5981-66-87
12. Torta, J. M., A. Marcuello, J. Campanyà, S. Marsal, P. Queralt, and J. Ledo (2017), Improving the modeling of geomagnetically induced currents in Spain, *Space Weather*, 15, 691–703, doi: 10.1002/2017SW001628
13. Tozzi, R., P. De Michelis, I. Coco, and F. Giannattasio (2019), A preliminary risk assessment of geomagnetically induced currents over the Italian territory, *Space Weather*, 17(1), 46-58, doi:10.1029/2018SW002065
14. Bailey, R. L., T. S. Halbedl, I. Schattauer, A. Römer, G. Achleitner, C. D. Beggan, V. Wetztergom, R. Egli, and R. Leonhardt (2017), Modelling geomagnetically induced currents in midlatitude Central Europe using a thin-sheet approach, *Ann. Geophys.*, 35, 751-761, doi:10.5194/angeo-35-751-2017
15. Watari, S., M. Kunitake, K. Kitamura, T. Hori, T. Kikuchi, K. Shiokawa, N. Nishitani, R. Kataoka, Y. Kamide, T. Aso, Y. Watanabe, and Y. Tsuneta (2009), Measurements

-
- of geomagnetically induced current in a power grid in Hokkaido, Japan, *Space Weather*, 7, S03002, doi:10.1029/2008SW000417
16. Liu, C.-M., L.-G. Liu, and R. Pirjola (2009), Geomagnetically induced currents in the high-voltage power grid in China, *IEEE Trans. Power Deliv.*, 24, 2368–2374
 17. Beland, J., and K. Small (2005), Space weather effects on power transmission systems: The cases of Hydro-Québec and Transpower New Zealand Ltd., in: *Effects of space weather on technology infrastructure*, 287–299, Springer
 18. Marshall, R. A., E. A. Smith, M. J. Francis, C. L. Waters, and M. D. Sciffer (2011), A preliminary risk assessment of the Australian region power network to space weather, *Space Weather*, 9, S10004, doi:10.1029/2011SW000685
 19. Ngwira, C. M., A. Pulkkinen, L.-A. McKinnell, and P. J. Cilliers (2008), Improved modeling of geomagnetically induced currents in the South African power network, *Space Weather*, 6, S11004, doi:10.1029/2008SW000408
 20. Papadimitriou, C., G. Balasis, A. Z. Boutsis, A. Antonopoulou, G. Moutsiana, I. A. Daglis, O. Giannakis, P. De Michelis, G. Consolini, J. Gjerloev, et al. (2021), Swarm-derived indices of geomagnetic activity. *J. Geophys. Res. Space Phys.*, 126, e2021JA029394
 21. Shannon, C. E. (1948), A mathematical theory of communication, *Bell Syst. Tech. J.*, 27, 379–423
 22. Tsallis, C. (2009), Introduction to Nonextensive Statistical Mechanics: Approaching a Complex World, *Springer: New York, NY, USA*, Volume 1
 23. Balasis, G., I. A. Daglis, C. Papadimitriou, A. Anastasiadis, I. Sandberg, and K. Eftaxias (2011), Quantifying dynamical complexity of magnetic storms and solar flares via nonextensive Tsallis entropy, *Entropy*, 13, 1865–1881
 24. Fisher, R. A. (1925), Theory of statistical estimation. In *Mathematical Proceedings of the Cambridge Philosophical Society*, Cambridge University Press: Cambridge, UK, Volume 22, pp. 700–725
 25. Balasis G., I. A. Daglis, Y. Contoyiannis, S. M. Potirakis, C. Papadimitriou, N. S. Melis, O. Giannakis, A. Papaioannou, A. Anastasiadis, and C. Kontoes (2018), Observation of intermittency-induced critical dynamics in geomagnetic field time series prior to the intense magnetic storms of March, June and December 2015, *J. Geophys. Res.: Space Physics*, 123. doi:10.1002/2017JA025131
 26. Ádám, A., E. Prácsér, and V. Wesztergom, (2012), Estimation of the electric resistivity distribution (EURHOM) in the european lithosphere in the frame of the EURISGIC wp2 project. *Acta Geodaetica et Geophysica Hungarica*, 47 (4), 377 – 553, 387, doi:10.1556/ageod.47.2012.4.1
 27. Balasis, G., Boutsis, A. Z., Papadimitriou, C., Potirakis, S. M., Pitsis, V., Daglis, I. A., Anastasiadis, A., Giannakis, O. (2023), Investigation of Dynamical Complexity in Swarm-Derived Geomagnetic Activity Indices Using Information Theory. *Atmosphere*, 14(5):890. <https://doi.org/10.3390/atmos14050890>
 28. Boutsis, A. Z., G. Balasis, S. Dimitrakoudis, I. A. Daglis, K. Tsinganos, C. Papadimitriou, & O. Giannakis (2023). Investigation of the geomagnetically induced current index levels in the Mediterranean region during the strongest magnetic storms of solar cycle 24. *Space Weather*, 21, e2022SW003122. doi:10.1029/2022SW003122

ABSTRACT

Strong electric currents that flow in the near-Earth space and close through the upper atmosphere can be generated during geospace magnetic storms. The magnetic field of these currents induces currents in the Earth's surface called Geomagnetically Induced Currents (GICs), the intensity of which depends on the distribution of the electrical properties in specific areas of the Earth's solid crust. GIC occurrence can potentially result in causing serious disrupts or damages to the electricity transmission and distribution network. GICs are the ground end of the space weather chain: Sun – solar wind – magnetosphere – ionosphere – Earth's surface. Hence, nowadays they constitute an integral part of the space weather research. Traditionally, it was thought that only electricity networks located in high latitudes (Northern America, Scandinavia) are affected by GICs. But this cannot explain the recently reported existence of electrical power issues in areas of low latitudes (e.g., Spain, South Africa, Italy, Japan, China), that is latitudes similar to those of Greece.

Here, we primarily investigate the possibility of GIC development in Greece. We analyze magnetic field timeseries from ground-based magnetometers located mainly in Europe, focusing on the Mediterranean region, spaceborne magnetometers from the European Space Agency (ESA) Swarm satellites, as well as geomagnetic activity indices during magnetic storms and substorms. For the analysis, we use advanced signal processing methods based on wavelet transforms, Hurst exponent calculations, and entropy measures to capture the potential existence of characteristic signatures prior to the occurrence of magnetic storms. Since GICs are related to space weather events, indications of impending storms contribute to early warnings for the development of GICs in areas hosting critical technological infrastructure. Next, we calculate the GIC index for Greece and South Europe, in general, focusing on magnetic storms that occurred during the previous (24th) solar cycle. Furthermore, we calculate the intensity of the geoelectric field E , taking into account the electrical conductivity of the ground and, consequently, conducting an analytical assessment of the vulnerability of the electrical power system in our country as well as in southern Europe during the occurrence of extreme space weather events, such as magnetic storms.

The question we are called upon to answer is whether Greece's electrical power grid, located in a middle geomagnetic latitude region, is at risk and to what extent from GICs that are expected to develop in the case of a strong magnetic storm. Calculating a GIC index can significantly contribute to the implementation of protective measures by electricity providers and distribution network operators in Greece, as well as in Europe,

on a future basis. This also contributes to research towards space weather prediction.

This is the first attempt to assess GIC development in the Greek territory, a study that aligns perfectly with similar research conducted worldwide. Therefore, this dissertation largely fills the existing gap in the literature by providing an estimation and model construction of GIC distribution patterns in Greece.

In detail, after an introductory chapter dedicated to the necessary physical framework regarding the study of space weather phenomena and specifically geospace magnetic storms and GICs, we present the geomagnetic field timeseries (and geomagnetic activity indices) analysis methods used for this dissertation. In particular, we discuss the wavelet spectral analysis, the Hurst exponent, and the entropy measures of Shannon entropy, nonextensive Tsallis entropy, and Fisher information.

In Chapter 3, we investigate the dynamical complexity of geomagnetic activity indices, using Information Theory. The methods described in Chapter 2 are applied to the SYM-H and AE indices of geomagnetic activity, as well as to the Swarm-derived SYM-H and Swarm-derived AE indices, two geomagnetic activity indices emanating from spaceborne data from the ESA Swarm constellation of satellites.

Chapter 4 is dedicated to the GIC index calculation. The data and methodology are presented and the GIC index is calculated for the strongest magnetic storms (i.e., minimum Dst index < -150 nT) of solar cycle 24 in magnetic stations / observatories of Greece and the wider Mediterranean area. Results are displayed in plots where a five-level color scale is used to match the five risk levels (very low to severe). Correlations with the Storm Sudden Commencement (SSC) of each storm are also presented.

In Chapter 5 contour maps of activity are presented. They focus on the Mediterranean region during the strongest magnetic storm of solar cycle 24, that occurred on 17 March 2015 (St. Patrick's Day storm). Contour maps present either the GIC index along with the conductivity of the ground (1-D model) or the calculated geoelectric field E along with the electricity network (<https://www.entsoe.eu/data/map/>).

The conclusions of this dissertation can be summarized in the following:

1. *Wavelet spectral analysis, Hurst exponent analysis and entropic analysis of spaceborne and ground-based Earth's magnetic field time series, as well as geomagnetic activity indices*

The spectral analysis in terms of wavelet transforms revealed that concurrently with each storm there is intense spectral content, characteristic of these events. In the case of the geomagnetic activity indices SYM-H and Swarm-derived SYM-H, the Hurst exponent and the entropy measures of Shannon entropy, nonextensive Tsallis entropy, and Fisher information indicated the existence of two different patterns:

- A pattern associated with strong magnetic storms, characterized by high values of the Hurst exponent, implying higher "organization" in the magnetosphere.

-
- A pattern related to the quiet periods of the magnetosphere, characterized by lower values of the Hurst exponent, indicating less "organization" in the magnetosphere.

In the case of AE and Swarm-derived AE indices the wavelet spectral analysis revealed similar underlying features in the power spectra for the three storms, despite the fact that we are dealing with substorm indices: the big picture of the preconditioned magnetosphere is still present. However, the Hurst exponent and entropic analyses did not result in a clear depiction of two distinct patterns. This finding is attributed to the fact that these indices are related to substorms, which are more transient and dynamic, occur more frequently than storms and have different characteristic time scales and generation mechanisms compared to magnetic storms.

2. *GIC index analysis of ground-based Earth's magnetic field time series*

Regarding the GIC index, our results showed a good correlation between the SSC and the increase in the GIC index. Furthermore, the maximum values of the GICy and GICx indices occur within the first four minutes from the abrupt onset of each respective storm at all the magnetic stations / observatories under study.

At first glance, based on the GIC index values calculated for the time periods of the four magnetic storms, it appears that despite the elevated GIC index values, the expected detrimental effects due to GICs remain at low levels for the areas covered by the specific magnetic stations / observatories. However, the GIC index provides us with an initial estimate of the level of risk posed by the development of such currents to critical technological infrastructure without taking into account the geoelectric structure of the broader region, i.e., the distribution of electrical conductivity with depth, which could contribute to the variation in GIC values during a magnetic storm.

3. *Comparisons between GIC index values and electrical conductivity of the Earth's crust*

As for the contour maps, it is observed that the contour lines are relatively sparse before (March 16, 2015) and after (March 18, 2015) the storm. However, they tend to become more horizontal and graded in intensity (increasing from south to north) during the storm on March 17, 2015, confirming the presence of higher "organization" in the Earth's magnetosphere.

Taking into account the values of ground resistance (conductivity) and the GIC index allows us, to some extent, to visualize the impact of GICs on southern Europe. In the contour maps, it is noticeable that the contour lines of the GIC index appear smooth but traverse areas with significantly different ground conductivities. Therefore, this may have varying consequences concerning the development of GICs in critical infrastructure located in these regions. Hence, this specific parameter should be considered in assessing the risk associated with GICs.

4. *Comparisons between GIC index values and geoelectric field E*

Comparing the estimated E fields and GIC indices, using measurements from the magnetic stations Chambon la Forêt (CLF), Castello Tesino (CTS), Dionysos (DIO), Ebro (EBR), San Fernando (SFS), and Velies (VLI) over a period of three days covering the magnetic storm of March 17, 2015 we found that their correlation coefficients range between 0.54 and 0.65. This suggests that while there is a discernible positive linear relationship between E fields and GIC indices, other factors may also influence the geoelectric field, resulting in moderate variability.

The large disparity of ground conductivity values of 1D (layer) ground models for Europe means that local conductances can vary by a factor of over 100 even on the scale of countries, such as Spain or Greece. The calculated E fields vary locally by at least as much. This variability is added to local variations by a factor of around 1.5 to 2 in the calculated GIC_x and GIC_y indices for those two countries during the height of St. Patrick's Day storm. This shows the inadequacy of using a single observatory for the calculation of a nationwide index. Therefore, it is suggested that multiple magnetometers per big European country are needed to capture the complexity of induced E fields.

DEDICATION AND ACKNOWLEDGEMENTS

The work presented in this thesis has been primarily carried out at the Institute of Astronomy, Astrophysics, Space Applications and Remote Sensing (IAASARS), National Observatory of Athens (NOA), Greece. I am first and foremost indebted to my advisors Res. Dir. Dr. Georgios Balasis, Prof. Dr. Ioannis A. Dagalos and Prof. Dr. Kanaris Tsinganos.

In particular, I wish to extend my heartfelt appreciation to my supervisor, Dr. Georgios Balasis, for affording me the opportunity to pursue my PhD at IAASARS, for consistently being available for guidance, and for patiently explaining intricate matters. His unwavering support throughout my doctoral journey has been invaluable. Dr. Balasis not only inspired me to embark on a PhD in the field of Space Physics, after our initial collaboration in my MSc studies, but also guided me through the complexities of my doctoral research. His mentorship has significantly contributed to my growth as a researcher and a professional. I am deeply thankful for his supervision, which has imparted a wealth of knowledge and experience while continuously providing inspiration and encouragement during the past six years.

I also would like to warmly thank the members of my doctoral committee Prof. Ioannis A. Dagalos and Prof. Kanaris Tsinganos for their invaluable comments and thorough reviews. Their contributions significantly enhanced the technical and theoretical quality of this dissertation. Especially, Prof. Ioannis A. Dagalos, an exemplary teacher and distinguished scientist, possesses extensive knowledge of relevant work in the field and I want to thank him for the opportunity he has given me to join his Space Physics Team at the National and Kapodistrian University of Athens (NKUA), as well as for his dedication to providing guidance on my work despite his tight schedule. I am also much obliged to Prof. Kanaris Tsinganos, whom I first encountered as an undergraduate student, for sparing time to be part of my committee. His adept identification of pertinent issues was immensely beneficial. I feel privileged to have been granted an opportunity to work with such front-line scientists in a field that always amazed me.

I'd like to express my appreciation to the other committee members who evaluated this thesis: Professor Despina Hatzidimitriou, Professor Nicholas Sarlis, Research Director Anastasios Anastasiadis and Research Director Anna Belehaki. I'm grateful for their dedication in reviewing my work and offering invaluable insights and suggestions.

I would also like to thank my colleagues at IAASARS and NKUA, with whom I collaborated throughout the development of this thesis, particularly Dr. Omiros Giannakis, Constantinos Papadimitriou, George Vasalos, Dr. Stavros Dimitrakoudis, Dr. Marina

Georgiou, Dr. Christos Katsavrias, Afroditi Nasi, Alexandra Antonopoulou and many others. I am sincerely grateful for their support, the fruitful discussions we engaged in, and the wonderful moments we shared together.

I am also compelled to express my gratitude to all my friends who stood by me and provided their support. Amongst many, I am deeply thankful to Alexandra, Savvina, Lilly, Maria, Giorgos, Panagiotis, Sofia and Lia. Their friendship and support went the extra mile in mitigating anxiety, overcoming difficulties and dispelling ill thoughts that occurred along the way.

Ultimately, I wish to convey my deepest appreciation and affection to my parents, Antonis Boutsis and Sophia Chionidou, for their unconditional, endless love and support, to my brother Ioannis for the invaluable assistance with computer-related issues and the emotional support, and to my partner in life Pantelis for the perpetual brainstorming sessions, the encouragement and assistance whenever I felt I was on a dead-end. Last but not - by any means - least I would like to dedicate this to my little "sunshine", my baby son Angelos-Raphael, who, over the last year and a half, has brought a smile to my face during times when nothing seemed to go as planned.

Zoe Boutsis

AUTHOR'S DECLARATION

I declare that the work in this dissertation was carried out in accordance with the requirements of the University's Regulations and Code of Practice for Research Degree Programmes and that it has not been submitted for any other academic award. Except where indicated by specific reference in the text, the work is the candidate's own work. Work done in collaboration with, or with the assistance of, others, is indicated as such. Any views expressed in the dissertation are those of the author.

SIGNED:  DATE: 28/11/2023

TABLE OF CONTENTS

	Page
List of Tables	xxiii
List of Figures	xxv
1 Introduction	1
1.1 The Sun	4
1.1.1 Solar Wind	5
1.1.2 Solar Cycle	7
1.1.3 Solar Activity	9
1.1.4 Interplanetary Coronal Mass Ejections (ICMEs)	9
1.2 Earth's Magnetosphere	10
1.3 Earth's Magnetic Field	13
1.3.1 Primary Current Systems	14
1.3.2 Earth's Polarity	16
1.3.3 Temporal Variations of the Earth's Magnetic Field	16
1.4 Geospace Disturbances	17
1.4.1 Geomagnetic Activity Indices	17
1.4.2 Geomagnetic Activity	20
1.5 Geomagnetically Induced Currents (GICs)	25
1.5.1 Geophysical Background and Calculation of GIC	27
1.5.2 GICs in High Latitudes	30
1.5.3 GICs at Middle and Low Latitudes	31
1.5.4 Transformers in Electrical Power Networks	33
1.6 Geomagnetic Field Data	36
1.7 Fluxgate Magnetometers	38
1.7.1 ENIGMA Instrumentation	39

TABLE OF CONTENTS

2	Timeseries Analysis Methods of Geomagnetic Field Data	43
2.1	Pre-processing	44
2.1.1	Data Gaps	44
2.1.2	Decimate	45
2.1.3	Detrend	45
2.1.4	Spikes	46
2.1.5	Geomagnetic Field Components	47
2.2	Fourier Transform	49
2.3	Wavelet Spectral Analysis	50
2.4	Hurst Exponent	53
2.5	Entropy Measures	55
2.5.1	Shannon Entropy	56
2.5.2	Tsallis Entropy	56
2.5.3	Fisher Information	57
3	Dynamical Complexity in Geomagnetic Activity Indices Using Information Theory	59
3.1	Data Description	60
3.1.1	Swarm-derived SYM-H Index	63
3.1.2	Swarm-Derived AE Index	64
3.2	Results	65
3.3	Discussion and Conclusions	69
4	Application of GIC Index to Magnetic Field Data	73
4.1	Data Selection	74
4.2	Methodology	77
4.3	Results	81
4.4	Solar Cycle 25	86
4.5	Discussion	88
5	Maps of Activity for the Mediterranean Region	93
5.1	Data Selection and Methodology	94
5.2	Results	95
5.3	Discussion	99
5.4	Conclusions	102
6	Overall Discussion and Conclusions	105

Bibliography	113
Appendix A	139
GIC index figures: Results from all stations / observatories	139
Appendix B	151
International Geomagnetic Reference Field (IGRF): the 13th generation	151
Appendix C	153
ESA SSA SWE portal: GIC-related products	153
Appendix D	155
List of publications in peer-reviewed journals	155
List of publications in conference proceedings	156
List of presentations in international conferences	157

LIST OF TABLES

TABLE	Page
1.1 Basic solar wind characteristics near Earth’s orbit. Source: [Bothmer and Zhukov, 2007].	6
3.1 Intense geospace magnetic storms of 2015, including the St. Patrick’s Day storm, which was the strongest storm of solar cycle 24 (2008–2019). Storm date, time and minimum Dst index value reached are given in the first, second and third columns, respectively.	62
3.2 Geospace magnetic storms between mid-August and mid-October 2015. Storm date, time and minimum Dst index value reached are given in the first, second and third columns, respectively.	68
4.1 Strongest geospace magnetic storms of solar cycle 24 (2008-2019), based on minimum Dst index values. Storm date and time (fourth and fifth column) refer to the hour of minimum Dst occurrence. Respective SC occurrences (date and time) are shown in the second and third column. For cases #1 and #3 the SCs coincide with the SSCs, while for case #2 the SSC is the third SC. Not available data are marked as N/A.	76
4.2 Geographic and altitude-adjusted corrected geomagnetic (AACGM) coordinates of all used stations / observatories in the present study; L-shell values (in geocentric coordinates, height above sphere $R_e = 6371.2$ km) are also shown in the last column.	79
4.3 GIC risk levels and corresponding GICy and GICx index thresholds, according to Marshall et al. [2011].	80
4.4 Maximum GIC index values calculated for the four magnetic storms. For each maximum value, corresponding day and time (UT) of occurrence are marked. Not available data are marked as N/A.	86

LIST OF TABLES

4.5	Maximum GIC index values calculated for the magnetic storm of November 2021. For each maximum value, corresponding day and time (UT) of occurrence are marked.	88
5.1	Maximum GIC index values calculated at the SSC occurrence (04:45:00 UT \pm 5 minutes) on 17 March 2015.	95
5.2	Daily maximum GIC index values calculated for 16, 17 and 18 March 2015.	98
5.3	Correlation coefficients r_x and r_y are calculated between E_x and GIC $_x$ index and E_y and GIC $_y$ index, respectively, for the stations CLF, CTS, EBR, DIO, VLI and SFS during 17 March 2015.	101
6.1	Strongest geospace magnetic storms of solar cycle 25 (so far), based on minimum Dst index values. Storm date and time refer to the hour of minimum Dst occurrence.	111

LIST OF FIGURES

FIGURE	Page
1.1 Technological infrastructure affected by adverse space weather effects on the Earth. Source: Courtesy of NASA: https://www.nasa.gov/mission_pages/sunearth/news/agu2011-spaceweather.html	2
1.2 The space weather / GIC chain starts from the Sun, contains complicated space and geophysical processes, and ends at GIC in technological systems at the Earth's surface. Source: Pirjola [2000].	3
1.3 Left: Schematic geometry of IMF in the ecliptic plane for solar wind with speed V_R at a distance R . The situation sketches the observed structure for a solar wind speed of 400km/s near 1 AU. The magnetic polarity of the IMF is assumed to be in anti-sunward direction (i.e., positive). Right: Curvature of the Parker spiral at the orbit of Earth for solar wind speeds between 200 and 900 km/s. Source: Bothmer and Zhukov [2007].	6
1.4 Sun's rotation periods decrease from poles to the equatorial plane. Source: https://www.nasa.gov/mission_pages/sunearth/science/solar-rotation.html . . .	8
1.5 Schematic of the basic features of an ICME: the leading shock, a compressed ambient solar-wind "sheath" where the magnetic field may be perturbed by the shock and foreshock, and a shock "driver" consisting of the coronal "ejecta" including a flux-rope-like magnetic field structure. Source: Zurbuchen and Richardson [2006].	10
1.6 Simplified schematic outline of Earth's magnetosphere structure. Source: Courtesy of NASA: https://www.nasa.gov/mission_pages/sunearth/multimedia/magnetosphere.html	11

LIST OF FIGURES

1.7	Schematic illustration of the invisible magnetic field lines generated by the Earth, represented as a dipole magnet field. Actually, our magnetic shield is squeezed in closer to Earth on the Sun-facing side and extremely elongated on the night-side due to the solar wind. Notably, the magnetic and geographic poles do not align precisely.	13
1.8	Sketch of the various sources contributing to the near-Earth magnetic field. Source: Courtesy of NOAA NCEI: https://www.ncei.noaa.gov/news/HDGM . . .	14
1.9	Schematic illustration of the (a) current systems in the ionosphere: Field-Aligned Currents (FAC), Pedersen currents and Hall currents and (b) current systems in the magnetosphere: magnetopause current, ring current and cross-tail current. Source: (a) Le et al. [2010] and (b) Koskinen [2011a] (Figure by courtesy of T. Makinen).	15
1.10	The Dst network consists of four ground-based magnetometer stations: (1) Hermanus (19.22° E -34.40° N); (2) Kakioka (140.18° E 36.23° N); (3) Honolulu (201.98° E 21.32° N) and (4) San Juan (293.88° E 18.11° N). Source: https://wdc.kugi.kyoto-u.ac.jp/dst/dir/dst2/onDstindex.html	18
1.11	Characteristic examples of Dst profiles during (a) an ICME magnetic storm and (b) a CIR magnetic storm. Source: Tsurutani [2000].	23
1.12	A sequence of images of the southern auroral zone during a major substorm taken by Dynamics Explorer 1 from 02:02 to 05:17 UT on June 13, 1983 . The substorm onset is observed in the first image at the upper left; time runs from top to bottom and then from left to right. The auroral brightening was initially localized and appears as a bright spot. The disturbance spread longitudinally and poleward. The last four images (the four right-most images) show the recovery phase of the event as the auroral luminosity decreased. Courtesy of Lou A. Frank and John D. Craven. Source: https://secwww.jhuapl.edu/techdigest/Content/techdigest/pdf/V11-N3-4/11-03-Lopez.pdf	25
1.13	Schematic illustration of the geophysics involved in the GICs development in an earthed network. Variations of the ionospheric currents generate an electric field ($E(t)$) through geomagnetic induction in the Earth's crust and surface. This electric field then drives GICs on ground conductors. Source: Viljanen and Pirjola [1994].	28

1.14	GIC flowing along the transmission line between two transformers. A time-varying ionospheric current, i.e., the primary driver of GICs is also schematically shown. Source: Wik et al. [2008]	34
1.15	Schematic illustration of the inrush current versus saturation curve versus applied voltage. Source: https://www.electrical4u.com/magnetizing-inrush-current-in-power-transformer/?utm_content=cmp-true	35
1.16	During the magnetic storm of Halloween 2003, GICs damaged the high voltage winding of this transformer at a large Eskom power station (South Africa), leading within a few weeks to a melted copper conductor and burned insulation, taking the transformer and associated 665 MW generator out of service. Credit: Trevor Gaunt, UCT. Source: https://www.sansa.org.za	36
1.17	Schematics of a fluxgate magnetometer.	40
1.18	Photograph from DIO station instrumentation (GEOMAG-02M fluxgate magnetometer).	42
1.19	Photographs from FIN station instrumentation (GEOMAG-02 magnetotelluric station)	42
2.1	Example of linear interpolation. What the function does is to return interpolated values of a 1-D function at specific query points using linear interpolation. In this example the query points are the ones marked with the blue circles. Source: Mathworks.	45
2.2	The original sinusoidal signal is decimated by a factor of 4, using a lowpass filter. Source: Mathworks.	46
2.3	Original magnetometer data (Bx component) from TAM observatory with an obvious spike in the left panel, its despiked and interpolated version in the middle panel and its detrended version in the right panel.	47
2.4	Original magnetometer data (Bx component) from IZN observatory with an obvious spike in the left panel, its despiked and interpolated version in the middle panel and its detrended version in the right panel.	48
2.5	The seven elements of the (local) magnetic field in the Cartesian coordinate system. Source: https://www.ngdc.noaa.gov/geomag/geomaginfo.shtml	49
2.6	(a) Morlet wavelet of arbitrary width and amplitude, with time along the x-axis. (b) Construction of the Morlet wavelet (blue dashed) as a Sine curve (green) modulated by a Gaussian (red). Source: https://paos.colorado.edu/research/wavelets/wavelet2.html .	52

LIST OF FIGURES

3.1 Artist’s view of the three Swarm spacecraft. Source: https://www.esa.int/ESA_Multimedia/Images/2013/11/Swarm_constellation 61

3.2 Swarm SYM-H index (**left** column) and SYM-H index (**right** column): time series (**top** row), wavelet spectra analysis (**middle** row) and Hurst exponent (**bottom** row) for the year 2015. The red line at 0.5 marks the transition from the anti-persistent behavior (blue) into the persistent fractional Brownian motion (red). 66

3.3 Swarm AE index (**left** column) and AE index (**right** column): time series (**top** row), wavelet spectra analysis (**middle** row) and Hurst exponent (**bottom** row) for the year 2015. The red line at 0.5 marks the transition from the anti-persistent behavior (blue) into the persistent fractional Brownian motion (red). 67

3.4 SYM-H index (**left** column) and SYM-H index (**right** column): time series (**top** row), Shannon entropy, Tsallis entropy and Fisher information (**bottom** row) for the year 2015. Red color is used to highlight the entropy values around the three magnetic storms of 2015 (17/3, 23/6 and 20/12). 70

3.5 Swarm AE index (**left** column) and AE index (**right** column): time series (**top** row), Shannon entropy, Tsallis entropy and Fisher information (**bottom** row) for the year 2015. Red color is used to highlight the entropy values around the three magnetic storms of 2015 (17/3, 23/6 and 20/12). 71

4.1 Geographic map displaying all the geomagnetic stations / observatories used for the present study. From North to South: Hartland (HAD, United Kingdom), Chambon la Forêt (CLF, France), Castello Tesino (CTS, Italy), Surlari (SUA, Romania), Ebro (EBR, Spain), Iznik (IZN, Turkey), Klokotos (THL, Greece), Dionysos (DIO, Greece), Velies (VLI, Greece), San Fernando (SFS, Spain), Finokalia (FIN, Greece) and Tamanrasset (TAM, Algeria). 78

4.2 Storm of 17 March 2015: (From top to bottom the magnetic stations / observatories are: CTS, DIO and VLI). In each panel are shown the Dst index (in cyan), the geomagnetic field’s X (left column) or Y component (right column) (in grey, right y-axis) and the GICy (left column) or GICx index (right column) (in blue, left y-axis). Green and yellow dashed lines represent the risk levels, associated with the GIC index values, according to Marshall et al. [2011]. The arrow pointing on the x-axis denotes the SC of the storm, according to ISGI. 82

-
- 4.3 Storm of 23 June 2015: (From top to bottom the magnetic stations / observatories are: CTS, THL and DIO). In each panel are shown the Dst index (in cyan), the geomagnetic field's X (left column) or Y component (right column) (in grey, right y-axis) and the GICy (left column) or GICx index (right column) (in blue, left y-axis). Green and yellow dashed lines represent the risk levels, associated with the GIC index values, according to Marshall et al. [2011]. The arrow pointing on the x-axis denotes the three SCs of the storm, according to ISGI. 83
- 4.4 Storm of 20 December 2015: (From top to bottom the magnetic stations / observatories are: CTS, THL and DIO). In each panel are shown the Dst index (in cyan), the geomagnetic field's X (left column) or Y component (right column) (in grey, right y-axis) and the GICy (left column) or GICx index (right column) (in blue, left y-axis). Green and yellow dashed lines represent the risk levels, associated with the GIC index values, according to Marshall et al. [2011]. The arrow pointing on the x-axis denotes the SC of the storm, according to ISGI. 84
- 4.5 Storm of 26 August 2018: (From top to bottom the magnetic stations / observatories are: CTS, SFS and FIN). In each panel are shown the Dst index (in cyan), the geomagnetic field's X (left column) or Y component (right column) (in grey, right y-axis) and the GICy (left column) or GICx index (right column) (in blue, left y-axis). Green and yellow dashed lines represent the risk levels, associated with the GIC index values, according to Marshall et al. [2011]. 85
- 4.6 ULF power in the 2-7 mHz frequency range measured in four ground magnetometer stations on 26 August 2018, arranged by L-shell. 87
- 4.7 Storm of 4 November 2021: (From top to bottom the magnetic stations / observatories are: CLF, EBR, IZN, PEG and TAM). In each panel are shown the Dst index (in cyan), the geomagnetic field's X (left column) or Y component (right column) (in grey, right y-axis) and the GICy (left column) or GICx index (right column) (in blue, left y-axis). Green and yellow dashed lines represent the risk levels, associated with the GIC index values, according to Marshall et al. [2011]. 91

LIST OF FIGURES

5.1 Contour maps of GICy (top panels) and GICx (bottom panels) indices at the occurrence of the SSC (04:45:00 UT \pm 5 minutes) on 17 March 2015. Here, we zoom in the “Very Low” (available for GICy and GICx) and “Low” (available for GICx) risk levels, represented by green and yellow colors, and thus different intensities of GIC index can be identified by the different hues of green / yellow. Focus is on geographic latitudes between 20° and 55° and geographic longitudes between -10° and 35°. Red dots represent locations of magnetic stations / observatories. Overplotted in the panels on the left is a ground conductivity map of Europe in the form of a grid, each cell of which corresponds to a 1-D ground model *Ádám et al. [2012]*, denoted by its respective number as listed at <http://real.mtak.hu/2957/>; while overplotted in the panels on the right are the respective conductances, in base 10 logarithmic scale, with units of log(S), with an integration depth of 80 km. 96

5.2 Contour maps of GICy (top panels) and GICx (bottom panels) indices for 16, 17 and 18 March 2015. Here, we zoom in the “Very Low” (available for GICy and GICx) and “Low” (available for GICx) risk levels, represented by green and yellow colors, and thus different intensities of GIC index can be identified by the different hues of green / yellow. Focus is on geographic latitudes between 20° and 55° and geographic longitudes between -10° and 35°. Red dots represent locations of magnetic stations / observatories. Overplotted is a ground conductivity map of Europe in the form of a grid, each cell of which corresponds to a 1-D ground model *Ádám et al. [2012]*, denoted by its respective conductances (in base 10 logarithmic scale, with units of log(S)) with an integration depth of 80 km. 97

5.3 Contour maps of Ey (top panel) and Ex (bottom panel) calculated at the time when the SSC occurred (04:45:00 UT \pm 5 minutes) on 17 March 2015. Overplotted is a map of the electrical grid in Europe and Northern Africa. . . 99

5.4 Storm of 17 March 2015: (From top to bottom the magnetic stations / observatories are: CTS, DIO and VLI). Correlation between E (mV/km) (in blue, left y-axis) and GIC index (in orange, right y-axis). 100

5.5 Storm of 17 March 2015: (From top left to bottom right) Comparative plots between Bx and LDi, dBx/dt and LCi, GICy index and Ey; at EBR. 101

6.1 NOAA’s SWPC revised prediction for solar activity during Solar Cycle 25. The new Experimental Solar Cycle Prediction concludes that solar activity will increase more quickly and peak at a higher level than previously predicted. Source: <https://www.weather.gov/news/102523-solar-cycle-25-update> 110

A.1 Storm of 17 March 2015: (From top to bottom: CLF, CTS and EBR). In each panel are shown the Dst index (in cyan), the geomagnetic field’s X (left column) or Y component (right column) (in grey, right y-axis) and the GICy (left column) or GICx index (right column) (in blue, left y-axis). Green and yellow dashed lines represent the risk levels, associated with the GIC index values, according to Marshall et al. (2011). 140

A.2 Storm of 17 March 2015: (From top to bottom: IZN, DIO and VLI). In each panel are shown the Dst index (in cyan), the geomagnetic field’s X (left column) or Y component (right column) (in grey, right y-axis) and the GICy (left column) or GICx index (right column) (in blue, left y-axis). Green and yellow dashed lines represent the risk levels, associated with the GIC index values, according to Marshall et al. (2011). 141

A.3 Storm of 17 March 2015: (From top to bottom: SFS and TAM). In each panel are shown the Dst index (in cyan), the geomagnetic field’s X (left column) or Y component (right column) (in grey, right y-axis) and the GICy (left column) or GICx index (right column) (in blue, left y-axis). Green and yellow dashed lines represent the risk levels, associated with the GIC index values, according to Marshall et al. (2011). 142

A.4 Storm of 23 June 2015: (From top to bottom: CLF, CTS and EBR). In each panel are shown the Dst index (in cyan), the geomagnetic field’s X (left column) or Y component (right column) (in grey, right y-axis) and the GICy (left column) or GICx index (right column) (in blue, left y-axis). Green and yellow dashed lines represent the risk levels, associated with the GIC index values, according to Marshall et al. (2011). 143

A.5 Storm of 23 June 2015: (From top to bottom: IZN, THL and DIO). In each panel are shown the Dst index (in cyan), the geomagnetic field’s X (left column) or Y component (right column) (in grey, right y-axis) and the GICy (left column) or GICx index (right column) (in blue, left y-axis). Green and yellow dashed lines represent the risk levels, associated with the GIC index values, according to Marshall et al. (2011). 144

LIST OF FIGURES

- A.6 Storm of 23 June 2015: (From top to bottom: SFS and TAM). In each panel are shown the Dst index (in cyan), the geomagnetic field's X (left column) or Y component (right column) (in grey, right y-axis) and the GICy (left column) or GICx index (right column) (in blue, left y-axis). Green and yellow dashed lines represent the risk levels, associated with the GIC index values, according to Marshall et al. (2011). 145
- A.7 Storm of 20 December 2015: (From top to bottom: CLF, CTS and EBR). In each panel are shown the Dst index (in cyan), the geomagnetic field's X (left column) or Y component (right column) (in grey, right y-axis) and the GICy (left column) or GICx index (right column) (in blue, left y-axis). Green and yellow dashed lines represent the risk levels, associated with the GIC index values, according to Marshall et al. (2011). 146
- A.8 Storm of 20 December 2015: (From top to bottom: THL, DIO, SFS and TAM). In each panel are shown the Dst index (in cyan), the geomagnetic field's X (left column) or Y component (right column) (in grey, right y-axis) and the GICy (left column) or GICx index (right column) (in blue, left y-axis). Green and yellow dashed lines represent the risk levels, associated with the GIC index values, according to Marshall et al. (2011). 147
- A.9 Storm of 26 August 2018: (From top to bottom: CLF, CTS and EBR). In each panel are shown the Dst index (in cyan), the geomagnetic field's X (left column) or Y component (right column) (in grey, right y-axis) and the GICy (left column) or GICx index (right column) (in blue, left y-axis). Green and yellow dashed lines represent the risk levels, associated with the GIC index values, according to Marshall et al. (2011). 148
- A.10 Storm of 26 August 2018: (From top to bottom: IZN, PEG and SFS). In each panel are shown the Dst index (in cyan), the geomagnetic field's X (left column) or Y component (right column) (in grey, right y-axis) and the GICy (left column) or GICx index (right column) (in blue, left y-axis). Green and yellow dashed lines represent the risk levels, associated with the GIC index values, according to Marshall et al. (2011). 149

A.11 Storm of 26 August 2018: (From top to bottom: FIN and TAM). In each panel are shown the Dst index (in cyan), the geomagnetic field's X (left column) or Y component (right column) (in grey, right y-axis) and the GICy (left column) or GICx index (right column) (in blue, left y-axis). Green and yellow dashed lines represent the risk levels, associated with the GIC index values, according to Marshall et al. (2011).	150
---------------------------------------------------------------------------------------------------------------------------------------------------------------------------------------------------------------------------------------------------------------------------------------------------------------------------------------------------------------------------------------------------------------------------------------------	-----

INTRODUCTION

Space Weather, a term which has become accepted over the past few decades, refers to the dynamic and ever-changing conditions in the space environment surrounding Earth, driven by the interactions between the solar wind, the Earth's magnetic field, and the Earth's atmosphere. Similar to how Earth experiences weather conditions such as rain, wind, and storms, space weather involves a range of phenomena that can impact satellites, communication systems, navigation technologies, power grids, and even astronauts in space (Figure 1.1). The primary source of space weather is the Sun. The Sun constantly emits energy, as flares of electromagnetic radiation, and as energetic electrically charged particles. The outer solar atmosphere is the source of the solar wind, a stream of charged energetic particles, which travel from the Sun throughout interplanetary space. Although the electromagnetic radiation travels at the speed of light and takes about eight minutes to move from Sun to Earth, the charged particles travel more slowly, requiring a few hours to several days to reach Earth. The radiation and particles interact with the Earth's magnetic field and outer atmosphere in complex ways, causing amounts of energetic particles to concentrate and electric currents to flow in regions of the outer atmosphere (magnetosphere and ionosphere). Additionally, the fast (typical velocity of 750 km/s) and slow (typical velocity of 300-500 km/s) solar wind can be interrupted by large, usually fast-moving bursts of plasma called Coronal Mass Ejections (CMEs) that are sometimes associated with solar flares, which can be detected from radio waves to gamma-rays. The special case of a southward interplanetary magnetic field (IMF) orientation (in the GSM - Geocentric Solar Magnetic - coordinates frame) favors

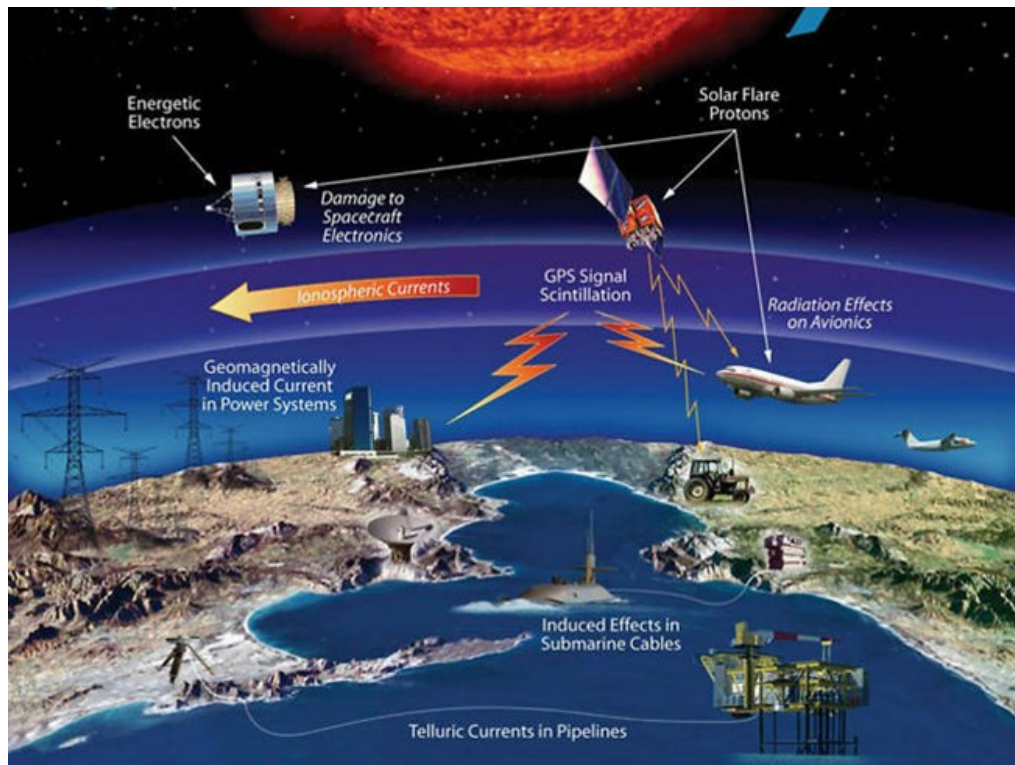


Figure 1.1: Technological infrastructure affected by adverse space weather effects on the Earth. Source: Courtesy of NASA: https://www.nasa.gov/mission_pages/sunearth/news/agu2011-spaceweather.html.

the efficient transfer of energy into the terrestrial magnetosphere, resulting in probably the most important phenomenon of space physics, the magnetic storm [Daglis et al., 2003, Balasis et al., 2006]. The prerequisite conditions for magnetic storms dominate predominantly in fast-moving CMEs that also lead to the occurrence of the Storm Sudden Commencement (SSC) because of the shocks in front of them.

This complex and dynamic system of interactions can lead to various space weather effects, ranging from mild (e.g., aurora borealis and australis) to extreme (e.g., disruptions in satellite operations, communications, navigation, and electric power distribution grids). The impacts of space weather have been noticeable since the introduction of the telegraph in the 19th century. Presently, we possess an understanding that space weather exerts its influence on diverse communication systems, encompassing wired, wireless, and satellite-based systems. Furthermore, the risks associated with adverse space weather conditions encompass the potential disruption or enduring harm to power grids and communication networks, as well as the impairment of telecommunication, navigation, and surveillance satellites. Additionally, space weather disturbances can

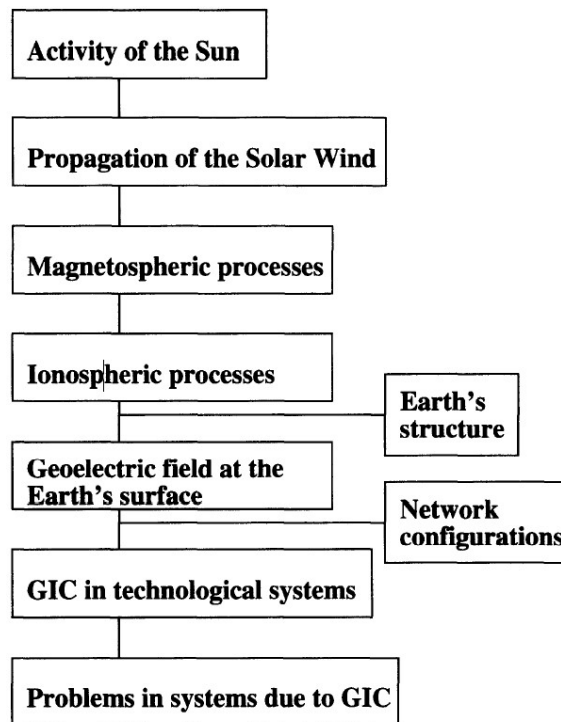


Figure 1.2: The space weather / GIC chain starts from the Sun, contains complicated space and geophysical processes, and ends at GIC in technological systems at the Earth's surface. Source: Pirjola [2000].

affect technologies like over-the-horizon (OTH) radar, high frequency (HF), very high frequency (VHF), and ultra high frequency (UHF) communications, along with systems reliant on Global Positioning System (GPS) satellites for surveying and navigation. Impacts on surveillance systems, both optical and radar-based, as well as satellite tracking, are also part of these hazards. Exploring the correlation between space weather and weather within Earth's atmosphere and climate remains a developing field of study (see, e.g., Varotsos et al. [2023]). Our understanding of the biological effects of space weather, particularly concerning astronauts, remains limited [Daglis, 2001].

Throughout the solar cycle, the impacts of space weather are consistently observable, but they become especially notable during the zenith of the 11-year cycle of sunspot activity. In this dissertation our primary focus lies on the maximum of cycle 24, which reached its peak in April 2014.

Geomagnetically induced currents (GICs) represent the ground end of the complicated sequence of space weather events originating from the Sun (Figure 1.2). These currents pertain to electric currents flowing through technological infrastructures, such as electric

power transmission grids, oil and gas pipelines, telephone cables, and railway systems. They result from the geoelectric field induced by geomagnetic disturbances or storms on the Earth's surface. GICs have been the subject of extensive investigation over the years, with research commencing shortly after the first telegraph systems came into operation, about 150 years ago [Pirjola, 2000].

1.1 The Sun

The Sun is the primary source of all space weather phenomena within the heliosphere. Abrupt and violent eruptions of solar material from the Sun's outer layer, known as the corona, are referred to as coronal mass ejections (CMEs). These eruptions signify the commencement of significant space weather events that ultimately give rise to geomagnetic storms (disturbances) within the Earth's upper atmosphere [Tsinganos, 2017, 2020].

The Sun's activity is closely governed by the solar activity cycle, which typically spans an average duration of approximately 11 years. This cycle is characterized by the count of discernible active sunspots on the solar surface. Throughout the solar maximum period, characterized by heightened solar activity, the Sun has the capacity to launch numerous CMEs in the direction towards Earth (but not only) on a daily basis. A CME can be perceived as a plasma cloud containing the solar magnetic field, referred to as IMF, embedded within its structure. When CMEs reach near-Earth space environment, they interact with the magnetosphere, an area of lower particle density and partially ionised plasma encircling the upper atmosphere that is primarily influenced by Earth's magnetic field. This interaction subsequently triggers geomagnetic disturbances (GMDs) that lead to intense global magnetic field variations. Orientation of the IMF fluctuates over time and holds significance in facilitating the interplay between the solar wind and the Earth's magnetic field domination within the magnetosphere.

Historically, the most intense disturbances have been documented during instances where the B_z component of the IMF, which is parallel to the solar rotation axis is oppositely directed to the Earth's magnetic field. This condition is commonly denoted as a southward or negative IMF orientation. In situations where a southward orientation prevails, the coupling between the solar wind and the magnetosphere is enhanced and the transfer of CME plasma, momentum, and energy into the near-Earth space environment is intensified. This enhanced energy inflow triggers a series of complex processes within the magnetosphere–ionosphere (M–I) coupled system that regulate phenomena such

as storms, enhanced particles density, ionospheric irregularities, substorms, GICs, and auroral displays at high-latitudes. Alongside these impacts, space weather has the potential to undermine the reliability and functionality of our technological systems [Lanzerotti, 2001]. Figure 1.1 highlights several key technological assets affected by adverse space weather effects. This thesis focuses on GICs, that occur at the end of the space weather chain.

1.1.1 Solar Wind

Solar wind constitutes a continuous magnetized plasma outflow that emerges from the solar corona [Verscharen et al., 2019]. This extension of the Sun’s outer atmosphere propagates through interplanetary space, at velocities exceeding 1.5 million km/hour, carrying parts of the Sun’s magnetic field towards Earth. While the link between solar activity and disturbances in the Earth’s magnetic field was established during the 19th century, [Sabine, 1851, 1852, Hodgson, 1859, Stewart, 1861], the association of these events with “corpuscular radiation” wasn’t recognized until the beginning of the 20th century [Birkeland, 1914, Chapman, 1917]. The origin of the solar corpuscular radiation remained unclear until the mid-1950s when a young physicist named Eugene N. Parker [1958] introduced a series of ideas elucidating how our Sun, as well as stars in general, emit energy. He showed that a solar corona characterized by high temperatures is incapable of upholding hydrostatic equilibrium. Instead, the pressure-gradient force surpasses gravity and leads to a radial acceleration of the coronal plasma to supersonic velocities. Parker coined the term “solar wind” for this phenomenon. Soon after his prediction, the solar wind was measured in situ by spacecraft (e.g., Gringauz et al. [1960]). For the last six decades, the solar wind has been monitored almost continuously in situ.

1.1.1.1 Solar Wind Categories

The observed solar wind characteristics have shown a consistent pattern of two distinct streams, one slow and the other fast. This pattern, recurring every 27 days, indicates that their solar source regions rotated along with the Sun [Bothmer and Zhukov, 2007].

Concurrent in situ measurements of the solar wind alongside X-ray imaging of the solar corona revealed that the origins of fast solar wind streams are coronal holes on the Sun. Conversely, the source of slow solar wind, a phenomenon that remains partially comprehended, is thought to emerge from the upper regions of coronal streamers in a

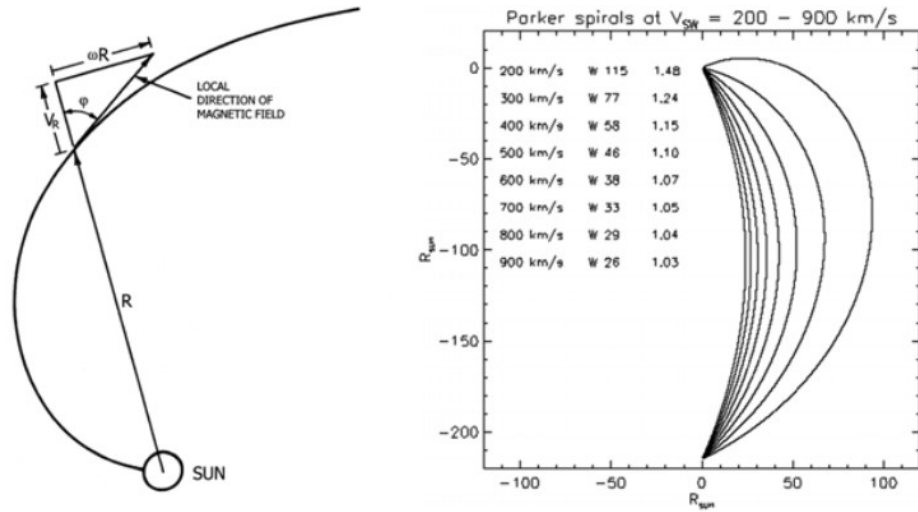


Figure 1.3: Left: Schematic geometry of IMF in the ecliptic plane for solar wind with speed V_R at a distance R . The situation sketches the observed structure for a solar wind speed of 400 km/s near 1 AU. The magnetic polarity of the IMF is assumed to be in anti-sunward direction (i.e., positive). Right: Curvature of the Parker spiral at the orbit of Earth for solar wind speeds between 200 and 900 km/s. Source: Bothmer and Zhukov [2007].

'drop-like' matter. Due to the Sun's rotation period of approximately 25.4 days (or 27.73 days with respect to Earth) the outward-convected solar magnetic field imbedded in the solar wind gets structured into the configuration of an Archimedian spiral, often referred to as a "Parker spiral" (see Figure 1.3). The magnetic field swept out of the expanding solar wind is termed IMF. Typical field strengths along with the average properties of the fast and slow solar wind near Earth's orbit (1 AU) are provided in Table 1.1.

	Fast wind	Slow wind
Flow speed v_p	450–800km/s	<~ 450km/s
Proton density n_p	~ 3 cm ⁻³	7–10 cm ⁻³
Composition	~ 95% H, 5% He, minor ions and same number of electrons	~ 94% H, ~ 4% He, minor ions and same number of electrons - great variability
Proton Temperature T_p	~ 2 · 10 ⁴ K	~ 4 · 10 ⁵ K
Magnetic field intensity	~ 5nT	~ 4nT
Fluctuations	Alfvenic	Density
Origin	in coronal holes	'above' coronal streamers and through small-scale transients

Table 1.1: Basic solar wind characteristics near Earth's orbit. Source: [Bothmer and Zhukov, 2007]

Besides the slow and fast solar wind, there is another category which includes the variable/eruptive events, such as CMEs, with speeds from a few hundreds up to 2000 km/s [Verscharen et al., 2019].

Under typical conditions, the solar wind is highly varying and seems nearly unpredictable. However, the drivers of geomagnetic storms follow distinct sequences that persist for periods ranging from several hours to days. The principal contributors to geomagnetic storms are interplanetary coronal mass ejections (ICMEs) and stream interaction regions (SIRs). Both of them can generate shocks, leading to the production and acceleration of particles. These particles, in turn, exert an influence on planetary magnetospheres and ionospheres.

1.1.2 Solar Cycle

The Sun rotates around its axis once in about 27.73 days (with respect to Earth). This rotation was first detected through the observation of sunspot movement. The Sun's rotation axis is tilted at an angle of approximately 7.25 degrees relative to the axis of Earth's orbit. Consequently, during September of each year, a larger portion of the Sun's North Pole becomes visible, while in March, a greater portion of its South Pole comes into view. Given that the Sun is an immense spherical body consisting of gas/plasma, it is subjected to differential rotation. This entails the equatorial zones completing rotations at a swifter pace (~ 24 days) compared to the polar areas (> 30 days). This characteristic periodicity has been noted to give rise to other phenomena periodicities at $T = 27$ days and $T = 13-14$ days. Moreover, it typically precedes the observed geomagnetic periodicity on Earth [Mursula and Zieger, 1996]. To be more precise, it's worth noting that these aren't the sole observed periodicities. The frequency distribution extends to approximately $1/(6T)$, $1/(8T)$, $(1/12T)$, and $(1/24T)$, where $T = 1$ hour [Balasis et al., 2006]. Figure 1.4 illustrates an image of the Sun, depicting the varying rotational periods of its different regions.

Commencing at the Zurich Observatory in 1849, a continuous series of daily observations began to track the count of sunspots emerging on the Sun's surface. This record was subsequently expanded by incorporating earlier observations, extending the dataset back to 1610 [Clette et al., 2014]. The relative sunspot number R is calculated by first counting the total number of sunspots (N_s) and then the number of sunspot groups (N_g). Then it can be calculated as the sum of the number of individual sunspots and ten times

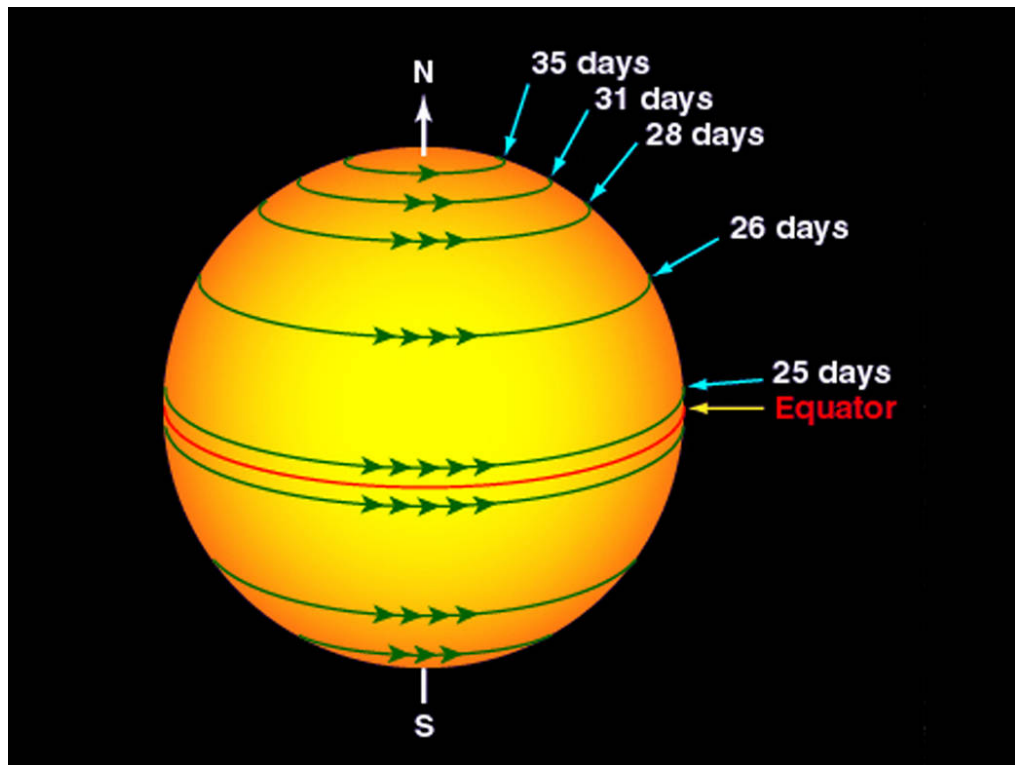


Figure 1.4: Sun's rotation periods decrease from poles to the equatorial plane. Source: https://www.nasa.gov/mission_pages/sunearth/science/solar-rotation.html.

the number of groups, according to the following well-known formula:

$$(1.1) \quad R = k(10 * Ng + Ns)$$

where the scaling coefficient k , often referred to as the observer's personal coefficient, serves the purpose of adjusting for variations in the count of recorded sunspots among different observers. Since most sunspot groups have, on average, about ten spots, this formula ensures reliable sunspot counts even when the observing conditions are less than ideal and small spots are hard to see. Averages of monthly updated sunspot numbers reveal that the number of sunspots visible on the Sun waxes and wanes with an approximate 11-year cycle.

Solar cycles are counted from one solar minimum to the next [Bothmer and Zhukov, 2007]. During periods of low solar activity, the Sun's internal magnetic field can be approximated, in principle, as a magnetic dipole. Consequently, a full reversal of the Sun's magnetic polarity encompasses a duration of around 22 years, commonly referred to as the 'Hale Cycle'. Starting from solar cycle "1", spanning from 1755 to 1766, and counting, we have now reached solar cycle "25". For the scope of this dissertation, our

attention was directed toward solar cycle 24, which initiated on January 4, 2008, upon the appearance of a reversed-polarity sunspot. Characterized by a relatively subdued level of activity, cycle 24 saw its peak sunspot count recorded in April 2014, totaling 116. Notably, the year 2015 marked a period of major geomagnetic activity within this cycle.

1.1.3 Solar Activity

As the solar wind approaches our planet, it is deflected by the Earth's magnetic field. On the other hand, the solar wind is so powerful that confines the Earth's magnetic field to a cavity with a prolonged, extended tail, called the "magnetosphere" (for a more analytical description see Section 1.2). Three categories of solar phenomena can have major impacts on Earth by disturbing our space environment:

1. CMEs, which are large explosions that hurl superheated plasma (charged gas) into interplanetary space;
2. Coronal holes, which release high-speed streams (HSS) of plasma that enhance the solar wind. HSS from persistent coronal holes over multiple solar rotations are referred to as corotating interaction regions (CIRs).
3. Solar flares, which are an intense burst of radiation coming from the release of magnetic energy.

Under the right conditions (e.g., southward IMF orientation), CMEs and HSS can trigger geomagnetic storms in our magnetosphere (for a more analytical description see Section 1.4.3.).

1.1.4 Interplanetary Coronal Mass Ejections (ICMEs)

CMEs are spectacular manifestations of solar activity and have been a topic of extensive study since their discovery. CMEs are plasma eruptions from the solar atmosphere involving previously closed magnetic field regions which are expelled into the interplanetary medium [Gosling et al., 1991]. It was estimated that the typical mass ejection encompasses roughly $10^{15} - 10^{16}$ g of material and may achieve a speed of several thousand kilometres per second. A key feature is their propagation through interplanetary space and their subsequent interaction with Earth. An ICME is commonly acknowledged as the heliospheric counterpart of the CME. ICMEs that approach Earth frequently have geospace effects on our planet, manifesting as either geomagnetic storms or solar

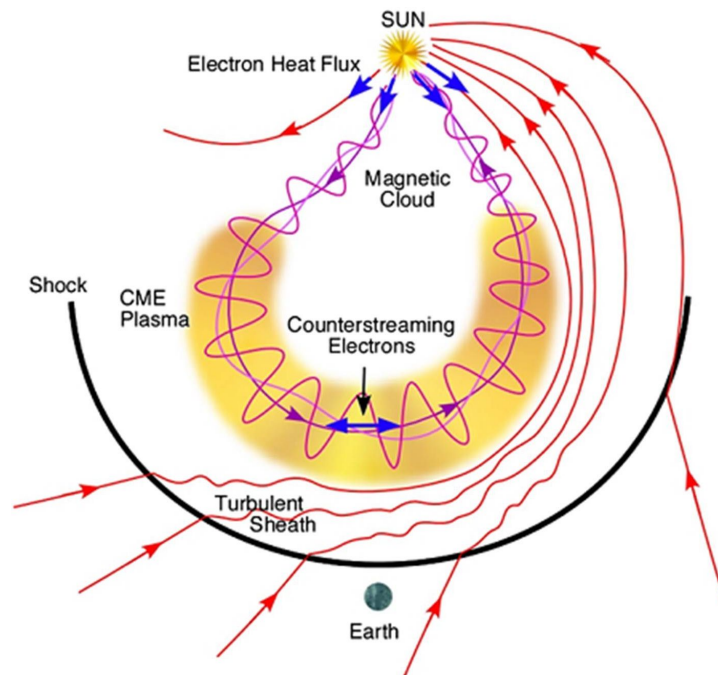


Figure 1.5: Schematic of the basic features of an ICME: the leading shock, a compressed ambient solar-wind “sheath” where the magnetic field may be perturbed by the shock and foreshock, and a shock “driver” consisting of the coronal “ejecta” including a flux-rope-like magnetic field structure. Source: Zurbuchen and Richardson [2006].

energetic particles (SEPs). The in situ observations of the ICME reveal three notable structures, i.e., the forward propagating shock (if present), the compressed, deflected solar-wind plasma and the field behind the shock (“sheath”), and the coronal ejecta (the “driver”) – often called a “magnetic cloud” [Luhmann et al., 2020] (see Figure 1.5). As already mentioned, the southward IMF component is a dominant parameter governing the intensity of geomagnetic activity; as this is strongly enhanced within some ICMEs or the associated sheaths, the majority of severe geomagnetic storms are ICME-related [Richardson et al., 2001].

1.2 Earth’s Magnetosphere

The Earth’s magnetosphere is a highly complex system of fields and currents that envelop the Earth and interact with each other producing a wide range of phenomena [Papadimitriou et al., 2021]. It is a low-density region of partially ionized gas around the upper atmosphere, dominated by Earth’s magnetic field. Along with Earth’s atmosphere, it serves as the planet’s protective shield against the supersonic magnetized

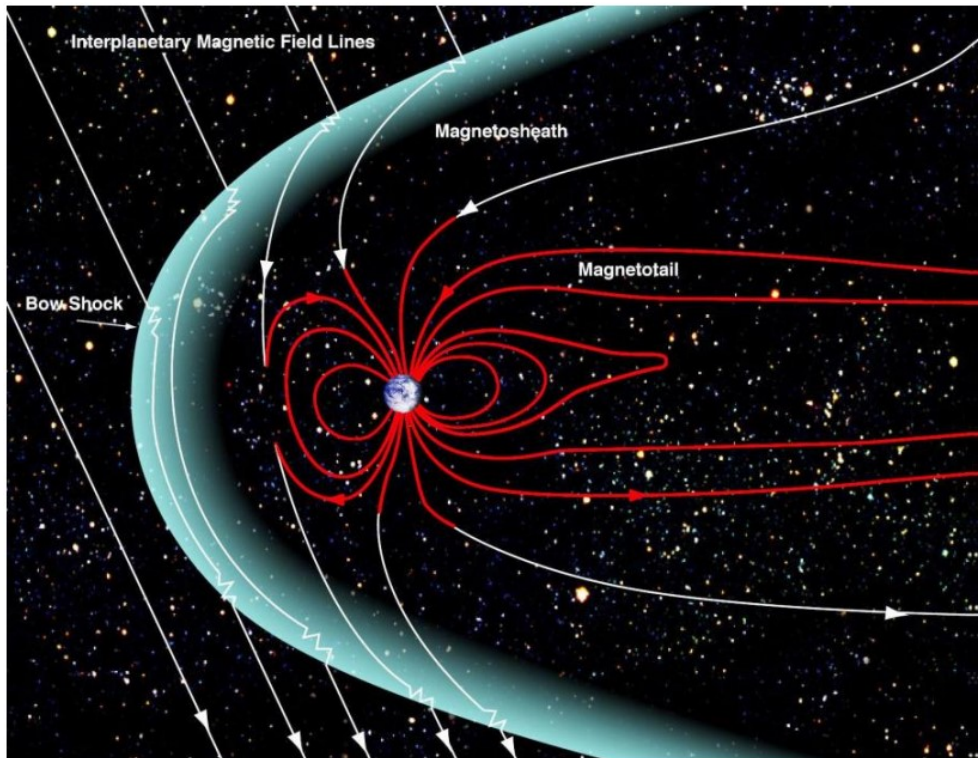


Figure 1.6: Simplified schematic outline of Earth's magnetosphere structure. Source: Courtesy of NASA: https://www.nasa.gov/mission_pages/sunearth/multimedia/magnetosphere.html

solar wind (and other kinds of solar and cosmic radiation). However, it's not inaccessible; a substantial portion of the solar wind plasma resides within it. The shape of the Earth's magnetosphere is the direct result of the impact it undergoes from the solar wind. The solar wind compresses its sunward side to a distance of only 6 to 10 times the radius of the Earth, R_E ($R_E = 6.371$ km). A supersonic shock wave is created towards the dayside of Earth, called the bow shock (see Figure 1.6). Most of the solar wind particles are heated and slowed at the bow shock and detour around the Earth in the magnetosheath. The solar wind drags out the night-side magnetosphere up to possibly 1000 times the Earth's radius (its exact length is unknown). This extension of the magnetosphere is known as the magnetotail. The outer boundary of Earth's confined geomagnetic field is called the magnetopause. The Earth's magnetosphere is a highly dynamic structure that responds dramatically to solar variations.

The distinct areas of the Earth's magnetosphere (Figure 1.6), from the outermost regions to those in closer proximity to Earth, are briefly described below:

1. The bow shock constitutes the outermost layer of the magnetosphere, serving

as the boundary between the magnetosphere and the surrounding environment. The terrestrial magnetic field decelerates the supermagnetosonic solar wind to submagnetosonic speeds, leading to the formation of a fast-mode standing shock wave [Dimmock et al., 2020].

2. Downstream of the bow shock, the plasma is slower, denser, hotter, and more turbulent compared to its upstream counterpart. This complex region is the magnetosheath, and it extends all the way to the magnetopause [Dimmock et al., 2020]. It is formed mainly from shocked solar wind, though it contains a small amount of plasma originating from the magnetosphere. The complexity of the magnetosheath is amplified by the existence of numerous small-scale structures, which are also coupled to the solar wind properties. The magnetosheath is an area exhibiting high particle energy flux, characterized by unpredictable fluctuations in both the direction and intensity of the magnetic field, due to the accumulation of solar wind gas that has effectively undergone thermalization. In general, the magnetosheath is a transition layer, acting as a natural boundary between the solar wind and the inner-magnetosphere. Hence, it plays crucial role as its conditions regulate the processes that transfer mass and momentum to the inner-magnetosphere.
3. The magnetopause is the area of the magnetosphere wherein the magnetic pressure from the Earth's magnetic field is balanced with the dynamic pressure from the solar wind. It contains magnetized plasma from both the magnetosheath (denser and cooler) and the inner-magnetosphere (less dense and warmer) and, therefore, the interactions between them are complex. The structure of the magnetopause depends upon the Mach number and beta parameter of the plasma, as well as the magnetic field; it changes size and shape as the pressure from the solar wind fluctuates.
4. Opposite the compressed magnetic field in the Sun facing side of the magnetosphere is the magnetotail, where the magnetosphere extends far beyond the Earth's orbit around the Sun. Within the magnetotail, there exist two lobes, the northern and southern taillobes. The northern taillobe points towards Earth and the southern taillobe points away. These taillobes are relatively sparse, with few charged particles opposing the flow of the solar wind. The two lobes are separated by a plasma sheet, an area where the magnetic field is weaker and the density of charged particles is higher.

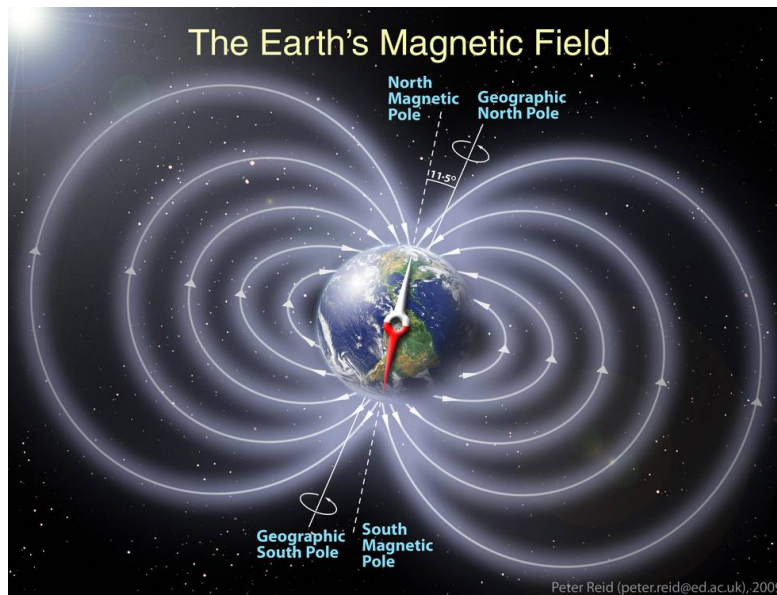


Figure 1.7: Schematic illustration of the invisible magnetic field lines generated by the Earth, represented as a dipole magnet field. Actually, our magnetic shield is squeezed in closer to Earth on the Sun-facing side and extremely elongated on the night-side due to the solar wind. Notably, the magnetic and geographic poles do not align precisely.

1.3 Earth's Magnetic Field

On the Earth's surface, a small, freely turning magnetic needle (e.g., a compass needle) aligns itself roughly with the north-south direction. The head of the needle pointing northward is called the north pole (N) of the needle, and the head pointing southward is called the south pole (S) (see Figure 1.7). If a magnetic needle at a certain location aligns itself with a certain direction, it is said that there is a magnetic field at that location. According to observations, the Earth is surrounded by a magnetic field that varies with time and location.

The Earth's magnetic field is the superposition of fields with different origins and varying magnitudes (Figure 1.8). Predominantly, it is generated by the fluid "ocean" of hot, liquid metal found in the outer core (ranging from a depth of 2900 to 5100 kilometers), which envelops the solid iron core (known as the main or core field). Convective motions of liquid metal, primarily composed of elements such as iron and nickel, in the Earth's core create electric currents. These electric currents operate as a self-sustaining dynamo, producing the magnetic field. As the flow of electric currents evolves slowly, the magnetic field they generate undergoes corresponding changes. Consequently, variations in both the intensity and orientation of the magnetic field occur over time at the Earth's surface.

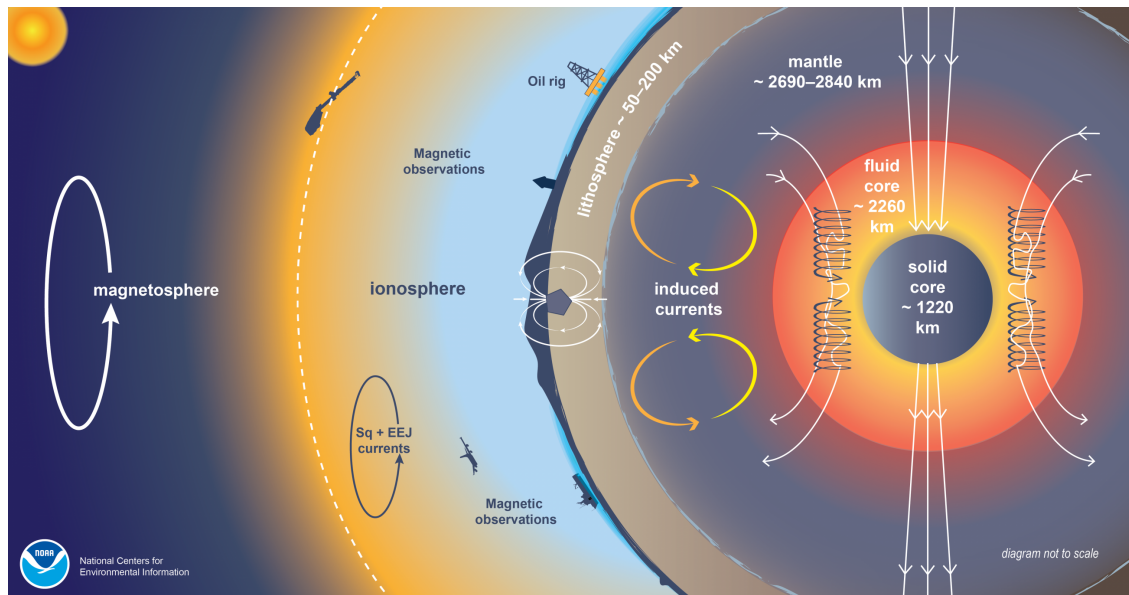


Figure 1.8: Sketch of the various sources contributing to the near-Earth magnetic field. Source: Courtesy of NOAA NCEI: <https://www.ncei.noaa.gov/news/HDGM>

The field's strength varies approximately from $30 \mu\text{T}$ at the equator to $60 \mu\text{T}$ at the poles.

The Earth's magnetic field is also contributed to:

- by magnetised rocks in the lithosphere (at depths of less than 50 km, known as the lithospheric or crustal field)
- by electric currents flowing in the near Earth space (above altitudes of 100 km: ionosphere, magnetosphere) and oceans. In particular, the ionosphere hosts the solar quiet Sq magnetic field variation, the equatorial electrojet (EEJ) and the auroral electrojet (AEJ) and the magnetosphere the ring current, whereas there are also coupling currents between the ionosphere and magnetosphere
- by currents induced in the Earth's mantle by time-varying external fields.

Although the external contribution is on average $<1\%$, during magnetic storms, it can go up to several percent of the main field for a few hours.

1.3.1 Primary Current Systems

Electric currents flowing through the vicinity of Earth ($R \leq 12R_E$) are capable of considerably altering magnetic field topology, which in turn modifies the paths along which particles drift. This interaction produces a nonlinear feedback on the currents themselves

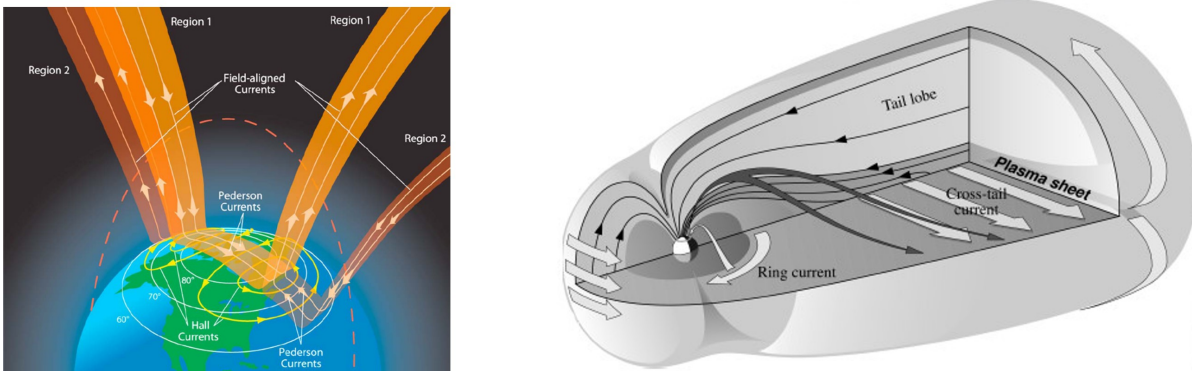


Figure 1.9: Schematic illustration of the (a) current systems in the ionosphere: Field-Aligned Currents (FAC), Pedersen currents and Hall currents and (b) current systems in the magnetosphere: magnetopause current, ring current and cross-tail current. Source: (a) Le et al. [2010] and (b) Koskinen [2011a] (Figure by courtesy of T. Makinen).

[Ganushkina et al., 2015]. The main current systems that exist in the magnetosphere are (1) the dayside magnetopause Chapman–Ferraro currents (the nightside part is the cross-tail current, which closes around the tail lobes), (2) the Birkeland field-aligned currents with high latitude “region 1” and lower-latitude “region 2” currents connected to the partial ring current, (3) the magnetotail currents, and (4) the symmetric ring current. Moreover, various current systems emerge at certain times and places (e.g., substorm current wedge), further complicating the identification and understanding of electric current flow within geospace and the nonlinear consequences it brings to the system. Additionally, the ionospheric current is made up of two components: Pedersen and Hall currents flowing perpendicular to each other. Figure 1.9 illustrates where the main electric currents are formed and toward which direction flow.

A current system of special importance is the aptly named “ring current.” The ring current is a toroidal electric current encircling Earth, formed by the azimuthal motion of electrons and ions, stretching from 3 to 8 times the Earth’s radius on the equatorial plane of the magnetosphere [Daglis et al., 1999]. Due to its shape and direction, it forms its own magnetic field component, with an axis almost parallel to that of the Earth’s dipole and the same polarity (southward). A direct outcome of this configuration is that the induced magnetic field produced by the ring current on the Earth’s surface opposes the planet’s natural magnetic field. Thus, in cases where the incoming solar wind has the appropriate properties (e.g., velocity and/or dynamic pressure), to cause particle injection in the inner magnetosphere, thereby intensifying the ring current, the magnetic field strength experienced at the Earth’s surface diminishes due to the increase of the

counteracting ring current field [Papadimitriou et al., 2021].

1.3.2 Earth's Polarity

Earth's polarity is not a constant, unlike a traditional bar magnet. The matter governing the Earth's magnetic field is dynamic, causing regular reversals where the north and south poles switch positions. Such flips seem to occur at regular intervals averaging about 300,000 years, although the last one occurred about 780,000 years ago. Although it remains uncertain if another reversal is imminent, we are aware that when a reversal occurs, it takes several thousand years to complete. During this transition, Earth's magnetic field doesn't disappear; instead, it becomes more complicated, with twisted and tangled magnetic field lines. Despite this complexity, the magnetic field continues to shield us from solar radiation and space weather. The magnetic and corresponding geographic poles are not located in the exact same spot.

To fully describe the geomagnetic field it is necessary to either measure the strength and two angles of direction or three orthogonal components. On one hand, the angles are declination (the deviation of the local geomagnetic field lines from geographic north) and inclination (the angle of intersection with the Earth's surface). On the other hand, orthogonal components are commonly chosen to be X, Y and Z for the directions towards geographic north, east and vertically down, respectively.

Typically, geomagnetic fields are weak: the unit used to describe the geomagnetic field is nanotesla (nT), $1 \text{ nT} = 10^{-9} \text{ T}$.

1.3.3 Temporal Variations of the Earth's Magnetic Field

There are two types of temporal variations in the Earth's magnetic field:

1. Transient variations: these are irregular variations with periods from seconds to hours, caused by electric currents in the near-Earth space (> 100 km altitude) that are driven by solar activity.
2. Secular variations: these are changes in the Earth's magnetic field on time scales of about a year or more, caused by changes in the strength and direction of the electric currents in the Earth's liquid core at 2900-5100 km depth.

1.4 Geospace Disturbances

Geospace disturbances encompass variations in both the geomagnetic field and the trapped particle populations in the near-Earth space. These arise due to intermittent and recurrent solar activity, which consequently drives the variable solar wind. They may appear in various timescales, spanning from fractions of seconds to days, months or even years [Katsavrias et al., 2022]

In general, we can categorize geospace disturbances into 3 main groups, based on their frequencies and the underlying cause for their occurrence.

1. **Large scale variations:** they are mainly periodic changes due to oscillations in the Sun and the solar wind, such as the 27-day periodicity due to the rotation of the Sun and the 11-year periodicity due to the solar activity.
2. **Middle scale variations:** it refers to variations lasting from several hours to a few days, such as geomagnetic storms and magnetospheric substorms. These disturbances define geomagnetic activity and are primarily driven by magnetic reconnection, which is directly linked to changes in the diverse current systems within the magnetosphere.
3. **Small scale variations:** this category includes variations lasting from several minutes down to fractions of a second. They correspond to the generation of oscillations (or waves) in the terrestrial magnetosphere. Small scale oscillations are significant as the mechanisms behind these variations play a crucial role in the dynamic nature of the various particle populations within the inner magnetosphere.

1.4.1 Geomagnetic Activity Indices

Geomagnetic activity indices, such as the Dst and AE, have been used for decades to monitor the interaction between Earth's magnetosphere and the solar wind. These indices provide measurable indications into the overall state of geomagnetic activity [Papadimitriou et al., 2021]. Traditionally, they have been derived from ground-based observations from magnetometer stations all around the globe.

1.4.1.1 Dst and SYM-H Indices

Disturbance storm-time (Dst) index is an hourly index that has been computed and distributed from the World Data Center for Geomagnetism, Kyoto on a continuous basis

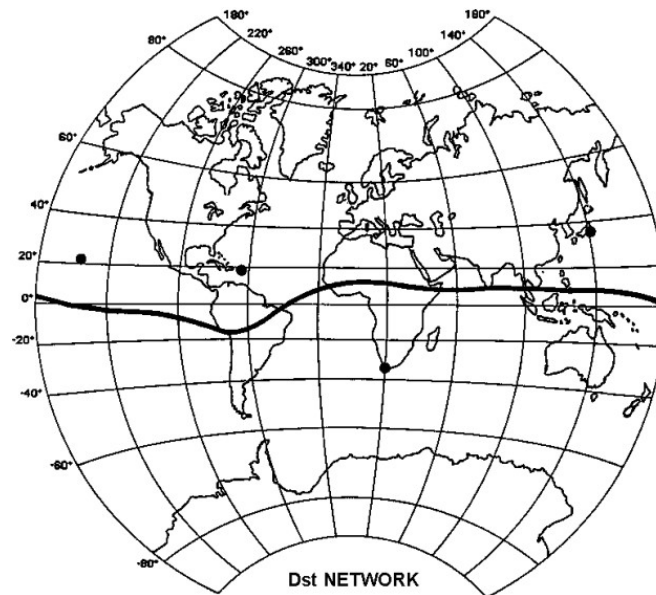


Figure 1.10: The Dst network consists of four ground-based magnetometer stations: (1) Hermanus (19.22° E -34.40° N); (2) Kakioka (140.18° E 36.23° N); (3) Honolulu (201.98° E 21.32° N) and (4) San Juan (293.88° E 18.11° N). Source: <https://wdc.kugi.kyoto-u.ac.jp/dstdir/dst2/onDstindex.html>

since October 1985. It has been traditionally used to monitor geomagnetic storms, which produce global magnetic disturbances on the Earth's surface. The Dst index represents the axially symmetric disturbance of the horizontal component of the magnetic field at the magnetic equator on the Earth's surface [Sugiura and Kamei, 1981]. As such, it acts as a proxy for the enhancement and subsequent weakening of the ring current, consequently indicating the onset and evolution of magnetic storms. Dst index is derived from the variations of the horizontal component of the Earth's magnetic field, using data from four observatories, located at magnetic latitudes ranging from approximately -30° to $+30^{\circ}$ (away from the auroral and equatorial electrojets). The derivation process includes the baseline definition based on the five quietest days of each month for each observatory and the subtraction of the resulting annual mean values of the horizontal component from the observed ones. The solar quiet daily variation, Sq, is also determined and removed, resulting in the disturbance variation for each observatory, which is then averaged over the four observatories and normalized to the dipole equator, thus producing the Dst index (<http://wdc.kugi.kyoto-u.ac.jp/dstdir/dst2/onDstindex.html>).

SYM-H index (symmetric disturbance field in the horizontal direction H), resembles the Dst [Sugiura and Poros, 1971], but it relies on 1-minute data from various stations and employs a slightly different coordinate system. SYM-H also represents the magni-

tude of the uniform field parallel to the dipole axis generated by the ring current and consequently, its interpretation mirrors that of Dst. Its derivation procedure is similar to the Dst one; it includes the subtraction of the geomagnetic main field and the Sq to calculate the disturbance field component, a coordinate transformation to a dipole coordinate system and finally the calculation of both the longitudinally symmetric (SYM-H and SYM-D) components, by averaging the disturbance component at each minute for the 6 selected stations [Iyemori et al., 2010]. Hence, its superiority over the Dst index lies in its ability to capture storm-related effects with notably enhanced temporal resolution.

In case of geomagnetic activity, both indices generally exhibit negative values. This is due to the main influence of the westward-directed ring current on the horizontal component of the magnetic field at the equator. Consequently, the induced magnetic field has a southward direction, leading to a reduction of the horizontal component.

1.4.1.2 Auroral Indices: AE, AL and AU

Another significant category of current systems responsible for numerous spectacular phenomena are the auroral electrojets. These currents flow through highly conductive pathways within the terrestrial ionosphere and are carried by particles that generate the auroral light. The auroral electrojets move both eastward (forming the East—ElectroJet—EEJ) and westward (forming the West ElectroJet—WEJ) [Papadimitriou et al., 2021]. These current systems are mainly responsible for the disturbances known as magnetospheric substorms [Akasofu, 1964, McPherron, 1979]. These collective phenomena are considered a primary mechanism for releasing accumulated energy within Earth’s magnetosphere [Kamide and Chian, 2007]. When the substorm expansion phase initiates, a dynamic process within the near-Earth magnetosphere redirects cross-tail current into the ionosphere. As a result, a substorm current wedge is formed; it consists of downward (upward) FACs on the dawnside (duskside) of the wedge and a westward auroral electrojet in the ionosphere Kepko et al. [2015]. The Auroral Electrojet index AE [Davis and Sugiura, 1966] is a measure of the intensity of this substorm enhanced westward ionospheric electrojet through its diamagnetic influence on the horizontal component of the terrestrial magnetic field.

The AE index represents the overall activity of the electrojets and is derived from geomagnetic variations in the horizontal component recorded at specific observatories along the auroral zone, exclusively in the Northern Hemisphere, at magnetic latitudes between $+60^\circ$ and $+70^\circ$. The derivation process includes the following steps (a) the data normalization, by averaging all the data on the five international quietest days, thus

calculating a base value for each station for each month; (b) this base value is subtracted from each 1-min value obtained at the station during that month; (c) among the data from all the stations at each given time (UT), the largest and smallest values are selected, defining the Auroral Upper (AU) and Auroral Lower (AL) indices; (d) their difference defines the AE index (<http://wdc.kugi.kyoto-u.ac.jp/aedir/ae2/onAEindex.html>).

1.4.2 Geomagnetic Activity

Geomagnetic variation consists of (a) quiet variation, which is regular in appearance and mostly of solar electromagnetic radiation origin, and (b) geomagnetic activity, which is irregular in appearance and mostly driven by the solar wind [Matzka et al., 2021]. Geomagnetic activity or disturbances include geomagnetic pulsations, magnetospheric substorms, geomagnetic storms, fast changes in the ring-current and other magnetospheric and ionospheric currents. Here, we will only discuss the two main categories: a) geomagnetic storms and b) magnetospheric substorms, as they are the most relevant to the scope of this dissertation.

1.4.2.1 Geomagnetic Storms

A geomagnetic storm is a major disturbance of the Earth's magnetosphere that occurs when the accumulated input power from the solar wind exceeds a certain threshold [Balasis et al., 2006]. Obviously, during a geomagnetic storm there is a very efficient exchange of energy between the solar wind and the space environment surrounding Earth. These storms are caused by sudden, strong variations in the speed, density and magnetic properties of the solar wind. The latter produces major changes in the currents, plasmas and fields of the Earth's magnetosphere. The storm conditions can last from several hours to a few days, and sometimes a new storm commences before the magnetosphere has fully recovered from the previous perturbation [Koskinen, 2011b]. Prerequisites for the occurrence of geomagnetic storms are sustained periods of high-speed solar wind, and most importantly, a strong southward directed Interplanetary Magnetic Field (IMF) (opposite the direction of Earth's field) at the dayside of the magnetosphere. This condition is effective for transferring energy from the solar wind into Earth's magnetosphere. Although there is no unique lower threshold for the magnetic perturbation above which it should be called a storm, in this thesis we adopted the convention that values of Dst index lower than -50 nT represent the threshold for geomagnetic storms. Typically, a geomagnetic storm consists of three distinct phases,

that is the initial phase, the main phase, and the recovery phase. Depending on the magnetic storm's driver these phases have characteristic features.

The largest storms that result from the aforementioned conditions are associated with two main drivers:

1. Solar CMEs. During the solar maximum phase, CMEs and their interplanetary counterparts ICMEs can travel in such a way as to dynamically interact with the Earth's magnetosphere, causing the compression of the magnetosphere due to the relatively high density and increased velocity of the sheath plasma [Gosling et al., 1991]. If the storm is driven by an ICME with a shock, it begins with a rapid positive deviation of the magnetic north component (H), referred to as storm sudden commencement (SSC), which is a signature of an ICME shock hitting the Earth's magnetopause. As the ICME pushes the magnetopause closer to the Earth, the Chapman–Ferraro current intensifies in order to shield the enhanced geomagnetic flux density from the solar wind. Because the direction of the dayside Chapman–Ferraro current is eastward, i.e., opposite to the ring current, the enhanced current, which is at the same time pushed closer to the Earth, causes a positive deviation in the H component Koskinen [2011b]; this behavior is captured by the Dst index, as indicatively shown in Figure 1.11.

The SSC is a global phenomenon and the perturbation of the magnetosphere is observable in magnetometers even within the auroral regions and on the nightside. Magnetic storms can also be driven by low-speed ICMEs and by fast solar wind without a preceding shock. Thus there are storms without a sudden commencement signature. On the other hand, a shock wave hitting the magnetopause does not necessarily lead to a storm development. In such cases the positive deviation of Dst index is called a sudden impulse (SI).

The enhanced Dst period that follows the SSC is the storm initial phase. The duration of the initial phase can vary significantly based on the structure of the solar wind driver. If the IMF in the sheath region between the shock and the ejecta is oriented southward, the initial phase may be quite brief. Conversely, if the sheath IMF is northward, the main phase will not commence until a southward field from the ejecta enhances reconnection at the dayside magnetopause. If there is no southward IMF within the part of the ICME interacting with the magnetosphere, a storm isn't anticipated, unless the event is followed by fast and long-lasting solar wind with a southward IMF component capable of driving a storm on its own [Koskinen,

2011b]. Normally, during a storm the initial phase will last for a few hours.

The interval during which the horizontal component of the magnetic field (and also Dst index) is decreasing dramatically is the storm main phase, which can last for tens of hours. This phase is caused by a sustained southward IMF reaching the magnetosphere and leads to a strong enhancement of the westward ring current.

Following the transit of the southward-oriented part of the IMF structure, the recovery phase begins. This phase typically unfolds at a much slower pace compared to the main phase, primarily because the loss processes of the current carriers are much slower than the enhancement of the ring current Koskinen [2011b]. During this phase, the trapped particles in the ring current region begin to disperse through various mechanisms (such as wave-particle interactions, Coulomb scattering, Joule heating) and the Dst index gradually returns to its background activity levels Daglis et al. [1999].

Figure 1.11 a shows a typical profile of an ICME storm. CMEs typically take several days to arrive at Earth, but have been observed, for some of the most intense storms, to arrive in as short as 18 hours. Storms attributed to the interplanetary counterparts of CMEs can be severe and last 1-2 days. The Dst index during such events may decrease by hundreds of nT. Also, it is during ICME storms that the most intense auroral emissions are noted. These emissions can extend over almost all local times. The auroral oval also expands, and can reach middle and low latitudes in extreme events. During the main phase and around the minimum Dst several substorms may occur.

2. High-Speed solar wind Streams (HSSs). During the descending and minimum phases of solar cycles, the occurrence of flares and CMEs diminishes, while another solar phenomenon becomes more prevalent: coronal holes. These coronal holes, observed as dark regions in x-ray images of the Sun, are initially located at the solar poles during the solar maximum phase. However, as the solar cycle enters its declining phase, they expand in size and shift towards the solar equator [Gosling et al., 1991]. These coronal holes are open magnetic field regions, from which emanate HSSs. These streams collide with the slower solar wind ahead of them, leading to the formation of Corotating Interaction Regions (CIRs).¹ These regions

¹Coronal holes are long living structures that can persist for more than one solar rotation. The HSSs, originated from a same region, reappear at intervals of approximately 27 days and this reappearance leads to the term “recurrent streams”. The spiral-like structure formed by these streams, distorted due to the solar rotation and its interaction regions with slower streams, is known as Corotating Interaction

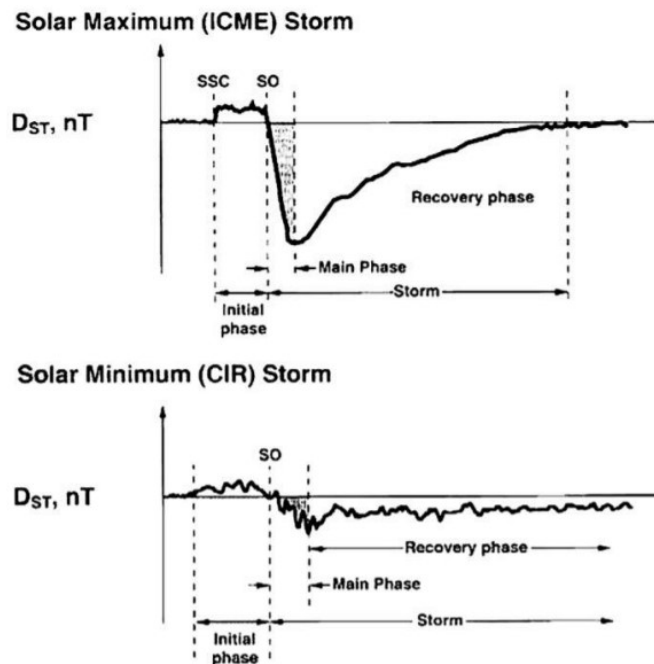


Figure 1.11: Characteristic examples of Dst profiles during (a) an ICME magnetic storm and (b) a CIR magnetic storm. Source: Tsurutani [2000].

are often related to geomagnetic storms that while less intense than CME storms since the B_z component within CIRs have large fluctuations[Gonzalez et al., 1999], often can deposit more energy in the Earth's magnetosphere over a longer interval. HSS driven storms typically last longer than CME driven storms (3-4 days). A schematic depicting the typical pattern of a CIR storm is presented in Figure 1.11b. In general, storms triggered by CIRs have initial, main and recovery phases. The initial phase is characterized by an increase in the Dst index, primarily induced by the high-density plasma region linked with the heliospheric plasma sheet (HPS) in front of the high-speed stream. This density increase is gradual, giving rise to a similarly gradual initial phase, in contrast to the abrupt commencement often seen in ICME-driven storms [Tsurutani et al., 1995]. The duration of CIR recoveries can be considerably longer than those observed during ICME storms. This prolonged recovery is attributed to the presence of southward-propagating Alfvén waves within the high-speed streams.

Roughly, the geomagnetic storms rate is 1-2 per month, but this number increases and decreases in line with the sunspot cycle.

Regions (CIRs).

1.4.2.2 Magnetospheric Substorms

Magnetospheric substorms constitute the main display of geomagnetic activity, together with the magnetic storms. While magnetic storms occur at the equator, magnetospheric substorms or simply substorms occur mainly at the auroral oval around both magnetic poles. Aurora Borealis and Aurora Australis are the visible signs of substorms. However, similarly to magnetic storms, these brief magnetospheric disturbances occur when the IMF is oriented southward, permitting interplanetary and terrestrial magnetic field lines to merge at the dayside magnetopause and energy to be transferred from the solar wind to the magnetosphere.

In contrast to geomagnetic storms, magnetospheric substorms represent a different type of disturbance that occurs within a more limited spatial and temporal scope. They take place over a span of several minutes to a few hours, predominantly manifesting in polar regions. Unlike geomagnetic storms, substorms do not inject a substantial number of particles into the radiation belt. They are relatively frequent, occurring at a rate of one to four substorms per day during disturbed periods and often occurring only a few hours apart from each other. It's noteworthy that substorms can be more intense and frequent during a geomagnetic storm, sometimes initiating before the previous one has completed.

A magnetospheric substorm is composed of three distinct phases [Lopez, 1990]:

1. **Growth phase.** Before the onset of auroral activity, during the growth phase, the magnetotail accumulates energy acquired from the solar wind. During this period, the cross-tail current intensifies, leading to an increase of the magnetic field within the lobes. At the same time the magnetotail experiences increased tension as the magnetic field lines stretch into a more elongated tail-like configuration. This heightened stress causes the near-Earth plasma sheet to narrow in the north-south direction, a process termed plasma-sheet thinning.
2. **Expansion phase.** The onset of the expansion phase of a substorm initiates when a discrete auroral arc, typically located in the midnight sector, undergoes a sudden intensification and expands towards the polar regions.
3. **Recovery phase.** Typically, after approximately one hour, the activity diminishes, and the auroral oval subsides to its quiet state during the recovery stage.

The whole substorm sequence takes typically 2–4 hours.

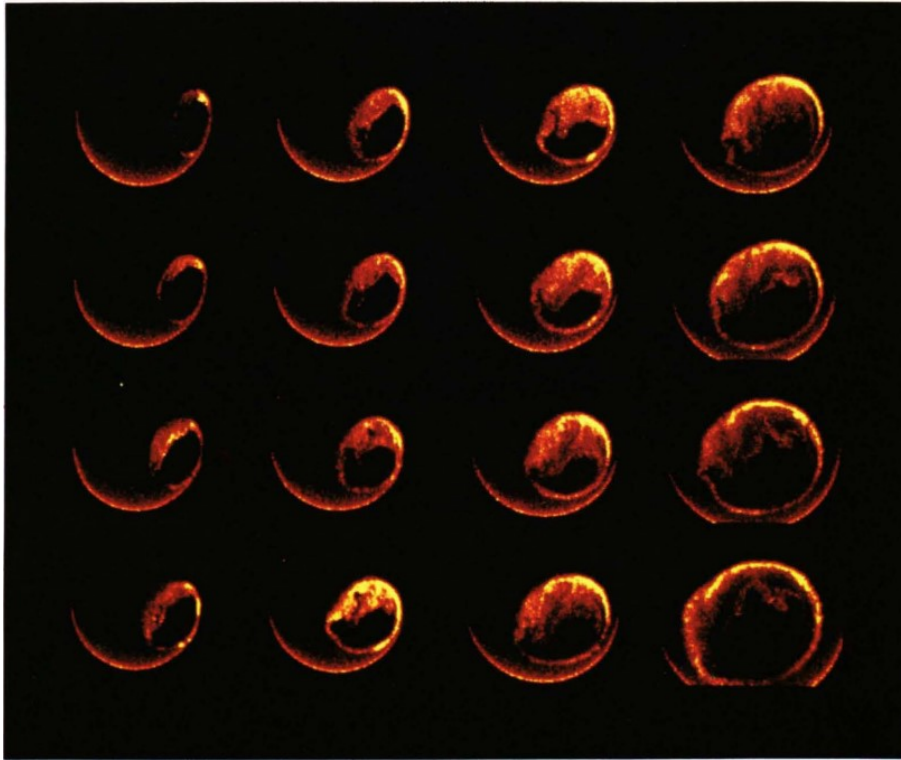


Figure 1.12: A sequence of images of the southern auroral zone during a major substorm taken by Dynamics Explorer 1 from 02:02 to 05:17 UT on June 13, 1983 . The substorm onset is observed in the first image at the upper left; time runs from top to bottom and then from left to right. The auroral brightening was initially localized and appears as a bright spot. The disturbance spread longitudinally and poleward. The last four images (the four right-most images) show the recovery phase of the event as the auroral luminosity decreased. Courtesy of Lou A. Frank and John D. Craven. Source: <https://secwww.jhuapl.edu/techdigest/Content/techdigest/pdf/V11-N3-4/11-03-Lopez.pdf>.

It should be pointed out that the enhanced electric field driven by southward IMF magnetic fields dominates the effects of the induced electric field in the magnetosphere resulting from substorm expansion onsets and, therefore, plays a central role in enhancing the storm-time ring current.

1.5 Geomagnetically Induced Currents (GICs)

Several space weather phenomena are linked to or triggered by either a geomagnetic storm or a magnetospheric substorm. The effects of these phenomena range from mild (e.g., interference with aeromagnetic surveys) to extreme (e.g., electric power grids may

experience blackouts or collapse).

Strong electric currents that flow in the near-Earth space and close through the upper atmosphere can be generated during geospace magnetic storms. The magnetic field of these currents induces currents in the Earth's surface (GICs), the intensity of which depends on the electrical properties distribution within specific regions of the Earth's solid crust. GICs occur at the ground end of the complicated "space weather chain": Sun – solar wind – magnetosphere – ionosphere – Earth's surface. In case where technological systems of critical infrastructure, such as electricity transmission networks, oil and natural gas pipelines, telecommunication cables and railway equipment are situated within areas where GICs develop, these currents can flow along these systems as well, potentially leading to significant disruptions or damages. Traditionally, it was thought that only electricity networks located in high latitudes (Northern America, Scandinavia) were susceptible to GICs. Indeed, rapid changes in the horizontal component of the Earth's magnetic field dB/dt due to substorms (which take place in high latitudes) can excite substantial GICs that can have harmful effects on technological systems. However, in recent decades, there have been reports of electrical power issues occurring in lower-latitude areas (e.g., South Africa [Ngwira et al., 2008]) and research into GICs in middle and low latitude regions, akin to Greece's latitudinal position, has gained significant scientific interest, with studies conducted in many countries (e.g., Italy [Tozzi et al., 2019a], Japan [Watari et al., 2009] and China [Liu et al., 2009]).

Within power systems, GICs represent (quasi-)direct current (DC) flows² and thus, can potentially lead to transformer saturation [Pirjola, 2000]. Consequently, this saturation results in a nonlinear operation of the transformer and in a remarkable increase of the exciting current. Possible consequences include the generation of harmonics in the electrical system, unnecessary relay trippings, increased reactive power demands, voltage fluctuations and drops, and, in the worst case scenario, a complete system blackout. Transformers may be overheated and in even permanently damaged. Furthermore, in the case of underground pipelines, GICs can contribute directly to corrosion. However, more detrimental is the disruption that GICs impose on corrosion control, monitoring, and protection systems. Less significant issues may arise in phone cables, railway equipment, and transoceanic seafloor cables.

²GICs are slowly varying compared to the 50-Hz mains. Their frequencies are typically in the mHz range, and thus, they can be considered quasi-DC currents.

1.5.1 Geophysical Background and Calculation of GIC

Intense time-varying magnetospheric and ionospheric currents lead to rapid fluctuations of the geomagnetic field on the ground. The physical principle that describes the flow of GICs in a technological system is based on Faraday's law of electromagnetic induction

$$(1.2) \quad \nabla \times \vec{E} = -\frac{\partial \vec{B}}{\partial t}.$$

Essentially, when a conductor is exposed to a changing magnetic field, an electromotive force gets induced along the conductor. If the conductor forms a closed circuit then an induced current will flow through it. In the case of the Earth's crust and surface, Faraday's law implies the existence of a geoelectric field during a temporal variation of the geomagnetic field. This geoelectric field drives currents that flow on ground conductors, such as power grids, according to Ohm's law

$$(1.3) \quad \vec{J} = \sigma \vec{E}$$

where \vec{J} is the current density, σ is the conductivity and \vec{E} is the electric field. Both the geomagnetic variation and the geoelectric field observed on the Earth's surface primarily depend on magnetospheric and ionospheric currents, which in turn are determined by the prevailing space weather conditions in the Earth's space environment. Secondly, the surface fields are affected by currents and charges generated within the Earth (Figure 1.13).

Analytical estimation of GICs in a power grid infrastructure during a geomagnetic storm is a challenging task that can be described as a two-step process. It consists of the "geophysical step", which refers to the determination of the geoelectric field that develops on the surface of the Earth during a magnetic storm, and the "engineering step", which requires knowledge of transmission line design parameters and includes the final determination of the induced currents. The geophysical step is independent of the technical characteristics that the grid under examination has and requires knowledge of the electrical conductivity of the respective terrestrial solid crust's sector that hosts the technical infrastructure under discussion.

To calculate the geoelectric field, there are three main methods: the Complex Image Method (CIM), the Spherical Elementary Current Systems (SECS) and the plane wave model. The simple 1-dimensional (1-D) model that assumes a plane wave propagating vertically downwards and a uniform half-space Earth with conductivity σ is traditionally used [Ngwira and Pulkkinen, 2019]. The fields are all presumed to be horizontally

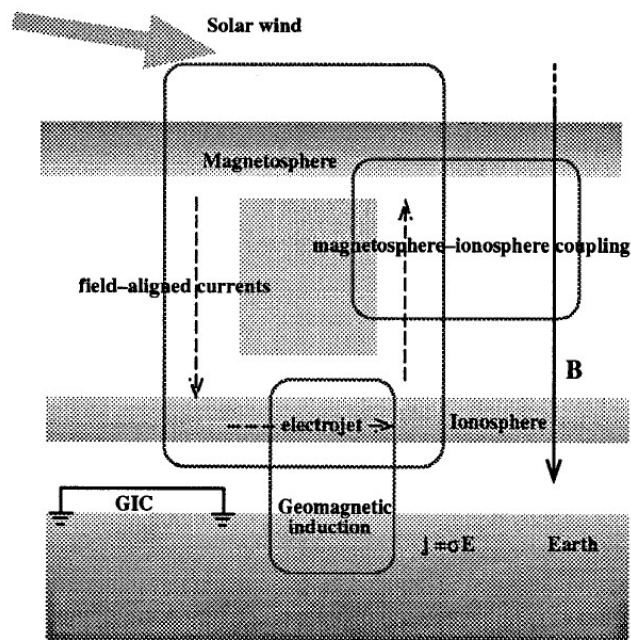


Figure 1.13: Schematic illustration of the geophysics involved in the GICs development in an earthed network. Variations of the ionospheric currents generate an electric field ($E(t)$) through geomagnetic induction in the Earth’s crust and surface. This electric field then drives GICs on ground conductors. Source: Viljanen and Pirjola [1994].

uniform to simplify the modeling. Adopting a single frequency ω , then the geoelectric field E_x and E_y components can be deduced in terms of the perpendicular geomagnetic field component B_y and B_x as:

$$(1.4) \quad E_{x,y}(\omega) = \pm \sqrt{\frac{\omega}{\mu_0 \sigma}} e^{\frac{i\pi}{4}} B_{y,x}$$

where μ_0 is permeability of free space, whereas the layer of air between the ground and the ionosphere is taken to have zero conductivity to limit significant attenuation of external electromagnetic fields. Since Equation 1.4 outlines the basis for deriving the Earth’s conductivity using geoelectric and geomagnetic field measurements recorded at the surface, it is considered as the “basic equation of magnetotellurics.”

1.5.1.1 Ground Conductivity

The Earth’s geology also plays a significant role in the geomagnetic induction process. The extent to which the geomagnetic field penetrates into the Earth’s crust is determined by the ground conductivity and the frequency of geomagnetic field fluctuations. Upper

layers exert greater influence over shorter time periods, while deeper layers have a more pronounced impact over longer durations.

Regarding the conductivity models used for GIC applications, there are two main approaches:

1. The plane wave model, which relies on the 1-D layered conductivity σ (being depth dependent) and is applied to a specific location.
2. The thin sheet model, which relies on a spatially varying conductance on a 2-D surface covering the region of interest, combined with a 1-D layered conductivity of upper lithosphere conductance. This approach incorporates the effect of lateral conductivity variations on redistribution of regional currents induced elsewhere (e.g., oceans or shelf seas).

Two more approaches with limited application are the homogeneous model (impedance Z is considered constant) and the full tensor.

1.5.1.2 Engineering Step

GICs flowing through a given node for any ground system can be calculated by considering the geoelectric field to be uniform in the near vicinity of the network using the expression

$$(1.5) \quad GIC(t) = aE_x(t) + bE_y(t)$$

where a and b are the network coefficients specific to each network node, depending only on the resistance and geometrical composition of the system [Viljanen and Pirjola, 1994].

Knowing the number of substations, the number of transformers and the number of transmission lines within the network, as well as their topology and electrical resistances is required in order to calculate the network coefficients, a and b . The most commonly used methods are:

1. Lehtinen-Pirjola (LP) method was developed by Lehtinen and Pirjola (1985) and computes the GIC in a single-voltage-level network, by solving Ohm's and Kirchoff's laws for the earthing current at each node of the network, as well as Thévenin's theorem.
2. Nodal Admittance Matrix (NAM) method is widely used in engineering to describe power systems and has proved to be mathematically equivalent to the LP method [Boteler and Pirjola, 2014].

3. Mesh Impedance Matrix (MIM) method applies Kirchhoff's voltage law to each loop of a resistive network, leading to a mesh impedance matrix equation that can be solved to give the currents in each loop [Boteler, 2014].

1.5.2 GICs in High Latitudes

At high latitude regions, such as Scandinavia and North America, the Earth's magnetic field lines tend to become more vertical and thus, they intersect the surface at steeper angles. Consequently, these regions are more susceptible to GICs because the varying magnetic field can induce larger electric fields near the ground.

At high latitudes, GICs can be a result of either geomagnetic storms, which as previously discussed are global phenomena, or magnetospheric substorms, which are localized disturbances in Earth's magnetosphere that occur predominantly in high-latitude regions. During a substorm, the ionospheric currents become more dynamic and have the potential to generate GICs. These regions often host extensive networks of conductive infrastructure, such as power lines and pipelines, running across the Earth's upper surface and, as already mentioned, the induced electric fields can drive GICs to flow through these conductive paths.

Historically, GICs were first noticed in 1847 [Barlow, 1849]. Back then, telegraph was the primary method of communication and relied on batteries for power. During the occurrence of Aurora Borealis, telegraph operators observed a disruption in the transmission of communications and once the power was switched off transmissions were conducted at an enhanced quality than with the use of batteries! After almost a decade, in September 1859, one of largest space weather events of the last 150 years, the so-called Carrington event, took place [Tsurutani et al., 2003]. During this event, the auroras (i.e., Aurora Borealis and Aurora Australis) associated with the magnetic storm were observed at much lower latitudes, while telegraph networks across Europe and North America experienced widespread failures, with some telegraph operators even receiving electric shocks and telegraph poles emitting sparks. However, the significance of GICs' impact on power systems was underscored by incidents during a large geomagnetic storm in March 1989 [Allen et al., 1989, Batista et al., 1991], which seriously affected North America. During this event, the SSC occurred concurrently with a substorm, so this combination led to the development of large GICs [Boteler, 2019]. The most notable effect occurred on March 13, 1989 at 07:45 UT when GICs in the Hydro-Québec electricity transmission system led to a province-wide electric black-out for approximately nine hours. Despite the restoration of 83% percent of full power after this period (i.e., nine

hours), one million customers remained without electrical power. The incident incurred a substantial cost, with the total estimated damage reaching six billion dollars. In response to this event, the Canadian government has set up protective measures at the Hydro-Québec site, such as the installation of transmission line series capacitors, a significant investment exceeding 1.2 billion dollars, aimed at mitigating the impact of GICs and preventing damage to the national power system. For further details, refer to the Organization for Economic Cooperation and Development (OECD) report at <https://www.oecd.org/gov/risk/46891645.pdf>.

More recently, the Halloween 2003 storms led to a power outage in Sweden, lasting approximately one hour. During these events, there were also reports of transformer failures in South Africa, which were linked to prolonged exposure to GICs with lower intensity.

1.5.3 GICs at Middle and Low Latitudes

Adverse effects due to GICs were initially studied only at high geomagnetic latitudes, where the auroral ionospheric currents are dominant, driving the magnetic field fluctuations on the ground to large deviations, especially during disturbed periods (e.g., Viljanen and Pirjola [1994], Pirjola et al. [2003]). While GICs are typically more prominent at high latitudes (closer to the polar regions), they can also occur at low latitudes under certain conditions. Indeed, in recent years, GIC estimation in low and middle latitudes receives ever-growing awareness from the scientific community and the power transmission industry, with studies conducted in several regions [Pulkkinen et al., 2017]. This comes as a result of large GIC values (and transformer failures due to them) reported at low and middle geomagnetic latitudes at a considerably increasing rate. Especially in Europe, the model of GIC emergence throughout the continent [Viljanen et al., 2014] reinforces the fact that large GICs can occur at low and middle latitudes, strongly depending on the ground conductivity and the topology of the power grid.

The early 2000s ushered in bibliographical references of GICs at low and middle latitudes [Koen and Gaunt, 2003]. Gaunt and Coetzee [2007] investigated an interesting case of reported transformer failures in the South African region (approximate magnetic latitude MLat for South Africa: 40° S) and associated them with the development of significant GICs. Ngwira et al. [2008] followed a multilayered ground conductivity structure approach to improve GIC modeling in the South African power network, while Matandirotya et al. [2015] compared modeled and measured GIC values focusing on the

2003 Halloween storm which, as already discussed in the aforementioned studies, had a significant impact on the South African power grid.

In Asia, Liu et al. [2009] compared magnetic storm recordings with measured transformer neutral current data to confirm that the observed disturbances in the Chinese high-voltage power grid were caused by GICs (approximate MLat for China: 31° N). Concurrently, Watari et al. [2009] performed GIC measurements in a power grid located in Japan (approximate MLat for Japan: 30° N) and associated them with variations due to geomagnetic activity, while in a later study [Watari, 2015] estimated GIC values from an empirical equation using geomagnetic and geoelectric field data as input. They found the maximum absolute values of the GICs associated with the March 13–15, 1989 and the October 29–30, 2003 magnetic storms to be approximately 6.4 and 4.2 A, respectively. In another study, Zhang et al. [2015] found that GICs were two or even three times higher during the SSC compared to the main phase of the 2015 St. Patrick’s Day storm in two low-latitude Chinese substations. Moreover, they ran a global magnetohydrodynamic (MHD) model to simulate the GICs during this SSC event, using as input solar wind observations, denoting that the eastward component of the geoelectric field is dominant for low-latitude locations during SSC events.

Transformer failure on the Transpower electricity system in New Zealand (approximate MLat for New Zealand: 47° S) during the 2001 event was studied by Béland and Small [2004], who reported that it was coincident with an SSC, and Marshall et al. [2012], who associated it with a change of nearly 20 nPa in the solar wind dynamic pressure and also calculated the GIC index to find a good correlation with GIC measurements recorded on the neutral lines of transformers across the Transpower network. In another study [Rodger et al., 2017], a 14-year-long data set of GIC measurements in a transformer located in Islington, New Zealand was analyzed and a correlation with local dB_H/dt , i.e., time derivative of the magnetic field’s horizontal component, was shown. Recently, Divett et al. [2020] used a thin-sheet model and a model of the electrical transmission network to calculate GICs in transformers of the New Zealand’s South Island. Then, they compared the modeled GICs with observations in the modeled frequency range and in the time domain for the 2015 St. Patrick’s Day magnetic storm. On the same continent, a preliminary risk assessment for the Australian power network was conducted by Marshall et al. [2011] aiming to study space weather-related GIC activity (approximate MLat for Australia: 35° S).

In the Mediterranean region, Torta et al. [2012] conducted an initial GIC study focusing on a power grid of Northeastern Spain, while Torta et al. [2014] assessed the

maximum expected GIC values in each transformer of the Spanish high-voltage power grid by adopting a plane wave approach and a homogeneous conductivity structure (approximate MLat for Spain: 33° N). They also examined 100-year and 200-year return period scenarios and evaluated the model's uncertainties, which Torta et al. [2017] improved by performing magnetotelluric sounding. More recently, Tozzi et al. [2019a] performed a preliminary risk assessment regarding GICs in the Italian territory, including the northernmost Italian region, which is characterized by low ground conductivity (approximate MLat for Italy: 35° N).

A number of studies focusing on central Europe have also been conducted. For example, Bailey et al. [2017] used a thin-sheet approach and conductivity models to compute the geoelectric field in Austria (approximate MLat for Austria: 42° N), showing that the Austrian power grid is susceptible to large GICs, especially from intense geomagnetic variations in the east-west direction.

A significant remark is that GICs flowing at low and middle latitudes are linked to ionospheric fields different from the ones observed at high-latitudes (e.g., auroral electrojets). According to Kappenman [2005], the source of sustained GICs at low and middle latitudes is linked to high rates of change of the geomagnetic field associated with impulsive increases in the solar wind's dynamical pressure or ring current intensification. In these regions, the maximum values of the time variation of the magnetic field's horizontal component (dB_H/dt) usually occur at the abrupt storm onset and not during its main phase, therefore vulnerability is higher around these times [Kappenman, 2003]. Indeed, the majority of intense GICs seem to occur as a consequence of sudden impulses (SIs) or SSCs that usually precede a geomagnetic storm. SIs are generated as a result of enhanced magnetopause currents due to the compression of the magnetosphere by plasma arriving from the Sun following the occurrence of extreme solar phenomena, such as CMEs or CIRs [Gosling and Pizzo, 1999]. Moreover, another interesting observation correlates large voltages at middle latitudes during the recovery phase of geomagnetic storms to Pc5 pulsations (e.g., Hejda and Bochníček [2005], Tozzi et al. [2019b]).

1.5.4 Transformers in Electrical Power Networks

The geoelectric field implies the existence of potential differences between several points across the Earth's surface. For example, there is a potential difference between the earthing points of two transformers. Thus, a GIC will flow in the transmission line that connects the two transformers (Figure 1.14). GICs are slowly varying compared to the 50-Hz mains. Their frequencies are typically in the mHz range, and thus, they can be

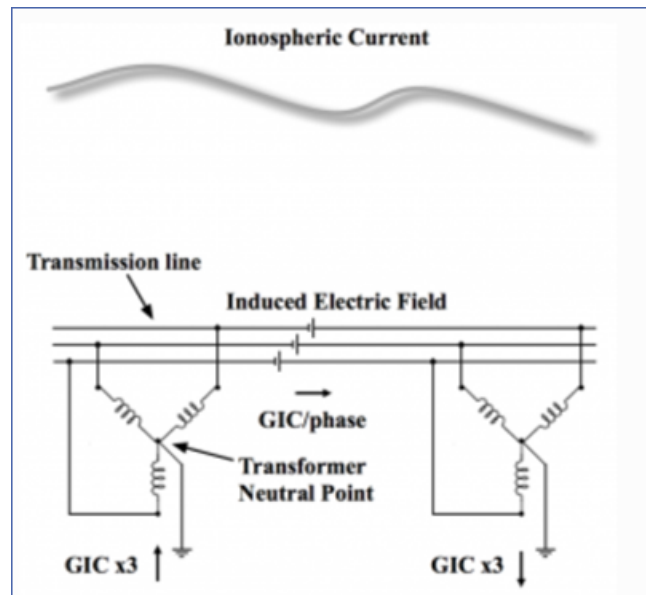


Figure 1.14: GIC flowing along the transmission line between two transformers. A time-varying ionospheric current, i.e., the primary driver of GICs is also schematically shown. Source: Wik et al. [2008]

considered quasi-direct currents (quasi-DC). GIC sizes in an electric energy system are also affected by its geometrical and structural details. Normally, GICs vary significantly between different areas in an extensive system of electric energy transmission. In general, large transmission lines suffer from greater GIC values. Problems caused in electric energy transmission networks are due to half-cycle saturation of the transformers, resulting from GIC flow. This means that a transformer normally functioning with a very small excitation current starts developing even 100 times greater current leading to a great asymmetry and the transformer working beyond the limits of its design (Figure 1.15).

Transformer cores can saturate under the effect of GICs by operating in the saturation region of the magnetization curve (B-H) of their steel core. A saturated transformer:

- consumes major amounts of reactive power, which reduces the ability of AC transmission in the system, while voltage tends to obtain lower values.
- creates many harmonics³ in electricity, which can lead to false relay trippings of the protective devices, but also to additional losses in various devices.

³Harmonics are currents or voltages with frequencies that are integer multiples of the fundamental power frequency, which in the U.S. is 60 Hertz. If the first fundamental frequency is 60 Hz, then the second is 120 Hz, and the third is 180 Hz.

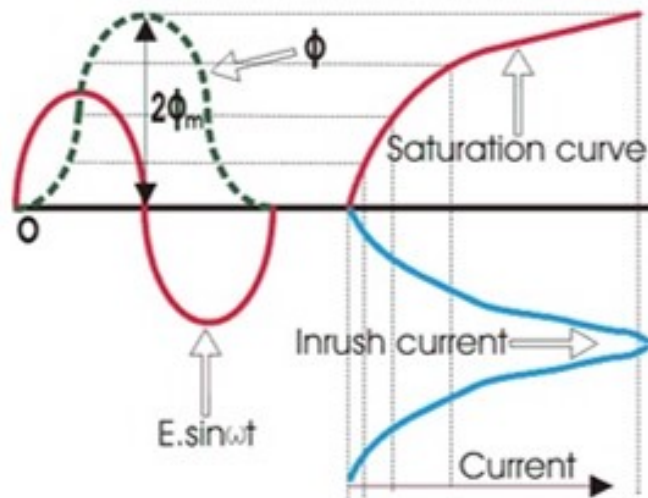


Figure 1.15: Schematic illustration of the inrush current versus saturation curve versus applied voltage. Source: https://www.electrical4u.com/magnetizing-inrush-current-in-power-transformer/?utm_content=cmp-true

- causes increment of the magnetic flux in a transformer and can take paths not designed for transferring magnetic fluxes. This can cause overheating of the transformer and localized hot spots may appear. The worst case scenario is a permanent damage of the transformer as the final consequence (Figure 1.16).

When a large number of transformers experience GIC saturation, the demand for reactive power and the harmonics of the system voltage are significantly increased. Reactive power demands of this magnitude can cause serious changes in the system voltage. The change in the size of the ferromagnetic material (magnetostriction) between the saturated and the unsaturated states at twice the power frequency produces heat, noise and mechanical vibration damage. The transformers may also suffer premature aging due to the effects of GICs.

Nowadays, power companies often implement protective measures to mitigate the impact of GICs on their electrical power systems, including the transformer design and operation. Some transformers are designed or modified to better withstand the effects of GICs. Additionally, operators may adjust the tap settings on transformers to reduce the impact of induced currents. Furthermore, utilities may install neutral blocking devices or grounding transformers to prevent GICs from entering the power system through the neutral connection. These devices can help isolate the power system from the geomagnetic activity effects. Also, adding series of capacitors to transmission lines in order to alter the system's impedance reduces the flow of GICs. This can help protect



Figure 1.16: During the magnetic storm of Halloween 2003, GICs damaged the high voltage winding of this transformer at a large Eskom power station (South Africa), leading within a few weeks to a melted copper conductor and burned insulation, taking the transformer and associated 665 MW generator out of service. Credit: Trevor Gaunt, UCT. Source: <https://www.sansa.org.za>

transformers and other equipment. Other possible measures aiming at the enhancement of the power grid's resilience against the adverse effects of GICs and minimization of the risk of power outages and equipment damage during geomagnetic storms include (a) the geomagnetic storm monitoring with early warning systems and alerts when geomagnetic storms are likely to occur, allowing utilities to take preventive actions, (b) the use of reactive power compensation devices, such as capacitors and reactors, to manage voltage levels and reduce the impact of GICs on the power system, (c) the temporal reduction of the system loading, rerouting power flows, or taking specific equipment offline.

1.6 Geomagnetic Field Data

Geomagnetic field data refers to information collected about the Earth's geomagnetic field and is typically collected through a network of instruments called magnetometers, which can be deployed on the Earth's surface, on satellites, or even on submarines.

Geomagnetic field data can include various measurements:

1. Magnetic Field Strength (Intensity): This refers to the measure of the strength

of the magnetic field at a particular location. It is often expressed in units of nanoteslas (nT). The Earth's magnetic field strength varies from place to place and changes over time due to both external factors (such as solar activity) and internal factors (such as the movement of molten material in the Earth's core).

2. **Magnetic Declination:** This refers to the angle between true north (geographic north) and magnetic north. It indicates the direction in which a compass needle points relative to geographic north.
3. **Magnetic Inclination (Dip Angle):** This is the angle between the magnetic field lines and the horizontal plane at a given location. It helps determine how steeply the magnetic field lines enter the Earth's surface.
4. **Magnetic Variation:** This is a general term used to describe the differences between true north and magnetic north, including both magnetic declination and magnetic inclination.
5. **Geomagnetic Anomalies:** These are localized variations in the Earth's magnetic field strength. They are mostly used by geologists and geophysicists to study the composition and structure of the Earth's crust and to locate subsurface geological features like mineral deposits or faults.

Magnetic fields are vector quantities characterized by both strength and direction. Measurements of the Earth's magnetic field are often quoted in units of nanotesla (nT), also called a gamma. The Earth's magnetic field can vary from 20,000 to 80,000 nT depending on the location; fluctuations in the Earth's magnetic field are on the order of 10^2 nT, and magnetic field variations due to magnetic anomalies can be found in the picotesla (pT) range.

Magnetometers measure the direction, strength or relative change of a magnetic field at a particular location. A compass is a simple example of magnetometer that measures the direction of the ambient magnetic field. The main types of magnetometers employed in magnetic observatories all over the world are (a) the fluxgate magnetometer, (b) the proton precision magnetometer, (c) the Overhauser and (d) the declination/inclination (D/I)-flux magnetometer. Magnetometers are sensitive against any type of magnetic noise, such as electricity pylons, cars, metallic fences etc. and are widely used for measuring the Earth's magnetic field and in geophysical surveys to detect magnetic anomalies of various types.

Depending on what the instrument measures, there are two categories:

1. Vector magnetometers measure the vector components of a magnetic field. We should note that the Earth's magnetic field at a given point is a vector.
2. Total field or scalar magnetometers measure the magnitude of the vector magnetic field to which they are subjected, but not its direction.

Ground-based magnetometers have proven to be the workhorse of magnetosphere-ionosphere coupling physics.

1.7 Fluxgate Magnetometers

Fluxgate magnetometers, originally developed during World War II as submarine detection devices for low-flying aircraft, have emerged as versatile instruments renowned for their precision in measuring and recording magnetic field intensity. Their applications span a wide range of fields, including geophysics, space science, navigation, and even consumer electronics.

Nowadays, magnetic observatories have been established worldwide to facilitate both long-term and short-term monitoring of the time-varying magnetic field. Fluxgate magnetometers have risen in popularity, becoming the cornerstone instruments in modern digital observatories. This popularity stems from their robust construction and reliable electronics. A typical magnetic observatory configuration includes a vector fluxgate magnetometer for measuring the three orthogonal components of the geomagnetic field (usually called a variometer), a scalar magnetometer for determining total field intensity, a theodolite for orienting the vector magnetometer, and a data collection platform for data storage. However, in magnetic stations, a vector fluxgate magnetometer is often sufficient for measuring abrupt changes in the geomagnetic field.

Operating on the principles of electromagnetic induction, fluxgate magnetometers (Figure 1.17) rely on Faraday's law⁴ to detect changes in the ambient magnetic field. They are based on a magnetic saturation circuit, where two closely spaced ferromagnetic bars exhibit nonlinear magnetic properties. When subjected to an external magnetic field, these bars reach magnetic saturation, generating induced magnetic fields. The susceptibility of the two bars is large enough so that even the Earth's relatively weak magnetic field can produce magnetic saturation in the bars. The induced fields are

⁴Faraday's law of electromagnetic induction states that a changing magnetic field induces an electromotive force (EMF) or voltage in a nearby conductor. When a magnetic field passes through a coil of wire, it induces an electrical current in the coil. In the context of fluxgate magnetometers, the magnetic field to be measured is introduced to induce a response in the instrument.

harnessed to measure the desired component of the Earth's magnetic field, with the instrument's orientation determining the direction.

The instrument's design incorporates a primary (excitation) coil wound around each bar, but the direction in which the coil is wrapped around the bars is reversed. An alternating electrical current (AC) is passed through the primary coils causing a large, inducing magnetic field that produces induced magnetic fields in the two cores that have the same intensities but opposite orientations. This alternating magnetic field drives the core through an alternating cycle of magnetic saturation (i.e., magnetised, unmagnetised, inversely magnetised, unmagnetised, magnetised, and so forth), causing its magnetic properties to change in response to the external magnetic field being measured.

A secondary (sensing) coil surrounds the two ferromagnetic cores and the primary coil and senses changes in the magnetic field due to the core's altered magnetic state. The magnetic fields induced in the cores by the primary coil produce a voltage potential in the secondary coil. In the absence of an external field, the induced fields in the bars cancel each other, resulting in zero voltage in the secondary coil. However, when the cores align with a component of a weak, external magnetic field, they produce a measurable voltage in the secondary coil, proportional to the field's strength along that direction.

Thus, this instrument is capable of measuring the strength of any component of the Earth's magnetic field by simply re-orienting the instrument so that the cores are parallel to the desired component.

Fluxgate magnetometers excel in measuring magnetic field strength, with a resolution typically reaching 0.1 nT or even 0.01 nT, and a bandwidth extending from DC to 5 Hz. In observatory-grade instruments, three orthogonal sensors are fixed to a common frame to record the three geomagnetic field components continuously. These sensors are compact and robust, designed to minimize instrument drift over time.

The heart of the fluxgate magnetometer lies in modulation and demodulation. The excitation coil generates a high-frequency alternating magnetic field, modulating the magnetic properties of the core. The detection coil senses changes in magnetic flux, resulting in an electrical signal representing the external magnetic field's variations. Demodulation extracts the low-frequency signal carrying information about the magnetic field's strength, providing a reliable measurement of the field's characteristics.

1.7.1 ENIGMA Instrumentation

The National Observatory of Athens (NOA) operates the HellENic GeoMagnetic Array (ENIGMA), a network of four ground-based magnetometer stations in Klokotos (abbe-

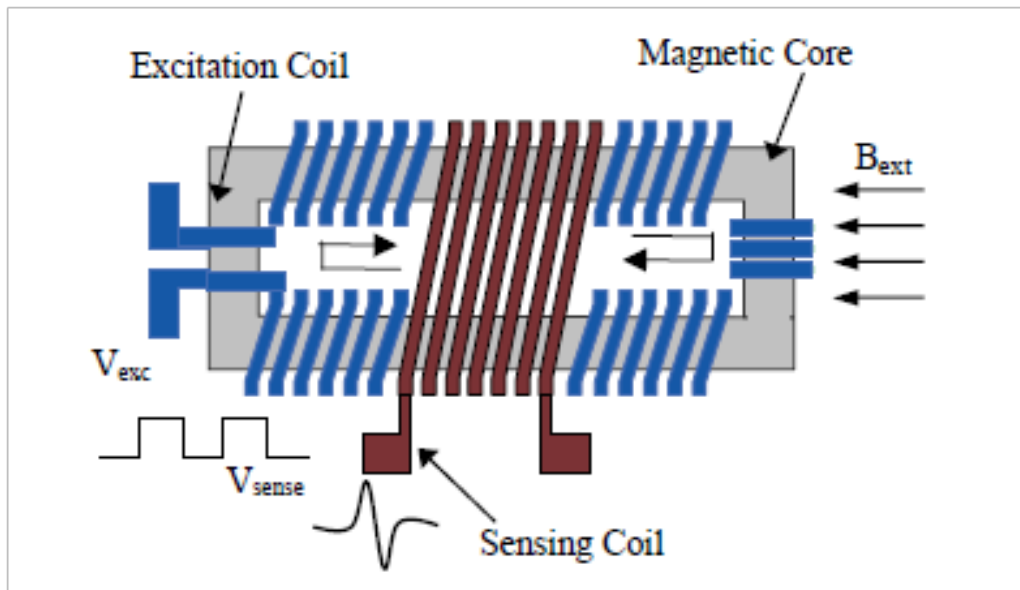


Figure 1.17: Schematics of a fluxgate magnetometer.

viated as THL), Dionysos (DIO), Velies (VLI) and Finokalia (FIN), located in central and southern Greece (<http://enigma.space.noa.gr/>). ENIGMA monitors the geomagnetic field variations associated with the occurrence of magnetic storms and ultra low frequency (ULF) waves using vector fluxgate magnetometers. Fluxgate magnetometers have three orthogonal sensors to measure the components of the geomagnetic field in all three dimensions, along with their fluctuations. The y-axis is horizontal and lies in the same vertical plane as the magnetic axis of the sensor. The x-axis is also horizontal and perpendicular to y, while z is pointing downwards. ENIGMA is a SuperMAG (<http://supermag.jhuapl.edu/>) contributor, a worldwide collaboration of organizations and national agencies that currently operate more than 300 ground-based magnetometers [Gjerloev, 2009]. In this study we have mainly employed geomagnetic field data from SuperMAG on a minute time resolution. Additionally, we have also used data from INTERMAGNET, a global network of observatories (<https://intermagnet.org/>).

In ENIGMA stations, they operate one GEOMAG02M and three GEOMAG02 instruments. Specifically,

- THL: GEOMAG-02 magnetotelluric station (MTS) (GEOMAGNET, Ukraine)
- DIO: GEOMAG-02M fluxgate magnetometer (GEOMAGNET, Ukraine) (Figure 1.18)
- VLI: GEOMAG-02 MTS (GEOMAGNET, Ukraine)

- FIN: GEOMAG-02 MTS (GEOMAGNET, Ukraine) (Figure 1.19)

GEOMAG-02M fluxgate magnetometer is an instrument specifically designed to measure the three components of the geomagnetic field (x-North, y-East and z-Downward) with 1 Hz cadence. It provides the following advantages: resolution of 0.01 nT, accuracy of 0.1 nT, operating range of $\pm 65,000$ nT.

A GEOMAG-02 MTS is designated for simultaneous measurements of both the magnetic and the electric (telluric) field variations of the Earth, with 1 Hz cadence. It consists of a three-component meter of magnetic field variations (magnetometer) based on a fluxgate sensor and a two-component meter of electric field (telluric current) variations based on the measurement of potential difference of non-polarized electrodes⁵. Fluxgate magnetometers share the same characteristics with the GEOMAG-02M instrument. Both GEOMAG-02M and GEOMAG-02 are manufactured by the «Research Center Geomagnet» in Lviv, Ukraine and are characterized by low noise level and good stability. Detailed technical characteristics can be found in Dobrodnyak et al. [2013] and Reda and Neska [2016].

Fieldwork is an important aspect of a PhD focusing on GICs. Within the scope of my doctoral studies, I actively engaged in significant fieldwork. Specifically, I took part in the Pre-Tect field campaign in Finokalia, Crete, during April 2017 (<http://pre-tect.space.noa.gr/>). In the course of this campaign, the fourth magnetometer of the ENIGMA network, a GEOMAG-02 magnetotelluric station providing high-resolution measurements at a frequency of 10 Hz, was successfully installed (FIN station). Furthermore, I participated in the installation of the NEO station in Methoni, which includes the instrument Observatory Fluxgate Variometer – CTU⁶ (Vario 15) and was established for a trial operation (i.e., not a permanent station) in August 2018. This hands-on involvement not only enriched my academic knowledge in the field but also contributed to the practical implementation and expansion of the ENIGMA network.

⁵In ENIGMA stations we use 6 Ag/AgCl-type electrodes, manufactured in GFZ Potsdam, to measure simultaneously the geomagnetic and the geoelectric (telluric) fields.

⁶CTU stands for Czech Technical University (in Prague)



Figure 1.18: Photograph from DIO station instrumentation (GEOMAG-02M fluxgate magnetometer).



Figure 1.19: Photographs from FIN station instrumentation (GEOMAG-02 magnetotel-
luric station)

TIMESERIES ANALYSIS METHODS OF GEOMAGNETIC FIELD DATA

The solar wind–magnetosphere–ionosphere coupled system is known to exhibit nonlinearity, as demonstrated by various studies (e.g., see Johnson and Wing [2005], Wing et al. [2022] and references therein). This highly dynamic system represents an open spatially extended, and non-equilibrium complex system with input and output interactions [Baker et al., 1990, Tsurutani et al., 1990, Vassiliadis et al., 1990, Sharma et al., 1993, Sitnov et al., 2001, Consolini et al., 2008]. Information theory has proven to be a valuable tool for exploring this coupled system [Balasis et al., 2009, 2013, Wing et al., 2016, Donner et al., 2018, 2019, Johnson et al., 2018, Runge et al., 2018, Stumpo et al., 2020, Manshour et al., 2021, Osmane et al., 2022]. Notably, recent investigations have utilized Swarm data and information theory techniques to delve into the intricate dynamics of the near-Earth electromagnetic environment [Balasis et al., 2020, De Michelis et al., 2020, 2021, Papadimitriou et al., 2020, Consolini et al., 2021].

Recent publications have contributed significantly to the field of space science research, as evidenced by a recently published eBook dedicated to the applications of statistical methods in space sciences [Poduval et al., 2023]. For instance, Delzanno and Borovsky [2022] emphasize the significance of a holistic system science approach to both global magnetospheric models and spacecraft magnetospheric data. In a related context, Telloni [2022] focuses on the value of statistical analyses concerning interplanetary and geomagnetic data for space weather prediction. Furthermore, Verkhoglyadova et al. [2022] discuss the implementation of a mixture method approach and a computer vision

approach to quantitatively address anomalies and high density regions (HDRs) that are present within a global ionospheric map. Their research sheds light on how the number of HDRs and their intensities are influenced by solar and geomagnetic activities.

This Chapter is dedicated to the analytical methods used to study the time series data of the geomagnetic field in the context this dissertation. In Section 2.1 we provide a concise overview of the preprocessing procedures applied to the time series data acquired from ground-based magnetometers. Section 2.2 focuses on fundamental principles of wavelet spectral analysis, while Section 2.3 is dedicated to the Hurst exponent. Sections 2.4 to 2.6 focus on the entropy measures of Shannon entropy and Tsallis entropy, as well as Fisher information, respectively.

2.1 Pre-processing

Preprocessing time series data is a critical step in data analysis to ensure that the data is reliable and suitable for further analysis. One common problem that often needs to be addressed during time series preprocessing is, for example, the presence of spikes or outliers. Geomagnetic field indices (i.e., SYM-H and AE) derive from corrected, averaged and normalized data, so we use them as provided. Swarm-derived indices are produced by following a specific methodology which will be briefly described in the following chapter and we will use them as such. Magnetometer data, when obtained from repositories like SuperMAG and INTERMAGNET, have in most cases undergone some substantial processing (e.g., may have the baselines subtracted), so are not entirely raw data. Yet, they may contain spikes or data gaps which need to be cured (if possible) before applying the various analysis methods. In this section it is this type of data that we discuss about.

2.1.1 Data Gaps

For the ground-based magnetic field data to be analysed in this dissertation, there were cases where no recordings from the sensor (magnetometer) were available for long periods of time (e.g., one - or more - days or even a whole month). For these cases, no analysis was attempted. However, if there were data gaps of several minutes, the time series was kept and the data gaps were filled by linear interpolation (Matlab's integrated `interp1` function). In Figure 2.1 we provide an example of simple linear interpolation implementation, where the denoted blue circles represent the added values in-between the original time series values.

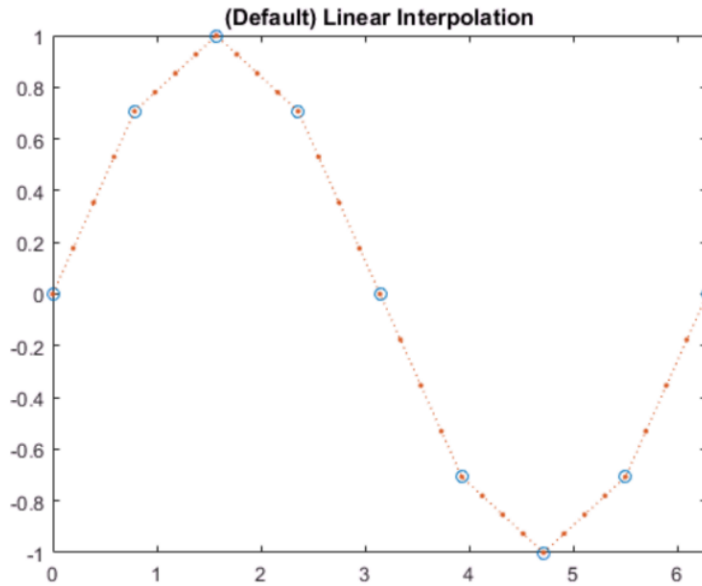


Figure 2.1: Example of linear interpolation. What the function does is to return interpolated values of a 1-D function at specific query points using linear interpolation. In this example the query points are the ones marked with the blue circles. Source: Mathworks.

2.1.2 Decimate

The desired sampling rate for all time series was 1 minute, and indeed the majority of the selected time series were downloaded at 1 minute cadence. Nevertheless, ENIGMA had finer time resolutions (1 Hz for DIO and VLI and 5 Hz for THL) and so, the next step to follow was to perform decimation in order to reduce the original sampling rate from one (or five) value(s) per second to one value per minute. Decimation was succeeded, using the Matlab's function *decimate*; the specifications suggested that in order to obtain better results, when r is greater than 13 (in our case it was 60), it should be divided into smaller factors and call *decimate* several times. This suggestion was adopted and so we consecutively performed decimation, with r equal to 10, 3 and 2 ($10 \cdot 3 \cdot 2 = 60$) in the case of DIO and VLI stations and 10, 10 and 3 ($10 \cdot 10 \cdot 3 = 300$) in the case of THL station. In Figure 2.2 we provide an example of simple decimation implementation, where the original data set is downsampled by a factor of 4.

2.1.3 Detrend

Detrending time series data is a crucial step in the analysis of temporal trends and patterns. Time series data often exhibit various forms of underlying trends or seasonality, which can obscure the true relationships and structures within the data. These trends

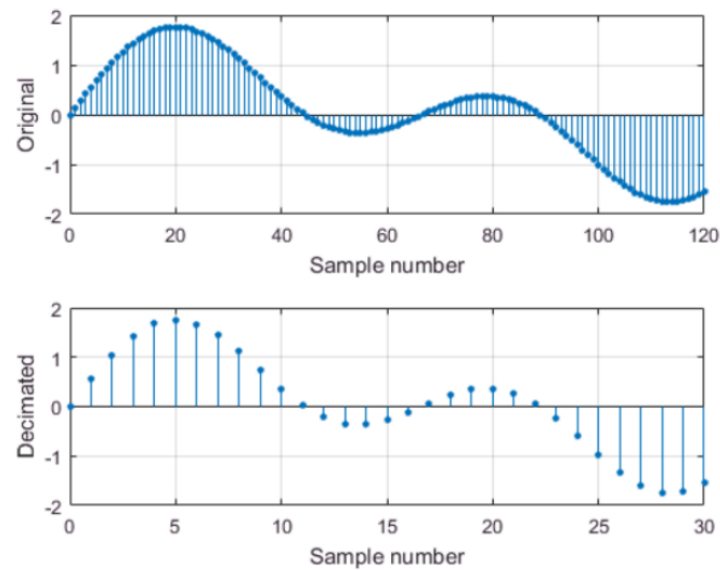


Figure 2.2: The original sinusoidal signal is decimated by a factor of 4, using a lowpass filter. Source: Mathworks.

can be a result of various factors such as long-term growth, cyclic patterns, or other systematic variations. By removing these trends, researchers and analysts can gain a clearer understanding of the inherent fluctuations and underlying patterns in the data, making it easier to detect anomalies, make more accurate forecasts, and identify potential causal relationships.

The data cleaning process of our time series includes the removal of trends, thus, all data were detrended to remove linear local trends and shifting all variations around zero. To do so Matlab's function *detrend* was employed.

2.1.4 Spikes

It is very common for recording instruments (in our case magnetometers) to be subject to external effects that affect the quality of the records. Anomalies (artifacts) generally arise for several reasons, such as natural phenomena (e.g., thunderstorms, which induce electric currents inside the Earth and cause transient changes of the natural behavior of the Earth's magnetic field), anthropogenic phenomena (e.g., due to the proximity of large cities, airports, railways, and power lines), calibration of the measuring instrument or distortion of data during their transfer from observatories to information nodes via the Internet [Bogoutdinov et al., 2010]. In several instances our data were "infected" by spikes or outliers. In order to remove the majority of them, we had to impose a logical

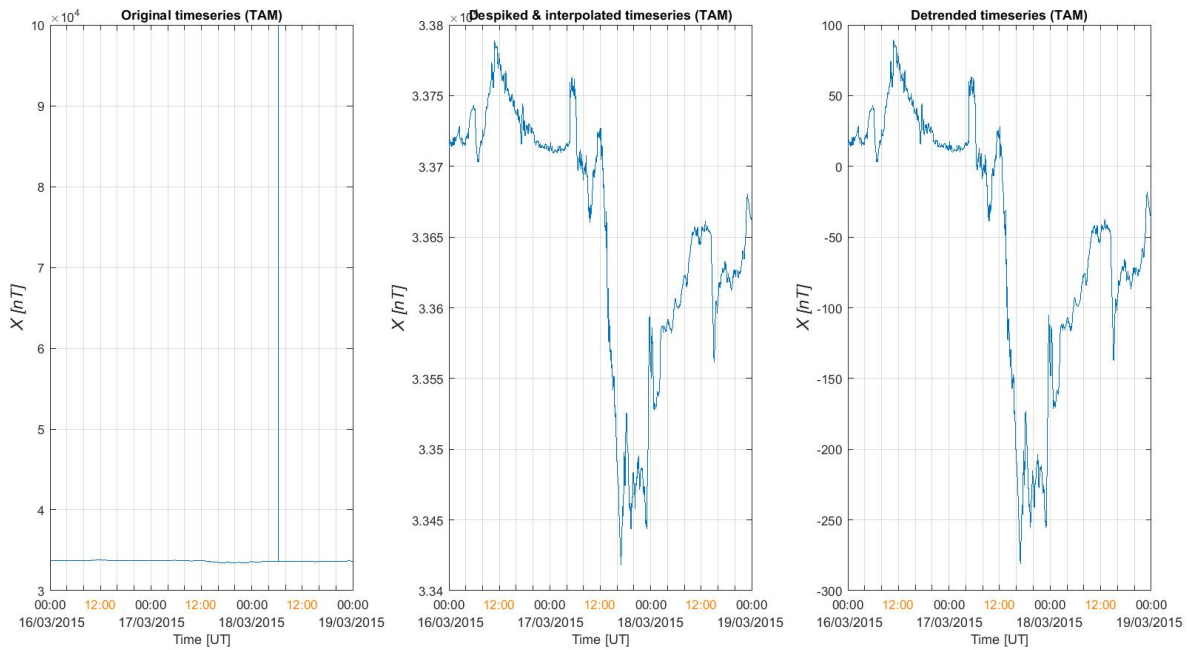


Figure 2.3: Original magnetometer data (Bx component) from TAM observatory with an obvious spike in the left panel, its despiked and interpolated version in the middle panel and its detrended version in the right panel.

threshold value and cut off all values exceeding them. The cut-off values were replaced by NaN and then linearly interpolated, following the exact same method as discussed before. In Figures 2.3, 2.4 are displayed two examples of the spikes which were removed from original magnetometer data (TAM and IZN station, respectively).

2.1.5 Geomagnetic Field Components

Since geomagnetic field is a vector field, at least three elements (components) are necessary to represent the field. The elements describing the direction of the field are declination (D) and inclination (I), measured in degrees. D is the angle between magnetic north and true north and I is the angle between the horizontal plane and the total field vector. The elements describing the field intensity is the total intensity (F), horizontal component (H), vertical component (Z), and the north (X) and east (Y) components of the horizontal intensity. These elements are generally expressed in units of in nanoTesla (10^{-9} Tesla / 10^{-5} Gauss or 1 Gamma in CGS). By convention, D is considered positive when the angle measured is east of true north and negative when west, I and Z positive down, X positive north, and Y positive east (Figure 2.5). The most

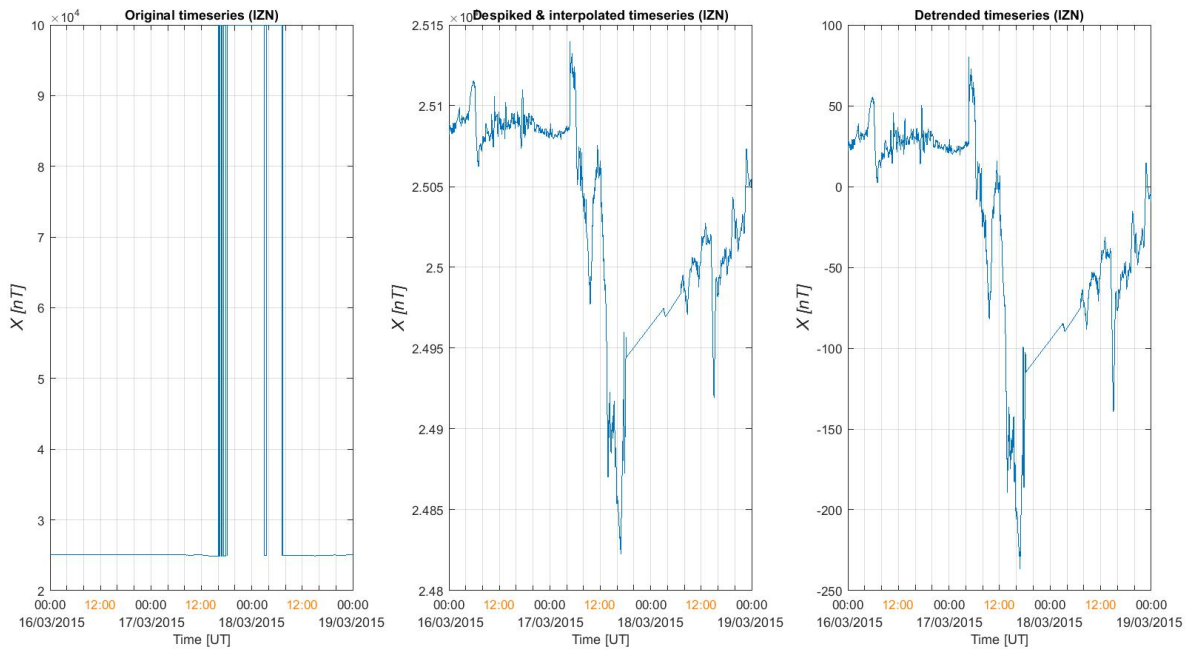


Figure 2.4: Original magnetometer data (Bx component) from IZN observatory with an obvious spike in the left panel, its despiked and interpolated version in the middle panel and its detrended version in the right panel.

frequently used combinations of three elements in geomagnetism are HDZ, XYZ and FDI.

For our analysis we wanted all data sets to be in XYZ. Originally, the majority of the time series used were indeed in this coordinate system, with few exceptions which were in DHZF. The principal equations relating the values of the elements which were used for the coordinate conversion are the following:

Principal equations relating the values of the elements are as follows:

$$\begin{aligned}
 F &= (X^2 + Y^2 + Z^2)^{1/2} = (H^2 + Z^2)^{1/2}, \\
 H &= F * \cos(I), \\
 Z &= F * \sin(I), \\
 X &= H * \cos(D), \\
 Y &= H * \sin(D)
 \end{aligned}$$

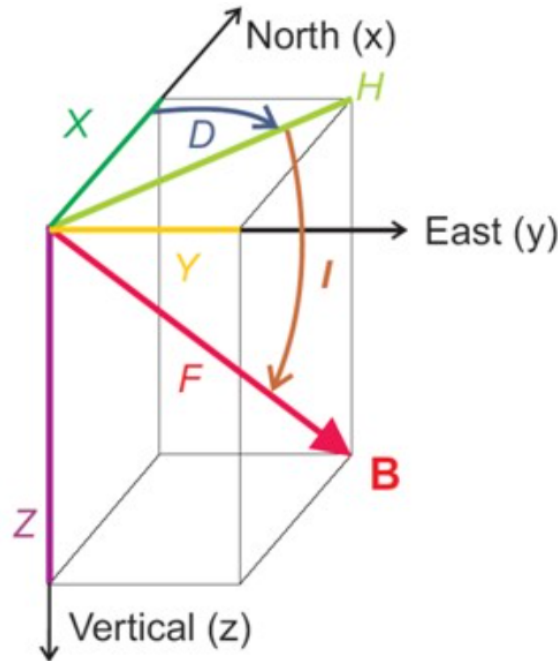


Figure 2.5: The seven elements of the (local) magnetic field in the Cartesian coordinate system. Source: <https://www.ngdc.noaa.gov/geomag/geomaginfo.shtml>

2.2 Fourier Transform

The Fourier Transform is a mathematical tool used to analyze the frequency components of a time-domain signal. It takes a function of time (often referred to as a time-domain signal) and transforms it into a function of frequency (frequency-domain signal). This transformation allows us to understand how different frequencies contribute to the original signal.

The Discrete Fourier Transform (DFT) converts a finite sequence of N equally-spaced samples complex numbers $\{x_n\} := x_0, x_1, \dots, x_{N-1}$ into a same-length sequence of equally-spaced samples $\{X_k\} := X_0, X_1, \dots, X_{N-1}$ of the discrete-time Fourier transform (DTFT), which is a complex-valued function of frequency:

$$(2.1) \quad X_k = \sum_{n=0}^{N-1} x_n e^{-\frac{i2\pi}{N} kn}$$

Its inverse is referred to as Inverse Discrete Fourier Transform (IDFT) and is given by:

$$(2.2) \quad x_n = \frac{1}{N} \sum_{k=0}^{N-1} X_k e^{-\frac{i2\pi}{N} kn}$$

The Fast Fourier Transform (FFT) is an efficient algorithm for computing the DFT of a sequence or time-domain signal. It's a numerical method used to compute the Fourier Transform, and it significantly speeds up the process compared to traditional methods. The FFT is widely used in practical applications due to its computational efficiency. It breaks down a signal into its constituent frequencies and their corresponding amplitudes and phases.

The Inverse Fast Fourier Transform (IFFT) is the reverse process of the FFT. It takes a frequency-domain signal and transforms it back into the original time-domain signal.

2.3 Wavelet Spectral Analysis

Complex systems and natural phenomena often exhibit chaotic and inherently unpredictable behaviors, frequently involving various interacting components across multiple scales. This is evident through the presence of scaling laws, which highlight their (multi)fractal characteristics. Additionally, these systems are marked - among others - by transitions between various states, which signify distinct dynamic patterns within the system. Hence, the initial approach to understanding these aspects hinges on the utilization of decomposition techniques [Balasis et al., 2023].

A prevalent characteristic found in many geophysical time series data is their non-stationary statistical behavior. Even though these series may encompass predominant periodic patterns, these patterns often exhibit fluctuations in both their intensity and frequency over extended periods of time. In signal analysis, the primary objective is to separate the shorter-period oscillations from the longer-period ones. The simplest approach for addressing such cases is to compute statistical parameters, such as the mean and variance, for different time intervals and assess if they display significant disparities. While the running variance gives information over the overall signal strength at specific intervals, it suffers from two significant defects:

- **Time Localization:** The curve's shape is highly dependent on the chosen window's length.
- **Frequency Localization:** The running variance contains no information about the periodic signal's frequency, only revealing its amplitude (and only when a wide window is employed).

One potential approach to address the aforementioned issues involves applying a windowed (or running) Fourier transform (WFT). This technique entails selecting a

specific window size and sliding it along in time, while computing the FFT at each time step using only the data contained within the window. While this method can effectively resolve the frequency localization challenge, it remains dependent on the chosen window size. The primary drawback associated with the WFT lies in its inconsistent handling of distinct frequencies. Specifically, low frequencies, characterized by few oscillations within the window, result in the loss of frequency localization, while high frequencies, featuring numerous oscillations, lead to the loss of temporal localization. Moreover, it's important to note that the WFT assumes that the signal can be of varying frequencies.

The Wavelet Transform (WT) offers a promising solution to these challenges by enabling a quantitative assessment of localized power variations within time series data (for reference, see Balasis et al. [2006, 2013]). Indeed, wavelet spectral analysis stands out as a widely used and effective technique for investigating geomagnetic field variations. It facilitates the simultaneous local decomposition of nonstationary time series data by converting the one-dimensional time domain signal into a two-dimensional time-frequency domain signal (wavelets). The wavelet algorithm uses basis functions with transient nature, called mother wavelets, which are not restricted to a single family of functions, like the simple sinusoidal wave base functions used by traditional Fourier analysis [Katsavrias et al., 2022]. Mother wavelets have a wave-like nature that is localized in time, capable of locating the occurrence of a sharp event in the time domain. The wavelet functions can be obtained as a linear combination of scaled and shifted mother wavelets. By conducting this decomposition, the method provides insights into the amplitude of any "periodic" signals present in the series and how this amplitude evolves over time [Torrence and Compo, 1998].

Figure 2.6 illustrates an example of a finite-duration wave "packet", with a specific frequency. Such a shape can serve as the window function for the variance analysis. This "wavelet" has the advantage of encapsulating a wave of specific period while remaining limited in its extent. To be precise, it represents the Morlet wavelet, a sine wave multiplied by a Gaussian envelope.

By sliding this wavelet along the time series it is possible to construct a new time series depicting the amplitude projection over time. Furthermore, we have the flexibility to adjust the wavelet's "scale" by altering its width. This aspect is where wavelet analysis excels compared to a moving Fourier spectrum because it maintains a consistent wavelet shape, with the only variable being the scaling, adjusting in proportion to the window's size.

In the continuous wavelet transform (CWT) algorithm, the function Ψ can serve as

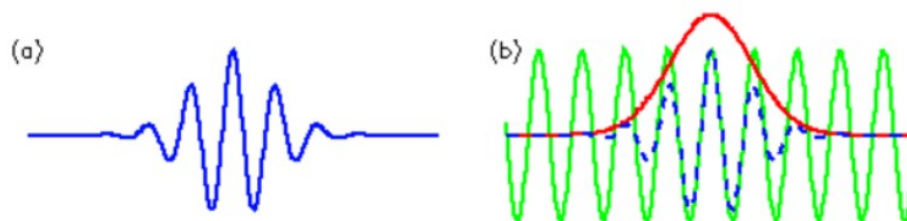


Figure 2.6: (a) Morlet wavelet of arbitrary width and amplitude, with time along the x-axis. (b) Construction of the Morlet wavelet (blue dashed) as a Sine curve (green) modulated by a Gaussian (red). Source: <https://paos.colorado.edu/research/wavelets/wavelet2.html>.

a mother wavelet if it meets two essential criteria: it must have zero-mean and finite energy (or, equivalently, must be square integrable).

In the context of the Morlet wavelet, the phase of a periodic signal is defined as the product of a complex exponential wave and a Gaussian envelope:

$$(2.3) \quad \Psi_0(n) = \pi^{-1/4} e^{i\omega_0 n} e^{-n^2/2}$$

where Ψ is the wavelet value at non-dimensional time n , and ω_0 is the non-dimensional frequency (wavenumber) [Torrence and Compo, 1998]. This is the basic wavelet function, but to adjust the overall size and shift the entire wavelet in time, it is essential to introduce the concept of "scaled wavelets:

$$(2.4) \quad \Psi_{\theta,s}(t) = \frac{1}{\sqrt{s}} \Psi\left(\frac{t-\theta}{s}\right)$$

where θ is the "translation" parameter used to shift in time and s is the "dilation" parameter used to change the scale. In fact, θ indicates the location of the wavelet in time. When $s > 1$ the wavelet is extended along the time axis, whereas for $0 < s < 1$ the wavelet is contracted. The factor of $s^{-1/2}$ serves as a normalization to maintain a constant total energy for the scaled wavelet.

For a time series $x(t)$, consisting of discrete values x_n , at time index n , where each value is separated by a constant time interval dt , the CWT, typically complex, at a specific location and scale involves the convolution of the wavelet function with the original time series $x(t)$:

$$(2.5) \quad CWT_x^{\theta,s} = \int_{-\infty}^{+\infty} x_t \Psi_{\theta,s}^*(t) dt$$

where the asterisk (*) denotes the complex conjugate. In fact, the CWT provides the local similarity (or correlation) between a specific segment of a signal and the corresponding wavelet. By adjusting the shift and scale parameters, it's possible to create a two-dimensional representation that illustrates the amplitude of any features in relation to both scale (or frequency) and the time resolution of this amplitude.

In this thesis we exploited the Wavelet Software for Matlab [Torrence and Compo, 1998], a freely available software with compatibility in various programming languages. Although this algorithm was originally developed for atmospheric data, it can be customized to cater to diverse fields of study, much like our own case. To achieve high time resolution, yet low frequency resolution (which is particularly suitable for analyzing phenomena like, for example, Pc4-5 ULF waves), we opted for a low non-dimensional frequency parameter ω_0 within the range of 5 to 10. For our time series, we consistently employed the Morlet non-orthogonal basis function (with $\omega_0 = 6$). Each time series had uniform time spacing between data points ¹. As previously stated, the Morlet function is a complex function that can provide information over both amplitude and phase. Regarding the width, we have chosen a narrow function, which provides good time resolution at the expense of poor frequency resolution.

The datasets analyzed and discussed in the following Chapter were collected at one-minute intervals. When considering the entire year of 2015, this leads to a data matrix with dimensions of $65 \times (365 \times 24 \times 60)$, after applying the wavelet transform to the various indices, each of which oscillates at a frequency of 1/60 Hz (where 65 corresponds to the number of frequencies). The selection of the specific number of frequencies to include in a spectrum varies depending on the particular phenomenon under examination and is also contingent on the sensor's frequency capabilities.

2.4 Hurst Exponent

Long-range dependence is a common feature of real-world dynamical systems. It is primarily linked to a fundamental concept in linear time series analysis, the characteristic behaviour of a signal's autocorrelation function. For many geophysical systems in the real world, this autocorrelation function exhibits a power-law decay, or equivalently, the associated power spectral density displays characteristic power-law scaling. These two

¹It's worth noting that the choice of the basis function predefines the decomposition pattern of the time-frequency plane [Balasis et al., 2006] (for instance, the Paul function has a better accuracy in the temporal dimension, while the Morlet function is more accurate in the frequency domain).

aspects are intimately connected through a simple Fourier transform [Balasis et al., 2023].

Identifying the scaling behavior of the autocorrelation function can be challenging, especially when dealing with time series of limited length. However, the corresponding behavior of the spectral density offers a straightforward and robust method for estimating a characteristic parameter known as the power spectral exponent, denoted as β . This exponent is closely related to another classical measure of long-range dependence, known as the Hurst exponent H , originally introduced by the British hydrologist E.E. Hurst in the 1950s. Specifically, β is linked to the Hurst exponent H through the equation $\beta = 2H + 1$.

The identification of long-range dependence in stochastic processes is linked to the statistical self-similarity exhibited by the time series graph. This property is characterized by an additional scaling exponent, which measures the roughness of this object within two-dimensional space, as the scale of resolution undergoes progressive changes. Estimators of this scaling exponent provide a measure of the fractal dimension D from a univariate stochastic process perspective. In the context of self-similar time series and in situations where heavy-tailed probability distribution functions are absent, we encounter a straightforward relationship between fractal dimension and the Hurst exponent. Specifically, it can be expressed as $D + H = 2$ [Balasis et al., 2023]. Fundamentally, estimates of the Hurst exponent and the fractal dimension of the time series graph can serve as interchangeable indicators, provided that there are no additional complexities such as the presence of heavy-tailed probability distributions, a common characteristic of intermittency. In contrast, when dealing with intermittent signals frequently encountered in space physics, these two concepts offer complementary insights.

If a time series is a temporal fractal, then a power law of the form $S(f) \sim f^{-\beta}$ is obeyed with $S(f)$ the power spectral density, f the frequency and β the spectral scaling exponent, a measure of the strength of time correlations (see for instance Balasis et al. [2006], Pitsis et al. [2023] and references therein).

In general, $-1 < \beta < 3$, but it describes two classes of signal Heneghan and McDarby [2000]:

- $-1 < \beta < 1$: fractional Gaussian noise (fGn)
- $+1 < \beta < 3$: fractional Brownian motion (fBm)

For the fBm case, $\beta = 2H + 1$, where H is the Hurst exponent Balasis et al. [2006], Alberti et al. [2021]. The exponent H characterizes the persistent/anti-persistent proper-

ties of the signal. The range $0 < H < 0.5$ ($1 < \beta < 2$) indicates anti-persistence, reflecting that if the fluctuations increase in a period, they are likely to decrease in the interval immediately following, and vice versa. The range $0.5 < H < 1$ ($2 < \beta < 3$) indicates persistence, which means that if the amplitude of fluctuations increases in a time interval, it is likely to continue increasing in the interval immediately following. $H = 0.5$ ($\beta = 2$) suggests no correlation between the repeated increments. Consequently, this particular value takes on a special physical meaning: it marks the transition between persistent and anti-persistent behavior in the time series.

The Hurst exponent provides crucial information on the kind of noise (either white or red, coming from the multifractal nature of the signal in some cases; see, for instance, Kantelhardt et al. [2002], or a slightly different application in Agarwal et al. [2016]).

Balasis et al. [2006] analyzed the Dst index around magnetic storms in terms of the exponent H , calculated from wavelet spectra. The wavelet spectral analysis followed a power law of the form $f^{-\beta}$ and showed the existence of two different patterns: (i) a pattern associated with intense magnetic storms, which can be interpreted as a fractional Brownian persistent behavior ($H > 0.5$); (ii) a pattern associated with lower activity periods, which is interpreted as a fractional Brownian anti-persistent behavior ($H < 0.5$). Furthermore, a series of articles Balasis et al. [2008, 2009, 2013] showed the complexity dissimilarity among “physiological” (normal) and “pathological” states (intense magnetic storms) of the magnetosphere. Entropy analysis implied the existence of two distinct patterns: (i) a pattern associated with intense magnetic storms, which is characterized by a higher degree of organization / lower complexity, and (ii) a pattern associated with lower-activity periods, which is characterized by a lower degree of organization / higher complexity.

Pitsis et al. [2023] extended and verified the results of Balasis et al. [2006] by applying the same wavelet analysis to the SYM-H index, the solar wind convection electric field component ($V \times B_{south}$) and several time series of the horizontal component of the Earth’s magnetic field at various locations, covering a wide range of magnetic latitudes.

2.5 Entropy Measures

Univariate time series deal with a single scalar observable. In order to gain insights into the system’s underlying dynamics we can examine these deterministic or stochastic time series and extract valuable information from them. To assess the inherent information content, a wide array of information theoretic metrics has been introduced. Univariate

metrics typically aim to characterize the complexity of the dynamics. These include measures such as Shannon entropy, which shares formalism with the Boltzmann-Gibbs entropic form, nonextensive Tsallis entropy, Fisher information and others (Balasis et al. [2023] and references therein).

2.5.1 Shannon Entropy

In 1948, Shannon introduced a statistical concept to investigate the information size of a transmitted message [Shannon, 1948], called information or Shannon entropy. The Shannon entropy quantifies the amount of information contained in a random variable or a data distribution. In essence, it tells us how unpredictable or uncertain an event or data point is within that distribution.

For a discrete random variable X with a set of values Ξ , the Shannon entropy $H(X)$ is defined as

$$H(X) = - \sum_{x \in \Xi} p(x) \log p(x)$$

where $p(x) = Pr\{X = x\}$, $x \in \Xi$ is the probability distribution function of X .

The entropy value, $H(X)$, is a non-negative quantity, and it is at its minimum when the random variable X is fixed (i.e., there is no uncertainty), and at its maximum when all events are equally likely, indicating maximum uncertainty. Thus, the higher the entropy, the more uncertain or random the data or variable is and the lower the entropy, the more predictable or ordered the data or variable is.

2.5.2 Tsallis Entropy

Tsallis entropy can be considered a generalization of the Boltzmann–Gibbs entropy in statistical physics. It is a mathematical concept used to measure the information content, or disorder, in a probability distribution or a system, and it is defined as follows:

$$S_q(X) = \frac{k}{q-1} \left(1 - \sum_{x \in \Xi} p(x)^q \right)$$

where k is Boltzmann's constant and q is a real parameter that characterizes the degree of non-extensivity. For $q \rightarrow 1$, one can recover the Boltzmann–Gibbs entropy, which is a thermodynamic analogy of the Shannon entropy. Tsallis entropy provides an alternative approach to characterizing randomness and uncertainty, and it has been widely applied in various fields of research [Tsallis, 2009]. For example, Balasis et al. have applied Tsallis entropy to quantify the dynamical complexity of magnetic storms and solar flares

[Balasis et al., 2011b], and of time series of the disturbance storm time index [Balasis et al., 2008, 2009].

Tsallis entropy quantifies the information content or uncertainty of a system, but it does so differently from Shannon entropy. The parameter q introduces a nonlinearity that makes Tsallis entropy more sensitive to the tails of the probability distribution. A higher value of q results in greater sensitivity to rare events or outliers in the distribution. Tsallis entropy is often referred to as "non-extensive entropy" because it does not obey the additive property of Shannon entropy. In systems where q is not equal to 1, the entropy of a composite system is not simply the sum of the entropies of its individual parts. Tsallis entropy is maximized when the probability distribution is non-uniform. In other words, it is largest when all events have equal probabilities in the distribution.

2.5.3 Fisher Information

In 1925, Fisher introduced a measure of the amount of information that can be obtained from a set of measurements [Fisher, 1925], called Fisher information. In other words, Fisher information quantifies the sensitivity of the likelihood function (or the probability density function) to changes in the parameter of interest. One can write the Fisher information in its discrete form as

$$F = \sum_{n=1}^{N-1} \frac{[p(x_{n+1}) - p(x_n)]^2}{p(x_n)}$$

where x_n is the random variable X at time n , $p(x_n)$ is its probability and N is the total number of time steps. Fisher information is always non-negative. It is an intrinsic property of the statistical model and does not depend on the parameterization. A larger Fisher information indicates that the data provides more information about the parameter, making it more suitable for estimating the parameter with precision. Fisher information has proved itself as a powerful method to study various nonstationary and nonlinear time series [Martin et al., 1999]. For example, it has been used to detect dynamical complexity changes associated with geomagnetic jerks [Balasis et al., 2016].

DYNAMICAL COMPLEXITY IN GEOMAGNETIC ACTIVITY INDICES USING INFORMATION THEORY

The ESA's ongoing Swarm satellite mission provides an exceptional opportunity for enhancing our understanding of the near-Earth electromagnetic environment. It achieves this by detecting and measuring magnetic signals stemming from diverse sources, such as the Earth's core, mantle, lithosphere, oceans, ionosphere, and magnetosphere [Friis-Christensen et al., 2006]. Furthermore, Swarm data are used to study solar influence on the Earth's system, encompassing the analysis of electric currents within the magnetosphere and ionosphere. These data also contribute to our comprehension of how the solar wind affects the dynamics of the upper atmosphere. Thus, the Swarm mission currently stands as one of the most comprehensive endeavors for surveying the Earth's core and crustal magnetic field, as well as the near-Earth electromagnetic environment [<https://earth.esa.int/eogateway/missions/swarm/publications>, accessed on 11 April 2023].

For decades, ground-based geomagnetic activity indices have served as vital tools for monitoring the Earth's magnetosphere dynamics. They offer valuable insights into two primary categories of space weather phenomena, that is, the occurrence and intensity of magnetic storms and magnetospheric substorms. Notably, Papadimitriou et al. [2021] and Balasis et al. [2019] have showcased the utilization of magnetic field data obtained from the Swarm satellite constellation to derive analogous space-based geomagnetic activity indices. The comparison between Swarm-derived with ground-based indices

reveals a very good agreement, underscoring the potential of Swarm magnetic field data in establishing novel global satellite-based indices for tracking geomagnetic activity levels. Notably, the existing official ground-based substorm activity index relies on data from 12 ground stations, all located in the northern hemisphere. Consequently, this index predominantly characterizes northern activity. In contrast, the Swarm-derived substorm activity index draws from measurements in both hemispheres, making it a more representative indicator of global conditions.

In this chapter, we utilize the Swarm-derived geomagnetic activity indices and apply the various analytical methods described in Chapter 2, that is wavelet transforms, the Hurst exponent, Shannon entropy, nonextensive Tsallis entropy and Fisher information. Our focus is on investigating the significant "markers" associated with the transition from the quiet-time (normal state) to the storm-time (pathological state) of the magnetosphere during the most intense magnetic storms of the previous solar cycle. This analysis aims to contribute to the enhancement of space weather diagnosis and forecasting schemes. In Section 3.1 we provide details about the data used in this study, while the the discussion of the methods has already been covered in Chapter 2. Section 3.2 presents the obtained results and their discussion is outlined in Section 3.3.

3.1 Data Description

We analyze Swarm-derived SYM-H and AE activity indices in conjunction with the standard SYM-H and AE geomagnetic indices from the year 2015. The SYM-H index characterizes disturbances in the longitudinal SYM-(metric) H-(horizontal) component of the Earth's magnetic field [Dungey, 1961], similar to the hourly Disturbance storm-time (Dst) index. However, the SYM-H index is computed from a more extensive array of ground-based stations and features a finer 1-min time resolution. Dst (as well as SYM-H) variation serves as a quantitative measure of geomagnetic disturbances that can be correlated with various solar and geophysical parameters. The AE index is one of the four Auroral Electrojet indices (AU, AL, AE, and AO) and is employed as an indicator of global electrojet activity in the auroral zone. These indices are calculated at 1-min cadence base on geomagnetic field data acquired from 10 to 13 stations located in magnetic latitudes spanning from $+61.7^\circ$ to $+70^\circ$ (for additional information on both indices, please refer to: <https://wdc.kugi.kyoto-u.ac.jp/>, accessed on 11 April 2023).

Swarm constitutes the fifth mission in ESA's fleet of Earth Explorers, which launched on November 23, 2013 and consists of three spacecraft (Figure 3.1). Swarm A and



Figure 3.1: Artist's view of the three Swarm spacecraft. Source: https://www.esa.int/ESA_Multimedia/Images/2013/11/Swarm_constellation

C occupy nearly circular orbits, with an inclination of 87.35° , at an altitude of 462 km. Swarm B follows an orbit with an inclination of 87.75° and is positioned at an altitude of 510 km. The final configuration of the mission was successfully achieved on April 17, 2014. As demonstrated by Papadimitriou et al. [2021], Swarm's magnetic field data can be effectively employed to replicate the three primary indices of geomagnetic activity (i.e., Dst, ap or Kp, and AE indices) through a straightforward and intuitive method. The extensive global coverage provided by a constellation of low-Earth orbiting satellites makes them ideal for capturing the Earth's magnetic field in its entirety, enabling the detection of changes at broader spatial scales. Moreover, their altitudes position them directly within the region of ionospheric currents, which are responsible for many of the phenomena that constitute our understanding of space weather.

Furthermore, due to the prolonged periods during which the satellites maintain relatively constant local times (LTs), their data can significantly enhance recent investigations into regional indices related to electrojet or ring current activity. This includes the regional versions of SuperMAG SME (electrojet) and SMR (ring current) indices [Bergin et al., 2020] (<https://supermag.jhuapl.edu/indices/>, accessed on 11 April 2023). In this context, satellite magnetic observatories have the potential to complement their ground-based counterparts, offering new insights into the condition of the magnetosphere

and holding the promise of more precise space weather condition assessments.

The Combined Model of the Earth’s Magnetic Field (CHAOS) 7 geomagnetic field model stands as an advanced and refined model utilized in understanding Earth’s magnetic field. Its intricate design integrates data collected by the low-Earth orbit satellites Swarm, CryoSat-2, CHAMP, SAC-C and Ørsted, and annual differences of monthly means of ground observatory measurements, to create a comprehensive representation of the ever-changing geomagnetic field [Finlay et al., 2020]. This model, known for its accuracy and high-resolution output, provides a detailed portrayal of the complex dynamics within the Earth’s core. As the seventh iteration in the CHAOS series, this model incorporates the most recent and updated datasets, offering scientists and researchers an invaluable tool for studying and predicting the behaviors of Earth’s magnetic field. Typically, the CHAOS series includes sophisticated mathematical formulations to represent Earth’s magnetic field; CHAOS-7 (or any other model) employs a series expansion involving spherical harmonic coefficients to model the magnetic field variations at the Earth’s surface. The model represents the field as a sum of Gauss coefficients (spherical harmonic coefficients) up to a certain degree and order, which allows for a mathematical representation of the varying magnetic field strength and direction across the globe.

The most intense period of geomagnetic storm activity during solar cycle 24 took place in 2015, characterized by the occurrence of the most powerful storm of this solar cycle, commonly known as the St. Patrick’s Day storm. Detailed discussions of the space weather effects on the Earth’s surface resulting from the St. Patrick’s Day storm can be found in references Balasis et al. [2018], Tozzi et al. [2019a] and Boutsis et al. [2023]. Furthermore, numerous researchers have examined this storm event using Swarm time series data and applied information theory methods (e.g., Balasis et al. [2020], De Michelis et al. [2020], Papadimitriou et al. [2020], Consolini et al. [2021]). In Table 3.1, we present information about the three strongest magnetic storms of 2015, based on the minimum Dst index values.

Storm Date	Storm Time (UT)	Dst (nT)
17 March 2015	22:00:00	-223
23 June 2015	04:00:00	-204
20 December 2015	22:00:00	-155

Table 3.1: Intense geospace magnetic storms of 2015, including the St. Patrick’s Day storm, which was the strongest storm of solar cycle 24 (2008–2019). Storm date, time and minimum Dst index value reached are given in the first, second and third columns, respectively.

3.1.1 Swarm-derived SYM-H Index

The Swarm SYM-H and Swarm AE indices are derived based on a specific methodology, as elaborated in Papadimitriou et al. [2021]. In this section, we provide a concise overview of the steps involved in producing these indices.

First, the magnetic field measurements from the Swarm’s vector field magnetometer (VFM) instrument are received as a three-dimensional vector in the North-East-Center coordinate system. To remove the static, background magnetic field, we subtract the internal mode of the CHAOS-7 model Finlay et al. [2020], which accounts for the contributions of the Earth’s core and crustal magnetic fields. This results in measurements that are then mapped to the Quasi-Dipole coordinate system [Emmert et al., 2010]. Subsequently, it is simple to map the vector to a mean-field-aligned coordinate system. This transformation is achieved by projecting the total vector field onto a direction parallel to the model field, yielding the Bpar component, alongside two perpendicular components, Bper1 and Bper2. The Bper1 component primarily aligns with the meridional plane, pointing outward, while Bper2 mainly aligns along the East-West direction, pointing eastward. To derive the Swarm SYM-H index, we utilize the Bpar component, as it closely resembles the horizontal component of the terrestrial magnetic field used in constructing the ground-based SYM-H index, particularly for the latitude region under examination. For the Swarm AE index, we utilize the total magnitude of the vector field.

The derivation of the Swarm SYM-H index is based on the following steps:

- Extract Bpar Field Series from MAG_LR (1 Hz) product
- Subtract CHAOS-7 [Finlay et al., 2020] Internal Field Model
- Remove obvious outliers
- Remove values that lie above $+30^\circ$ or below -30° in Magnetic Latitude
- Apply a non-overlapping, moving average scheme on the time series, with a window of 60 s, so that the series are set to a 1-min time resolution, effectively filling up some of the smaller gaps
- Merge Swarm A and Swarm B time series, in a joint 1-min resolution data set
- Interpolate the remaining data gaps, using a simple linear scheme, to produce a complete time series

- Apply a low-pass Chebyshev Type I filter with a cutoff period of 4 hours, to filter out some of the small perturbations in the signal that arise from the fast motion of the satellites
- Apply a linear transform to get the Swarm Index: $S_{SYM-H} = 1.53B_f + 12.85$

3.1.2 Swarm-Derived AE Index

Similarly, the Swarm AE index is derived, based on the following logic, but using simply the magnitude of the Swarm magnetic field:

- Extract Total Magnetic Field Series from MAG_LR (1 Hz) product
- Subtract CHAOS-7 [Finlay et al., 2020] Internal Field Model
- Remove obvious outliers
- Keep only measurements between $+65^\circ$ and $+75^\circ$ (and correspondingly -75° to -65°) in Magnetic Latitude
- Apply a non-overlapping, moving average scheme on the time series, with a window of 60 s, so that the series are set to a 1-min time resolution, effectively filling up some of the smaller gaps
- Merge Swarm A and Swarm B time series in a joint 1-min resolution data set
- Interpolate the remaining data gaps, using a simple linear scheme, to produce a complete time series
- Apply a low-pass Chebyshev Type I filter with a cutoff period of 2.6 hours, to filter out some of the small perturbations in the signal that arise from the fast motion of the satellites
- Apply a linear transform to get the Swarm Index: $S_{AE} = 2.2B_f - 8.9$

We conducted several experiments with different filtering thresholds and methodologies to identify the most suitable parameters for achieving the highest correlation scores with the respective ground-based SYM-H and AE indices. This analysis of the entire year 2015 led to the determination of optimal parameters, resulting in 4 hours for SYM-H and 2.6 hours for AE. In the last phase, we implemented a linear transformation, selecting parameters that aimed to minimize the root mean square of the differences between each Swarm index and its corresponding ground-based counterpart.

3.2 Results

In Chapter 2, we thoroughly examined the analytical methods to be employed in this dissertation, that is wavelet power spectra, Hurst exponent, Shannon entropy, non-extensive Tsallis entropy, and Fisher information. Thus, in this Chapter we will apply each one of these methods to our data and discuss the outcomes. We employ the methodology previously followed by Balasis et al. [2006], Pitsis et al. [2023] to compare between the Swarm SYM-H index and SYM-H index, as well as between the Swarm AE index and AE index.

In particular, following the approach described in Balasis et al. [2006], we utilized the wavelet analysis technique with the Morlet wavelet as the basis function [Torrence and Compo, 1998] for analyzing the time variations of each index. Subsequently, we derived the coefficients for their power spectra. We estimated the power spectral densities in the frequency range spanning from 0.5 to 60 hours, employing a moving window of 256 hours (according to the Nyquist theorem) with hourly steps along the time series. For each window, we calculated the linear correlation coefficient (denoted as "r") to ensure that a power-law of the form $S(f) \sim f^{-\beta}$ is, indeed, obeyed. Finally, the spectral scaling exponent β , and consequently the Hurst exponent H , for each window was calculated by conducting a linear fit to the power spectral densities versus frequency diagram (c.f. Balasis et al. [2006], Pitsis et al. [2023]).

Figure 3.2 displays the wavelet power spectra and the temporal variation of the Hurst exponent for both the Swarm SYM-H index and the SYM-H index throughout the year 2015. Likewise, Figure 3.3 showcases the wavelet power spectra and the temporal variation of the Hurst exponent for both the Swarm AE index and the AE index during the year 2015.

In the wavelet power spectra (middle panels) of Figure 3.2, one can readily identify the occurrence of three intense magnetic storms on 27 March, 23 June, and 20 December 2015. As an intense magnetic storm approaches, there are distinct changes in the scaling parameters of the SYM-H index time series, reflecting a gradual reduction in complexity. The time-frequency plane offers insights into the frequency distribution of a signal at each moment. This feature of the wavelet transform is useful for the SYM-H time series, given its non-stationary nature and evolving frequency content [Balasis et al., 2006]. Intense power signals are observed around the peak of each magnetic storm, covering a broad frequency range (beginning at approximately 18 hours and extending down to the lowest periods of the spectra), signifying a large-scale extreme event that keeps the

CHAPTER 3. DYNAMICAL COMPLEXITY IN GEOMAGNETIC ACTIVITY INDICES USING INFORMATION THEORY

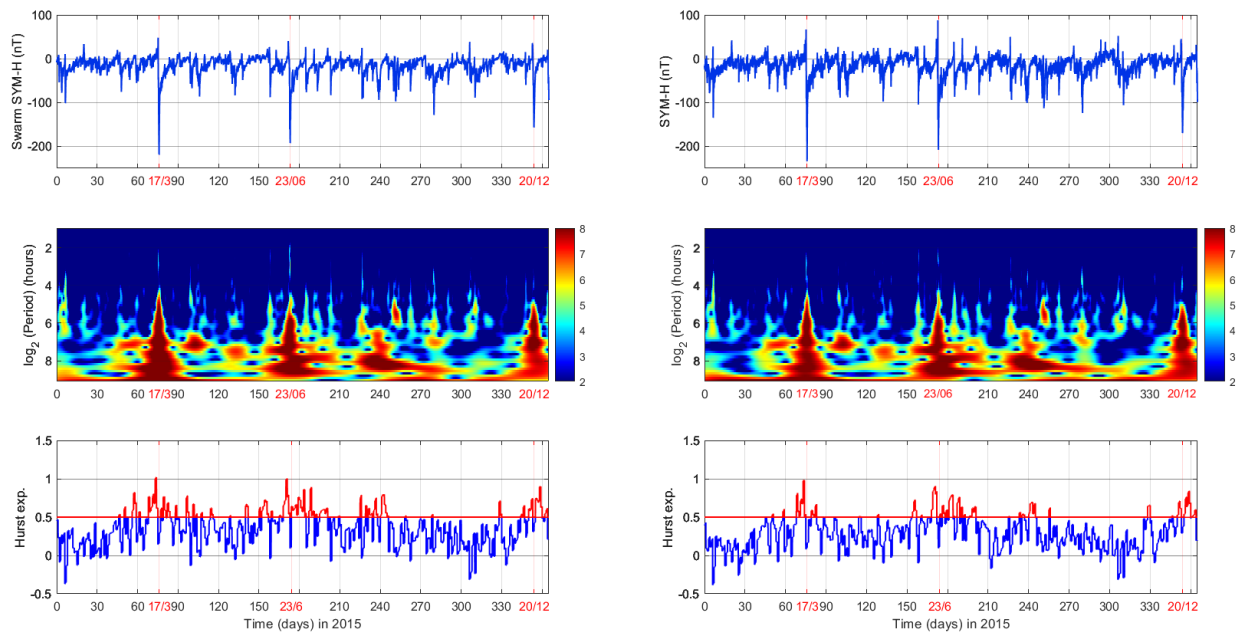


Figure 3.2: Swarm SYM-H index (**left** column) and SYM-H index (**right** column): time series (**top** row), wavelet spectra analysis (**middle** row) and Hurst exponent (**bottom** row) for the year 2015. The red line at 0.5 marks the transition from the anti-persistent behavior (blue) into the persistent fractional Brownian motion (red).

magnetosphere preconditioned for an extended time interval (spanning nearly a month around each of these three events). These observations are even more pronounced in the case of the Swarm SYM-H index.

Regarding Figure 3.3, we can discern similar underlying features in the spectra for the three storms, even though we are examining substorm indices. This means that the "big picture" of a preconditioned magnetosphere remains evident. In the power spectra of all four indices (Swarm SYM-H, SYM-H, Swarm AE and AE), we also observe another region marked by a prominent spectral signature, roughly spanning from day 220 to day 280 (from mid-August to mid-October). This corresponds to the influence of multiple subsequent storms (see Table 3.2) characterized by lower intensities, approximately around -100 nT. This influence is more prominently captured by the Swarm AE index. Substorm activity also appears to be effectively represented by the auroral indices, with Swarm AE exhibiting a more pronounced power spectrum compared to AE throughout the entire year.

Hurst exponent plots serve as effective identifiers of disturbed periods, not only due to the increase in the exponent's value, but particularly due to its transition into the region

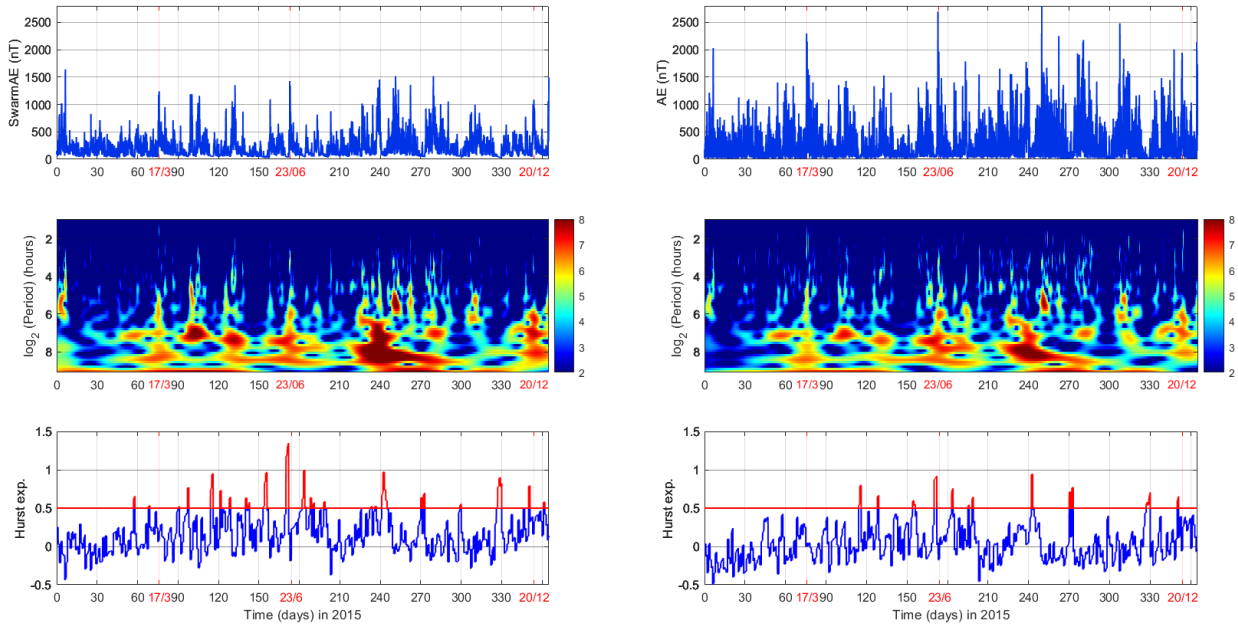


Figure 3.3: Swarm AE index (**left** column) and AE index (**right** column): time series (**top** row), wavelet spectra analysis (**middle** row) and Hurst exponent (**bottom** row) for the year 2015. The red line at 0.5 marks the transition from the anti-persistent behavior (blue) into the persistent fractional Brownian motion (red).

of values exceeding 0.5. This transition marks the shift from anti-persistent behavior to the regime of persistent fractional Brownian motion. Such a transition signifies that the temporal correlations within the various signal increments become long-scale during these pathological states of the magnetosphere¹. This shift could also imply an increased level of interconnectivity among the various subsystems within the terrestrial electromagnetic environment. In the case of the SYM-H and Swarm SYM-H indices, these periods coincide with the geomagnetic storms of March, June and December, as well as, to a somewhat lesser extent, with the period spanning August to October. However, for the AE indices, the picture is not as straightforward, as the Hurst exponent values predominantly remain within the range of 0 to 0.5, indicative of anti-persistent behavior.

¹The specific conclusion derives from the time series analysis by calculating the Hurst exponent using sliding windows and concerns windows for which the calculated Hurst exponent had values exceeding 0.5 and therefore these time windows had "persistent" behavior. Hurst exponent values > 0.5 indicate long-term positive autocorrelation in the time series, which means that the decrease of autocorrelation (within the time series) is slower than exponential, following a power law. In order to say exactly how long this long-term autocorrelation extends one must look in detail at each window of the analyzed time series, but since we used a sliding window of 256 h, the term long-scale refers to times of the order of several tens of hours, i.e., of the order of a few days.

This finding aligns with the more transient and dynamic nature of substorms, in contrast to global magnetic storms.

Storm Date	Storm Time (UT)	Dst (nT)
16 August 2015	08:00:00	-98
26 August 2015	22:00:00	-79
27 August 2015	21:00:00	-103
28 August 2015	10:00:00	-102
09 September 2015	13:00:00	-105
11 September 2015	15:00:00	-87
20 September 2015	16:00:00	-81
07 October 2015	23:00:00	-130

Table 3.2: Geospace magnetic storms between mid-August and mid-October 2015. Storm date, time and minimum Dst index value reached are given in the first, second and third columns, respectively.

From the indices themselves we cannot discern whether the transition between anti-persistent and persistent regimes accompanies the occurrence of either an intense storm (e.g., March, June, December) or a cluster of milder storms (e.g., days 220–280). However, when we perform the wavelet spectral and Hurst exponent analyses on the indices, distinctive patterns emerge. For the intense events, these analyses reveal evidence of magnetosphere preconditioning over a significantly longer time interval than the storm’s actual duration, as illustrated in both the lower-frequencies region of the wavelet spectra and the Hurst exponent values in Figure 3.2). In contrast, for the grouped weaker events, the results of the same analyses suggest that these storms are interconnected (again, see both wavelet spectra at lower frequencies and Hurst exponent values in Figure 3.2). Furthermore, when we compare the results between satellite and ground-based indices in Figure 3.2, a similar pattern is observed for both types of indices.

Figure 3.4 shows the Shannon and Tsallis entropy measures, along with Fisher information, for both the Swarm SYM-H index and the SYM-H index throughout the year 2015. Meanwhile, Figure 3.5 shows the Shannon and Tsallis entropy measures, as well as Fisher information, for both the Swarm AE index and AE index during the same year. Regarding the Tsallis entropy, the parameter q equals 1.84, as previously identified in Balasis et al. [2011a], by employing nonextensive modeling of the frequency-size distribution in Dst timeseries (like Gutenberg–Richter (G–R) type law for the nonextensive Tsallis statistics). Notably, the same q value has been consistently applied in other research articles that analyze the Dst index, (e.g., Balasis et al. [2011c]).

A significant resemblance is evident between the plots of ground-based and Swarm-derived indices, across all instances and various information measures. This similarity suggests that the spaceborne indices possess the capacity to capture equivalent dynamics and behaviors in terms of their informational content, as observed in the conventionally used ground-based indices. Particularly in the case of the ring current indices (as seen in Figure 3.4), which are mainly associated with the three major magnetic storms of 2015, one can readily observe the transition towards a more ordered state (i.e., high degree of organization) during these three events. This is indicated by the lower values of both Shannon and Tsallis entropies and an increase in Fisher information. Hence, the state of the geomagnetic system shifts from a relatively random one, characterized by the random noise fluctuations of the quiet magnetosphere, to a highly organized state, as the various subsystems interact and synchronize to manifest a particular phenomenon. Notably, in Figure 3.4, it's observable that around the time of three intense storms, the absolute values of the three information theory measures are generally lower for the Swarm SYM-H index compared to the SYM-H index. Nonetheless, the general pattern of the lower complexity during the periods of the intense storms, in comparison to the rest of the year, remains consistent for both satellite and ground indices.

This pattern, characterized by lower complexity during the three intense storms in comparison to the remainder of the year, is not a common feature in the AE-related plots (Figure 3.5). The reason behind this disparity lies in the nature of the auroral indices, which are primarily associated with substorms rather than major storms. These indices vary in response to the development of ionospheric currents in the auroral regions, phenomena that operate on very different time scales and exhibit varying frequencies of occurrence. However, it's important to note an exception in the case of the June storm. During this period, all information measures (i.e., Hurst exponent, entropy values and Fisher information) for the Swarm AE index attain maximum values, as indicated in Figures 3.3 and 3.5.

3.3 Discussion and Conclusions

In this chapter, we conducted an analysis of 1-year-long time series spanning 2015. We utilized both spaceborne and ground-based geomagnetic activity indices and applied various information theory measures, namely Hurst exponent, Shannon entropy, nonextensive Tsallis entropy and Fisher information. The Low Earth Orbit (LEO) satellite magnetic indices were derived from data collected by the Swarm mission, encompassing

CHAPTER 3. DYNAMICAL COMPLEXITY IN GEOMAGNETIC ACTIVITY INDICES USING INFORMATION THEORY

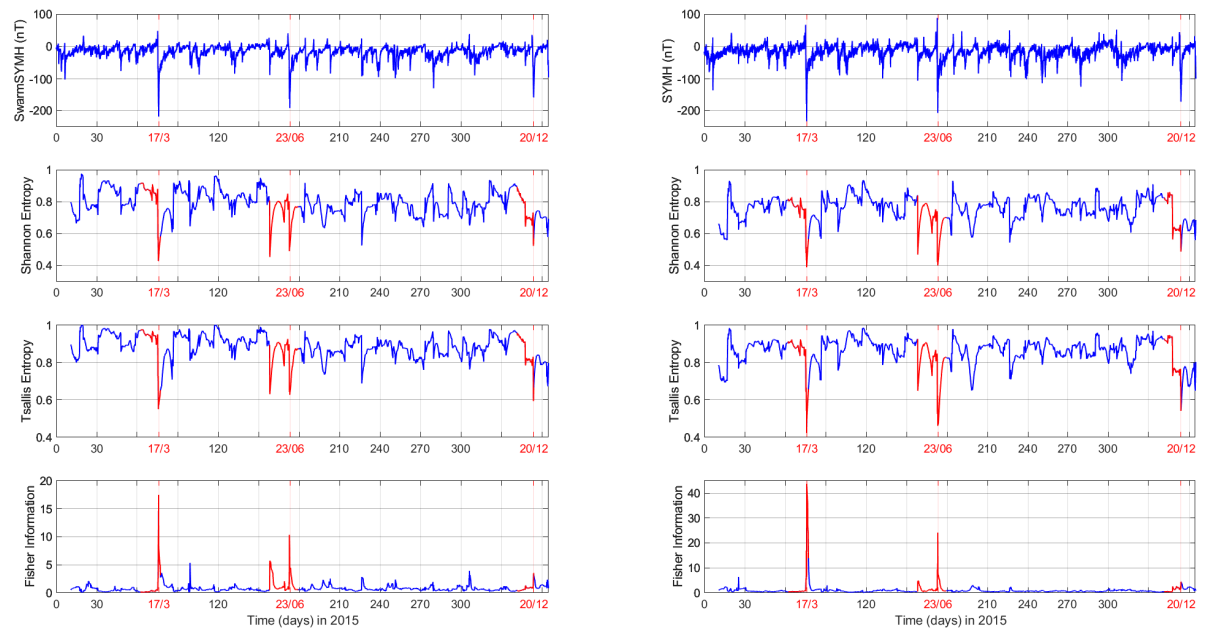


Figure 3.4: SYM-H index (**left** column) and SYM-H index (**right** column): time series (**top** row), Shannon entropy, Tsallis entropy and Fisher information (**bottom** row) for the year 2015. Red color is used to highlight the entropy values around the three magnetic storms of 2015 (17/3, 23/6 and 20/12).

the most intense magnetic storms of the previous solar cycle, including its strongest storm event, the St. Patrick’s Day storm. The analyzed indices were selected to capture both storm and substorm activity.

Regarding the Swarm-derived SYM-H index and standard SYM-H index, the Hurst exponent and various entropy measures reveal the complexity dissimilarity among different “physiological” (normal) and “pathological” (intense magnetic storms) states of the magnetosphere. These findings suggest the emergence of two distinct patterns:

1. a pattern associated with normal periods, which is characterized by a lower degree of organization and a higher level of complexity
2. a pattern associated with intense magnetic storms, which is characterized by a higher degree of organization and a lower level of complexity.

These outcomes align with previous research that has emphasized the shift from anti-persistent to persistent behavior around the onset of an intense storm (e.g., as discussed

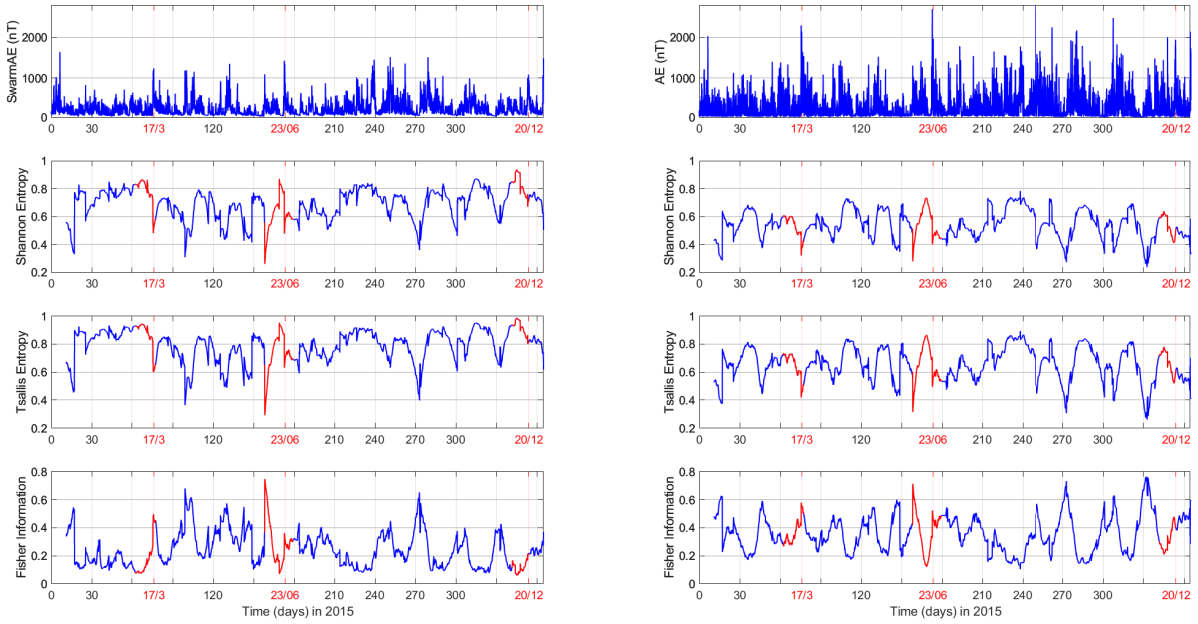


Figure 3.5: Swarm AE index (**left** column) and AE index (**right** column): time series (**top** row), Shannon entropy, Tsallis entropy and Fisher information (**bottom** row) for the year 2015. Red color is used to highlight the entropy values around the three magnetic storms of 2015 (17/3, 23/6 and 20/12).

in works by Balasis et al. [2006, 2008, 2009, 2013], Papadimitriou et al. [2020], Alberti et al. [2021]).

In the case of the Swarm-derived AE index and the standard AE index, the same analyses did not reveal a similar pattern around the onset of storms in terms of the information theory measures. This discrepancy is due to the nature of these indices, which primarily focus on substorms. Substorms have notably different characteristic time scales and generation mechanisms compared to storms. Additionally, substorm events occur far more often than storm events, which may contaminate the picture of the anti-persistent / persistent regime we observed in storm-monitoring indices. It's noteworthy that the wavelet transform effectively captures similar spectral signatures for both spaceborne and ground-based SYM-H and AE indices around the time of the three intense storms. This implies that the global character of an extreme storm event is not only reflected in storm-monitoring time series but also in substorm-monitoring time variations.

Finally, it's worth highlighting that the application of the various information theory measures yields highly consistent outcomes between the newly acquired Swarm-derived

and the standard ground-based geomagnetic activity indices. This serves as strong evidence supporting the capacity of satellite indices to capture equivalent dynamics and behaviors, particularly concerning their informational content, akin to the well-established ground-based indices.

APPLICATION OF GIC INDEX TO MAGNETIC FIELD DATA

A manifestation of space weather at ground level are the Geomagnetically Induced Currents (GIC), which flow along power transmission lines and other electrically conductive infrastructure, as the result of an induced geoelectric field associated with geomagnetic disturbances (e.g., magnetic storms), according to Faraday's law of electromagnetic induction. These currents can cause disruptions or even widespread blackouts across power grids, resulting in the loss of electric power [Pirjola, 2000, Daglis et al., 2001, Daglis, 2004, Baker et al., 2004]. Hence, nowadays GIC constitute an integral part of space weather research.

Our initial efforts to study GIC in Greece (approximate MLat for Greece: 33° N) started in 2019 and during this period we have complemented the analysis with data from the Mediterranean region (e.g., <https://register-as.oma.be/esww16/contributions/public/S1-P1/S1-P1-01-BoutsiAdamantia-Zoe/>). Until now, GIC in Greece have only been studied in terms of statistical correlations, linking transformer failures in the Greek national electric power grid with intense solar activity Zois [2013].

The GIC index was initially introduced by Marshall et al. [2010]. It is derived entirely from geomagnetic field data, without need of knowing the ground conductivity, ionospheric current system geometry and the relevant infrastructure details and, therefore, acts as a geoelectric field proxy. According to the authors, the superiority of the GIC index over dB_H/dt is due to the frequency dependence between the geoelectric field and dB_H/dt as discussed by Pirjola [1982]. The index has been tested in various studies (e.g., Tozzi et al. [2019a,b]) and seems to perform well for low and middle latitudes, which

is to say it tracks the historical instances of increased GIC risk with minimal input requirements.

While such an index does not, and cannot, on its own provide information on the geoelectric field (lacking any input on ground conductivity) or the actual effect on technological infrastructure (lacking any input on the topology or load of an affected network), it has the advantage of being a consistent measure that can be combined with ground conductivity models of one's choice and juxtaposed on any current or future infrastructure one is interested in. For a single location, the GIC index is a good measure of relative risk over time, under the reasonable assumption that the GIC flow at a node in the pipeline or power transmission network is proportional to the local geoelectric field. Comparison across locations that may have different geology is then less of a measure of the possible impact (due to variations in conductivity) and more of a measure of the "geoeffectiveness" of the driving magnetic field fluctuations (e.g., Pulkkinen et al. [2015]) that can be used to illustrate the likely response for different conductivity regions.

In this chapter, we extend the analysis performed by Tozzi et al. [2019a] for Italy and we present the results of a preliminary analysis on the geophysical conditions known to generate GIC, by calculating the GIC index, a useful GIC proxy for high-level studies, in four different locations which host the Hellenic GeoMagnetic Array (ENIGMA), complemented by data analysis of magnetic observatories in the Mediterranean region. We focus on the four most intense magnetic storms of solar cycle 24 ($Dst < -150$ nT) to make an assessment of the GIC-imposed risk in Greece and the wider Mediterranean region. Section 4.1 is dedicated to the data we worked with for the selected magnetic storm events. In Section 4.2 we delve into the methodology we applied in order to calculate GIC index, and Section 4.3 showcases the outcomes of our study (with additional figures available in Appendix A). In Section 4.4 we present the results of one more strong magnetic storm that occurred in the beginning of Solar Cycle 25. Finally, Section 4.5 engages in a detailed discussion of the study's most intriguing discoveries, including comparisons with other well-established GIC proxies.

4.1 Data Selection

Solar cycle 24, characterized as a rather weak cycle, initiated on 4 January 2008, upon the appearance of a reversed-polarity sunspot, and lasted until December 2019. The year of major geomagnetic activity was 2015, while according to the World Data Center for Sunspot Index and Long-term Solar Observation (WDC-SILSO), Royal Observatory

of Belgium, Brussels, solar cycle 24 reached the maximum number of sunspots (SSN = 116.4) in April 2014 [Watari, 2017]. Compared to solar cycles of the recent past, it was weakened in terms of solar activity, average solar wind parameters and solar wind-magnetosphere energy coupling. It was reduced by more than 50% in high-intensity long-duration continuous auroral electrojet (AE) activity (HILDCAA) occurrence rate (per year), about 15 - 34% in moderate storms ($-50 \text{ nT} \geq \text{Dst} > -100 \text{ nT}$) and about 49 - 75% in intense storms ($-100 \text{ nT} \geq \text{Dst} > -250 \text{ nT}$), while superstorms ($\text{Dst} \leq -250 \text{ nT}$) were absent [Hajra, 2021].

The Dst index is a proxy of the intensity of the westward ring current flowing around the Earth and, therefore, of the magnetic disturbances it produces on the ground (e.g., Sugiura and Kamei [1991]). It has been historically used to characterize the intensity of a geomagnetic storm, thus we employ Dst time series as a measure of reference for the major magnetic storms of solar cycle 24.

In light of the above, we select our case studies focusing on the strongest geospace magnetic storms of solar cycle 24. Based on Dst index values (<http://wdc.kugi.kyoto-u.ac.jp/dst/dir/index.html>) less than -150 nT , the events under investigation occurred on 17 March 2015, 23 June 2015, 20 December 2015 and 26 August 2018. During the aforementioned events the Dst index reached the minimum values of -223 nT , -204 nT , -155 nT and -174 nT , respectively (Table 4.1).

The onset of a magnetic storm is often characterized by a global sudden increase in the horizontal component, H, of the geomagnetic field, which is referred to as the Storm Sudden Commencement (SSC). In general, a Sudden Commencement (SC) is basically an unexpected sharp increase in the Northern (X) magnetic component of a considered observatory, which usually, but not always, is the precursor to a geomagnetic storm (defined by, for example, a minimum of the Dst index). If an SC precedes the imminent geomagnetic storm it is considered an SSC. It has to be noted that more emphasis is put on the “change of rhythm” in the magnetic activity [Mayaud, 1973, Segarra and Curto, 2013] than on the amplitude of the possible succeeding magnetic storm. Since 1976, the SC determination has been made by the Service of Rapid Variations, hosted at the Observatorio del Ebro, and is published regularly in the IAGA Bulletin no. 32 series by the International Service of Geomagnetic Indices (ISGI) [Curto et al., 2007]. Definitive lists of SC are made on the basis of visual inspection of magnetograms from five selected low latitude observatories. We employ the definitive SC list of 2015 and the preliminary SC list of 2018 for assisting us in the determination of the onset of the magnetic storms under study.

Table 4.1: Strongest geospace magnetic storms of solar cycle 24 (2008-2019), based on minimum Dst index values. Storm date and time (fourth and fifth column) refer to the hour of minimum Dst occurrence. Respective SC occurrences (date and time) are shown in the second and third column. For cases #1 and #3 the SCs coincide with the SSCs, while for case #2 the SSC is the third SC. Not available data are marked as N/A.

Case	SC Date	SC Time (UT)	Storm Date	Storm Time (UT)	Dst (nT)
#1	17/03/2015	04:45:00	17/03/2015	22:00:00	-223
	21/06/2015	16:44:00			
#2	22/06/2015	05:44:24	23/06/2015	04:00:00	-204
	22/06/2015	18:33:00			
#3	19/12/2015	16:16:12	20/12/2015	22:00:00	-155
#4	N/A	N/A	26/08/2018	06:00:00	-174

As stated in the list, there was an SC on 17 March 2015, at 04:45:00 UT with a mean amplitude (i.e., mean out of five values) of 39.9 nT, prior to the St. Patrick’s Day magnetic storm. Accordingly, before the 23 June 2015 storm, there was an SC on 21 June 2015, at 16:44:00 UT with a mean amplitude of 35.3 nT, followed by two more SCs on 22 June 2015, at 05:44:24 and 18:33:00, with mean amplitudes 21.2 nT and 88.8 nT, respectively. Another SC was registered on 19 December 2015, at 16:16:12 UT with mean amplitude 25.2 nT, foretelling the upcoming geomagnetic storm of 20 December 2015. According to the SC list and reinforced by Astafyeva et al. [2020], no sudden geomagnetic commencement was recorded prior to the 26 August 2018 storm. In Table 4.1 the date, time and Dst index values corresponding to each case’s SCs are displayed. For the storms of March and December 2015 the SCs are indeed the SSCs, while for the June 2015 storm the SSC is the third out of the three SCs.

The National Observatory of Athens (NOA) operates the Hellenic GeoMagnetic Array (ENIGMA), a network of 4 ground-based magnetometer stations in the areas of Klokotos (abbreviated as THL), Dionysos (DIO), Velies (VLI) and Finokalia (FIN), located in central and southern Greece (<http://enigma.space.noa.gr/>). ENIGMA monitors the geomagnetic field variations associated with the occurrence of magnetic storms and ultra low frequency (ULF) waves using vector fluxgate magnetometer instruments. ENIGMA is a SuperMAG (<http://supermag.jhuapl.edu/>) contributor, a worldwide collaboration of organizations and national agencies that currently operate more than 300 ground-based magnetometers [Gjerloev, 2009]. An analysis of the ENIGMA data during the three intense magnetic storms of 2015 was performed by Balasis et al. [2018] in terms of the critical fluctuation method. FIN operates since April 2018, thus this is the first time that recordings from this magnetometer station are analyzed.

Only for the case of the August 2018 storm we also employ magnetic field data from the Penteli Observatory (PEG), which is located in Nea Makri, central Greece, maintained by the Institute of Geology and Mineral Exploration (IGME) and belongs to the Intermagnet network. This was decided as ENIGMA DIO data were not available for the specific storm and PEG is located very close to the DIO station. Since for the other three storms there were DIO data available, it was considered abundant to also show results from the PEG station.

In order to extend this study towards the wider Mediterranean region, we employ data from six magnetic observatories located in Italy (Castello Tesino - CTS), France (Chambon la Forêt - CLF), Spain (Ebro - EBR and San Fernando - SFS), Algeria (Tamanrasset - TAM) and Turkey (Izmir - IZN). Although not all observatories are ideally located close to the Mediterranean, they were selected as the best available options in terms of location and data availability (for example, TAM is relatively remote, but the best available observatory in the southern expanse). Furthermore, whereas there are three magnetic observatories currently operating in Italy (CTS, Duronia - DUR and Lampedusa - LMP), the choice of CTS was mainly based on data availability during the investigated time intervals. St. Patrick's Day 2015 magnetic storm had already been studied by Tozzi et al. [2019a] using CTS, DUR and LMP data. Therefore, a thorough analysis of the GIC index in Italy was beyond the scope of the present study. A map of all the geomagnetic stations / observatories used for this study, in geographic coordinates is shown in Figure 4.1. Table 4.2 shows the geographic and the altitude-adjusted corrected geomagnetic (AACGM) coordinates of each station, estimated for the epoch 2015.0¹, as well as the corresponding L-shell values.

4.2 Methodology

The GIC index is derived according to the method described in Marshall et al. [2010]. The method involves applying a frequency domain filter to geomagnetic field data, of either the geographic North (X) or the East (Y) component of the horizontal intensity, after they have been transformed into the frequency domain. This filter function is practically the “surface impedance” for a half-space uniformly conducting one-dimensional (1D) Earth model, having its roots in the fundamental equation of magnetotellurics, that is, an electric field component is linearly related to its orthogonal magnetic field component

¹The AACGM coordinates were calculated using the online calculator available at <http://superdarn.thayer.dartmouth.edu/aacgm.html>. The latest AACGM coefficients were derived using the secular variation of the IGRF-13 model, which is briefly discussed in Appendix B.

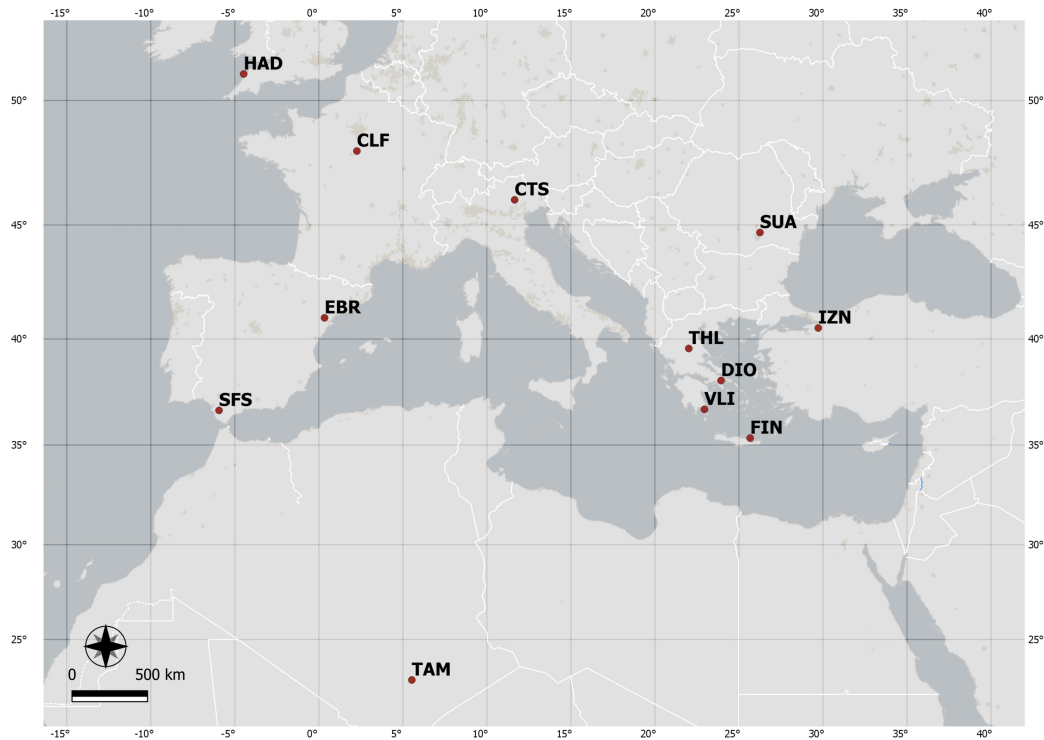


Figure 4.1: Geographic map displaying all the geomagnetic stations / observatories used for the present study. From North to South: Hartland (HAD, United Kingdom), Chambon la Forêt (CLF, France), Castello Tesino (CTS, Italy), Surlari (SUA, Romania), Ebro (EBR, Spain), Iznik (IZN, Turkey), Klokotos (THL, Greece), Dionysos (DIO, Greece), Velies (VLI, Greece), San Fernando (SFS, Spain), Finokalia (FIN, Greece) and Tamanrasset (TAM, Algeria).

through a single valued complex scalar transfer function (e.g., Cagniard [1953]). The GIC index, in either Y or X direction, derives from the absolute value of the inverse transformation into the time domain. According to Marshall et al. [2010] users are eligible to select the index aligned with their particular infrastructure system (i.e., GIC_x or GIC_y).

Typically, a complete day of 1 min sampled single component geomagnetic field data is transformed into the frequency domain, filtered, and reverse transformed. The GIC-index is the absolute value of the reverse transformed data. Geomagnetic field variations measured in the north-south direction (x-component) were used to calculate the GIC_y-indices as a proxy for the east-west geoelectric field (y-direction). Geomagnetic field variations measured in the east-west direction (y-component) were used to calculate the GIC_x-indices as a proxy for the north-south geoelectric field (x-direction).

Initially, all magnetometer datasets were sampled at 1 min cadence. They were

Table 4.2: Geographic and altitude-adjusted corrected geomagnetic (AACGM) coordinates of all used stations / observatories in the present study; L-shell values (in geocentric coordinates, height above sphere $R_e = 6371.2$ km) are also shown in the last column.

Station	Abbrev.	GLat ($^{\circ}N$)	GLon ($^{\circ}E$)	Alt. (m)	MLat ($^{\circ}N$)	MLon ($^{\circ}E$)	L (R_e)
Hartland	HAD	50.995	355.515	95	46.8316	74.1324	2.204
Chambon la Forêt	CLF	48.025	2.260	145	42.8010	78.8839	1.909
Castello Tesino	CTS	46.047	11.649	1175	40.4040	86.4340	1.758
Surlari	SUA	44.680	26.250	84	39.4936	99.4377	1.688
Ebro	EBR	40.957	0.333	531.5	33.3990	75.8665	1.472
Izник	IZN	40.500	29.720	256	34.9423	102.3087	1.483
Klokotos	THL	39.565	22.014	86	33.0750	94.8640	1.428
Penteli	PEG	38.100	23.900	380	31.6850	96.2190	1.372
Dionysos	DIO	38.078	23.933	460	31.4660	96.5380	1.373
Velies	VLI	36.718	22.947	220	29.6600	95.4890	1.321
San Fernando	SFS	36.667	354.055	111	26.9410	70.0313	1.302
Finokalia	FIN	35.333	25.667	250	28.3200	98.0000	1.280
Tamanrasset	TAM	22.790	5.530	1373	11.9010	78.9260	1.012

inspected for spikes and small data gaps, which were then cured by minor preprocessing applied wherever necessary (example shown in §2.1.4). As pointed out by Tozzi et al. [2019b], linear interpolation used to fill in small data gaps, does not play a significant role to the results, but if it is to affect the GIC index, it will only be to underestimate it. Next, all time series were detrended in order to remove the linear trend from the geomagnetic field data. The formulas applied to the detrended geomagnetic field data, according to Marshall et al. [2011] are the following:

$$(4.1) \quad GIC_x(t) = |FFT\{Y(f)Z(f)\}^{-1}|$$

$$(4.2) \quad GIC_y(t) = |FFT\{X(f)Z(f)\}^{-1}|$$

$$(4.3) \quad Z(f) = e^{i\frac{\pi}{4}} \sqrt{\frac{f}{f_N}}$$

where $X(f)$ and $Y(f)$ are the North and East components of the magnetic field in the frequency domain, $FFT\{\dots\}^{-1}$ is the inverse Fourier Transform of the formula inside the brackets, $||$ represents the absolute value, $Z(f)^2$ is the filter function with normalized

²In a homogeneous and isotropic half-space, the magnetic field lags behind the electric field by $\pi/4$ rad.

Table 4.3: GIC risk levels and corresponding GICy and GICx index thresholds, according to Marshall et al. [2011].

Risk level	GICy index values	GICx index values	Color scale
Very Low (< 5%)	≤50	≤25	Green
Low (5 – 35%)	50-100	25-50	Yellow
Moderate (35 – 65%)	100-250	50-125	Orange
High (65 – 95%)	250-600	125-300	Red
Extreme (> 95%)	>600	>300	Dark red

amplitude and phase characteristics, f is frequency and f_N is the Nyquist frequency ($f_N = 8.3$ mHz for sampling rate: 1 value / min).

The aforementioned formulas were handled under the prism of a moving window approach (length of each window being 1-day), as described in Tozzi et al. [2019a]. All calculations were performed on monthly time series and plots focus on three-day intervals including magnetic storms and SSC prior to each storm.

In Marshall et al. [2011] a scale to determine the GIC risk level according to GIC index thresholds was also introduced. The risk levels derive from a relative probability model determined from historical events of documented GIC activity in power networks from around the world: Canada, China, Japan, New Zealand, Scotland, Sweden, UK and USA. Herein, we adopt the same risk levels, namely “very low”, “low”, “moderate”, “high” and “extreme” corresponding to GICy index values of “≤50”, “50-100”, “100-250”, “250-600” and “>600”, respectively and GICx index values of lowered thresholds by half, namely “≤25”, “25-50”, “50-125”, “125-300” and “>300” (Table 4.3). Tozzi et al. [2019a] suggests that these values should be calibrated for countries at middle latitudes. Although we are in favor of the latter suggestion, for this study we use the same thresholds [Marshall et al., 2011], for a first risk level estimation of our results.

In general, at low and middle latitudes, the Y component is less affected than the X component by the external fields of the Earth’s magnetic field, mainly due to the morphology, geometry, characteristic amplitudes, and typical evolution timescales of the sources responsible for the variations in each geomagnetic field component [Yamazaki and Kosch, 2014]. Additionally, it’s important to note that the spherical harmonics formulation of the Y component doesn’t include zonal terms [Campbell, 2003], which represent the most intense external contributions, such as the ring current.

4.3 Results

In this section we present the results obtained after having applied the method described in Section 4.2 to the datasets. In Figures 4.2-4.5 we choose to display indicatively the GIC indices for three stations / observatories per storm, in order to be able to display the GIC index values in an appropriate way, i.e., to be visible, for the reader. Plots from all magnetic stations / observatories are available at Appendix A. We note here that for some storm events data were not available for all the stations / observatories.

Figure 4.2 focuses on the 2015 St. Patrick’s Day magnetic storm, displaying results from CTS, DIO and VLI. In each panel the Dst index is represented in cyan, magnetic field data in grey and the GIC index in blue. Additionally, green and yellow dashed lines represent the risk level thresholds [Marshall et al., 2011, Tozzi et al., 2019a]. X-axis covers a time period of three days, right Y-axis corresponds to the geomagnetic field data (and Dst index) and left Y-axis corresponds to the GIC index. The three panels on the left depict Bx and the GICy index, respectively, while the three panels on the right depict By and the GICx index. In all panels a red arrow pointing on the X-axis denotes the SSC. Likewise, Figures 4.3-4.5 focus on the storms of 23 June 2015, 20 December 2015 and 26 August 2018, respectively. Figures 4.3-4.4 display results from CTS, THL and DIO and Figure 4.5 displays results from CTS, SFS and FIN.

Table 4.4 shows the maximum GIC index values calculated for all storm events, throughout the three-day intervals. For each maximum value the day and time of occurrence are noted. We observe that in most cases maximum GIC index values are below the minimum threshold line (“very low”) of the GIC risk level scale (c.f. Table 4.3). Exceptions are GICx index for CLF and CTS stations during the 2015 St. Patrick’s Day storm and GICy index for CLF and IZN stations during the 23 June 2015 storm.

In general, an increase of the GIC index in accordance with the SSC occurrence is observed, as expected for middle latitude regions [Kappenman, 2003]. In some cases the GIC index attains its maximum value for the whole storm, while in others it reaches a local maximum. This is partially shown in Table 4.4 and in Figures 4.2-4.5. To be more specific, the GICy index (i.e., corresponding to the East-West direction of the geoelectric field) reaches its maximum value around the SSC in many instances, while the GICx index mainly increases locally around the SSC. For example, during the storm of 23 June 2015, maximum GICy index values are obtained around the SSC in all stations / observatories, while maximum GICx index values are observed either concurrently (i.e., for CLF and THL), or after the SSC (and before the Dst minimum) for all stations, except

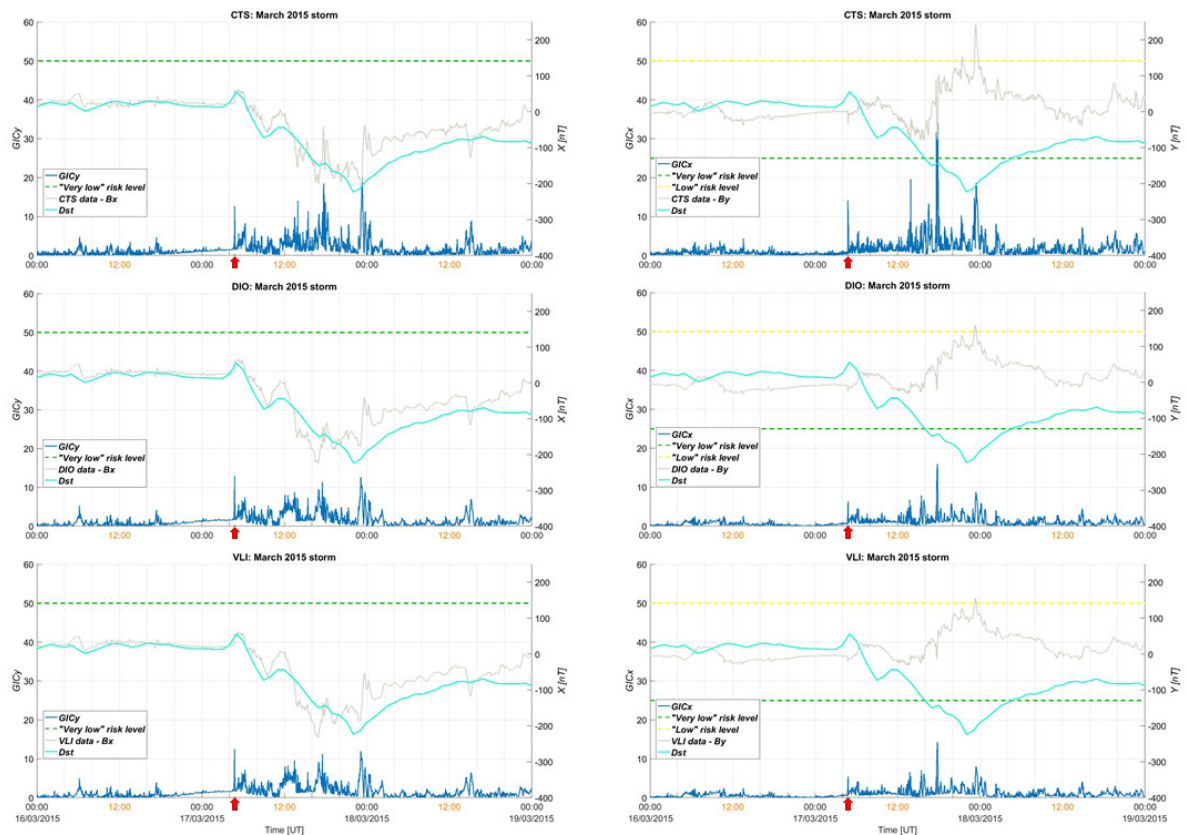


Figure 4.2: Storm of 17 March 2015: (From top to bottom the magnetic stations / observatories are: CTS, DIO and VLI). In each panel are shown the Dst index (in cyan), the geomagnetic field's X (left column) or Y component (right column) (in grey, right y-axis) and the GICy (left column) or GICx index (right column) (in blue, left y-axis). Green and yellow dashed lines represent the risk levels, associated with the GIC index values, according to Marshall et al. [2011]. The arrow pointing on the x-axis denotes the SC of the storm, according to ISGI.

for IZN. It is also worth mentioning that around the first and second SCs (on 21 and 22 June 2015, respectively) an abrupt increase, compared to neighboring values is observed at all stations (more unambiguous for GICy than GICx). Local increases apply also for GICx around the SSC at all stations / observatories.

During the 2015 St. Patrick's Day magnetic storm, maximum GICy index values for DIO, VLI and TAM stations occur around the SSC, while maximum GICx index values for all stations / observatories occur after the SSC and during the storm's main phase (i.e., around four hours before the minimum Dst, for the majority of the stations). Still, in all stations / observatories a local increase of both the GICy and the GICx index around the SSC is observed. An additional point to note is that the GICy index values obtained around the SSC seem to increase as we move towards lower latitudes for the majority of

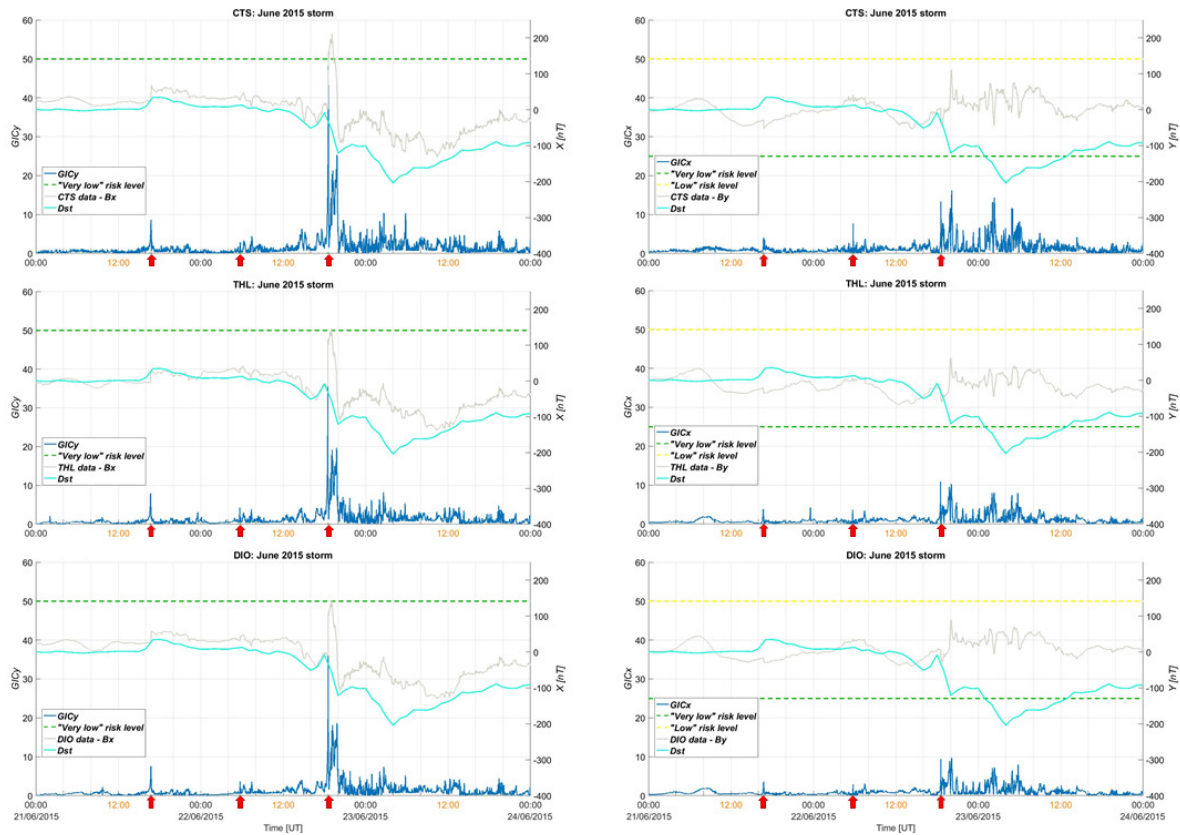


Figure 4.3: Storm of 23 June 2015: (From top to bottom the magnetic stations / observatories are: CTS, THL and DIO). In each panel are shown the Dst index (in cyan), the geomagnetic field's X (left column) or Y component (right column) (in grey, right y-axis) and the GICy (left column) or GICx index (right column) (in blue, left y-axis). Green and yellow dashed lines represent the risk levels, associated with the GIC index values, according to Marshall et al. [2011]. The arrow pointing on the x-axis denotes the three SCs of the storm, according to ISGI.

the stations / observatories, while the GICx index values seem to decrease. We remind here that in the study of Zhang et al. [2015] for the same event, it was found that two substations in China (low latitudes) had GICy index values 2 or 3 times higher at the SSC than during the main phase of the magnetic storm. According to Carter et al. [2016] the magnetic field variations at middle and low latitudes were smaller compared to high latitudes, but they occurred concurrently with the SSC, predominantly on the dayside. At equatorial latitudes, GIC activity was enhanced not only at the occurrence of the SSC, but also approximately 10 hours into the storm, at similar times to the largest perturbations in the high-latitude regions.

In the case of the 20 December 2015 storm, maximum GICy index values appear around the denoted SSC in CLF, CTS, DIO, SFS and TAM, while local maximum GICy

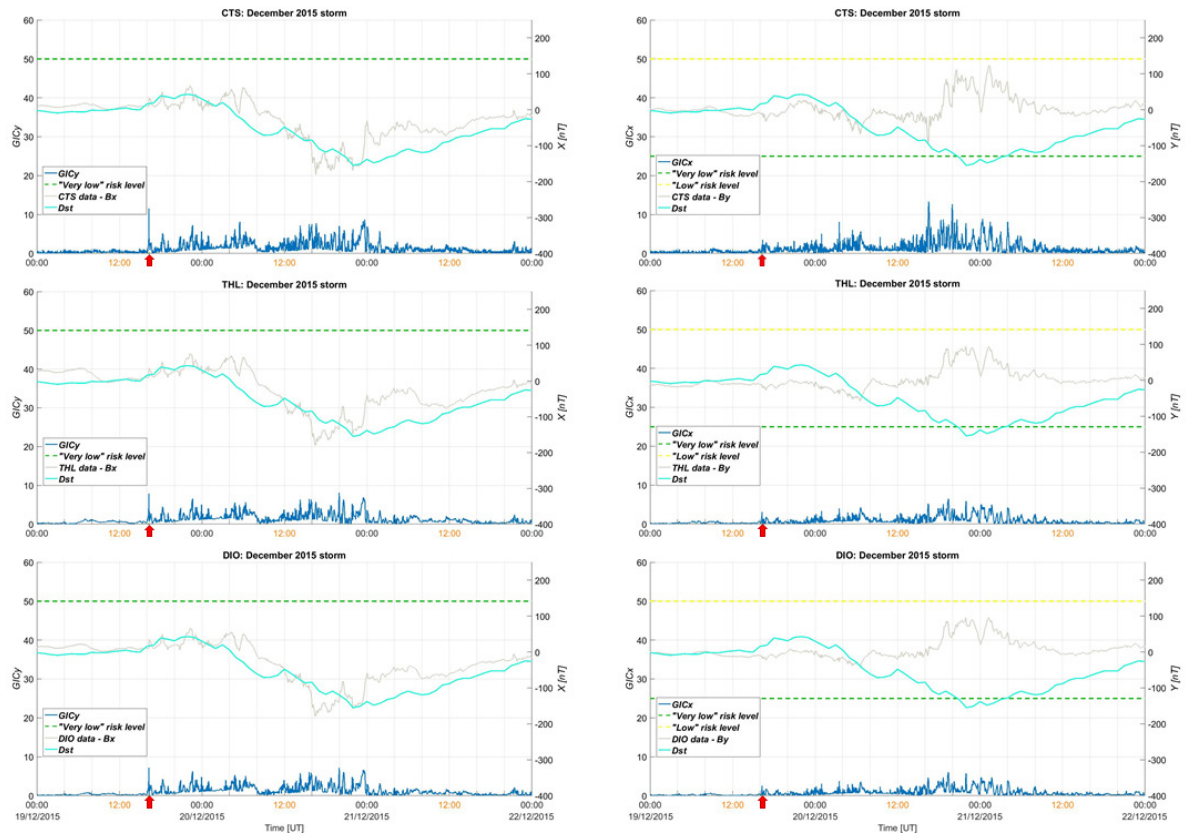


Figure 4.4: Storm of 20 December 2015: (From top to bottom the magnetic stations / observatories are: CTS, THL and DIO). In each panel are shown the Dst index (in cyan), the geomagnetic field's X (left column) or Y component (right column) (in grey, right y-axis) and the GICy (left column) or GICx index (right column) (in blue, left y-axis). Green and yellow dashed lines represent the risk levels, associated with the GIC index values, according to Marshall et al. [2011]. The arrow pointing on the x-axis denotes the SC of the storm, according to ISGI.

index values are reached in the rest of the stations / observatories. Maximum GICx values appear again after the SSC and before the Dst index reaches its minimum value. In this case the correlation between the SSC and the GICx index seems to be imperceptible.

Regarding the 26 August 2018 storm, that officially was not preceded by an SSC, GIC index values for all stations start to slightly increase before the main phase of the storm both in the North and the East directions. An interesting remark is that at CTS, EBR, IZN, PEG³, SFS, FIN and TAM maximum GICy index values are observed during the recovery phase of the storm. The same applies for EBR, IZN, PEG⁴, SFS and

³Results for PEG are not displayed in Table 4.4, as PEG data were only used for the August 2018 storm, where no DIO data were available. GICy index for PEG is 7.58.

⁴GICx index for PEG is 4.56.

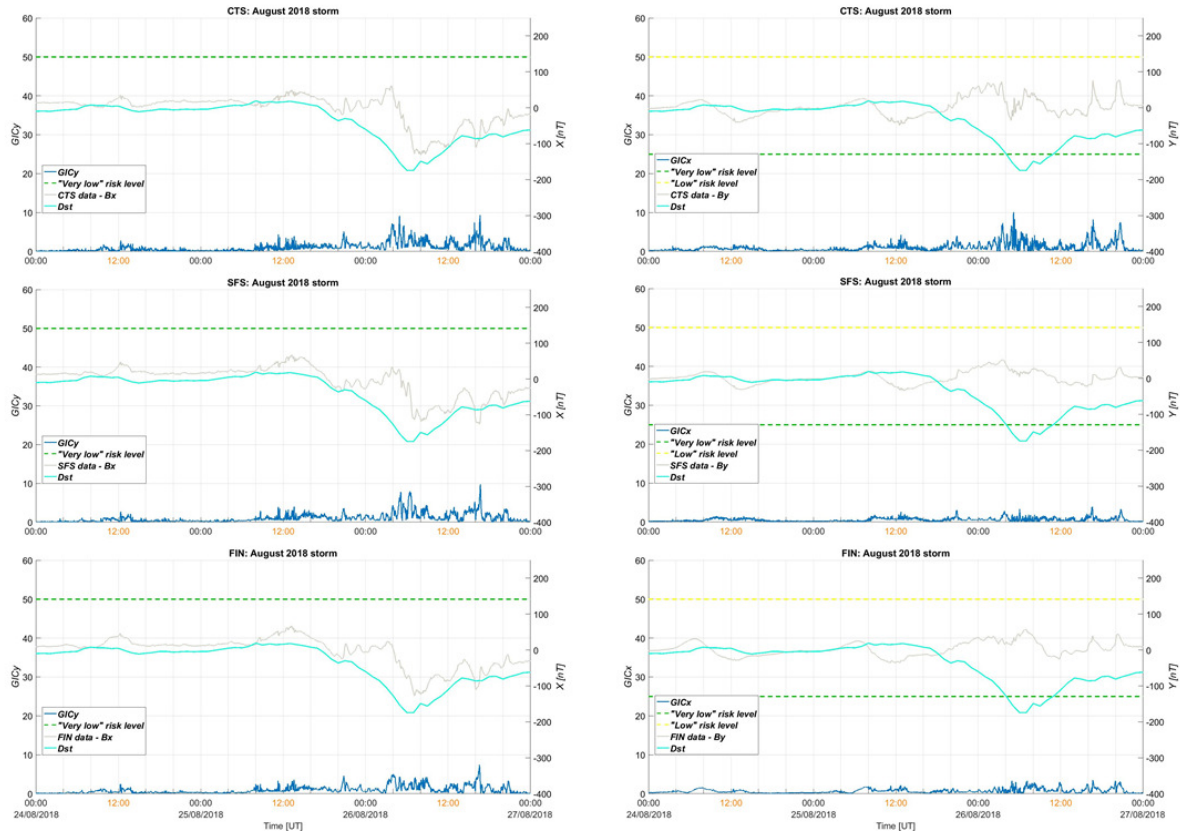


Figure 4.5: Storm of 26 August 2018: (From top to bottom the magnetic stations / observatories are: CTS, SFS and FIN). In each panel are shown the Dst index (in cyan), the geomagnetic field's X (left column) or Y component (right column) (in grey, right y-axis) and the GICy (left column) or GICx index (right column) (in blue, left y-axis). Green and yellow dashed lines represent the risk levels, associated with the GIC index values, according to Marshall et al. [2011].

FIN maximum GICx index values. A possible explanation could be that these values are linked to magnetospheric Ultra Low Frequency (ULF) pulsations of the Pc5 range ($f = 2 - 7 \text{ mHz}$); and indeed, as we can see in Figure 4.6, where the integrated ULF power is plotted per UT hour in that frequency range for four of our magnetometers (calculated as in Dimitrakoudis and Mann [2019]), there is a spike of ULF wave activity at that time, i.e., at 16:00 to 17:00 UT.

At this point, it is of importance to mention that IZN, SFS and FIN are located close to the sea, therefore the geomagnetic field recordings will have increased values due to the coast effect. It is widely known that the horizontal geoelectric field is amplified in coastal areas, due to the large lateral conductivity contrast at an ocean-land interface [Pirjola, 2013]. This is indeed observed in several instances of Table 4.4. Higher values,

Table 4.4: Maximum GIC index values calculated for the four magnetic storms. For each maximum value, corresponding day and time (UT) of occurrence are marked. Not available data are marked as N/A.

Station	16-18 Mar. 2015		21-23 Jun. 2015		19-21 Dec. 2015		24-26 Aug. 2018	
	GICy	GICx	GICy	GICx	GICy	GICx	GICy	GICx
	<i>Day time</i>							
CLF	23.30 <i>17 23:20</i>	38.97 <i>17 17:53</i>	51.25 <i>22 18:35</i>	19.59 <i>22 18:35</i>	11.37 <i>19 16:19</i>	18.13 <i>20 20:00</i>	11.09 <i>26 04:57</i>	11.71 <i>26 05:09</i>
CTS	20.70 <i>17 23:20</i>	34.73 <i>17 17:52</i>	48.15 <i>22 18:35</i>	16.18 <i>22 20:10</i>	11.53 <i>19 16:18</i>	13.36 <i>20 16:32</i>	9.31 <i>26 16:41</i>	10.09 <i>26 05:09</i>
EBR	16.17 <i>17 23:21</i>	21.87 <i>17 13:56</i>	40.69 <i>22 18:35</i>	9.64 <i>22 20:10</i>	8.46 <i>20 23:31</i>	12.48 <i>20 20:00</i>	8.10 <i>26 16:43</i>	6.99 <i>26 16:37</i>
IZN	16.20 <i>17 17:34</i>	18.27 <i>17 17:46</i>	59.58 <i>22 18:35</i>	9.59 <i>23 05:52</i>	N/A	N/A	9.79 <i>26 16:37</i>	7.35 <i>26 16:42</i>
THL	N/A	N/A	39.36 <i>22 18:31</i>	10.84 <i>22 18:31</i>	8.07 <i>20 19:59</i>	6.51 <i>20 19:24</i>	N/A	N/A
DIO	13.03 <i>17 04:46</i>	15.86 <i>17 17:48</i>	36.28 <i>22 18:35</i>	9.75 <i>22 20:08</i>	7.19 <i>19 16:18</i>	6.04 <i>20 19:24</i>	N/A	N/A
VLI	12.49 <i>17 04:46</i>	14.23 <i>17 17:48</i>	N/A	N/A	N/A	N/A	N/A	N/A
SFS	17.17 <i>17 23:25</i>	18.06 <i>17 13:56</i>	46.81 <i>22 18:35</i>	8.83 <i>22 20:11</i>	9.50 <i>19 16:19</i>	8.01 <i>20 20:01</i>	9.75 <i>26 16:44</i>	3.92 <i>26 16:37</i>
FIN	N/A	N/A	N/A	N/A	N/A	N/A	7.45 <i>26 16:36</i>	3.45 <i>26 16:42</i>
TAM	16.68 <i>17 04:47</i>	11.43 <i>17 17:52</i>	33.85 <i>22 18:35</i>	11.03 <i>22 20:10</i>	9.74 <i>19 16:19</i>	5.25 <i>20 05:28</i>	6.74 <i>26 16:42</i>	3.05 <i>26 06:03</i>

against the latitudinal decrease, are also observed in TAM during the three storms of 2015, in the component of lower magnitude (i.e., GICy during the March and December storms and GICx during the June storm). Overall, our results show that GIC index values (in both North and East directions) increase with increasing geographic latitude, namely CLF station, located in the northernmost region considered in this study, has the largest GIC index values.

4.4 Solar Cycle 25

Given that a significant part of this dissertation was conducted during the fading phase of solar cycle 24 and dawn of solar cycle 25 it was essential to investigate and record all magnetic storms that occurred after August 2018, in order to enrich our study and

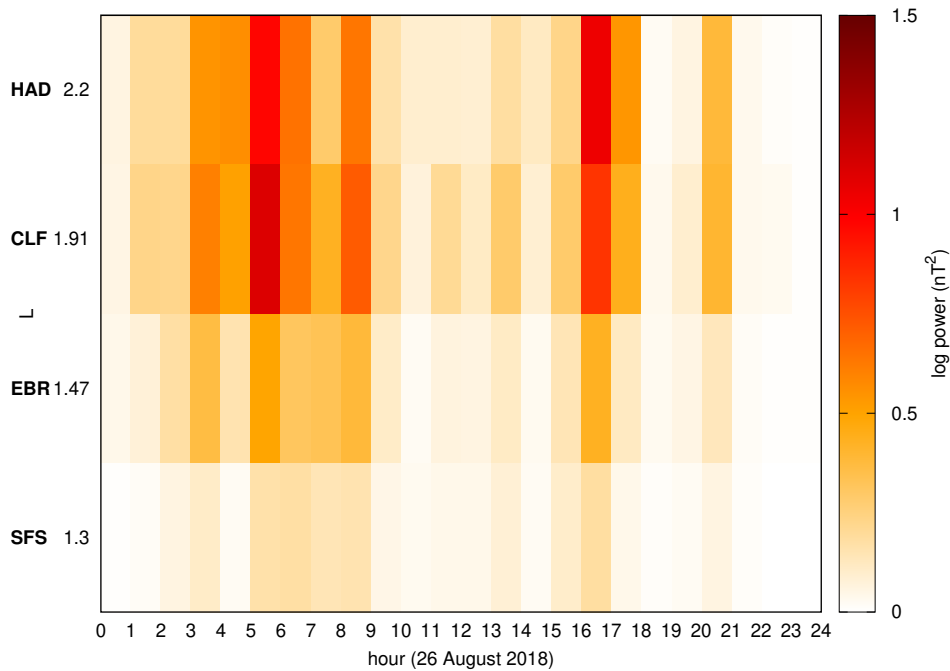


Figure 4.6: ULF power in the 2-7 mHz frequency range measured in four ground magnetometer stations on 26 August 2018, arranged by L-shell.

reinforce our results. For the time period spanning from September 2018 to August 2022 and based on the condition “Dst < -150 nT” considered for the main part of this dissertation (during solar cycle 24) no storm was recorded. However, a less intense magnetic storm occurred on the 4th of November 2021 (Dst = -105 nT) and six more storms of even lower intensity (Dst < -80 nT) occurred during the aforementioned time period.

A SC prior to the storm of 4 November 2021 storm was recorder on 3 November 2021, at 19:42:00 UT with mean amplitude 21.3 nT. During the main phase of the storm the Dst index reached its minimum value (Dst = -105 nT) on 4 November 2021, at 13:00:00 UT. The GIC indices, along with the magnetic field data and the Dst index), are plotted in Figure 4.7 for all stations / observatories with available data (i.e., CLF, EBR, IZN, PEG and TAM). Table 4.5 is similar to Table 4.4 and shows the maximum GIC index values throughout the three-day intervals.

Based on the GICy and GICx indices values (both are within the "very low" risk level), no strong GICs are anticipated to develop in the vicinity of the five stations during this moderate magnetic storm. Regardless, the majority of the stations obtain their maximum GICy index values very close to the occurrence of the SSC, as expected, while maximum GICx index values are very close in time to the SSC for CLF, EBR and IZN.

Table 4.5: Maximum GIC index values calculated for the magnetic storm of November 2021. For each maximum value, corresponding day and time (UT) of occurrence are marked.

Station	3-5 Nov. 2015	
	GIC _y	GIC _x
	<i>Day time</i>	<i>Day time</i>
CLF	17.24 <i>3 21:46</i>	16.11 <i>4 01:45</i>
EBR	14.98 <i>3 21:46</i>	13.13 <i>4 01:45</i>
IZN	18.48 <i>3 21:45</i>	10.60 <i>3 21:46</i>
PEG	14.42 <i>4 09:16</i>	7.17 <i>4 01:47</i>
TAM	14.24 <i>3 21:46</i>	10.82 <i>4 10:82</i>

4.5 Discussion

First, we compare the results of the GIC index for the Mediterranean region to recent studies on GIC activity for Italy and Spain. We observe that the GIC index calculations in CTS for the 2015 St. Patrick’s Day storm are in excellent agreement with the results of Tozzi et al. [2019a]; based on the thresholds established by Marshall et al. [2011] and considering the maximum values reached by either the GIC_x or GIC_y index, the St. Patrick’s Day 2015 storm represented a “low” or “very low” risk level to GIC related damage for latitudes around the CTS observatory, respectively.

Regarding the results of the Spanish stations (EBR and SFS) for the same storm, the most recent study was published by Cid et al. [2020]. In the latter, two new geomagnetic indices, namely the Local Disturbance index (LDi) and the Local Current index (LCi) were developed for nowcasting the local geomagnetic disturbances and as a proxy for the GIC risks in Spain, respectively. Both indices are available at the European Space Agency (ESA) Space Situational Awareness (SSA) Space Weather portal (<http://swe.ssa.esa.int/>). Besides the LCi index, ESA-SWE Services provide several GIC-related products which can be found in Appendix C. LDi and LCi have 1 min resolution and are derived from the horizontal component of the ground magnetic field data recorded in the magnetic observatory of San Pablo de los Montes (SPT) in Toledo, Spain. LDi is the residual horizontal component from a given magnetometer, after removal of the baseline and Sq-current signatures. The LCi is computed as the rate of change of the LDi and has

been demonstrated to be proportional to the GIC recorded at a substation of the Spanish power network. The correlation between LCI and the GIC is very similar to that between the GIC and $1 \text{ min } dB_H/dt$. Comparisons between different Spanish magnetic observatories has led to the conclusion that one observatory is enough to provide a “national” geomagnetic index, therefore the use of geomagnetic field data from different stations in our study (i.e., EBR and SFS) can test this statement.

Both indices are complemented by a five-level color scale, ranging from green (quiet) to red (highly disturbed), according to the probability of GIC occurrence. During the St. Patrick’s Day storm of 2015 the LCI index reached the so-called “elevated” level (third out of five). In our study the GICx and GICy indices for both EBR and SFS observatories obtained values within the “very low” risk level. This comparison, although not between values of the same index, might indicate that a potential calibration of the GIC index thresholds provided by Marshall et al. [2011] should be performed for the Mediterranean region. The reason is that the current GIC index thresholds could underestimate the associated risk (see also Tozzi et al. [2019a]) for the Mediterranean region. As for the statement that one observatory is enough to represent a nationwide index, from our analysis it turns out that although both the GICy and GICx indices obtain values within the “very low” risk level, the difference between EBR and SFS reaches ~ 6 units for the case of the GICy index during the June 2015 storm, therefore GIC index seems to perform in a more sophisticated way. The fact that the GIC index differentiates between the North and East components while the LCI does not makes the former more versatile at capturing information that may be of more importance in other parts of Europe.

In Figures 4.2-4.5 the Dst index has been used as a measure of reference. It should be pointed out that discrepancies between the minimum (or maximum) Dst index, which has a resolution of one value per hour, and the GIC index, which has a resolution of one value per minute are expected to exist. On top of that, characteristics of local character are expected to disappear in the Dst index.

To conclude, in this chapter we presented the results of a risk assessment for the Mediterranean region (i.e., Greece, Italy, France, Spain, Algeria and Turkey) to space weather-related GIC activity. We have calculated the GIC indices (i.e., GICx index derived from the East (Y) component of the geomagnetic field and GICy index derived from the North (X) component) around the most intense magnetic storms ($Dst < -150 \text{ nT}$) of solar cycle 24 (i.e., March, June and December 2015 and August 2018) and observed that GIC index values are elevated during the selected storms, although they do not exceed thresholds indicating high risk for infrastructure installed at these locations. Moreover,

the GIC index increases appear simultaneously with the SSC occurrence, in agreement with other GIC studies for low and middle latitudes (e.g., Kappenman [2003], Zhang et al. [2015]). It should be noted that the GIC index gives only a first estimation of the risk level due to GIC around the area of the magnetic station / observatory, without taking into account the geoelectrical structure of the area where the station is located (i.e., the electrical conductivity of the subsurface provided for instance by a magnetotelluric survey), nor the topology of the power grid, which might seriously affect the development of GIC.

The electrical conductivity of the subsurface will be addressed in the next chapter, where we employ a compilation of 1D layer ground models for the north of the Mediterranean; to our knowledge, no such compilation exists as of yet for the south.

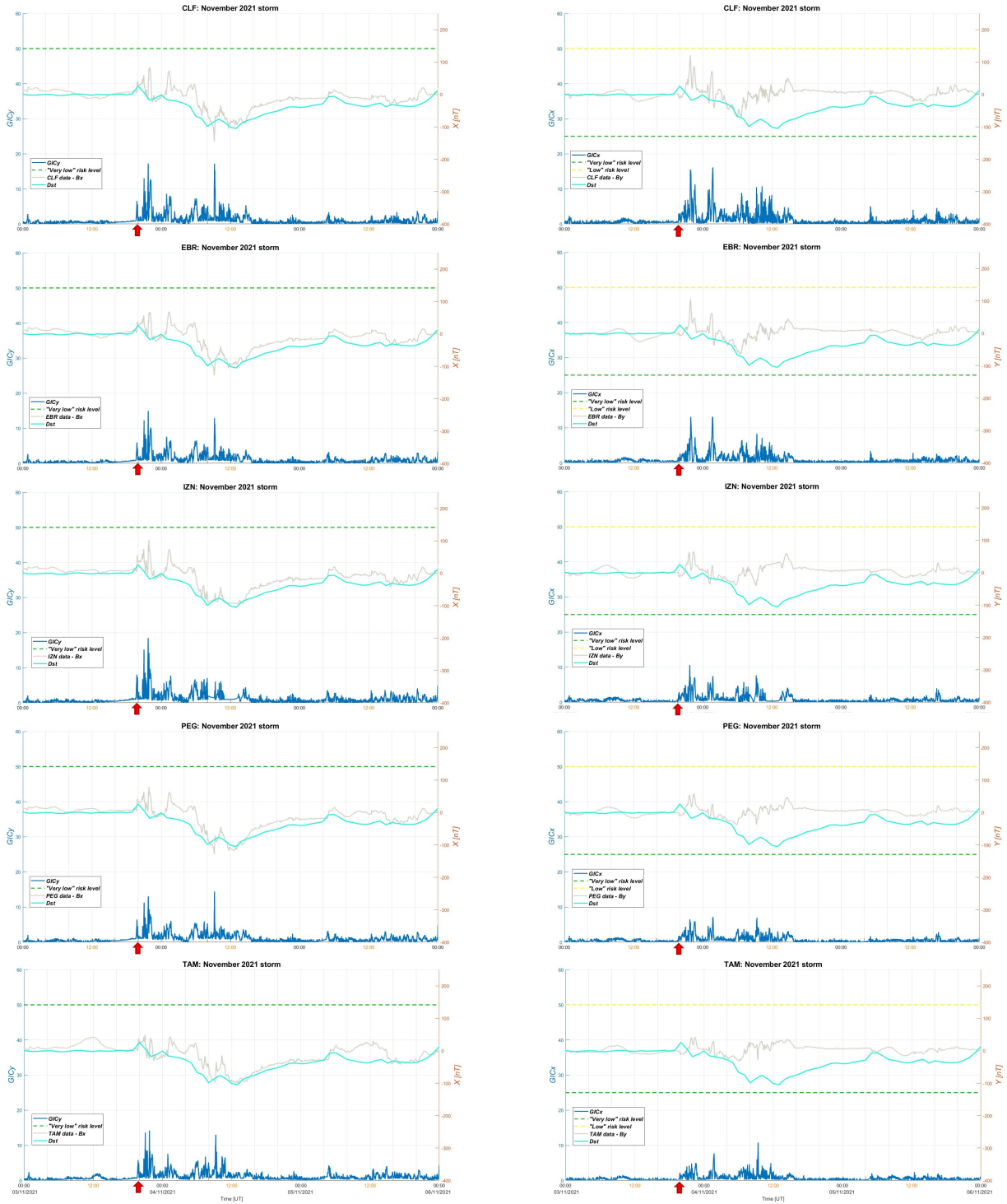


Figure 4.7: Storm of 4 November 2021: (From top to bottom the magnetic stations / observatories are: CLF, EBR, IZN, PEG and TAM). In each panel are shown the Dst index (in cyan), the geomagnetic field's X (left column) or Y component (right column) (in grey, right y-axis) and the GICy (left column) or GICx index (right column) (in blue, left y-axis). Green and yellow dashed lines represent the risk levels, associated with the GIC index values, according to Marshall et al. [2011].

MAPS OF ACTIVITY FOR THE MEDITERRANEAN REGION

Geomagnetically Induced Currents (GIC) constitute an integral part of space weather research and are a subject of ever-growing attention for countries located in the low and middle latitudes. A series of recent studies highlights the importance of considering GIC risks for the Mediterranean region. In Chapter 4, we exploited data from the Hellenic GeoMagnetic Array (ENIGMA), which is deployed in Greece, complemented by magnetic observatories in the Mediterranean region (Italy, France, Spain, Algeria and Turkey), to calculate values of the GIC index, i.e., a proxy of the geoelectric field calculated entirely from geomagnetic field variations. We performed our analysis for the most intense magnetic storms ($Dst < -150$ nT) of solar cycle 24. Results showed that GIC index increases are well correlated with Storm Sudden Commencements (SSCs). However, the GIC indices do not exceed “low” activity levels despite the increases in their values, at all magnetic stations / observatories under study during the selected storm events.

In this chapter, we will make an attempt to produce GIC index contour maps for the Mediterranean region, focusing on the 2015 St. Patrick’s Day storm. For estimates of the geoelectric field at each location, 1D layer models can be employed; with compilations of such models for larger areas (e.g., Kelbert [2019]). For Europe, one such compilation is provided by the European Risk from Geomagnetically Induced Currents (EURISGIC) project [Ádám et al., 2012, Viljanen et al., 2012, Viljanen et al., 2013] and we will be using it to put our GIC proxy values in context. Also, we validate the sensitivity of the widely-used GIC index against E field variations derived from the conductivity models

for the most well-known magnetic storms of the previous solar cycle.

In Section 5.1 we describe the data and the methodology used to produce the contour maps. Section 5.2 is dedicated to the results and some useful comparisons between several variables, while in the last two sections we discuss our findings and provide useful conclusions.

5.1 Data Selection and Methodology

The activity maps of this chapter have been produced solely for the 2015 St. Patrick's day magnetic storm. Based on the GIC risk level scale of Table 4.3 and on maximum GIC index values either at the SSC occurrence (04:45:00 UT \pm 5 minutes) (Figure 5.1) or during the day of the storm (Figure 5.2) we derived contour maps (using biharmonic spline interpolation) in geographic latitude vs. geographic longitude of GIC index values for three days, zooming in what happens within the lowest activity levels ("very low" and "low"). Specifically, Figure 5.1 is produced based on maximum values around the occurrence of the SSC (04:45:00 UT \pm 5 minutes on 17 March 2015). In order to prevent edge effects embedded in the contouring algorithm, we had to employ auxiliary geomagnetic data from two magnetic observatories outside the Mediterranean region, namely Hartland (HAD) in the United Kingdom and Surlari (SUA) in Romania. The GIC index maps can be considered as a preliminary modeling attempt of GIC activity levels in the Mediterranean region.

These maps were produced after trying five different interpolation methods (i.e., linear, nearest neighbor, natural neighbor, cubic and biharmonic spline interpolation) and choosing the one that gives smoother contour lines (i.e., biharmonic spline interpolation). Although such a technique is purely mathematical, as it does not take into consideration physical processes involved, it offers a chance to get GIC index values in regions where no magnetic field measurements are sampled. This approach is strengthened by the fact that GIC index is calculated solely by geomagnetic field measurements, which in the middle latitudes can be well modelled using simple interpolation techniques (e.g., nearest neighbor) as discussed for example by Torta et al. [2017]. They were created with MATLAB's "contour" function. The interpolation method used for the initial data, which were "scattered", was MATLAB's *griddata* 'v4' method, which is not triangulation-based and is not affected by deterioration of the interpolation surface near the boundary.

For a better assessment of the geoelectric field that may be associated with these GIC indices we have overplotted a ground conductivity map of Europe in the form of a grid,

Table 5.1: Maximum GIC index values calculated at the SSC occurrence (04:45:00 UT \pm 5 minutes) on 17 March 2015.

17 March 2015				
Station	GICy	Time (UT)	GICx	Time (UT)
HAD	17.03	04:49:00	21.32	04:48:00
CLF	10.51	04:47:00	25.58	04:49:00
CTS	12.65	04:47:00	14.11	04:48:00
SUA	18.49	04:48:00	9.46	04:49:00
EBR	10.44	04:47:00	13.04	04:48:00
IZN	15.71	04:47:00	8.52	04:49:00
DIO	13.03	04:46:00	6.34	04:49:00
VLI	12.49	04:46:00	5.43	04:49:00
SFS	12.29	04:47:00	10.35	04:48:00
TAM	16.68	04:47:00	6.38	04:48:00

each cell of which corresponds to a 1-D ground model by *Ádám et al. [2012]* as denoted by its respective number. The parameters for each model (resistivity and thickness for each layer) are openly available at <http://real.mtak.hu/2957/>. In short, each cell is divided into several layers, of varying depths, with corresponding resistivities. Its conductance up to a certain depth is then calculated by adding up all the intervening layer depths divided by their resistivities. The cell numbers are shown in the left panels of Figure 5.1 while conductances for the upper 80 km are shown in the right panels of Figure 5.1 and all panels of Figure 5.2.

5.2 Results

Table 5.1 shows the maximum GIC index values, as well as their times of occurrence, calculated when the SSC occurred (04:45:00 UT \pm 5 minutes), on the 17 of March 2015, for all available data. Table 5.2 shows the daily maximum GIC index values calculated for the 16, 17 and 18 of March 2015 for all available data. One can observe that in most cases maximum GIC index values are below the minimum threshold line (“very low”) of the GIC risk level scale, except for the GICx index on the 17 March 2015 for HAD, CLF, CTS, and SUA observatories at the northernmost locations, that were classified under the “low” risk level.

Since the end goal of space weather research is to facilitate human activity for risk mitigation, we have added a map of the electrical grid in Europe and Northern Africa in Figure 5.3. This map shows all transmission lines designed for 132 kV voltage and higher

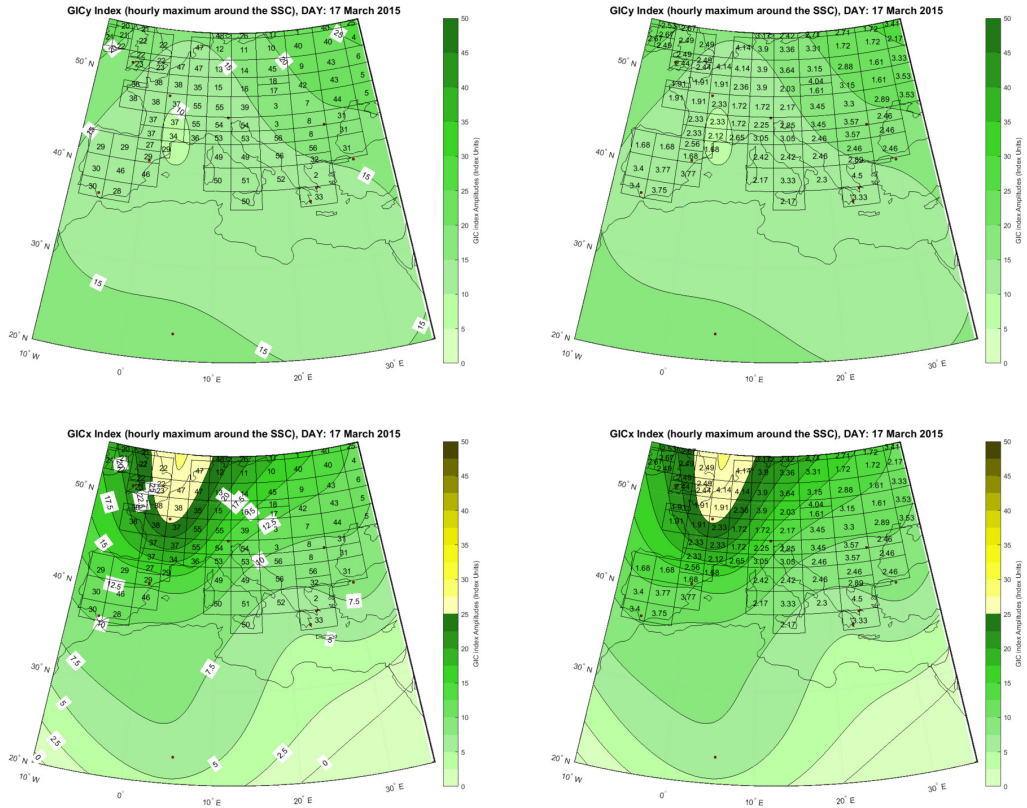


Figure 5.1: Contour maps of GICy (top panels) and GICx (bottom panels) indices at the occurrence of the SSC (04:45:00 UT \pm 5 minutes) on 17 March 2015. Here, we zoom in the “Very Low” (available for GICy and GICx) and “Low” (available for GICx) risk levels, represented by green and yellow colors, and thus different intensities of GIC index can be identified by the different hues of green / yellow. Focus is on geographic latitudes between 20° and 55° and geographic longitudes between -10° and 35°. Red dots represent locations of magnetic stations / observatories. Overplotted in the panels on the left is a ground conductivity map of Europe in the form of a grid, each cell of which corresponds to a 1-D ground model Ádám et al. [2012], denoted by its respective number as listed at <http://real.mtak.hu/2957/>; while overplotted in the panels on the right are the respective conductances, in base 10 logarithmic scale, with units of log(S), with an integration depth of 80 km.

(transmission lines network replicated from <https://www.entsoe.eu/data/map/>). We have also taken the ground conductivity data from the 1D model we had used for Figures 5.1 and 5.2 and used it to calculate electric fields from the magnetic field measurements. This approach aimed at initially producing contour maps of the magnetic field, based on available measurements at the occurrence (\pm 5 minutes) of the SSC on St. Patrick’s Day storm (magnetic field time series were handled under the prism of a moving window,

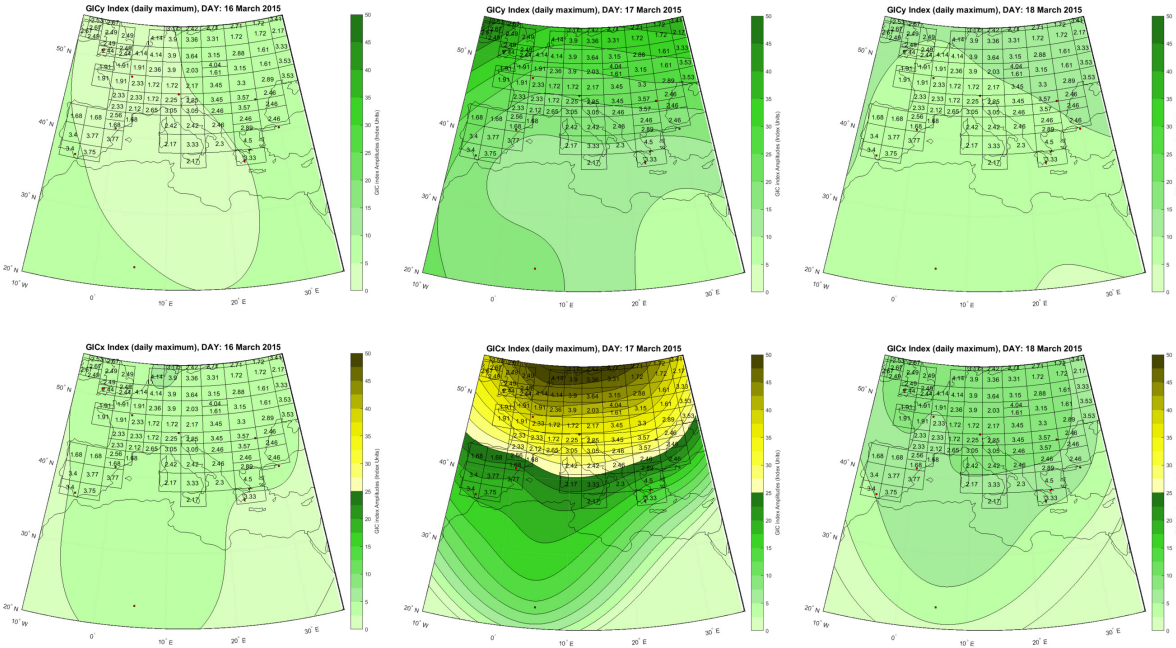


Figure 5.2: Contour maps of GICy (top panels) and GICx (bottom panels) indices for 16, 17 and 18 March 2015. Here, we zoom in the “Very Low” (available for GICy and GICx) and “Low” (available for GICx) risk levels, represented by green and yellow colors, and thus different intensities of GIC index can be identified by the different hues of green / yellow. Focus is on geographic latitudes between 20° and 55° and geographic longitudes between -10° and 35° . Red dots represent locations of magnetic stations / observatories. Overplotted is a ground conductivity map of Europe in the form of a grid, each cell of which corresponds to a 1-D ground model Ádám et al. [2012], denoted by its respective conductances (in base 10 logarithmic scale, with units of $\log(S)$) with an integration depth of 80 km.

similarly to the methodology used for the calculation of the GIC index). Then, by visual inspection, a magnetic field value was attributed to each cell of the grid and multiplied by each resistance value R (where $R = 1/\text{conductance}$). To calculate $E_{x,y}$ in each cell we also divided by the permeability of free space, μ_0 and adjusted units (by multiplying with 10^{-9} to convert nT to T and 10^6 to convert V/m to mV/km).

The estimated electric field time series have been plotted in Figure 5.4 along with the calculated GIC indices (see previous chapter) to show how the two correlate. Comparing the time series of E_x and E_y with GICx and GICy, respectively, for the stations CLF, CTS, DIO, EBR, SFS, and VLI over three days around 17 March 2015 we found that their correlation coefficients r_x (between E_x and GICx) and r_y (between E_y and GICy) range between 0.54 and 0.65 (Table 5.3). This suggests that while there is a discernible positive

Table 5.2: Daily maximum GIC index values calculated for 16, 17 and 18 March 2015.

Station	16 March 2015		17 March 2015		18 March 2015	
	GIC _y	GIC _x	GIC _y	GIC _x	GIC _y	GIC _x
HAD	4.65	3.65	35.49	38.54	10.04	8.47
CLF	4.12	4.51	23.30	38.97	8.58	7.39
CTS	4.82	4.36	20.70	34.73	8.98	8.12
SUA	5.71	3.36	21.68	29.86	10.58	8.02
EBR	3.83	3.00	16.17	21.87	7.87	7.30
IZN	6.12	2.83	16.20	18.27	9.74	5.72
DIO	5.27	2.56	13.03	15.86	7.00	5.88
VLI	4.95	2.39	12.49	14.23	6.46	5.32
SFS	5.23	2.61	17.17	18.06	9.47	5.10
TAM	5.12	3.49	16.68	11.43	7.29	3.78

linear relationship between E fields and GIC indices, other factors may also influence the geoelectric field, resulting in moderate variability. In a previous study, Marshall et al. [2012] found that correlation coefficients between GIC_y index and absolute values of the transformer neutral currents measured during the storm of 6 November 2001 at several stations in New Zealand were around 0.8 to 0.9 (although there were cases of much lower values). Comparing these values to our correlation coefficients could present an indication, in a quantitative manner, of the index's reliability in the Mediterranean region; however, it should be noted that this gives us only a hint and further investigations, including more case studies, would be required to obtain statistically significant results.

In section 4.5 we discussed about the LD_i and LC_i indices. Figure 5.5 shows a comparison between B_x, dB_x/dt , LD_i, LC_i [Ortega et al., 2019], the GIC_y index and E_y, as measured in EBR. Both dB_x/dt and LC_i display momentary rates of change of B, at a one minute time scale. While generally useful, this does not convey all pertinent information for the generation of currents. Indeed, if we look at the SSC at 4:48 on 17 March 2015 both dB_x/dt and LC_i show an abrupt spike at that moment but they don't inform us clearly on the temporal extent of a heightened E_y, which is informed for hours afterwards by both that initial spike and the plethora of smaller spikes after that. GIC_y, on the other hand, shows us both a spike at the moment of the SSC and a heightened level of GIC values long after that. The same can be seen afterwards in that time series.

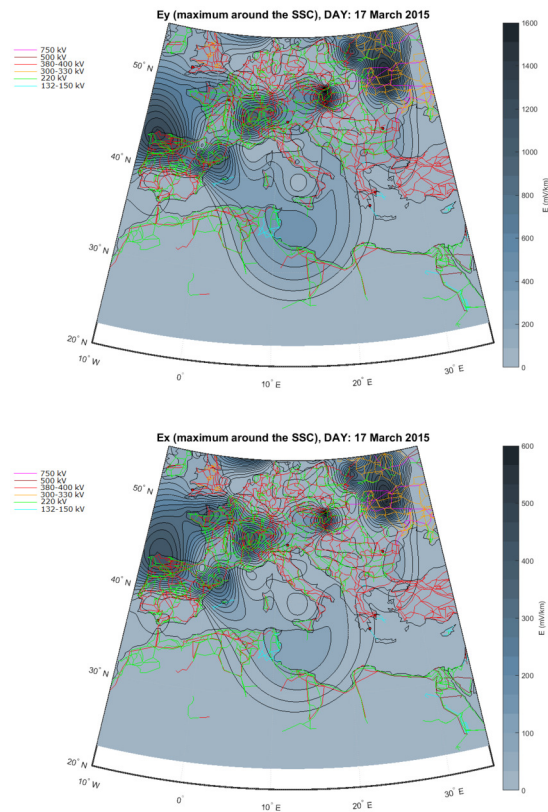


Figure 5.3: Contour maps of E_y (top panel) and E_x (bottom panel) calculated at the time when the SSC occurred ($04:45:00 \text{ UT} \pm 5 \text{ minutes}$) on 17 March 2015. Overplotted is a map of the electrical grid in Europe and Northern Africa.

5.3 Discussion

Figure 5.1 is an attempt to plot the calculated maximum GIC index values for each station at the SSC occurrence ($04:45:00 \text{ UT} \pm 5 \text{ minutes}$) (for the case of the St. Patrick's Day storm 2015) in order to show how the GIC index variations, primarily due to the SSC, are distributed in latitude and longitude. What is observed is that maximum values for both GIC_y and GIC_x occur within the first four (4) minutes of the occurrence of the SSC in all magnetic stations / observatories under study. Although the station separation distance is, with the exception of DIO and VLI, greater than the 500km recommended by Pulkkinen et al. [2015] and the 200km recommended by Dimitrakoudis et al. [2022], based on observations at higher latitude stations, there is little indication of small spatial scale fluctuations between stations.

SSC/SC events are latitude-dependent, so different values are expected for each magnetic station / observatory and, consequently, for each country. To estimate how



Figure 5.4: Storm of 17 March 2015: (From top to bottom the magnetic stations / observatories are: CTS, DIO and VLI). Correlation between E (mV/km) (in blue, left y-axis) and GIC index (in orange, right y-axis).

Table 5.3: Correlation coefficients r_x and r_y are calculated between E_x and GIC_x index and E_y and GIC_y index, respectively, for the stations CLF, CTS, EBR, DIO, VLI and SFS during 17 March 2015.

Station	r_x	r_y
CLF	0.5906	0.5442
CTS	0.6011	0.5473
EBR	0.6381	0.5880
DIO	0.6166	0.6283
VLI	0.6149	0.6498
SFS	0.6213	0.5824

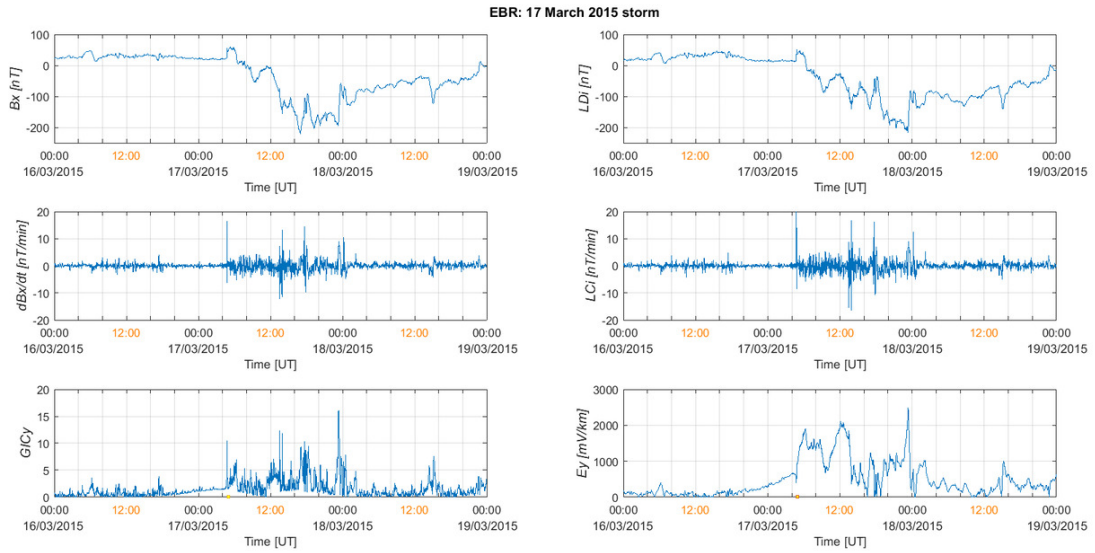


Figure 5.5: Storm of 17 March 2015: (From top left to bottom right) Comparative plots between B_x and LD_i , dB_x/dt and LC_i , GIC_y index and E_y ; at EBR.

typical the SSCs of this study are, based on Smith et al. [2019], we have calculated dB_H/dt values for HAD and we found 25.1 nT / min for March 2015, 67.3 nT / min for June 2015 and 36.3 nT / min for December 2015. March and December SSCs are below the 99th percentile, while the SSC preceding the June geomagnetic storm was above the 99th percentile, thus it was a large value, above the typical range.

A comparison with two extreme geomagnetic storms of previous solar cycles, March 1989 (with two recorded SCs on 13 March 1989; one at 01:27 UT with mean amplitude 60 nT and one at 07:43 UT with mean amplitude 11 nT) and Halloween 2003 (SSC at 06:10 UT with mean amplitude 68.4 nT), with well-known detrimental consequences for transformers reveals that the recorded values were also within the typical range. A

larger SSC disturbance was recorded during the geomagnetic storm of 24 March 1991 (mean amplitude 103 nT) and it is known to have produced some of the largest GICs ever measured in the USA at middle latitude locations [Kappenman, 2003]. These observations indicate that although GIC effects on transformers located in middle latitudes are strongly linked to SSCs, the correlation is not linear, as we deal with a complex system. For example, during the March 1989 storm, the SSC occurred concurrently with a substorm, so this combination led to large GICs [Boteler, 2019].

As for Figure 5.2, we observe that both the GICy and GICx indices have sparse contour lines before and after the storm, which doesn't give us much information on their structure; while on the day of the storm occurrence contour lines of both indices tend to become tightly clustered, which shows us a strong horizontal ordering with gradually increasing values from South to North. In other words, we observe a behavior similar to the one described for other intense magnetic storms [Balasis et al., 2006, 2008], as well as for the St. Patrick's Day storm [Papadimitriou et al., 2020] where the transition from quiet-time to storm-time magnetosphere correlates with the transition from a state of higher complexity / lower degree of organization to a state of lower complexity / higher degree of organization for the complex system of the Earth's magnetosphere.

To estimate the geoelectric field we used a compilation of 1D layer ground models for the north of the Mediterranean; to our knowledge, no such compilation exists as of yet for the south. However, the Canadian Quebec Province ground model of Boteler and Pirjola [1998] can be used to explore possible upper limits of geoelectric fields, since it represents a well-studied high resistivity ground structure (e.g., Pulkkinen et al. [2015]). Higher resistivity (represented by lower conductance in Figures 5.1 and 5.2) leads to a stronger geoelectric field, for a given geomagnetic field disturbance, as demonstrated in Figure 5.3. This allows us to visualise the different impact of the GIC index across southern Europe. The contours of electric fields generated by the magnetic field measurements become far less smooth - but in a consistently reproducible way, since the ground's electrical conductance does not vary with time. Figure 5.3 should offer an indication of the degree to which the risk factor of any given value of the GIC index should be scaled up or down depending on which part of Europe one is interested in.

5.4 Conclusions

In this chapter we investigated how an activity map displaying GIC index for the Mediterranean region would be. Ground conductivity values, based on 1D layer models,

were also integrated. The produced contour maps could be considered as a geoelectric field estimate per location and it could be useful for end-users, such as power grid operators.

The most obvious takeaway is that for all but the smallest countries in Europe no single observatory can provide definitive measurements for GIC risk. Taking Spain and Greece as example countries in southern Europe (where we had measurements from multiple magnetometers) their local conductances, according to the 1D models we used, can vary by a factor of over 100. Their calculated electric fields vary locally by at least as much¹. GIC_x and GIC_y indices are, by design, unaffected by that variable, but their (estimated) daily maximum values on 17 March 2015 (based on Figure 5.2) still vary locally by a factor of around 1.5 to 2.

The features of the network / topology, also shown in Figure 5.3, play an additional important role and are critical for a more precise estimation of the GIC intensity. Of course, the need to re-define the risk level thresholds (presented in the previous chapter) for the Mediterranean region is of great importance [Tozzi et al., 2019a]. This is also highlighted by the comparison between the GIC index and the LCi index for the Spanish region, during the St. Patrick's Day storm [Cid et al., 2020], as discussed in Chapter 4. Moreover, the 1-min sampling rate used for this analysis, as well as the linear interpolation used for small data gaps, could underestimate the actual GIC values. Higher time resolutions (e.g., 1 sec) could increase the estimated amplitudes of GIC.

¹For example, in Spain we have EBR and SFS stations. We know, from the 1D conductivity model, that $conductance(EBR) = 48$ and $conductance(SFS) = 2412$, as well as that $max(Ex_{EBR}) = 2388$ and $max(Ex_{SFS}) = 37$, so indeed variations by a factor of over 100 can be expected between two stations.

OVERALL DISCUSSION AND CONCLUSIONS

Extrême geospace events belong to the wider group of high risk and low occurrence frequency phenomena, such as earthquakes and tsunamis, while due to the complexity of the systems in which they evolve, their forecasting is an extremely challenging research field. The phenomenon is gaining ever-growing attention from the scientific community in the recent years, including Mediterranean countries, like Italy and Spain.

Geomagnetically Induced Currents (GIC) flowing along electrically conductive infrastructure, such as power transmission lines, are produced by a naturally induced geoelectric field during geomagnetic disturbances, such as magnetic storms. GIC can cause widespread blackouts across power grids, resulting in the loss of electric power (i.e., the Hydro-Québec's electricity transmission system experienced a nine-hour outage during the 1989 magnetic storm). Although GIC intensity is greater in high latitudes, recent studies highlight the importance of considering GIC risks for countries located in the low and middle latitudes, including the Mediterranean region.

In this dissertation, we primarily explored the possibility for GIC to develop in Greece. For our investigations we analyzed magnetic field timeseries obtained from ground-based magnetometers located mainly in Europe, focusing on the Mediterranean region, spaceborne magnetometers from the European Space Agency (ESA) Swarm satellites, as well as geomagnetic activity indices during magnetic storms and magnetospheric substorms. Our analytical approach utilized advanced signal processing methods, including wavelet transforms, Hurst exponent calculations, and entropy measures to identify potential

characteristic patterns preceding the occurrence of magnetic storms. Subsequently, we computed the GIC index for Greece and Southern Europe, in general, concentrating on magnetic storms that occurred during solar cycle 24 (2008 - 2019) and extending into solar cycle 25. GIC index is a proxy for the geoelectric fields, representing the GIC activity level and is calculated only from magnetic field measurements, without taking into account neither the electrical conductivity / resistivity structure of the Earth's subsurface nor the topology of the network. Furthermore, we assessed the intensity of the geoelectric field E , taking into account the ground's electrical conductivity. This assessment allowed us to conduct an analytical evaluation of the electrical power system's susceptibility in our country and Southern Europe during extreme space weather events, such as magnetic storms.

In what follows, we can summarize the conclusions of this dissertation in four categories:

1. Wavelet spectral analysis, Hurst exponent analysis and entropic analysis of spaceborne and ground-based Earth's magnetic field time series, as well as geomagnetic activity indices

The spectral analysis in terms of wavelet transforms revealed intense spectral content around each storm, exhibiting distinctive characteristics typical of these events. Concerning the geomagnetic activity indices SYM-H and Swarm SYM-H, the Hurst exponent, Shannon entropy, nonextensive Tsallis entropy, and Fisher information measures delineated the presence of two distinct patterns:

- a) A pattern associated with strong magnetic storms, characterized by notably high values of the Hurst exponent, indicating higher "organization" within the magnetosphere.
- b) A pattern linked to the quiet periods of the magnetosphere, characterized by lower values of the Hurst exponent, implying reduced "organization" within the magnetosphere.

For AE and Swarm AE indices, the wavelet power spectral analysis exhibited analogous underlying features in the spectra during the three storms, even though these are substorm indices. So, the overarching image of the magnetosphere's pre-conditioned state was still present. Nevertheless, the Hurst exponent and entropic analyses did not result in a clear depiction of two distinct patterns. This outcome could be attributed to the nature of these indices, which are associated with substorms. Substorms, being more transient and dynamic, occur more frequently than

storms and possess different characteristic time scales and generation mechanisms compared to magnetic storms.

Future work suggestions

The results derived from employing information-theoretic methods on the geomagnetic activity indices could offer valuable insights for future investigations conducted by space weather experts and space physics modellers. These insights could prove valuable in enhancing forecasting models and schemes for the coupled solar wind-magnetosphere-ionosphere system. They may contribute to the incorporation of information regarding the system's preconditioning based on the magnetosphere's existing state, as discussed in previous studies [Borovsky, 2021, Lockwood, 2022].

In the future, to establish a complete GIC forecasting scheme comprising several consecutive steps, the initial requirement would be accurate estimations of Dst activity levels. These preliminary assessments would enable predictions for upcoming magnetic storms. Subsequently, employing an advanced model/assimilation technique would allow for the estimation of GIC risk in specific geographic areas. This proactive approach aims to provide valuable insights into the potential impact on infrastructure, offering a predictive tool that could help power supply companies anticipate and mitigate possible damages caused by GICs. This comprehensive forecasting scheme seeks to enhance preparedness and resilience by providing a subtle understanding of the potential risks associated with geomagnetic activity, allowing for strategic planning and protective measures to be implemented effectively.

2. GIC index analysis of ground-based Earth's magnetic field time series

Our investigation of the GIC index levels in the Mediterranean region during the strongest magnetic storms of solar cycle 24 and part of solar cycle 25 showed a good correlation between the SSCs and the increases in the GIC index. Furthermore, the maximum values of the GIC_y and GIC_x indices occur within the first four (4) minutes from the abrupt onset of each respective storm at all the magnetic stations/observatories under study.

Considering the GIC index values calculated during the magnetic storm periods, it seems that despite the enhanced GIC index values, the anticipated adverse impacts attributed to GIC remain at relatively "low" levels for the regions encompassed by these particular magnetic stations / observatories. This result could be an underestimation due to the fact that GIC index thresholds are not calibrated for

the Mediterranean region. Nonetheless, the GIC index offers an initial assessment of the risk level posed by the development of such currents to critical technological infrastructure without taking into account the geoelectric structure of the broader area, i.e., the distribution of electrical conductivity across various depths, which might contribute to the variability in GIC values during a magnetic storm.

Future work suggestions

Enhanced magnetopause currents due to large changes in the solar wind's dynamic pressure may pose threats to low and middle latitude power networks, of at least equal significance to those occurring during the main phase of large magnetic storms. Future work could focus on the impacts of sudden impulse (SI) events on power systems, which depending on latitude, might differ from that observed during large main phase storms.

Calibration of the GIC index risk level thresholds should be performed in the future, so as to get a more appropriate risk level scale not only for middle latitudes, but specifically for the Mediterranean region. Towards this direction, a correlation between major storm events and transformer failures in critical locations over long periods of time could be employed.

Analysis of more cases of intense magnetic storms (including the ones which occurred after August 2022, during solar cycle 25) will shed more light upon the expected GIC in the Mediterranean region, during extreme events. Tozzi et al. [2019a] analyzed - among others - CTS data for a time interval spanning almost two solar cycles and found that during the Halloween 2003 storm, the GIC index reached values within the "moderate" risk level. Unfortunately, no ENIGMA or PEG data were available during that period in order to see the respective GIC index values for Greece.

Another interesting future study could focus not solely on magnitudes, but on summed GIC power, since their effect on transformers is cumulative.

3. Comparisons between GIC index values and electrical conductivity of the Earth's crust

In the contour maps the contour lines are relatively sparse before (March 16, 2015) and after (March 18, 2015) the storm, but on the day of the storm (March 17, 2015) they tend to become more horizontal and graded in intensity (increasing from south to north); this behavior can be associated with the presence of higher "organization" in the Earth's magnetosphere.

Taking into account the values of ground resistance (conductivity) and the GIC index allows us, to some extent, to visualize the impact of GIC on southern Europe. In the contour maps, it is noticeable that the contour lines of the GIC index appear smooth but traverse areas with significantly different ground conductivities. Therefore, this may have varying consequences concerning the development of GIC in critical infrastructure located in these regions. Hence, this specific parameter should be considered in assessing the risk associated with GIC.

Future work suggestions

The derivation of the GIC index contour maps for the Mediterranean region, although based on a simple technique, gave an overall display of the GIC intensity distribution around the Mediterranean region for a magnetic storm. The seemingly smooth contours of the GIC index intersect regions of very different resistivities and GIC risk should be evaluated accordingly. Future work could involve more case studies as well as an evaluation of these preliminary results. Additional magnetic stations / observatories would definitely enhance the accuracy of the estimated GIC index in the contour maps.

4. Comparisons between GIC index values and geoelectric field E

Comparing the estimated E fields and GIC indices in the Mediterranean region (magnetic stations: CLF, CTS, DIO, EBR, SFS, and VLI) over 3 days around the magnetic storm of 17 March 2015 we found that their correlation coefficients range between 0.54 and 0.65.

The significant differences in ground conductivity values of 1D layer ground models across Europe illustrate the potential for local conductances to vary by a factor of over 100 even within the boundaries of countries like Spain or Greece. The calculated electric fields vary locally by at least as much. Moreover, during the peak of the St. Patrick's Day storm, the calculated GIC_x and GIC_y indices for these two countries exhibit local variations by a factor of approximately 1.5 to 2. This underscores the insufficiency of relying on a single observatory for a nationwide index. Consequently, it's recommended that multiple magnetometers per major European country be employed to capture the complex nature of induced E fields.

Future work suggestions

In this dissertation we employed 1D ground conductivity models for a first estimation of the geoelectric field. Employing more sophisticated models (e.g. 3D) would significantly improve the accuracy of the results.

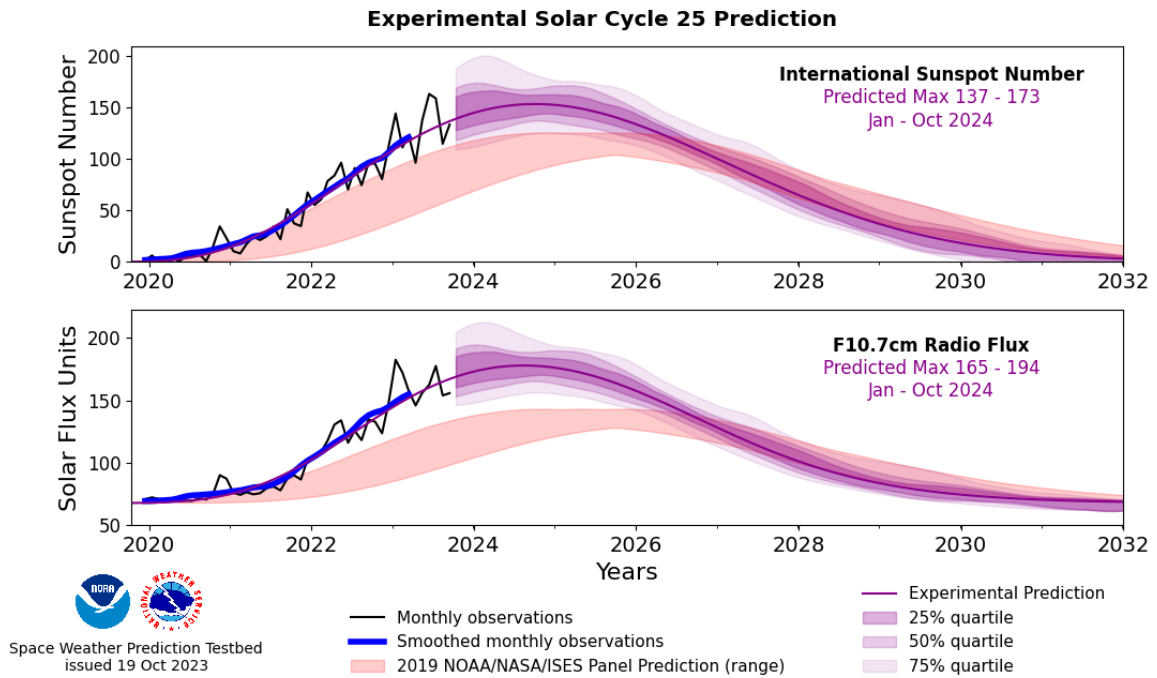


Figure 6.1: NOAA’s SWPC revised prediction for solar activity during Solar Cycle 25. The new Experimental Solar Cycle Prediction concludes that solar activity will increase more quickly and peak at a higher level than previously predicted. Source: <https://www.weather.gov/news/102523-solar-cycle-25-update>

Finally, we consider of utmost importance a future study that will correlate our results with transformer failures, as these might lead to power supply issues, especially in cases of extreme magnetic storms. Data will be provided by the Hellenic Electricity Distribution Network Operator (*Διαχειριστής Ελληνικού Δικτύου Διανομής Ηλεκτρικής Ενέργειας, ΔΕΔΔΗΕ*).

Overall future work suggestion

On 25 October 2023, NOAA’s Space Weather Prediction Center (SWPC) issued a revised solar activity prediction for Solar Cycle 25 that concludes solar activity will increase more quickly than originally predicted and peak somewhere between January and October of 2024, with a maximum sunspot number between 137 and 173 (Figure 6.1).

As of the beginning of 2023, three intense magnetic storms have already occurred (Table 6.1). Therefore, the analysis performed for this thesis could be expanded to encompass solar cycle 25 and focus on the most intense magnetic storms that occurred

Table 6.1: Strongest geospace magnetic storms of solar cycle 25 (so far), based on minimum Dst index values. Storm date and time refer to the hour of minimum Dst occurrence.

Storm Date	Storm Time (UT)	Dst (nT)
24/03/2023	03:00:00	-163
24/04/2023	06:00:00	-212
05/11/2023	20:00:00	-172

within its duration.

To conclude, the awareness around the possibility of the GIC development in low and middle latitudes, especially in Europe, is of great importance, since in our era, when most technological devices depend upon power supply, the economic impact in case of an extreme geospace event could be severe. Moreover, the negative impact on emergency services and the degradation of public safety associated with the loss of electric power will not be negligible. Thus, it is important that operating procedures are scheduled for large space weather events, even at low and middle latitude regions Eastwood et al. [2018].

Appendix D contains a comprehensive list detailing all publications in refereed journals, conference proceedings, and presentations at international conferences made during the duration of this PhD.

BIBLIOGRAPHY

- A. , E. Pr, and V. Wesztergom.
Estimation of the electric resistivity distribution (EURHOM) in the European lithosphere in the frame of the EURISGIC WP2 project.
Acta Geodaetica et Geophysica Hungarica, 47(4):377 – 387, 2012.
doi: 10.1556/ageod.47.2012.4.1.
- S. Agarwal, F. Del Sordo, and J. S. Wettlaufer.
Exoplanetary detection by multifractal spectral analysis.
Astronomical Journal, 153:12, 2016.
doi: 10.3847/1538-3881/153/1/12.
- S. I. Akasofu.
The development of the auroral substorm.
Planetary and Space Science, 12(4):273–282, 1964.
ISSN 0032-0633.
doi: 10.1016/0032-0633(64)90151-5.
- T. Alberti, G. Consolini, and P. De Michelis.
Complexity measures of geomagnetic indices in the last two solar cycles.
Journal of Atmospheric and Solar-Terrestrial Physics, 217:105583, 2021.
doi: 10.1016/j.jastp.2021.105583.
- P. Alken, E. Th, and C.D. et al. Beggan.
Special issue “International Geomagnetic Reference Field: the thirteenth generation”.
Earth Planets Space, 74, 2022.
doi: 10.1186/s40623-021-01569-z.
- J. Allen, H. Sauer, L. Frank, and P. Reiff.
Effects of the March 1989 solar activity.
Eos, Transactions American Geophysical Union, 70(46):1479–1488, 1989.

- E. Astafyeva, M. S. Bagiya, M. Förster, and N. Nishitani.
Unprecedented hemispheric asymmetries during a surprise ionospheric storm: A game of drivers.
Journal of Geophysical Research: Space Physics, 125(3):e2019JA027261, 2020.
doi: 10.1029/2019JA027261.
- R. L. Bailey, T. S. Halbedl, I. Schattauer, A. Römer, G. Achleitner, C. D. Beggan, V. Wetztergom, R. Egli, and R. Leonhardt.
Modelling geomagnetically induced currents in midlatitude Central Europe using a thin-sheet approach.
Annales Geophysicae, 35(3):751–761, 2017.
doi: 10.5194/angeo-35-751-2017.
- D. N. Baker, A. J. Klimas, R. L. McPherron, and J. Büchner.
The evolution from weak to strong geomagnetic activity: An interpretation in terms of deterministic chaos.
Geophysical Research Letters, 17(1):41–44, 1990.
doi: 10.1029/GL017i001p00041.
- D. N. Baker, E. Daly, I. A. Daglis, J. G. Kappenman, and M. Panasyuk.
Effects of space weather on technology infrastructure.
Space Weather, 2(2), 2004.
doi: 10.1029/2003SW000044.
- G. Balasis, I. A. Daglis, P. Kapiris, M. Manda, D. Vassiliadis, and K. Eftaxias.
From pre-storm activity to magnetic storms: a transition described in terms of fractal dynamics.
Annales Geophysicae, 24(12):3557—3567, 2006.
doi: 10.5194/angeo-24-3557-2006.
- G. Balasis, I. A. Daglis, C. Papadimitriou, M. Kalimeri, A. Anastasiadis, and K. Eftaxias.
Dynamical complexity in Dst time series using non-extensive Tsallis entropy.
Geophysical Research Letters, 35(14), 2008.
doi: 10.1029/2008GL034743.
- G. Balasis, I. A. Daglis, C. Papadimitriou, M. Kalimeri, A. Anastasiadis, and K. Eftaxias.
Investigating dynamical complexity in the magnetosphere using various entropy measures.

- Journal of Geophysical Research: Space Physics*, 114(A9):A00D06, 2009.
doi: 10.1029/2008JA014035.
- G. Balasis, I. A. Daglis, A. Anastasiadis, C. Papadimitriou, M. Manda, and K. Eftaxias.
Universality in solar flare, magnetic storm and earthquake dynamics using tsallis statistical mechanics.
Physica A: Statistical Mechanics and its Applications, 390(2):341–346, 2011a.
doi: 10.1016/j.physa.2010.09.029.
- G. Balasis, I. A. Daglis, C. Papadimitriou, A. Anastasiadis, I. Sandberg, and K. Eftaxias.
Quantifying dynamical complexity of magnetic storms and solar flares via nonextensive Tsallis entropy.
Entropy, 13(10):1865–1881, 2011b.
doi: 10.3390/e13101865.
- G. Balasis, I. A. Daglis, C. Papadimitriou, A. Anastasiadis, I. Sandberg, and K. Eftaxias.
Quantifying dynamical complexity of magnetic storms and solar flares via nonextensive tsallis entropy.
Entropy, 13(10):1865–1881, 2011c.
doi: 10.3390/e13101865.
- G. Balasis, R. V. Donner, S. M. Potirakis, J. Runge, C. Papadimitriou, I. A. Daglis, K. Eftaxias, and J. Kurths.
Statistical mechanics and information-theoretic perspectives on complexity in the earth system.
Entropy, 15(11):4844–4888, 2013.
doi: 10.3390/e15114844.
- G. Balasis, S. M. Potirakis, and M. Manda.
Investigating dynamical complexity of geomagnetic jerks using various entropy measures.
Frontiers in Earth Science, 4:71, 2016.
doi: 10.3389/feart.2016.00071.
- G. Balasis, I. A. Daglis, Y. Contoyiannis, S. M. Potirakis, C. Papadimitriou, N. S. Melis, O. Giannakis, A. Papaioannou, A. Anastasiadis, and C. Kontoes.
Observation of intermittency-induced critical dynamics in geomagnetic field time series prior to the intense magnetic storms of March, June, and December 2015.

BIBLIOGRAPHY

- Journal of Geophysical Research: Space Physics*, 123(6):4594—4613, 2018.
doi: 10.1002/2017JA025131.
- G. Balasis, C. Papadimitriou, and A. Z. Boutsis.
Ionospheric response to solar and interplanetary disturbances: a Swarm perspective.
Philosophical Transactions of the Royal Society A: Mathematical, Physical and Engineering Sciences, 377(2148):20180098, 2019.
doi: 10.1098/rsta.2018.0098.
- G. Balasis, C. Papadimitriou, A. Z. Boutsis, I. A. Daglis, O. Giannakis, A. Anastasiadis, P. De Michelis, and G. Consolini.
Dynamical complexity in Swarm electron density time series using Block entropy.
Europhysics Letters, 131(6):69001, nov 2020.
doi: 10.1209/0295-5075/131/69001.
- G. Balasis, M. A. Balikhin, S. C. Chapman, G. Consolini, I. A. Daglis, R. V. Donner, J. Kurths, M. Paluš, J. Runge, B. T. Tsurutani, D. Vassiliadis, S. Wing, J. W. Gjerloev, J. Johnson, M. Materassi, T. Alberti, C. Papadimitriou, P. Manshour, A. Z. Boutsis, and M. Stumpo.
Complex systems methods characterizing nonlinear processes in the near-earth electromagnetic environment: Recent advances and open challenges.
Space Science Reviews, 219, 2023.
doi: 10.1007/s11214-023-00979-7.
- W. H. Barlow.
VI. On the spontaneous electrical currents observed in the wires of the electric telegraph.
Philosophical Transactions of the Royal Society of London, (139):61–72, 1849.
- I. S. Batista, E. R. De Paula, M. A. Abdu, N. B. Trivedi, and M. E. Greenspan.
Ionospheric effects of the March 13, 1989, magnetic storm at low and equatorial latitudes.
Journal of Geophysical Research: Space Physics, 96(A8):13943–13952, 1991.
- A. Bergin, S. C. Chapman, and J. W. Gjerloev.
AE, Dst, and their SuperMAG counterparts: The effect of improved spatial resolution in geomagnetic indices.
Journal of Geophysical Research: Space Physics, 125(5):e2020JA027828, 2020.

doi: 10.1029/2020JA027828.

K. Birkeland.

A possible connection between magnetic and meteorologic phenomena.

Monthly Weather Review, 42(4):211–211, 1914.

Sh. R. Bogoutdinov, A. D. Gvishiani, S. M. Agayan, A. A. Solovyev, and E. Kin.

Recognition of disturbances with specified morphology in time series. Part 1: Spikes on magnetograms of the worldwide INTERMAGNET network.

Izvestiya, Physics of the Solid Earth, 46:1004–1016, 2010.

doi: 10.1134/S1069351310110091.

J. E. Borovsky.

Is our understanding of solar-wind/magnetosphere coupling satisfactory?

Frontiers in Astronomy and Space Sciences, 8, 2021.

doi: 10.3389/fspas.2021.634073.

D. Boteler.

Methodology for simulation of geomagnetically induced currents in power systems.

Journal of Space Weather and Space Climate, 4:A21, 2014.

doi: 10.1051/swsc/2014018.

D. H. Boteler.

A 21st century view of the March 1989 magnetic storm.

Space Weather, 17(10):1427–1441, 2019.

doi: 10.1029/2019SW002278.

D. H. Boteler and R. J. Pirjola.

The complex-image method for calculating the magnetic and electric fields produced at the surface of the Earth by the auroral electrojet.

Geophysical Journal International, 132(1):31–40, 1998.

doi: 10.1046/j.1365-246x.1998.00388.x.

D. H. Boteler and R. J. Pirjola.

Comparison of methods for modelling geomagnetically induced currents.

Annales Geophysicae, 32(9):1177–1187, 2014.

doi: 10.5194/angeo-32-1177-2014.

V. Bothmer and A. Zhukov.

- The Sun as the prime source of space weather*, pages 31–102.
Springer Berlin Heidelberg, Berlin, Heidelberg, 2007.
ISBN 978-3-540-34578-7.
doi: 10.1007/978-3-540-34578-7_3.
- A. Z. Boutsis, G. Balasis, S. Dimitrakoudis, I. A. Daglis, K. Tsinganos, C. Papadimitriou, and O. Giannakis.
Investigation of the geomagnetically induced current index levels in the mediterranean region during the strongest magnetic storms of solar cycle 24.
Space Weather, 21(2):e2022SW003122, 2023.
doi: 10.1029/2022SW003122.
- J. Béland and K. Small.
Space weather effects on power transmission systems: The cases of Hydro-Québec and Transpower New Zealand Ltd.
In I. A. Daglis, editor, *Effects of space weather on technology infrastructure*. NATO Science Series II: Mathematics, Physics and Chemistry, volume 176, pages 287–299, Dordrecht, 2004. Springer Netherlands.
doi: 10.1007/1-4020-2754-0_15.
- L. Cagniard.
Basic theory of the magneto-telluric method of geophysical prospecting.
Geophysics, 18(3):605—635, 1953.
doi: 10.1190/1.1437915.
- Wallace H. Campbell.
Introduction to Geomagnetic Fields.
Cambridge University Press, 2 edition, 2003.
doi: 10.1017/CBO9781139165136.
- B. A. Carter, E. Yizengaw, R. Pradipta, J. M. Weygand, M. Piersanti, A. Pulkkinen, M. B. Moldwin, R. Norman, and K. Zhang.
Geomagnetically induced currents around the world during the 17 March 2015 storm.
Journal of Geophysical Research: Space Physics, 121(10):10,496–10,507, 2016.
doi: 10.1002/2016JA023344.
- S. Chapman.
On the times of sudden commencement of magnetic storms.

Proceedings of the Physical Society of London, 30(1):205, 1917.

C. Cid, A. Guerrero, E. Saiz, A. J. Halford, and A. C. Kellerman.

Developing the LDi and LCi geomagnetic indices, an example of application of the AULs Framework.

Space Weather, 18(1):e2019SW002171, 2020.

doi: 10.1029/2019SW002171.

F. Clette, L. Svalgaard, J. M. Vaquero, and E. W. Cliver.

Revisiting the sunspot number: A 400-year perspective on the solar cycle.

Space Science Reviews, 186:35–103, 2014.

G. Consolini, P. De Michelis, and R. Tozzi.

On the earth's magnetospheric dynamics: Nonequilibrium evolution and the fluctuation theorem.

Journal of Geophysical Research: Space Physics, 113(A8), 2008.

doi: 10.1029/2008JA013074.

G. Consolini, R. Tozzi, P. De Michelis, I. Coco, F. Giannattasio, M. Pezzopane, M. F. Marcucci, and G. Balasis.

High-latitude polar pattern of ionospheric electron density: Scaling features and imf dependence.

Journal of Atmospheric and Solar-Terrestrial Physics, 217:105531, 2021.

doi: 10.1016/j.jastp.2020.105531.

J.J. Curto, T. Araki, and L.F. Alberca.

Evolution of the concept of Sudden Storm Commencements and their operative identification.

Earth, Planets and Space, 59:i–xii, 2007.

doi: 10.1186/BF03352059.

I. A. Daglis.

Space storms and space weather hazards, volume 64.

Springer Science & Business Media, 2001.

I. A. Daglis.

Geospace storm dynamics.

- In I. A. Daglis, editor, *Effects of space weather on technology infrastructure*. NATO Science Series II: Mathematics, Physics and Chemistry, volume 176, pages 27–42, Dordrecht, 2004. Springer Netherlands.
doi: 10.1007/1-4020-2754-0_2.
- I. A. Daglis, R. M. Thorne, W. Baumjohann, and S. Orsini.
The terrestrial ring current: Origin, formation, and decay.
Reviews of Geophysics, 37(4):407–438, 1999.
doi: 10.1029/1999RG900009.
- I. A. Daglis, D. N Baker, Y. Galperin, J. G. Kappenman, and L. J. Lanzerotti.
Technological impacts of space storms: Outstanding issues.
Eos, Transactions American Geophysical Union, 82(48):585, 591–592, 2001.
doi: 10.1029/01EO00340.
- I. A. Daglis, J. U. Kozyra, Y. Kamide, D. Vassiliadis, A. S. Sharma, M. W. Liemohn, W. D. Gonzalez, B. T. Tsurutani, and G. Lu.
Intense space storms: Critical issues and open disputes.
Journal of Geophysical Research: Space Physics, 108(A5), 2003.
doi: 10.1029/2002JA009722.
- T. N. Davis and M. Sugiura.
Auroral electrojet activity index AE and its universal time variations.
Journal of Geophysical Research (1896-1977), 71(3):785–801, 1966.
doi: 10.1029/JZ071i003p00785.
- P. De Michelis, A. Pignalberi, G. Consolini, I. Coco, R. Tozzi, M. Pezzopane, F. Giannattasio, and G. Balasis.
On the 2015 St. Patrick’s storm turbulent state of the ionosphere: Hints from the Swarm mission.
Journal of Geophysical Research: Space Physics, 125(8):e2020JA027934, 2020.
doi: 10.1029/2020JA027934.
- P. De Michelis, G. Consolini, A. Pignalberi, R. Tozzi, I. Coco, F. Giannattasio, M. Pezzopane, and G. Balasis.
Looking for a proxy of the ionospheric turbulence with Swarm data.
Scientific Reports, 11, 2021.
doi: 10.1038/s41598-021-84985-1.

- G. L. Delzanno and J. E. Borovsky.
The need for a system science approach to global magnetospheric models.
Frontiers in Astronomy and Space Sciences, 9, 2022.
doi: 10.3389/fspas.2022.808629.
- S. Dimitrakoudis and I. R. Mann.
On the close correspondence between storm time ULF wave power and the POES VLF chorus wave amplitude proxy.
Geophysical Research Letters, 46(4):1947–1955, 2019.
doi: 10.1029/2018GL081317.
- S. Dimitrakoudis, D. K. Milling, A. Kale, and I. R. Mann.
Sensitivity of ground magnetometer array elements for GIC applications I: Resolving spatial scales with the BEAR and CARISMA arrays.
Space Weather, 20(1):e02919, 2022.
doi: 10.1029/2021SW002919.
- A. P. Dimmock, H. Hietala, and Y. Zou.
Compiling magnetosheath statistical data sets under specific solar wind conditions: Lessons learnt from the dayside kinetic southward IMF GEM challenge.
Earth Space Sci, 7, 2020.
doi: 10.1029/2020EA001095.
- T. Divett, D. H. Mac Manus, G. S. Richardson, C. D. Beggan, C. J. Rodger, M. Ingham, E. Clarke, A. W. P. Thomson, M. Dalzell, and Y. Obana.
Geomagnetically induced current model validation from New Zealand’s South Island.
Space Weather, 18(8):e2020SW002494, 2020.
doi: 10.1029/2020SW002494.
- L. Dobrodnyak, I. Logvinov, E. Nakalov, L. Rakhlin, and S. Timoshin.
Application of magneto-telluric stations (Geomag-02) in geoelectric studies on the territory of Bulgaria.
In *Seminar proceedings*, volume 3, pages 16–20, 2013.
- R. V. Donner, V. Stolbova, G. Balasis, J. F. Donges, M. Georgiou, S. M. Potirakis, and J. Kurths.
Temporal organization of magnetospheric fluctuations unveiled by recurrence patterns in the Dst index.

BIBLIOGRAPHY

- Chaos: An Interdisciplinary Journal of Nonlinear Science*, 28(8):085716, 08 2018.
ISSN 1054-1500.
doi: 10.1063/1.5024792.
- R. V. Donner, G. Balasis, V. Stolbova, M. Georgiou, M. Wiedermann, and J. Kurths.
Recurrence-based quantification of dynamical complexity in the earth's magnetosphere at geospace storm timescales.
Journal of Geophysical Research: Space Physics, 124(1):90–108, 2019.
doi: 10.1029/2018JA025318.
- J. W. Dungey.
Interplanetary magnetic field and the auroral zones.
Physical Review Letters, 6:47–48, 1961.
doi: 10.1103/PhysRevLett.6.47.
- J. P. Eastwood, M. A. Hapgood, E. Biffis, D. Benedetti, M. M. Bisi, L. Green, R. D. Bentley, and C. Burnett.
Quantifying the economic value of space weather forecasting for power grids: An exploratory study.
Space Weather, 16(12):2052–2067, 2018.
doi: 10.1029/2018SW002003.
- J. T. Emmert, A. D. Richmond, and D. P. Drob.
A computationally compact representation of magnetic-apex and quasi-dipole coordinates with smooth base vectors.
Journal of Geophysical Research: Space Physics, 115(A8), 2010.
doi: 10.1029/2010JA015326.
- C. C. Finlay, C. Kloss, N. Olsen, M. D. Hammer, L. Tøffner-Clausen, A. Grayver, and A. Kuvshinov.
The CHAOS-7 geomagnetic field model and observed changes in the South Atlantic Anomaly.
Earth, Planets and Space, 72, 2020.
doi: 10.1186/s40623-020-01252-9.
- R. A. Fisher.
Theory of statistical estimation.
In *Mathematical Proceedings of the Cambridge Philosophical Society*, volume 22, pages 700–725. Cambridge University Press, 1925.

- E. Friis-Christensen, H. Lühr, and G. Hulot.
Swarm: A constellation to study the Earth's magnetic field.
Earth, Planets and Space, 58:351–358, 2006.
doi: 10.1186/BF03351933.
- N. Y. Ganushkina, M. W. Liemohn, S. Dubyagin, I. A. Daglis, I. Dandouras, D. L. De Zeeuw, Y. Ebihara, R. Ilie, R. Katus, M. Kubyshkina, S. E. Milan, S. Ohtani, N. Ostgaard, J. P. Reistad, P. Tenfjord, F. Toffoletto, S. Zaharia, and O. Amariutei.
Defining and resolving current systems in geospace.
Annales Geophysicae, 33(11):1369–1402, 2015.
doi: 10.5194/angeo-33-1369-2015.
- C. T. Gaunt and G. Coetzee.
Transformer failures in regions incorrectly considered to have low GIC-risk.
2007 IEEE Lausanne Power Tech, pages 807–812, 2007.
doi: 10.1109/PCT.2007.4538419.
- J. W. Gjerloev.
A global ground-based magnetometer initiative.
Eos, Transactions American Geophysical Union, 90(27):230–231, 2009.
doi: 10.1029/2009EO270002.
- W. D. Gonzalez, B. T. Tsurutani, and A. L. Clúa de Gonzalez.
Interplanetary origin of geomagnetic storms.
Space Science Reviews, 88:529–562, 1999.
doi: 10.1023/A:1005160129098.
- J. Gosling and V. Pizzo.
Formation and evolution of corotating interaction regions and their three dimensional structure.
Space Science Reviews, 89:21—52, 1999.
doi: 10.1023/A:1005291711900.
- J. T. Gosling, D. J. McComas, J. L. Phillips, and S. J. Bame.
Geomagnetic activity associated with Earth passage of interplanetary shock disturbances and coronal mass ejections.
Journal of Geophysical Research: Space Physics, 96(A5):7831–7839, 1991.
doi: 10.1029/91JA00316.

K. I. Gringauz, V. V. Bezrokhikh, V. D. Ozerov, and R. E. Rybchinskii.

A study of the interplanetary ionized gas, high-energy electrons and corpuscular radiation from the Sun by means of the three-electrode trap for charged particles on the second Soviet cosmic rocket.

In *Soviet Physics Doklady*, volume 5, page 361, 1960.

R. Hajra.

Weakest solar cycle of the space age: A study on solar wind–magnetosphere energy coupling and geomagnetic activity.

Solar Physics, 296:33, 2021.

doi: 10.1007/s11207-021-01774-9.

P. Hejda and J. Bochníček.

Geomagnetically induced pipe-to-soil voltages in the Czech oil pipelines during October–November 2003.

Annales Geophysicae, 23(9):3089–3093, 2005.

doi: 10.5194/angeo-23-3089-2005.

C. Heneghan and G. McDarby.

Establishing the relation between detrended fluctuation analysis and power spectral density analysis for stochastic processes.

Physical Review E, 62:6103—6110, 2000.

R. Hodgson.

On a curious appearance seen in the Sun.

Monthly Notices of the Royal Astronomical Society, 20:15–16, 1859.

T. Iyemori, M. Takeda, M. Nose, Y. Odagi, and H. Toh.

Mid-latitude geomagnetic indices “ASY” and “SYM” for 2009 (Provisional).

Data Analysis Center for Geomagnetism and Space Magnetism, Graduate School of Science, Kyoto University, Japan, 2010.

J. R. Johnson and S. Wing.

A solar cycle dependence of nonlinearity in magnetospheric activity.

Journal of Geophysical Research: Space Physics, 110(A4):A04211, 2005.

doi: 10.1029/2004JA010638.

J. R. Johnson, S. Wing, and E. Camporeale.

- Transfer entropy and cumulant-based cost as measures of nonlinear causal relationships in space plasmas: applications to D_{st} .
Annales Geophysicae, 36(4):945–952, 2018.
doi: 10.5194/angeo-36-945-2018.
- Y. Kamide and A. Chian, editors.
An Overview of the Solar–Terrestrial Environment, pages 1–23.
Springer Berlin Heidelberg, Berlin, Heidelberg, 2007.
doi: 10.1007/978-3-540-46315-3_1.
- J. W. Kantelhardt, S. A. Zschiegner, E. Koscielny-Bunde, S. Havlin, A. Bunde, and H. E. Stanley.
Multifractal detrended fluctuation analysis of nonstationary time series.
Phys. A Stat. Mech. Its Appl., 316:87–114, 2002.
doi: 10.1016/S0378-4371(02)01383-3.
- J. G. Kappenman.
Storm sudden commencement events and the associated geomagnetically induced current risks to ground-based systems at low-latitude and midlatitude locations.
Space Weather, 1(3):1016, 2003.
doi: 10.1029/2003SW000009.
- J. G. Kappenman.
An overview of the impulsive geomagnetic field disturbances and power grid impacts associated with the violent Sun–Earth connection events of 29–31 October 2003 and a comparative evaluation with other contemporary storms.
Space Weather, 3(8):S08C01, 2005.
doi: 10.1029/2004SW000128.
- C. Katsavrias, C. Papadimitriou, A. Hillaris, and G. Balasis.
Application of wavelet methods in the investigation of geospace disturbances: A review and an evaluation of the approach for quantifying wavelet power.
Atmosphere, 13(3), 2022.
doi: 10.3390/atmos13030499.
- A. Kelbert.
The role of global/regional Earth conductivity models in natural geomagnetic hazard mitigation.

BIBLIOGRAPHY

- Surveys in Geophysics*, 41(1):115–166, 2019.
doi: 10.1007/s10712-019-09579-z.
- L. Kepko, R. L. McPherron, O. Amm, S. Apatenkov, W. Baumjohann, J. Birn, M. Lester, R. Nakamura, T. I. Pulkkinen, and V. Sergeev.
Substorm current wedge revisited.
Space Science Reviews, 190:1–46, 2015.
doi: 10.1007/s11214-014-0124-9.
- J. Koen and T. Gaunt.
Geomagnetically induced currents in the Southern African electricity transmission network.
In *2003 IEEE Bologna Power Tech Conference Proceedings*, volume 1, page 7, 2003.
doi: 10.1109/PTC.2003.1304165.
- H. E. J. Koskinen.
Stormy Tour from the Sun to the Earth, pages 1–58.
Springer Berlin Heidelberg, Berlin, Heidelberg, 2011a.
doi: 10.1007/978-3-642-00319-6_1.
- H. E. J. Koskinen.
Storms in the Inner Magnetosphere, pages 371–391.
Springer Berlin Heidelberg, Berlin, Heidelberg, 2011b.
doi: 10.1007/978-3-642-00319-6_14.
- L. J. Lanzerotti.
Space weather effects on technologies.
Washington DC American Geophysical Union Geophysical Monograph Series, 125: 11–22, 2001.
- G. Le, J. A. Slavin, and R. J. Strangeway.
Space Technology 5 observations of the imbalance of regions 1 and 2 field-aligned currents and its implication to the cross-polar cap Pedersen currents.
Journal of Geophysical Research: Space Physics, 115(A7), 2010.
doi: 10.1029/2009JA014979.
- M Lehtinen.
Currents produced in earthed conductor networks by geomagnetically-induced electric fields.

Ann. Geophys., 3(4):479–484, 1985.

C. M. Liu, L. G. Liu, and R. Pirjola.

Geomagnetically induced currents in the high-voltage power grid in China.

IEEE Transactions on Power Delivery, 24(4):2368—2374, 2009.

doi: 10.1109/TPWRD.2009.2028490.

M. Lockwood.

The joined-up magnetosphere.

Frontiers in Astronomy and Space Sciences, 9, 2022.

doi: 10.3389/fspas.2022.856188.

R. E. Lopez.

Magnetospheric substorms.

Johns Hopkins Apl Technical Digest, 11(3-4):264–271, 1990.

J. Luhmann, N. Gopalswamy, L. Jian, and N. Lugaz.

Icme evolution in the inner heliosphere: Invited review.

Solar Physics, 295, 04 2020.

doi: 10.1007/s11207-020-01624-0.

P. Manshour, G. Balasis, G. Consolini, C. Papadimitriou, and M. Paluš.

Causality and information transfer between the solar wind and the magnetosphere–ionosphere system.

Entropy, 23(4), 2021.

doi: 10.3390/e23040390.

R. A. Marshall, C. L. Waters, and M. D. Sciffer.

Spectral analysis of pipe-to-soil potentials with variations of the Earth’s magnetic field in the Australian region.

Space Weather, 8(5):S05002, 2010.

doi: 10.1029/2009SW000553.

R. A. Marshall, E. A. Smith, M. J. Francis, C. L. Waters, and M. D. Sciffer.

A preliminary risk assessment of the Australian region power network to space weather.

Space Weather, 9(10):S10004, 2011.

doi: 10.1029/2011SW000685.

BIBLIOGRAPHY

- R. A. Marshall, M. Dalzell, C. L. Waters, P. Goldthorpe, and E. A. Smith.
Geomagnetically induced currents in the New Zealand power network.
Space Weather, 10(8):S08003, 2012.
doi: 10.1029/2012SW000806.
- M. T. Martin, F. Pennini, and A. Plastino.
Fisher's information and the analysis of complex signals.
Physics Letters A, 256:173–180, 1999.
- E. Matandirotya, P. J. Cilliers, and R. R. Van Zyl.
Modeling geomagnetically induced currents in the South African power transmission network using the finite element method.
Space Weather, 13(3):185—195, 2015.
doi: 10.1002/2014SW001135.
- J. Matzka, C. Stolle, Y. Yamazaki, O. Bronkalla, and A. Morschhauser.
The geomagnetic kp index and derived indices of geomagnetic activity.
Space Weather, 19(5):e2020SW002641, 2021.
doi: 10.1029/2020SW002641.
- P.-N. Mayaud.
A hundred year series of geomagnetic data 1868-1967.
AGA Bulletin, 33:1868–1967, 1973.
- R. L. McPherron.
Magnetospheric substorms.
Reviews of Geophysics, 17(4):657–681, 1979.
doi: 10.1029/RG017i004p00657.
- K. Mursula and B. Zieger.
The 13.5-day periodicity in the sun, solar wind, and geomagnetic activity: The last three solar cycles.
Journal of Geophysical Research: Space Physics, 101(A12):27077–27090, 1996.
- C. M. Ngwira and A. A. Pulkkinen.
An Introduction to Geomagnetically Induced Currents, chapter 1, pages 1–13.
American Geophysical Union (AGU), 2019.
ISBN 9781119434412.
doi: 10.1002/9781119434412.ch1.

- C. M. Ngwira, A. Pulkkinen, L. A. McKinnell, and P. J. Cilliers.
Improved modeling of geomagnetically induced currents in the South African power network.
Space Weather, 6(11):S11004, 2008.
doi: 10.1029/2008SW000408.
- A. G. Ortega, C. C. Tortuero, and E. S. Villanueva.
Local Geomagnetic index (LDi) for Spain from 1997-2017.
e-cienciaDatos, V1, 2019.
doi: 10.21950/HNTNCW.
- A. Osmane, M. Savola, E. Kilpua, H. Koskinen, J. E. Borovsky, and M. Kalliokoski.
Quantifying the non-linear dependence of energetic electron fluxes in the Earth's radiation belts with radial diffusion drivers.
Annales Geophysicae, 40(1):37–53, 2022.
doi: 10.5194/angeo-40-37-2022.
- C. Papadimitriou, G. Balasis, A. Z. Boutsis, I. A. Daglis, O. Giannakis, A. Anastasiadis, P. De Michelis, and G. Consolini.
Dynamical complexity of the 2015 St. Patrick's day magnetic storm at Swarm altitudes using entropy measures.
Entropy, 22(5), 2020.
doi: 10.3390/e22050574.
- C. Papadimitriou, G. Balasis, A. Z. Boutsis, A. Antonopoulou, G. Moutsiana, I. A. Daglis, O. Giannakis, P. de Michelis, G. Consolini, J. Gjerloev, and L. Trenchi.
Swarm-derived indices of geomagnetic activity.
Journal of Geophysical Research: Space Physics, 126(11):e2021JA029394, 2021.
doi: 10.1029/2021JA029394.
- E. N. Parker.
Dynamics of the interplanetary gas and magnetic fields.
Astrophysical Journal, page 664, 1958.
doi: 10.1086/146579.
- R. Pirjola.
Electromagnetic induction in the Earth by a plane wave or by fields of line current harmonic in time and space.

BIBLIOGRAPHY

- Geophysica*, 18:1–161, 1982.
- R. Pirjola.
Geomagnetically induced currents during magnetic storms.
IEEE Transactions on Plasma Science, 28(6):1867–1873, 2000.
doi: 10.1109/27.902215.
- R. Pirjola.
Practical model applicable to investigating the coast effect on the geoelectric field in connection with studies of geomagnetically induced currents.
Advances in Applied Physics, 1(1):9–28, 2013.
- R. Pirjola, A. Pulkkinen, and A. Viljanen.
Studies of space weather effects on the Finnish natural gas pipeline and on the Finnish high-voltage power system.
Advances in Space Research, 31(4):795–805, 2003.
doi: 10.1016/S0273-1177(02)00781-0.
- V. Pitsis, G. Balasis, I. A. Daglis, D. Vassiliadis, and A. Z. Boutsis.
Power-law dependence of the wavelet spectrum of ground magnetic variations during magnetic storms.
Advances in Space Research, 71(5):2288–2298, 2023.
doi: 10.1016/j.asr.2022.10.064.
- B. Poduval, K. M. Pitman, O. Verkhoglyadova, and P. Wintoft.
Editorial: Applications of statistical methods and machine learning in the space sciences.
Frontiers in Astronomy and Space Sciences, 10, 2023.
doi: 10.3389/fspas.2023.1163530.
- A. Pulkkinen, E. Bernabeu, J. Eichner, A. Viljanen, and C. Ngwira.
Regional-scale high-latitude extreme geoelectric fields pertaining to geomagnetically induced currents.
Earth, Planets and Space, 67(1):93, 2015.
doi: 10.1186/s40623-015-0255-6.
- A. Pulkkinen, E. Bernabeu, A. Thomson, A. Viljanen, R. Pirjola, D. Boteler, J. Eichner, P. J. Cilliers, D. Welling, N. P. Savani, R. S. Weigel, J. J. Love, C. Balch, C. M. Ng-

- wira, G. Crowley, A. Schultz, R. Kataoka, B. Anderson, D. Fugate, J. J. Simpson, and M. MacAlester.
Geomagnetically induced currents: Science, engineering, and applications readiness. *Space Weather*, 15(7):828—856, 2017.
doi: 10.1002/2016SW001501.
- J. Reda and M. Neska.
The one second data collection system in polish geomagnetic observatories. *Journal of Indian Geophysical Union*, 2:62–66, 2016.
- I. G. Richardson, E. W. Cliver, and H. V. Cane.
Sources of geomagnetic storms for solar minimum and maximum conditions during 1972–2000. *Geophysical Research Letters*, 28(13):2569–2572, 2001.
doi: 10.1029/2001GL013052.
- C. J. Rodger, D. H. Mac Manus, M. Dalzell, A. W. P. Thomson, E. Clarke, T. Petersen, M. A. Clilverd, and T. Divett.
Longterm geomagnetically induced current observations from New Zealand: Peak current estimates for extreme geomagnetic storms. *Space Weather*, 15(11):1447—1460, 2017.
doi: 10.1002/2017SW001691.
- J. Runge, G. Balasis, I. A. Daglis, C. Papadimitriou, and R. V. Donner.
Common solar wind drivers behind magnetic storm–magnetospheric substorm dependency. *Scientific Reports*, 8, 2018.
doi: 10.1038/s41598-018-35250-5.
- E. Sabine.
V. on periodical laws discoverable in the mean effects of the larger magnetic disturbances. *Philos Trans R Soc London*, 141:123–139, 1851.
doi: 10.1098/rstl.1851.0007.
- E. Sabine.
VIII. On periodical laws discoverable in the mean effects of the larger magnetic disturbance.—No. II.

BIBLIOGRAPHY

- Philos Trans R Soc London*, 142:103–124, 1852.
doi: 10.1098/rstl.1852.0009.
- A. Segarra and J. J. Curto.
Automatic detection of sudden commencements using neural networks.
Earth, Planets and Space, 65:791–797, 2013.
doi: 10.5047/eps.2012.12.011.
- C. E. Shannon.
A mathematical theory of communication.
Bell System Technical Journal, 27:379–423, 1948.
- A. S. Sharma, D. Vassiliadis, and K. Papadopoulos.
Reconstruction of low-dimensional magnetospheric dynamics by singular spectrum analysis.
Geophysical Research Letters, 20(5):335–338, 1993.
doi: 10.1029/93GL00242.
- M. I. Sitnov, A. S. Sharma, K. Papadopoulos, and D. Vassiliadis.
Modeling substorm dynamics of the magnetosphere: From self-organization and self-organized criticality to nonequilibrium phase transitions.
Physical Review E, 65:016116, 2001.
doi: 10.1103/PhysRevE.65.016116.
- A. W. Smith, M. P. Freeman, I. J. Rae, and C. Forsyth.
The influence of Sudden Commencements on the rate of change of the surface horizontal magnetic field in the United Kingdom.
Space Weather, 17(11):1605–1617, 2019.
doi: 10.1029/2019SW002281.
- B. Stewart.
XXII. On the great magnetic disturbance which extended from August 28 to September 7, 1859, as recorded by photography at the Kew Observatory.
Philosophical Transactions of the Royal Society of London, (151):423–430, 1861.
- M. Stumpo, G. Consolini, T. Alberti, and V. Quattrocioni.
Measuring information coupling between the solar wind and the magnetosphere–ionosphere system.
Entropy, 22(3), 2020.

doi: 10.3390/e22030276.

M. Sugiura and T. Kamei.

Description of the hourly Dst index.

IAGA Bulletin N°40, 1981.

M. Sugiura and T. Kamei.

Equatorial Dst Index 1957-1986.

IAGA Bulletin N°40, 1991.

URL <http://wdc.kugi.kyoto-u.ac.jp/dstdir/dst2/onDstindex.html>.

M. Sugiura and D. J. Poros.

Hourly values of equatorial Dst for the years 1957 to 1970.

NASA, Goddard Space Flight Center, Greenbelt, Md., 1971.

D. Telloni.

Statistical methods applied to space weather science.

Frontiers in Astronomy and Space Sciences, 9, 2022.

doi: 10.3389/fspas.2022.865880.

E. Thébault, C. C. Finlay, and C. D. et al. Beggan.

International Geomagnetic Reference Field: the 12th generation.

Earth Planet Sp, 67, 2015.

doi: 10.1186/s40623-015-0228-9.

C. Torrence and G. P. Compo.

A practical guide to wavelet analysis.

Bulletin of the American Meteorological Society, 79(1):61 – 78, 1998.

doi: 10.1175/1520-0477(1998)079<0061:APGTWA>2.0.CO;2.

J. M. Torta, L. Serrano, J. R. Regué, A. M. Sánchez, and E. Roldán.

Geomagnetically induced currents in a power grid of northeastern Spain.

Space Weather, 10(6), 2012.

doi: 10.1029/2012SW000793.

J. M. Torta, S. Marsal, and M. Quintana.

Assessing the hazard from geomagnetically induced currents to the Spanish entire high-voltage power network in Spain.

Earth, Planets and Space, 66:87, 2014.

doi: 10.1186/1880-5981-66-87.

BIBLIOGRAPHY

- J. M. Torta, A. Marcuello, J. Campanyà, S. Marsal, P. Queralt, and J. Ledo.
Improving the modeling of geomagnetically induced currents in Spain.
Space Weather, 15(5):691—703, 2017.
doi: 10.1002/2017SW001628.
- R. Tozzi, P. De Michelis, I. Coco, and F. Giannattasio.
A preliminary risk assessment of geomagnetically induced currents over the Italian territory.
Space Weather, 17(1):46–58, 2019a.
doi: 10.1029/2018SW002065.
- R. Tozzi, I. Coco, P. De Michelis, and F. Giannattasio.
Latitudinal dependence of geomagnetically induced currents during geomagnetic storms.
Annals of Geophysics, 62(4):448, 2019b.
doi: 10.4401/ag-7788.
- C. Tsallis.
Introduction to Nonextensive Statistical Mechanics: Approaching a Complex World.
Springer, New York, 2009.
ISBN 978-0-387-85358-1, 978-0-387-85359-8.
doi: 10.1007/978-0-387-85359-8.
- Kanaris Tsinganos.
ΑΣΤΡΟΦΥΣΙΚΗ ΠΛΑΣΜΑΤΟΣ.
ΣΤΑΜΟΥΛΗΣ, 2017.
ISBN 978-960-91748-3-1.
- Kanaris Tsinganos.
ΕΝΑ ΓΑΛΑΖΙΟ ΠΕΤΡΑΔΙ ΣΤΟ ΔΙΑΣΤΗΜΑ.
ΖΗΤΗ, 2020.
ISBN 10.1017/CBO9781139165136.
- B. T. Tsurutani.
Solar/interplanetary plasma phenomena causing geomagnetic activity at Earth.
In *Proc. Inter. Sch. Phys. “Enrico Fermi” Course CXLII*, edited by: Coppi, B., Ferrari, A., and Sin-doni, E., Amsterdam, 2000. IOS Press.

- B. T. Tsurutani, M. Sugiura, T. Iyemori, B. E. Goldstein, W. D. Gonzalez, S. I. Akasofu, and E. J. Smith.
The nonlinear response of AE to the IMF BS driver: A spectral break at 5 hours.
Geophysical Research Letters, 17(3):279–282, 1990.
doi: 10.1029/GL017i003p00279.
- B. T. Tsurutani, W. D. Gonzalez, A. L. C. Gonzalez, F. Tang, J. K. Arballo, and M. Okada.
Interplanetary origin of geomagnetic activity in the declining phase of the solar cycle.
Journal of Geophysical Research: Space Physics, 100(A11):21717–21733, 1995.
doi: 10.1029/95JA01476.
- B. T. Tsurutani, W. D. Gonzalez, G. S. Lakhina, and S. Alex.
The extreme magnetic storm of 1–2 September 1859.
Journal of Geophysical Research: Space Physics, 108(A7), 2003.
doi: 10.1029/2002JA009504.
- C. A. Varotsos, G. S. Golitsyn, Y. Xue, M. Efstathiou, N. Sarlis, and T. Voronova.
On the relation between rain, clouds, and cosmic rays.
Remote Sensing Letters, 14:301–312, 2023.
doi: 10.1080/2150704X.2023.2190468.
- D. V. Vassiliadis, A. S. Sharma, T. E. Eastman, and K. Papadopoulos.
Low-dimensional chaos in magnetospheric activity from AE time series.
Geophysical Research Letters, 17(11):1841–1844, 1990.
doi: 10.1029/GL017i011p01841.
- O. Verkhoglyadova, X. Meng, and J. Kosberg.
Understanding large-scale structure in global ionospheric maps with visual and statistical analyses.
Frontiers in Astronomy and Space Sciences, 9, 2022.
doi: 10.3389/fspas.2022.852222.
- D. Verscharen, K. G. Klein, and B. A. Maruca.
The multi-scale nature of the solar wind.
Living Reviews in Solar Physics, 16:1614–4961, 2019.
doi: 10.1007/s41116-019-0021-0.
- A. Viljanen and R. Pirjola.
Geomagnetically induced currents in the Finnish high-voltage power system.

BIBLIOGRAPHY

- Surveys in Geophysics*, 15:383—408, 1994.
doi: 10.1007/BF00665999.
- A. Viljanen, R. Pirjola, Wik M., A. Ádám, E. Prácsr, Y. Sakharov, and J. Katkalov.
Continental scale modelling of geomagnetically induced currents.
Journal of Space Weather and Space Climate, 2:A17, 2012.
doi: 10.1051/swsc/2012017.
- A. Viljanen, R. Pirjola, E. Prácsr, S. Ahmadzai, and V. Singh.
Geomagnetically induced currents in Europe: Characteristics based on a local power grid model.
Space Weather, 11(10):575–584, 2013.
doi: 10.1002/swe.20098.
- A. Viljanen, R. Pirjola, E. Prácsr, J. Katkalov, and M. Wik.
Geomagnetically induced currents in Europe.
Journal of Space Weather and Space Climate, 4:A09, 2014.
doi: 10.1051/swsc/2014006.
- S. Watari.
Estimation of geomagnetically induced currents based on the measurement data of a transformer in a Japanese power network and geoelectric field observations.
Earth, Planets and Space, 67:77, 2015.
doi: 10.1186/s40623-015-0253-8.
- S. Watari.
Geomagnetic storms of cycle 24 and their solar sources.
Earth, Planets and Space, 69:70, 2017.
doi: 10.1186/s40623-017-0653-z.
- S. Watari, M. Kunitake, K. Kitamura, T. Hori, T. Kikuchi, K. Shiokawa, N. Nishitani, R. Kataoka, Y. Kamide, T. Aso, Y. Watanabe, and Y. Tsuneta.
Measurements of geomagnetically induced current in a power grid in Hokkaido, Japan.
Space Weather, 7(3):S03002, 2009.
doi: 10.1029/2008SW000417.
- M. Wik, A. Viljanen, R. Pirjola, A. Pulkkinen, P. Wintoft, and H. Lundstedt.
Calculation of geomagnetically induced currents in the 400 kV power grid in southern Sweden.

Space Weather, 6(7), 2008.

S. Wing, J. R. Johnson, E. Camporeale, and G. D. Reeves.

Information theoretical approach to discovering solar wind drivers of the outer radiation belt.

Journal of Geophysical Research: Space Physics, 121(10):9378–9399, 2016.

doi: 10.1002/2016JA022711.

S. Wing, J. R. Johnson, D. L. Turner, A. Y. Ukhorskiy, and A. J. Boyd.

Untangling the solar wind and magnetospheric drivers of the radiation belt electrons.

Journal of Geophysical Research: Space Physics, 127(4):e2021JA030246, 2022.

doi: 10.1029/2021JA030246.

Y. Yamazaki and M. J. Kosch.

Geomagnetic lunar and solar daily variations during the last 100 years.

Journal of Geophysical Research: Space Physics, 119(8):6732–6744, 2014.

doi: 10.1002/2014JA020203.

J. J. Zhang, C. Wang, T. R. Sun, C. M. Liu, and K. R. Wang.

GIC due to storm sudden commencement in low-latitude high-voltage power network in China: Observation and simulation.

Space Weather, 13(10):643–655, 2015.

doi: 10.1002/2015SW001263.

I. P. Zois.

Solar activity and transformer failures in the Greek national electric grid.

Journal of Space Weather and Space Climate, 3:A32, 2013.

doi: 10.1051/swsc/2013055.

T. H. Zurbuchen and I. G. Richardson.

In-situ solar wind and magnetic field signatures of interplanetary coronal mass ejections.

Space Science Reviews, 123:31–43, 2006.

doi: 10.1007/s11214-006-9010-4.

GIC index figures: Results from all stations / observatories

In Chapter 4 we calculated GIC index for four intense magnetic storms of solar cycle 24 (i.e., 17 March 2015, 23 June 2015, 20 December 2015 and 26 August 2018). In Figures 4.2-4.5 we presented indicative results from three stations / observatories per storm, in order to be able to display the GIC index values in an appropriate way for the reader. Here, we provide the complete set of figures from all available stations / observatories per storm. In particular, we provide figures for the following:

1. Storm of 17 March 2015
 - Figure A.1: CLF, CTS and EBR
 - Figure A.2: IZN, DIO and VLI
 - Figure A.3: SFS and TAM
2. Storm of 23 June 2015
 - Figure A.4: CLF, CTS and EBR
 - Figure A.5: IZN, THL and DIO
 - Figure A.6: SFS and TAM
3. Storm of 20 December 2015
 - Figure A.7: CLF, CTS and EBR
 - Figure A.8: IZN, DIO, SFS and TAM
4. Storm of 26 August 2018
 - Figure A.9: CLF, CTS and EBR

APPENDIX A

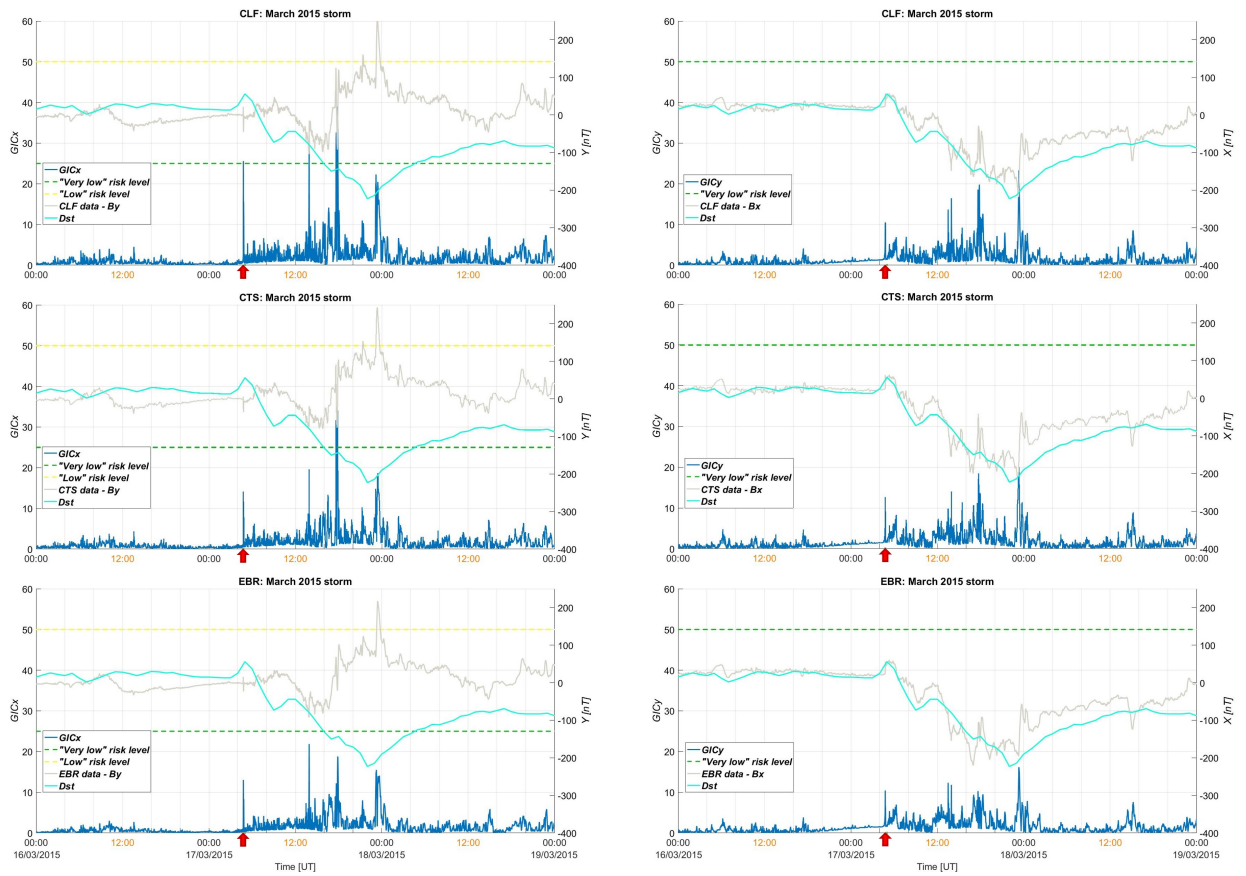


Figure A.1: Storm of 17 March 2015: (From top to bottom: CLF, CTS and EBR). In each panel are shown the Dst index (in cyan), the geomagnetic field's X (left column) or Y component (right column) (in grey, right y-axis) and the GICy (left column) or GICx index (right column) (in blue, left y-axis). Green and yellow dashed lines represent the risk levels, associated with the GIC index values, according to Marshall et al. (2011).

- Figure A.10: IZN, PEG and SFS
- Figure A.11: FIN and TAM

GIC INDEX FIGURES: RESULTS FROM ALL STATIONS / OBSERVATORIES

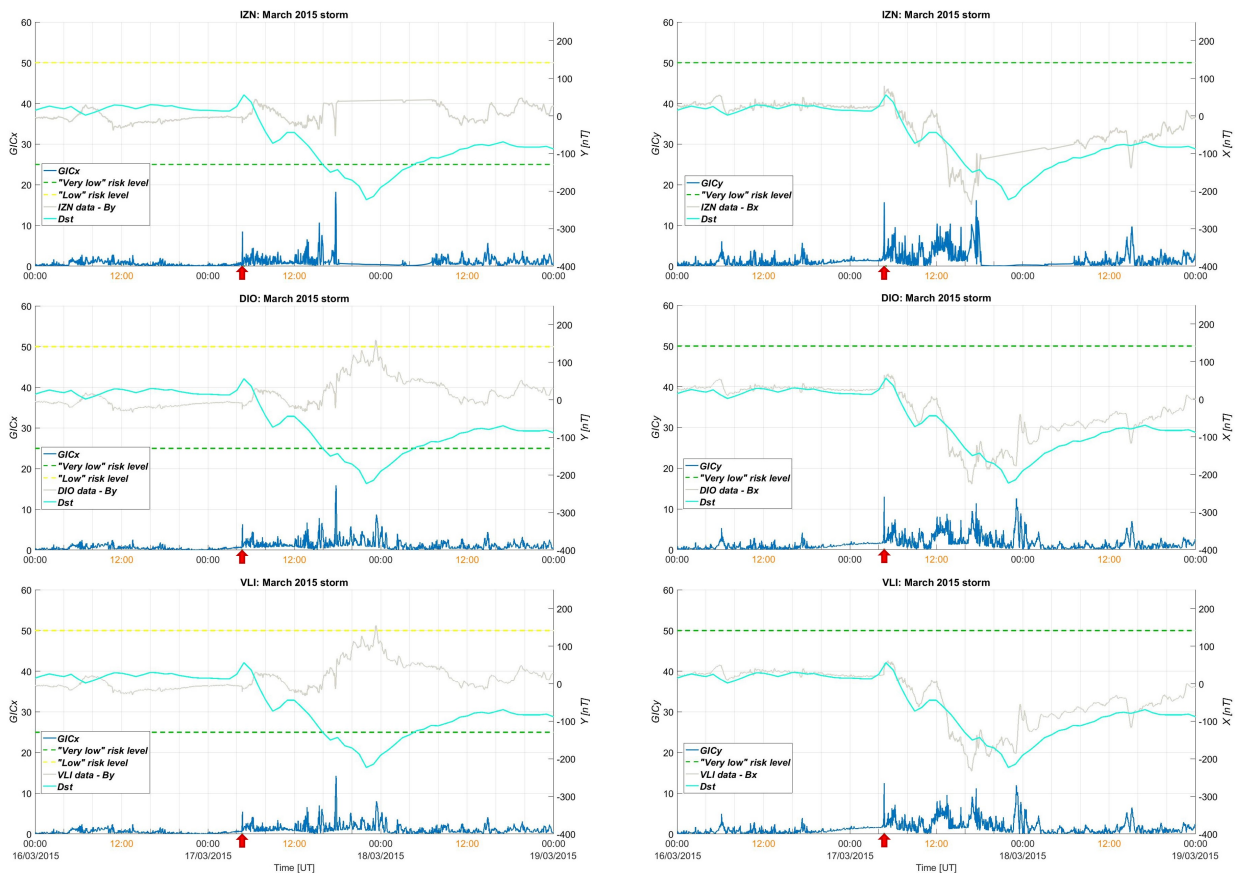


Figure A.2: Storm of 17 March 2015: (From top to bottom: IZN, DIO and VLI). In each panel are shown the Dst index (in cyan), the geomagnetic field's X (left column) or Y component (right column) (in grey, right y-axis) and the GICy (left column) or GICx index (right column) (in blue, left y-axis). Green and yellow dashed lines represent the risk levels, associated with the GIC index values, according to Marshall et al. (2011).

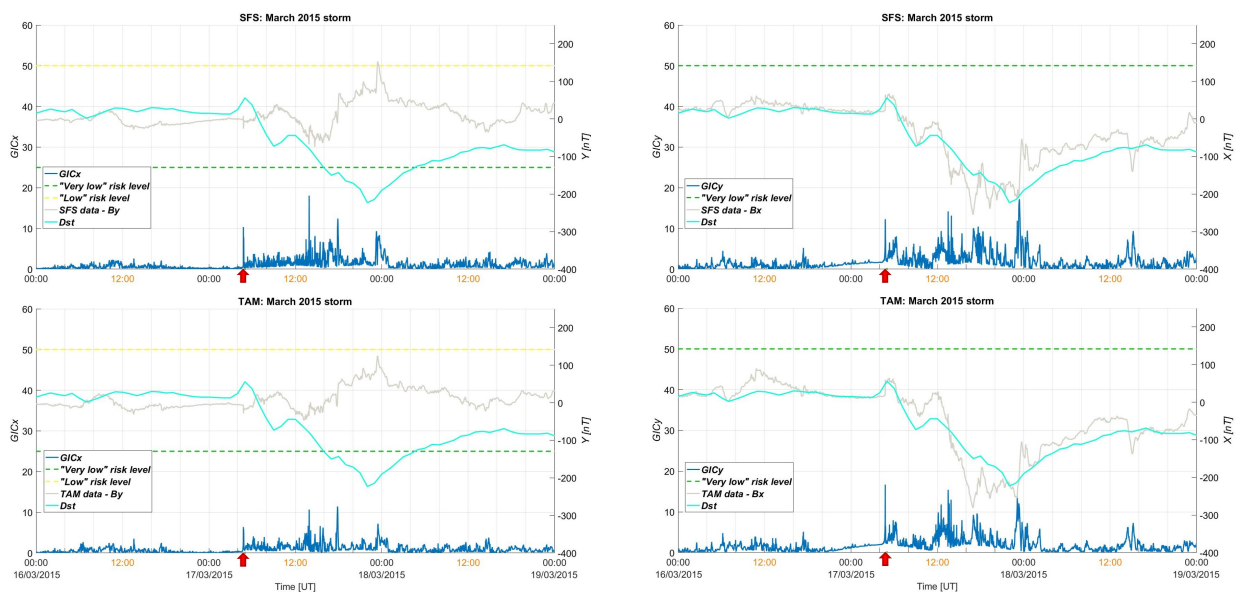


Figure A.3: Storm of 17 March 2015: (From top to bottom: SFS and TAM). In each panel are shown the Dst index (in cyan), the geomagnetic field's X (left column) or Y component (right column) (in grey, right y-axis) and the GICy (left column) or GICx index (right column) (in blue, left y-axis). Green and yellow dashed lines represent the risk levels, associated with the GIC index values, according to Marshall et al. (2011).

GIC INDEX FIGURES: RESULTS FROM ALL STATIONS / OBSERVATORIES

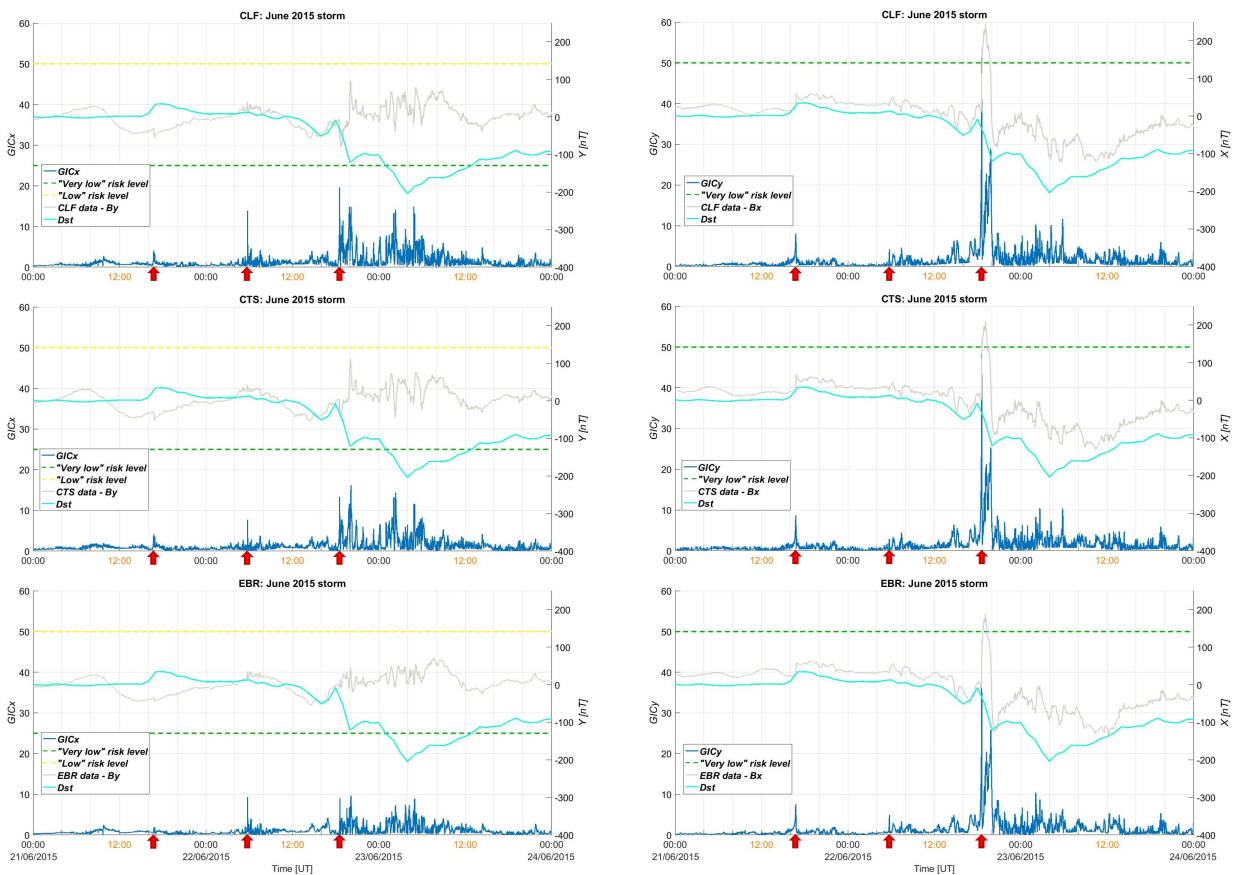


Figure A.4: Storm of 23 June 2015: (From top to bottom: CLF, CTS and EBR). In each panel are shown the Dst index (in cyan), the geomagnetic field's X (left column) or Y component (right column) (in grey, right y-axis) and the GICy (left column) or GICx index (right column) (in blue, left y-axis). Green and yellow dashed lines represent the risk levels, associated with the GIC index values, according to Marshall et al. (2011).

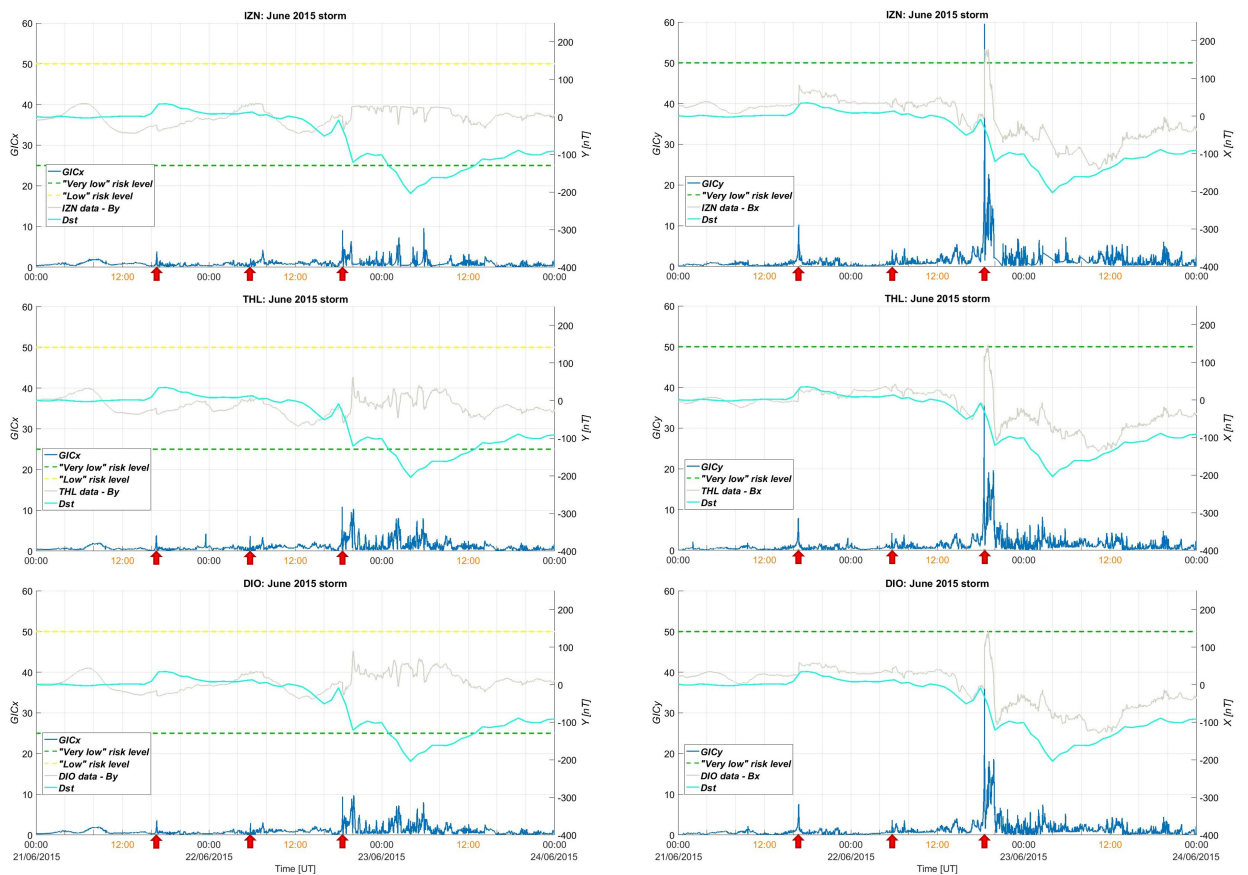


Figure A.5: Storm of 23 June 2015: (From top to bottom: IZN, THL and DIO). In each panel are shown the Dst index (in cyan), the geomagnetic field's X (left column) or Y component (right column) (in grey, right y-axis) and the GICy (left column) or GICx index (right column) (in blue, left y-axis). Green and yellow dashed lines represent the risk levels, associated with the GIC index values, according to Marshall et al. (2011).

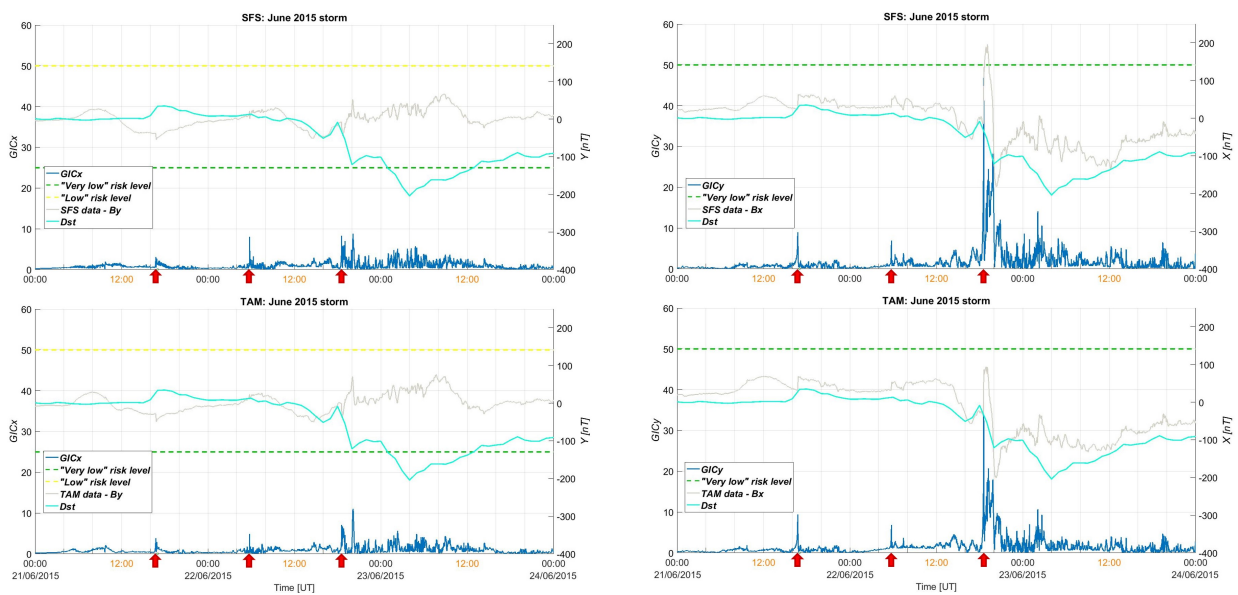


Figure A.6: Storm of 23 June 2015: (From top to bottom: SFS and TAM). In each panel are shown the Dst index (in cyan), the geomagnetic field's X (left column) or Y component (right column) (in grey, right y-axis) and the GICy (left column) or GICx index (right column) (in blue, left y-axis). Green and yellow dashed lines represent the risk levels, associated with the GIC index values, according to Marshall et al. (2011).

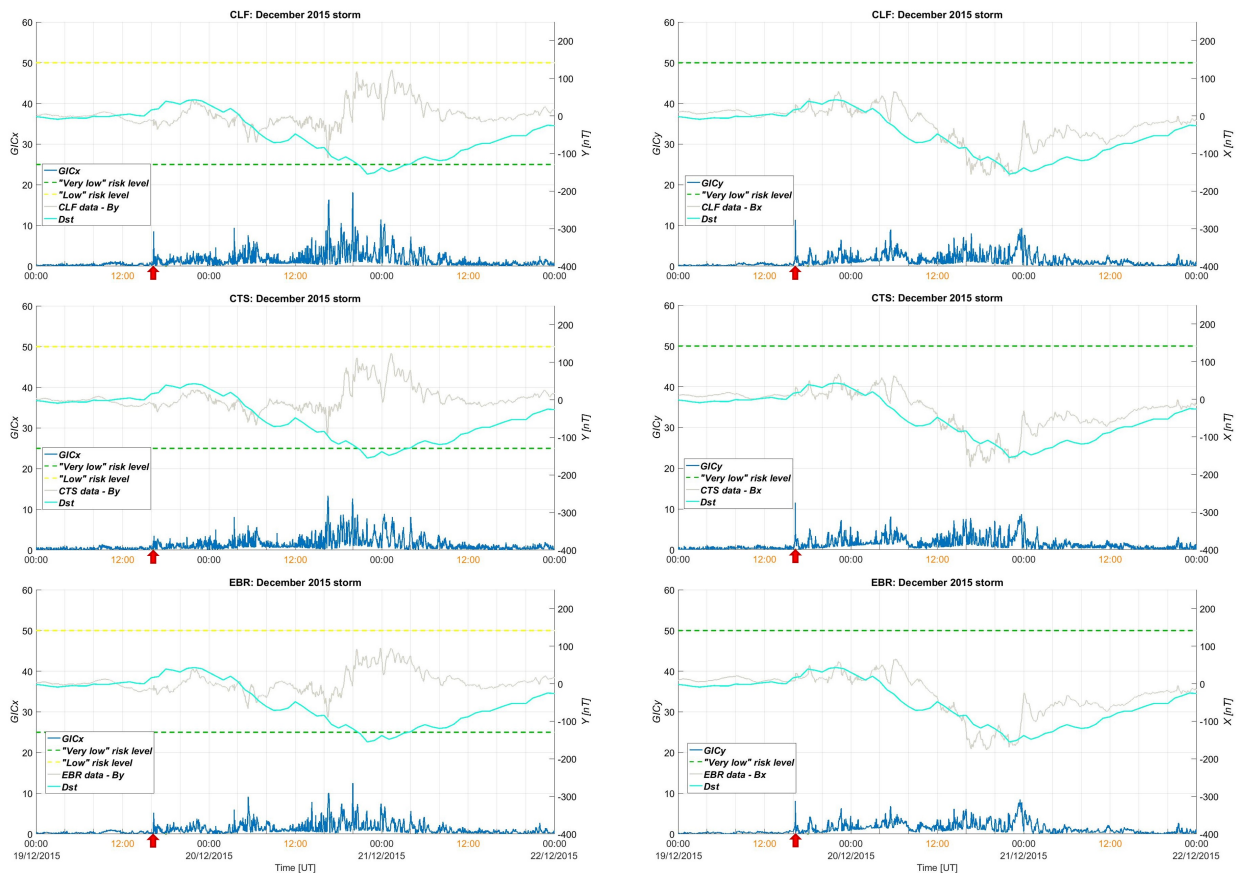


Figure A.7: Storm of 20 December 2015: (From top to bottom: CLF, CTS and EBR). In each panel are shown the Dst index (in cyan), the geomagnetic field's X (left column) or Y component (right column) (in grey, right y-axis) and the GICy (left column) or GICx index (right column) (in blue, left y-axis). Green and yellow dashed lines represent the risk levels, associated with the GIC index values, according to Marshall et al. (2011).

GIC INDEX FIGURES: RESULTS FROM ALL STATIONS / OBSERVATORIES

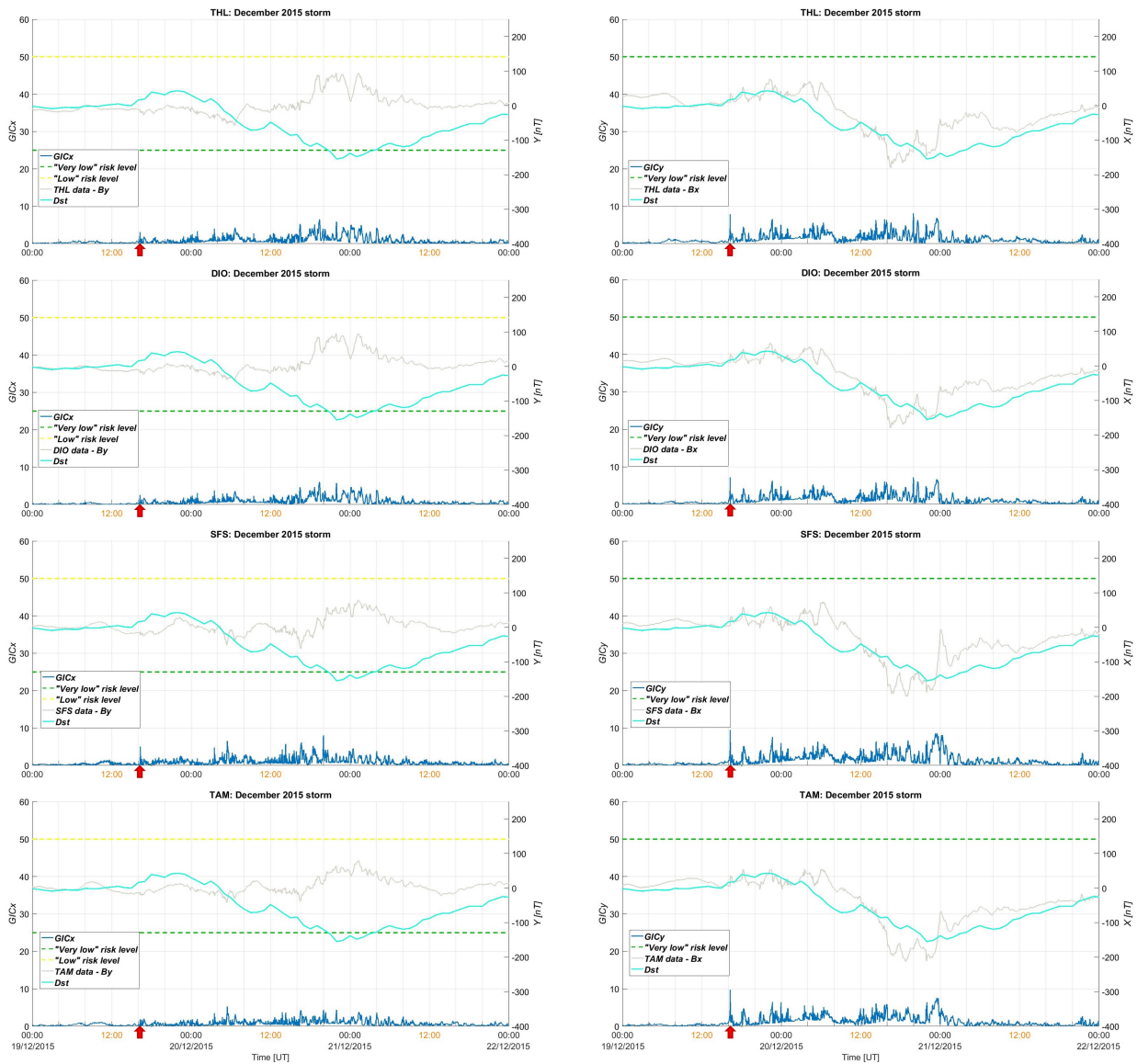


Figure A.8: Storm of 20 December 2015: (From top to bottom: THL, DIO, SFS and TAM). In each panel are shown the Dst index (in cyan), the geomagnetic field's X (left column) or Y component (right column) (in grey, right y-axis) and the GICy (left column) or GICx index (right column) (in blue, left y-axis). Green and yellow dashed lines represent the risk levels, associated with the GIC index values, according to Marshall et al. (2011).

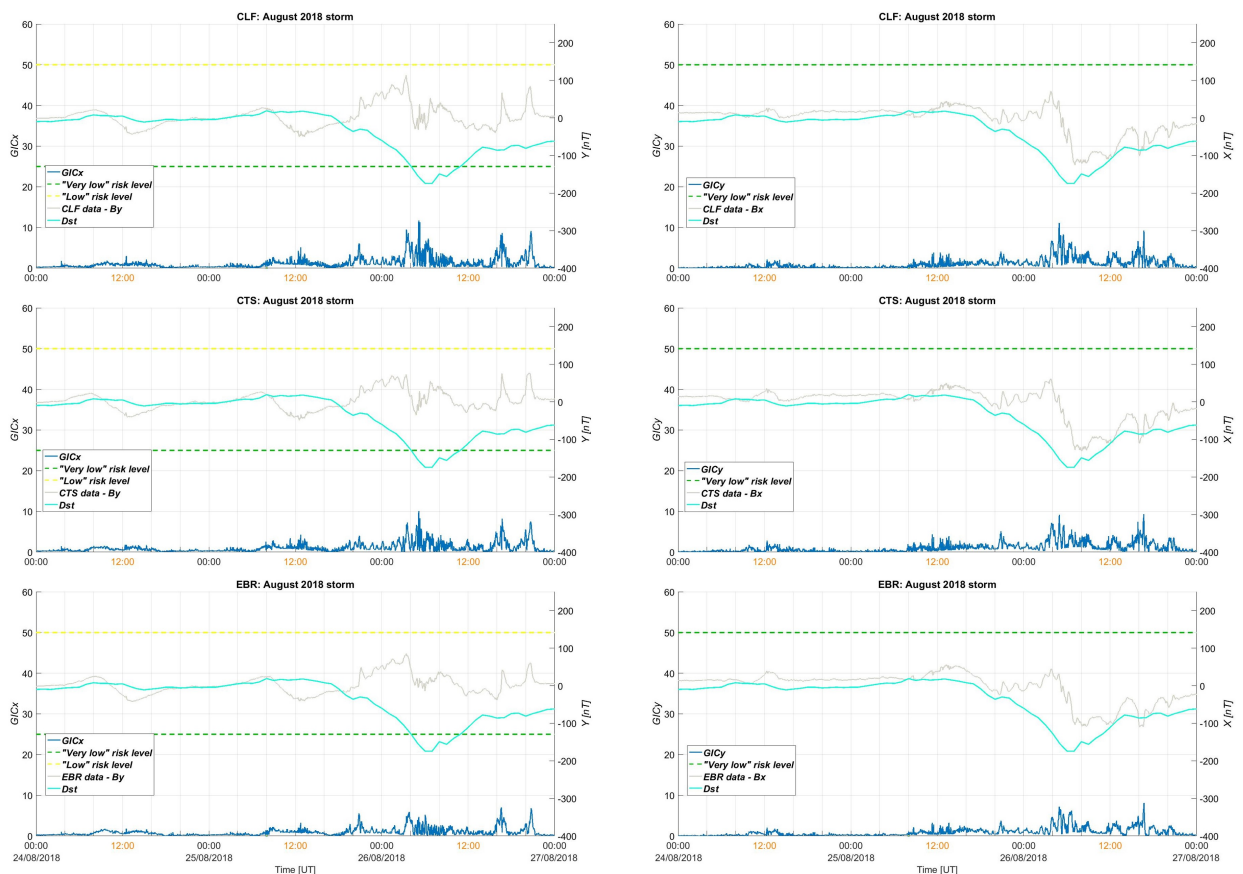


Figure A.9: Storm of 26 August 2018: (From top to bottom: CLF, CTS and EBR). In each panel are shown the Dst index (in cyan), the geomagnetic field's X (left column) or Y component (right column) (in grey, right y-axis) and the GICy (left column) or GICx index (right column) (in blue, left y-axis). Green and yellow dashed lines represent the risk levels, associated with the GIC index values, according to Marshall et al. (2011).

GIC INDEX FIGURES: RESULTS FROM ALL STATIONS / OBSERVATORIES



Figure A.10: Storm of 26 August 2018: (From top to bottom: IZN, PEG and SFS). In each panel are shown the Dst index (in cyan), the geomagnetic field's X (left column) or Y component (right column) (in grey, right y-axis) and the GICy (left column) or GICx index (right column) (in blue, left y-axis). Green and yellow dashed lines represent the risk levels, associated with the GIC index values, according to Marshall et al. (2011).

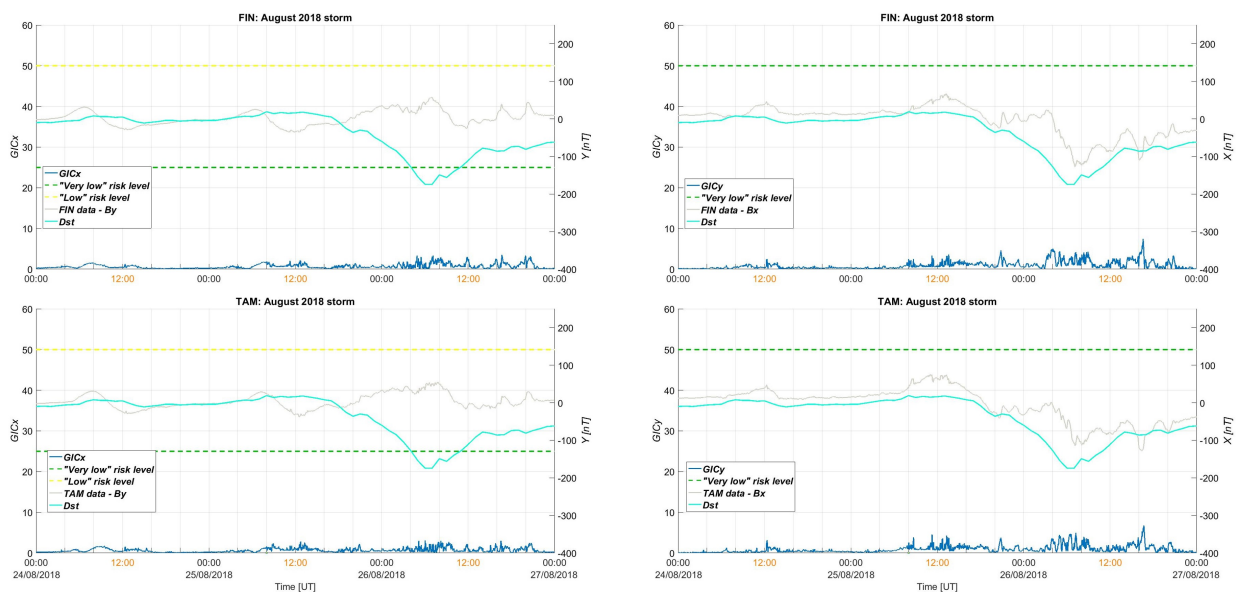


Figure A.11: Storm of 26 August 2018: (From top to bottom: FIN and TAM). In each panel are shown the Dst index (in cyan), the geomagnetic field's X (left column) or Y component (right column) (in grey, right y-axis) and the GICy (left column) or GICx index (right column) (in blue, left y-axis). Green and yellow dashed lines represent the risk levels, associated with the GIC index values, according to Marshall et al. (2011).

International Geomagnetic Reference Field (IGRF): the 13th generation

In section 4.1 we provided estimations of the altitude-adjusted corrected geomagnetic (AACGM) coordinates of each station for the epoch 2015.0 (<https://superdarn.thayer.dartmouth.edu/aacgm.html>). The AACGM coefficients were derived using the secular variation of the IGRF-13 model [Alken et al., 2022]. Notably, the IGRF model must be regularly revised in order to follow the continuous temporal changes of the geomagnetic field generated in the Earth's outer core [Thébault et al., 2015]. At the time this dissertation is being written the AACGM calculator has switched to using the IGRF-13. In this section we will briefly discuss the mathematical formulation of the IGRF model.

The International Geomagnetic Reference Field (IGRF) is a series of mathematical models describing the large-scale internal part of the geomagnetic field $\vec{B}(r, \theta, \phi, t)$ and its annual rate of change (secular variation). On and above the Earth's surface, \vec{B} is defined in terms of a magnetic scalar potential V by $\vec{B} = -\nabla V$ and where in spherical polar coordinates V is approximated by the finite series

$$(1) \quad V(r, \theta, \phi, t) = a \sum_{n=1}^N \sum_{m=0}^n \left(\frac{a}{r}\right)^{n+1} \times [g_n^m(t) \cos(m\phi) + h_n^m(t) \sin(m\phi) P_n^m(\cos\theta)]$$

with r denoting the radial distance from the center of the Earth, $a = 6371.2$ km being the geomagnetic conventional Earth's mean reference spherical radius, θ denoting geocentric co-latitude, and ϕ denoting east longitude. The functions $P_n^m(\cos\theta)$ are the Schmidt quasi-normalized associated Legendre functions of degree n and order m . The Gauss coefficients g_n^m , h_n^m are functions of time and are conventionally given in units of nanotesla (nT).

In the IGRF-13 model, the Gauss coefficients g_n^m and h_n^m are provided for the main field (MF) at epochs separated by 5 years between 1900.0 and 2025.0 A.D. The time dependence of the Gauss coefficients is assumed to be linear over 5-year intervals and is specified by the following expressions

$$(2) \quad g_n^m(t) = g_n^m(T_0) + \dot{g}_n^m(T_0).(t - T_0) \quad \text{and} \quad h_n^m(t) = h_n^m(T_0) + \dot{h}_n^m(T_0).(t - T_0),$$

where \dot{g}_n^m (or \dot{h}_n^m), given in units of nT/year, represent the 5-year average first time derivative (the linear secular variation) of the Gauss coefficients, t is the time of interest in units of year and T_0 is the epoch preceding t which is an exact multiple of 5 years, such that $T_0 \leq t < (T_0 + 5.0)$. When MF models exist for both T_0 and $T_0 + 5.0$, then coefficients $\dot{g}_n^m(T_0)$ can be computed as $[g_n^m(T_0 + 5.0) - g_n^m(T_0)]/5.0$.

The geocentric components of the geomagnetic field in the northward, eastward, and radially inwards directions (X , Y and Z) are obtained from the model coefficients using Equation 1 and by taking the gradient of V in spherical polar coordinates

$$(3) \quad X = \frac{1}{r} \frac{\partial V}{\partial \theta}, \quad Y = -\frac{1}{r \sin \theta} \frac{\partial V}{\partial \phi}, \quad Z = \frac{\partial V}{\partial r}.$$

For some applications, the declination D , the inclination I , the horizontal intensity H , and the total intensity F are required. These components are calculated from X , Y , and Z using the relations,

$$(4) \quad H = \sqrt{X^2 + Y^2}, \quad F = \sqrt{X^2 + Y^2 + Z^2}, \quad D = \arctan(Y/X), \quad I = \arctan(Z/H).$$

In Equation 1, the maximum spherical harmonic degree of the expansion N may vary from one epoch to another. The maximum degree N of the series is equal to 10 up to and including epoch 1995.0 and the coefficients are quoted to 1-nT precision. For epoch 2000, the coefficients are provided to degree and order 13 and quoted to 0.1-nT precision, and from epoch 2005 onwards they are quoted to 0.01-nT precision for the DGRF (and 0.1 nT for the latest non-definitive IGRF), to take advantage of the higher data quality and good coverage provided by the LEO satellite missions. The maximum truncation degree $N = 13$ for epochs after 2000 is defined so as not to include the crustal magnetic field contributions that dominate at higher degrees.

ESA SSA SWE portal: GIC-related products

The ESA Space Weather Service Network provides a plethora of services to a broad spectrum of end-users. Power systems operators, pipelines operators and resource exploitation system operators can be benefited from the following GIC-related products, applying to Earth atmosphere and geomagnetic environment. :

- Local External Magnetic Field on Ground
 - [G.143] Horizontal magnetic rate of change (dH/dt) (UK)
 - [G.159] $dMag/dt$ (i.e., dB_H/dt or dB_D/dt or dB_Z/dt)
 - [G.101] Magnetogrammes from North(West) Europe and Greenland
 - [G.113] Forecasts of dB/dt
 - [G.126] LDiñ
 - [G.127] LCiñ
 - [G.168] Regional Magnetograms
- Local Geomagnetic Induced Geoelectric Field
 - [G.140] Horizontal electric field data (UK)
 - [G.148] Peak Geomagnetically Induced Current (GIC) for Scotland, England, Wales and the UK
 - [G.149] Average Geomagnetically Induced Current (GIC) for Scotland, England, Wales and the UK
 - [G.150] Peak Pipe-to-Soil Potential (PSP) for Scotland, England, Wales and the UK

- [G.151] Average Pipe-to-Soil Potential (PSP) for Scotland, England, Wales and the UK
- [G.164] 3-hourly Telluric index (Lerwick, Eskdalemuir, Hartland)
- [G.165] GIC Index, Bgic for the UK
- [G.111] Maps for power and pipeline operators
- [G.112] Table of modelled GIC
- [G.114] Pipe-to-soil voltage (PSV)
- [G.167] Modelled surface electric field for UK and Ireland

List of publications in peer-reviewed journals

1. Balasis, G., M. A. Balikhin, S. C. Chapman, G. Consolini, I. A. Daglis, R. V. Donner, J. Kurths, M. Paluš, J. Runge, B. T. Tsurutani, D. Vassiliadis, S. Wing, J. W. Gjerloev, J. Johnson, M. Materassi, T. Alberti, C. Papadimitriou, P. Manshour, **A. Z. Boutsis** & M. Stumpo (2023). *Complex Systems Methods Characterizing Nonlinear Processes in the Near-Earth Electromagnetic Environment: Recent Advances and Open Challenges*. Space Sci Rev 219, 38. doi:10.1007/s11214-023-00979-7
2. Balasis, G., **A. Z. Boutsis**, C. Papadimitriou, S. M. Potirakis, V. Pitsis, I. A. Daglis, A. Anastasiadis, & O. Giannakis (2023). *Investigation of dynamical complexity in Swarm-derived geomagnetic activity indices using information theory*. Atmosphere, 14, 890. doi:10.3390/atmos14050890
3. **Boutsis, A. Z.**, G. Balasis, S. Dimitrakoudis, I. A. Daglis, K. Tsinganos, C. Papadimitriou, & O. Giannakis (2023). *Investigation of the geomagnetically induced current index levels in the Mediterranean region during the strongest magnetic storms of solar cycle 24*. Space Weather, 21, e2022SW003122. doi:10.1029/2022SW003122
4. Pitsis, V. G., Balasis, I. A. Daglis, D. Vassiliadis, & **A. Z. Boutsis** (2023). *Power-law dependence of the wavelet spectrum of ground magnetic variations during magnetic storms*. Advances in Space Research, 71, 5, 2288–2298. doi:10.1016/j.asr.2022.10.064
5. Antonopoulou, A., G. Balasis, C. Papadimitriou, **A. Z. Boutsis**, A. Rontogiannis, K. Koutroumbas, I. A. Daglis, & O. Giannakis (2022). *Convolutional Neural Networks for Automated ULF Wave Classification in Swarm Time Series*. Atmosphere, 13(9), 1488. doi:10.3390/atmos13091488

6. Papadimitriou, C., G. Balasis, **A. Z. Boutsis**, A. Antonopoulou, G. Moutsiana, I. A. Daglis, O. Giannakis, P. De Michelis, G. Consolini, J. Gjerloev, & L. Trenchi (2021). *Swarm-derived indices of geomagnetic activity*. JGR: Space Physics, 126, e2021JA029394. doi:10.1029/2021JA029394
7. Balasis, G., C. Papadimitriou, **A. Z. Boutsis**, I. A. Daglis, O. Giannakis, A. Anastasiadis, P. De Michelis & G. Consolini (2020). *Dynamical complexity in Swarm electron density time series using Block entropy*. EPL, 131, 69001. doi: 10.1209/0295-5075/131/69001
8. Papadimitriou, C., G. Balasis, **A. Z. Boutsis**, I. A. Daglis, O. Giannakis, A. Anastasiadis, P. De Michelis, & G. Consolini (2020). *Dynamical Complexity of the 2015 St. Patrick's Day Magnetic Storm at Swarm Altitudes Using Entropy Measures*. Entropy, 22(5), 574. doi:10.3390/e22050574
9. Balasis, G., C. Papadimitriou, & **A. Z. Boutsis** (2019). *Ionospheric response to solar and interplanetary disturbances: a Swarm perspective*. Philosophical Transactions of the Royal Society A: Mathematical, Physical and Engineering Sciences, 377. doi:10.1098/rsta.2018.0098
10. Potirakis, S. M., A. Schekotov, Y. Contoyiannis, G. Balasis, G. E. Koulouras, N. S. Melis, **A. Z. Boutsis**, M. Hayakawa, K. Eftaxias & C. Nomicos (2019). *On Possible Electromagnetic Precursors to a Significant Earthquake ($M_w = 6.3$) Occurred in Lesvos (Greece) on 12 June 2017*. Entropy, 21, 241. doi:10.3390/e21030241

List of publications in conference proceedings

1. Balasis, G., A. Antonopoulou, C. Papadimitriou, **A. Z. Boutsis**, O. Giannakis, & I. A. Daglis. *Machine Learning Techniques for Automated ULF Wave Recognition in Swarm Time Series*. Proceedings of the 2nd Machine Learning in Heliophysics, 21–25 March 2022, held in Boulder, CO, USA. Online at <https://ml-helio.github.io>, p.4
2. **Boutsis, A. Z.**, & G. Balasis. *Wavelet Spectral Analysis of the ENIGMA magnetometer array time series and solar wind conditions around the strongest magnetic storms of solar cycle 24*. Conrad Observatory Journal 2019, 5, 48; ISBN

Number: 978-3-903171-05-3, <https://cobs.zamg.ac.at/gsa/index.php/en/science/publications/conrad-observatory-journal/cobsjournal-5>

List of presentations in international conferences

1. **Boutsi A. Z.**, G. Balasis, S. Dimitrakoudis, I. A. Daglis, K. Tsinganos, C. Papadimitriou, & O. Giannakis, *Investigation of the Geomagnetically Induced Current Index levels in the Mediterranean region during the strongest magnetic storms of solar cycle 24*, (Contributed Oral), IUGG 28th General Assembly, 11–20 July 2023, Berlin, Germany.
2. Antonopoulou A., G. Balasis, C. Papadimitriou, **A. Z. Boutsi**, A. Rontogiannis, K. Koutroumbas, & I. A. Daglis, *Convolutional Neural Networks for Automated ULF Wave Classification in Swarm Time Series*, (Contributed Poster), 16th Hellenic Astronomical Conference, 26–28 June 2023, Athens, Greece.
3. Balasis, G., **Boutsi, A. Z.**, C. Papadimitriou, S. M. Potirakis, V. Pitsis, I. A. Daglis, A. Anastasiadis, & O. Giannakis, *Investigation of Dynamical Complexity in Swarm-Derived Geomagnetic Activity Indices Using Information Theory*, (Contributed Poster), 16th Hellenic Astronomical Conference, 26–28 June 2023, Athens, Greece.
4. **Boutsi A. Z.**, G. Balasis, S. Dimitrakoudis, I. A. Daglis, K. Tsinganos, C. Papadimitriou & O. Giannakis, *Investigation of the Geomagnetically Induced Current Index levels in the Mediterranean region during the strongest magnetic storms of solar cycle 24*, (Contributed Oral), 16th Hellenic Astronomical Conference, 26–28 June 2023, Athens, Greece.
5. Antonopoulou, A., G. Balasis, C. Papadimitriou, **A. Z. Boutsi**, I. A. Daglis, & O. Giannakis, *Convolutional Neural Networks for Automated ULF Wave Classification in Swarm Time Series*, (Contributed Poster), EGU General Assembly 2023, 23–28 April 2023, Vienna, Austria (Hybrid event).
6. Balasis, G., C. Papadimitriou, **A. Z. Boutsi**, G. Vasalos, A. Antonopoulou, O. Giannakis, & A. Smith, *The Time-Frequency Analysis (TFA) toolbox: a versatile processing tool for the recognition of magnetospheric and ionospheric signals in Swarm time series*, (Contributed Poster), EGU General Assembly 2023, 23–28 April 2023, Vienna, Austria (Hybrid event).

7. **Boutsi, A. Z.**, G. Balasis, S. Dimitrakoudis, I. A. Daglis, K. Tsinganos, C. Papadimitriou, & O. Giannakis, *Investigation of the Geomagnetically Induced Current Index levels in the Mediterranean region during the strongest magnetic storms of solar cycle 24*, (Contributed Poster), EGU General Assembly 2023, 23–28 April 2023, Vienna, Austria (Hybrid event).
8. Giannakis, O., I. Demiros, K. Koutroumbas, A. Rontogiannis, V. Antonopoulos, G. De Marchi, C. Arviset, G. Balasis, A. Daglis, G. Vasalos, **A. Z. Boutsi**, J. Tauber, M. Lopez-Caniego, M. Kidger, A. Masson, & P. Escoubet, *TACTICIAN: AI-based applications knowledge extraction from ESA’s mission scientific publications*, (Contributed Poster), EGU General Assembly 2023, 23–28 April 2023, Vienna, Austria (Hybrid event).
9. **Boutsi, A. Z.**, G. Balasis, S. Dimitrakoudis, I. A. Daglis, K. Tsinganos, C. Papadimitriou & O. Giannakis, *Investigation of the Geomagnetically Induced Current Index Levels in the Mediterranean Region During the Strongest Magnetic Storms of Solar Cycle 24*, (Contributed Talk), GIC Modelling in Europe: mini-meeting, 2 February 2023 (Online event).
10. Balasis, G., M. A. Balikhin, B. Tsurutani, S. Wing, I. A. Daglis, C. Papadimitriou, G. Consolini, R. Donner, J. Runge, J. Gjerloev, M. Materassi, J. Johnson, **A. Z. Boutsi**, T. Alberti, D. Vassiliadis, S. Chapman, J. Kurths, & M. Palus, *Complex systems methods characterizing nonlinear processes in the near-Earth electromagnetic environment: Recent advances and open challenges*, (Contributed Talk), 44th COSPAR Scientific Assembly, 16–24 July 2022, Athens, Greece.
11. Balasis, G., I. A. Daglis, O. Giannakis, C. Papadimitriou, A. Antonopoulou, & **A. Z. Boutsi**, *Automated ULF Wave Recognition in Swarm Time Series Using Machine Learning Techniques*, (Contributed Talk), 44th COSPAR Scientific Assembly, 16–24 July 2022, Athens, Greece.
12. **Boutsi, A. Z.**, G. Balasis, I. A. Daglis, K. Tsinganos, & O. Giannakis, *Investigating the levels of Geomagnetically Induced Currents in the Mediterranean region during the most intense geomagnetic storms of solar cycle 24*, (Contributed Talk), EGU General Assembly 2022, 23–27 May 2022, Vienna, Austria (Hybrid event).
13. Manshour, P., C. Papadimitriou, G. Balasis, M. Palus, S. Wing, I. A. Daglis, R. Donner, **A. Z. Boutsi**, G. Consolini, J. Kurths, & B. T. Tsurutani, *Causality and*

- information transfer in interactions of solar wind, radiation belts and geomagnetic field*, (Contributed Talk), EGU General Assembly 2022, 23–27 May 2022, Vienna, Austria (Hybrid event).
14. Papadimitriou, C., G. Balasis, **A. Z. Boutsis**, A. Antonopoulou, G. Moutsiana, I. A. Daglis, O. Giannakis, G. Consolini, J. Gjerloev, & L. Trenchi, ***Swarm-derived indices of geomagnetic activity***, (Contributed Talk), EGU General Assembly 2022, 23–27 May 2022, Vienna, Austria (Hybrid event).
 15. Balasis, G., A. Antonopoulou, C. Papadimitriou, **A. Z. Boutsis**, O. Giannakis, & I. A. Daglis, ***Machine Learning Techniques for Automated ULF Wave Recognition in Swarm Time Series***, (Contributed Talk), EGU General Assembly 2022, 23–27 May 2022, Vienna, Austria (Hybrid event).
 16. Balasis, G., M. A. Balikhin, S. C. Chapman, G. Consolini, I. A. Daglis, R. V. Donner, J. Kurths, M. Palus, J. Runge, B. Tsurutani, D. Vassiliadis, S. Wing, J. W. Gjerloev, J. Johnson, M. Materassi, T. Alberti, C. Papadimitriou & **A. Z. Boutsis**, ***Complex Systems Methods Characterizing Nonlinear Processes in the Near-Earth Electromagnetic Environment***, (Contributed Poster), 17th European Space Weather Week, 25–29 October 2021, Glasgow, Scotland (Hybrid event).
 17. **Boutsis, A. Z.**, G. Balasis, I. A. Daglis, K. Tsinganos, C. Papadimitriou & O. Giannakis, ***Investigation of the Geomagnetically Induced Currents levels in the Mediterranean region during the strongest magnetic storms of solar cycle 24***, (Contributed Talk), 17th European Space Weather Week, 25–29 October 2021, Glasgow, Scotland (Hybrid event).
 18. Balasis, G., C. Papadimitriou, **A. Z. Boutsis**, S. M. Potirakis, I. A. Daglis, O. Giannakis, A. Antonopoulou, P. De Michelis & G. Consolini, ***Dynamical complexity in Swarm time series using entropy analysis***, (Contributed Talk), 11th Swarm Data Quality Workshop, 11–15 October 2021, Athens, Greece (Hybrid event).
 19. Balasis, G., C. Papadimitriou, **A. Z. Boutsis**, S. M. Potirakis, I. A. Daglis, O. Giannakis, P. De Michelis & G. Consolini, ***Dynamical complexity in Swarm-derived storm and substorm indices using information theory measures***, (Contributed Poster), Joint Scientific Assembly: IAGA-IASPEI, 12-27 August 2021 (Virtual event).

20. **Boutsi, A. Z.**, G. Balasis, I. A. Daglis, K. Tsinganos & O. Giannakis, *Investigation of the possibility of GIC development in the Mediterranean region during the strongest magnetic storms of solar cycle 24*, (Contributed Poster), Joint Scientific Assembly: IAGA-IASPEI, 12-27 August 2021 (Virtual event).
21. **Boutsi, A. Z.**, G. Balasis, I. A. Daglis, K. Tsinganos & O. Giannakis, *Investigation of the GIC development in Mediterranean countries during the strongest magnetic storms of solar cycle 24*, (Contributed Poster), 15th Hellenic Astronomical Conference, 5–8 July 2021 (Virtual event).
22. Antonopoulou, A., G. Balasis, C. Papadimitriou, **A. Z. Boutsi**, O. Giannakis, K. Koutroumbas, & A. Rontogiannis, *A Machine Learning technique for ULF wave classification in Swarm magnetic field measurements*, (Contributed vPICO), EGU General Assembly 2021: Gather Online, 19–30 April 2021 (Virtual event).
23. Balasis, G., C. Papadimitriou, S. M. Potirakis, **A. Z. Boutsi**, I. A. Daglis, O. Giannakis, P. De Michelis, & G. Consolini, *A preliminary investigation of dynamical complexity in Swarm Dst-like time series using information theory techniques*, (Contributed vPICO), EGU General Assembly 2021: Gather Online, 19–30 April 2021 (Virtual event).
24. **Boutsi, A. Z.**, G. Balasis, I. A. Daglis, K. Tsinganos & O. Giannakis, *Investigation of the possibility of GIC development in Greece during the strongest magnetic storms of solar cycle 24*, (Contributed vPICO), EGU General Assembly 2021: Gather Online, 19–30 April 2021 (Virtual event).
25. Papadimitriou, C., G. Balasis, **A. Z. Boutsi**, I. A. Daglis, O. Giannakis, P. de Michelis, G. Consolini, J. W. Gjerloev, & L. Trenchi, *Indices of geomagnetic activity derived from space-born magnetic data from the Swarm mission*, (Contributed vPICO), EGU General Assembly 2021: Gather Online, 19–30 April 2021 (Virtual event).
26. Antonopoulou, A., C. Papadimitriou, G. Balasis, **A. Z. Boutsi**, O. Giannakis, K. Koutroumbas, & A. Rontogiannis, *ULF wave investigations at Swarm altitudes using machine learning techniques*, (Contributed Talk), European Space Weather Symposium, 2–8 November 2020 (Virtual event).

27. **Boutsi, A. Z.**, G. Balasis & I. A. Daglis, *Preliminary investigation of the GIC development during the strongest magnetic storms of solar cycle 24 in Greece*, (Contributed Talk), European Space Weather Symposium, 2–8 November 2020 (Virtual event).
28. Papadimitriou, C., G. Balasis, **A. Z. Boutsi**, I. A. Daglis, O. Giannakis, P. De Michelis, & G. Consolini, *Indices of geomagnetic activity derived from space-born magnetic data from the Swarm mission*, (Contributed Talk), European Space Weather Symposium, 2–8 November 2020 (Virtual event).
29. Antonopoulou, A., C. Papadimitriou, G. Balasis, **A. Z. Boutsi**, K. Koutroumbas, A. Rontogiannis, & O. Giannakis, *A deep learning technique for automated detection of ULF waves in Swarm time series*, (Contributed Poster), ESA Φ -week, 28 September–02 October 2020 (Virtual event).
30. Antonopoulou, A., C. Papadimitriou, G. Balasis, **A. Z. Boutsi**, K. Koutroumbas, A. Rontogiannis & O. Giannakis, *A Deep Learning Technique for Automated Detection of ULF Waves in Swarm Time Series*, (Contributed mini Talk), EGU General Assembly 2020: Sharing Geoscience Online, 4–8 May 2020 (Virtual event).
31. Balasis, G., M. A. Balikhin, S. C. Chapman, G. Consolini, I. A. Daglis, R. V. Donner, J. Kurths, M. Palus, J. Runge, B. Tsurutani, D. Vassiliadis, S. Wing, R. Floberghagen, J. W. Gjerloev, J. Johnson, M. Materassi, T. Alberti, **A. Z. Boutsi**, C. Papadimitriou, & A. Strømme, *Complex system perspectives of geospace electromagnetic environment research*, (Contributed mini Talk), EGU General Assembly 2020: Sharing Geoscience Online, 4–8 May 2020 (Virtual event).
32. **Boutsi, A. Z.**, G. Balasis & I. A. Daglis, *Preliminary investigation of the possibility of GIC development in Greece*, (Contributed mini Talk), EGU General Assembly 2020: Sharing Geoscience Online, 4–8 May 2020 (Virtual event).
33. Papadimitriou, C., G. Balasis, **A. Z. Boutsi**, O. Giannakis, A. Anastasiadis, I. A. Daglis, P. De Michelis, & G. Consolini, *Dynamical Complexity of Magnetic Storms at Swarm Altitudes Using Entropy Measures*, (Contributed mini Talk), EGU General Assembly 2020: Sharing Geoscience Online, 4–8 May 2020 (Virtual event).
34. Antonopoulou, A., C. Papadimitriou, **A. Z. Boutsi**, K. Koutroumbas, A. Rontogiannis, O. Giannakis & G. Balasis, *Convolutional Neural Networks for Automated*

- Detection of ULF Waves in Swarm Time Series*, (Contributed Poster), 16th European Space Weather Week, 18–22 November 2019, Liege, Belgium.
35. Balasis, G., R. V. Donner, J. Runge, I. A. Daglis, C. Papadimitriou & **A. Z. Boutsis**, *Complex systems perspectives pertaining to the research of space weather*, (Contributed p-Poster), 16th European Space Weather Week, 18–22 November 2019, Liege, Belgium.
36. Balasis, G., C. Papadimitriou, **A. Z. Boutsis**, P. De Michelis, G. Consolini & the INTENS team, *Investigating dynamical complexity at Swarm altitudes using information-theoretic Measures*, (Contributed Talk), 16th European Space Weather Week, 18–22 November 2019, Liege, Belgium.
37. Boutsis, A. Z., G. Balasis, & I. A. Daglis, *Preliminary investigation of the possibility of GIC development in Greece*, (Contributed p-Poster), 16th European Space Weather Week, 18–22 November 2019, Liege, Belgium.
38. Balasis, G., C. Papadimitriou, **A. Z. Boutsis**, I. A. Daglis, O. Giannakis, G. Hulot, P. Coisson, I. R. Mann, & I. Pakhotin, *New ULF wave indices derived from Swarm observations to investigate magnetosphere-ionosphere coupling*, (Contributed Talk), 9th Swarm Data Quality Workshop, 16–20 September 2019, CTU Prague, Czech Republic.
39. Balasis, G., C. Papadimitriou, **A. Z. Boutsis**, P. De Michelis, G. Consolini & the INTENS team, *Investigating dynamical complexity using a Swarm-derived Dst index and information-theoretic measures*, (Contributed Talk), 9th Swarm Data Quality Workshop, 16–20 September 2019, CTU Prague, Czech Republic.
40. Balasis, G., C. Papadimitriou & **A. Z. Boutsis**, *Investigating dynamical complexity in the topside ionosphere using information-theoretic measures*, (Contributed Talk), 14th Hellenic Astronomical Conference, 8–11 July 2019, Volos, Greece.
41. **Boutsis, A. Z.**, G. Balasis, & I. A. Daglis, *Wavelet spectral analysis of the ENIGMA magnetometer array and solar wind time series around the strongest magnetic storms of solar cycle 24*, (Contributed Poster), 14th Hellenic Astronomical Conference, 8–11 July 2019, Volos, Greece.
42. Balasis, G., C. Papadimitriou, **A. Z. Boutsis**, I. A. Daglis, O. Giannakis, G. Hulot, P. Coisson, I. R. Mann, & I. Pakhotin, *New ULF & ELF wave indices derived from*

- Swarm observations to investigate magnetosphere-ionosphere coupling***, (Contributed Talk), ESA Living Planet Symposium 2019, 13–17 May 2019, Milan, Italy.
43. Balasis, G., C. Papadimitriou, & **A. Z. Boutsis**, ***Investigating dynamical complexity at Swarm altitudes using information-theoretic measures***, (Contributed Poster), ESA Living Planet Symposium 2019, 13–17 May 2019, Milan, Italy.
44. Balasis, G., C. Papadimitriou, **A. Z. Boutsis**, I. A. Daglis, O. Giannakis, G. Hulot, P. Coisson, I. R. Mann, & I. Pakhotin, ***New indices derived from Swarm observations to investigate space weather and geomagnetic activity hazards***, (Contributed Talk), EGU General Assembly 2019, Vienna, Austria, 7–12 April 2019.
45. **Boutsis, A. Z.**, G. Balasis, & I. A. Daglis, ***Wavelet spectral analysis of the ENIGMA magnetometer array and solar wind time series around the strongest magnetic storms of solar cycle 24***, (Contributed PICO), EGU General Assembly 2019, Vienna, Austria, 7–12 April 2019.
46. Papadimitriou, C., G. Balasis, & **A. Z. Boutsis**, ***Investigating dynamical complexity in the topside ionosphere using information-theoretic measures***, (Contributed Poster), EGU General Assembly 2019, Vienna, Austria, 7–12 April 2019.
47. Balasis, G., C. Papadimitriou & **A. Z. Boutsis**, ***Investigating dynamical complexity in the topside ionosphere using information-theoretic measures***, (Contributed p-Poster), 15th European Space Weather Week, Leuven, Belgium, 5–9 November 2018.
48. **Boutsis, A. Z.**, & G. Balasis, ***Wavelet spectral analysis of the ENIGMA magnetometer array time series and solar wind conditions around the strongest magnetic storms of solar cycle 24***, (Contributed Talk), Europlanet NA1 Workshop 'Uniting Planetary Models and Data Analysis Tools / Resources', Kalamata, Greece, 11–14 September 2018.
49. **Boutsis, A. Z.**, & G. Balasis, ***Wavelet Spectral Analysis of the ENIGMA Magnetometer Array Time Series and Solar Wind Conditions around the Intense Magnetic Storms of March, June and December 2015***, (Contributed Talk),

25th Summer school - Workshop on Dynamical Systems and complexity, NCSR DEMOKRITOS, Athens, Greece, July 2018.

50. **Boutsi, A. Z.**, & G. Balasis, *Wavelet Spectral Analysis of the ENIGMA Magnetometer Array Time Series and Solar Wind Conditions around the Strongest Magnetic Storms of Solar Cycle 24*, (Contributed Talk), XVIIIth IAGA Workshop on Geomagnetic Observatory Instruments, Data Acquisition and Processing, Conrad Observatory of the Zentralanstalt für Meteorologie und Geodynamik (ZAMG), Austria, June 2018.